UNICA

UNIVERSITÀ
DEGLI STUDI
DI CAGLIARI

Ph.D. DEGREE IN
Mathematics and Computer Science

Cycle XXXVI

TITLE OF THE Ph.D. THESIS

Mathematical methods for radio pulsar searching and applications

Scientific Disciplinary Sector(s)

MAT/07

Ph.D. Student:	Viviana Piga
Supervisor	Roberto Tonelli
Co-Supervisors	Maura Pilia, Alessandro Ridolfi

Final exam. Academic Year 2022/2023
Thesis defence session: October 2024

Contents

Ringraziamenti **7**

Introduction and thesis structure **9**

1 Pulsars **11**
1.1 The discovery of pulsars . . . 11
1.2 Formation of pulsars . . . 12
1.3 Pulsar properties . . . 14
1.3.1 Dipole radiation and spin-down . . . 14
1.3.2 Age . . . 15
1.3.3 Magnetic field . . . 16
1.3.4 Emitted spectrum . . . 16
1.4 Interstellar medium and its effects . . . 16
1.4.1 Dispersion . . . 17
1.4.2 Scattering . . . 19
1.5 Pulsar populations . . . 19
1.5.1 Ordinary and young pulsars . . . 20
1.5.2 Magnetars . . . 21
1.5.3 Recycled pulsars . . . 21
1.6 Distribution of pulsars . . . 22
1.6.1 Pulsars in globular clusters . . . 23
1.6.2 Extra-galactic pulsars . . . 25
1.7 Radio telescopes and pulsar observations . . . 26
1.8 The many scientific applications of pulsars . . . 27
1.8.1 Study of the interstellar medium . . . 27
1.8.2 Tests of gravity and equations of state . . . 27
1.8.3 Detection of ultra-low-frequency gravitational waves . . . 28
1.8.4 Stellar and binary evolution . . . 28
1.8.5 Study of globular clusters . . . 29

2 Time-series analyses and techniques for radio pulsar searching **31**
2.1 The basics of how to find a pulsar . . . 31
2.2 A realistic pulsar searching pipeline . . . 32
2.2.1 Data acquisition . . . 34
2.2.2 RFI mitigation . . . 35
2.2.3 Search planning . . . 35
2.2.4 De-dispersion (+ barycentering) . . . 36
2.2.5 Periodicity search . . . 37
2.2.5.1 Frequency-domain algorithms . . . 37
2.2.5.2 Time-domain algorithms . . . 38
2.2.6 Sifting . . . 38
2.2.7 Folding . . . 38
2.2.8 Candidate inspection . . . 38

2.3 State of the art of pulsar searching algorithms . . . 39
2.3.1 Detecting pulsar in binary systems . . . 40
2.3.1.1 Acceleration search . . . 41
2.3.1.2 Jerk search . . . 43
2.3.1.3 "Phase-modulation" (or "side-band") search. . . . 44
2.3.1.4 Full Keplerian Template Bank search . . . 45
2.3.2 Improved algorithms for isolated pulsars . . . 46
2.3.2.1 The Fast Folding Algorithm . . . 46
2.3.2.2 Stack search . . . 47
2.3.3 Single pulse search . . . 48

3 Application to globular cluster data **49**
3.1 Introduction . . . 49
3.1.1 Pulsars in globular clusters at the "Murriyang" radio telescope . . . 49
3.1.2 Pulsars in globular clusters at the MeerKAT radio telescope . . . 51
3.2 Observations . . . 51
3.2.1 The Parkes dataset . . . 53
3.2.2 The MeerKAT dataset . . . 53
3.2.3 Sensitivity . . . 54
3.3 Data analysis . . . 56
3.4 Results . . . 60
3.5 Discussion and future work . . . 62

4 Searching for pulsars in Westerlund 1 **65**
4.1 Introduction . . . 65
4.2 Observations . . . 66
4.3 Data Analyses and Results . . . 68
4.3.1 Initial searches of radio pulsations from the magnetar . . . 68
4.3.2 Deep periodicity search . . . 68
4.3.3 Single pulse search . . . 70
4.3.4 Timing of the new pulsar PSR J1646−4545 . . . 71
4.4 Discussion . . . 72
4.4.1 The case of PSR J1646−4545 . . . 72
4.4.1.1 The position of the pulsar . . . 73
4.4.1.2 The dispersion measure of the pulsar . . . 75
4.4.1.3 The age of the pulsar . . . 75
4.4.2 No radio pulsars in Westerlund 1 . . . 76
4.5 Conclusions . . . 78

5 Summary and Outlook **79**
5.1 Summary . . . 79
5.2 Outlook . . . 80
5.2.1 Algorithm development and optimization . . . 81
5.2.2 Confirmation of globular cluster pulsar candidates . . . 81
5.2.3 Deeper searches in Westerlund 1 . . . 82

Appendices **83**

A Best candidate pulsars in globular clusters **85**
A.1 Best candidate pulsars found in NGC 288 85
A.2 Best candidate pulsars found in E3 87
A.3 Best candidate pulsars found in NGC 3201 88
A.4 Best candidate pulsars found in NGC 4372 91
A.5 Best candidate pulsars found in NGC 4590 96
A.6 Best candidate pulsars found in NGC 4833 98
A.7 Best candidate pulsars found in NGC 5286 99
A.8 Best candidate pulsars found in ESO 452 101
A.9 Best candidate pulsars found in NGC 6541 104
A.10 Best candidate pulsars found in NGC 6584 115

Bibliography **117**

Ringraziamenti

Luna! Luna!
Bettami fortuna,
bettami dinai,
po mi Coiai,
po mi fai Bella.
Sa Luna, Sa Stella

a Niky D' Amico,
ma soprattutto a mia Nonna.

Quasi 5 anni fa, grazie ad una coincidenza incredibile, sono stata catapultata nello strano mondo dell' Astrofisica, di cui non sapevo assolutamente nulla e che mi ha sconvolto la vita.

Il mio primo ringraziamento va dunque a Gemiliano e a Delphine, che hanno fatto accadere questa magia , dimostrandomi, per l'ennesima volta, che la vita è piena di sorprese.

L'elenco delle persone da ringraziare è pero lunghissimo, perchè sono stati anni davvero intensi, e difficili, per tutti. Una dottorato intervallato da una pandemia mondiale, in collaborazione con gli astrofisici.Che follia!!

Studiosi incredibili che, nonostante tutto, continuavano a scrutare l'Universo, guardando degli astrusi plot sugli schermi dei loro computer. Plot che presto, nel mio piccolo, avrei imparato a leggere anche io, sostenendo, ad ogni minima occasione, e con malcelata spocchia, che gli astrofisici sono più strambi dei matematici. Cosa che non credevo possibile.

I miei primi ringraziamenti vanno ai miei supervisor: Maura Pilia, Andrea Possenti, Scott Randsom e Roberto Tonelli. Le loro competenze, il loro sostegno e la loro fiducia hanno permesso la realizzazione di questo progetto .

Ringrazio sentitamente anche Marta Burgay, Alessandro Corongiu, Alessandro Papitto, Paolo Esposito, Gianluca Israel, Nanda Rea, Perna Rosalba e Colpi Monica, che hanno revisionato il mio articolo e la mia tesi, permettendole di venire alla luce.

Ancora grazie a tutti i colleghi e amici di OAC. Non posso non citare Eleonora L., Guglielmo M., Matteo T., Elisabetta L. ,Caterina T., Hamza, Claudia M., Sara M. e Paolo M., compagni di lavoro meravigliosi, ma anche testimoni di risate e di pianti. Il vostro sostegno e la vostra fiducia mi hanno permesso di arrivare sino alla fine.

A Vittorio de Falco, brillantissimo matematico partenopeo, capace di risponderti a qualsiasi ora . Onorata di aver potuto lavorare con te.

Grazie ad Emmanuel, che mi ha salvata dal mio terzo covid, durante una conferenza a Manchester, e che mi ha sostenuta, con grande affetto, sino a qui.

Ai miei colleghi del corso d'inglese, Vincenzo e Azzurra, e alla meravigliosa e dolcissima Estelle.

Un grazie enorme alla mia famiglia. Alla mia Mamma che è la mia pulsar, il mio faro. A Papà, che è sicuramente una stella luminosa, non visibile con i classici telescopi e satelliti, ma visibile da me, perchè emette alla frequenza del mio cuore. Vi amo tantissimo.

Alle danzatrici, e alle danza, che mi hanno accompagnata durante questi anni, facendomi riscoprire la vera passione e ricordandomi che sono una persona incline alle dipendenze. Siete la mia galassia felice, che non smetterò mai di amare.

Concludo questo lungo elenco con la persona a cui devo questo mio percorso, Alessandro Ridolfi. Non potrò mai dimenticare le sue lezioni di astronomia, di PRESTO e di quelle strane diavolerie che usa per scovare le pulsar. Le nostre interminabili chiacchierate in inglese, intervallate da modi di dire romani e dalle lezioni di sardo. L' infinita pazienza verso una sarda quadratica media, come ama definirmi, testarda , capricciosa, scalpitante e ansiosa. Ma spero con un grande cuore, mai come il suo.

Ricordo benissimo il suo salto nella sedia per la gioia alla scoperta della "mia" pulsar. Questa stella è stata chiamata da Marta " Serry", Serendipity. La Serendipità è la capacità di fare scoperte del tutto casuali quando si sta cercando altro. Marta non avrebbe potuto scegliere un nome migliore.

Ed è questo l'augurio che faccio al Ridolfi , perchè la vita è tutto quello che ti succede nel mentre.

Buona strada Ale, e grazie dal profondo del mio cuore.

Introduction and thesis structure

Since the dawn of civilization, mathematics has been a key tool that humans have used to try and understand the laws of nature and the world that surrounded them. The very first foundations of mathematics were laid by the ancient civilizations of Sumerians, Egyptians and Babylonias, which used mathematics as an instrument to quantify and describe their world. The Greeks further revolutionized this field, with Euclid and Pythagoras formalizing the mathematical thought into axioms and theorems that are still valid today. A major cornerstone, which consecrated the role of mathematics for our understanding of the universe, was the development of the scientific method, with Galileo Galilei being one of its greatest representatives. Galileo's empirical observations and innovative experiments laid the groundwork for modern physics. In particular, his use of the telescope to study celestial bodies, and his subsequent support for the heliocentric model, exemplified the power of mathematical precision and the scientific method in challenging long-held beliefs. Galileo's legacy is a testament to the key role of mathematics in our ability to understand the universe, and is the foundation of the scientific research method that we currently use.

The last few decades have witnessed yet another pivotal change in the way science is made: the technological revolution. The advent of computers, with their ability of doing computations extraordinarily fast, has opened up entire new possibilities that were simply inconceivable even just a few years ago. Besides allowing to numerically solve complex equations and non-linear systems that would have been impossible to solve otherwise, the exponential growth in the computing power has also led to the massive application of innovative techniques, such Artificial Intelligence algorithms, to all aspects of our lives, including science itself.

In this PhD thesis, we will focus on the applications of mathematical algorithms in astrophysics, specifically those used to search for radio pulsar signals in radio astronomical data. These algorithms are notoriously computationally extremely expensive, so we will also discuss their implementation on modern high-performance-computing systems, as well as possible ways to improve their efficiency. Here follows a brief outline of how this thesis is structured.

- In **Chapter 1** we provide a general introduction to pulsars for the non-expert reader. We briefly outline the challenges related to their observation and discuss the main astrophysical applications.
- In **Chapter 2** we delve into the details of pulsar searching. We explain the basic principles and mathematical tools that are used to the detect the radio signal emitted by pulsar, and we go into the details of the more sophisticated techniques that allow us to maximize our capability of detecting pulsars under particular conditions.
- In **Chapter 3** we apply some of the pulsar searching techniques discussed in the previous chapter to real observations of globular clusters acquired with the Australian Parkes radio telescope, and with the South African MeerKAT radio telescope.

- In **Chapter 4** we also apply different search algorithms to observations of the young massive cluster Westerlund 1, also observed with the Australian Parkes radio telescope.
- In **Chapter 5** we summarize our findings and provide some prospects for future work as follow-ups of the results obtained in this thesis.

Chapter 1

Pulsars

1.1 The discovery of pulsars

Pulsars are a particular subclass of fast-rotating neutron stars (NSs), endowed with a very strong dipolar magnetic field, that emit electromagnetic waves from their magnetic poles. This emission comes in the form of two highly collimated beams of radiation along the magnetic axis. Being the latter misaligned with respect to the rotation axis, the resulting effect is that the neutron star appears to emit a pulse of radiation every time that one beam sweeps across the line of sight of the distant observer, exactly like a lighthouse on Earth (see Figure 1.1).

The discovery and subsequent understanding of pulsars represent a milestone chapter in the history of astrophysics. In the early 20th century, the theoretical groundwork for the existence of neutron stars was laid shortly after the discovery of the neutron by James Chadwick in 1932. In particular, Baade and Zwicky were the first to propose the concept of "neutron stars" in 1934, suggesting that these objects could be the remnants of supernova explosions, i.e. the last act in the evolutionary cycle of massive stars (Baade & Zwicky, 1934). During one of these events, the core of the massive star would collapse, resulting in the formation of an extremely compact object made of neutrons. The first theoretical models that described the internal structure of a NS were developed by Oppenheimer & Volkoff (1939), and later refined by Fowler & Hoyle (1964). Their models predicted that NSs would have extremely high densities, higher than those of atomic nuclei. Shortly after, Colgate & White (1966) predicted that NSs would also have very strong magnetic fields and high spin rates of few tens to hundreds of rotations per second, as a consequence of the conservation of magnetic flux and angular momentum from the progenitor star. The strong magnetic field and high spin rate, combined together, would produce electromagnetic radiation. Indeed, Hoyle et al. (1964) and Pacini (1967), posited that a neutron star could be the engine that powers the observed X-ray emission of the Crab Nebula, a famous and well-studied remnant of a supernova explosion occurred in the year 1054 in the northern sky.

This theoretical framework set the stage for the discovery of pulsars, which occurred in 1967. In that year, Ph.D. student Jocelyn Bell Burnell, and her supervisor, Prof. Anthony Hewish, were working on a survey to study the effect of interplanetary scintillation. For this experiment, they were using a newly commissioned telescope at the Mullard Radio Astronomy Observatory near Cambridge (UK), which was observing the sky at a frequency of 81.5 MHz. Among the signals that Bell and Hewish were analyzing, they found one that was repeating in an extremely regular fashion, once every 1.337 seconds. The signal was appearing every day around the same time. However, they noticed that, every time, it was appearing approximately 4 minutes earlier than the previous day. This was a clear indication that the signal was not terrestrial, rather

it was coming from a distant location outside the Solar System, and they could hence record it every day at the same sidereal time. Although at the time it was not clear what the actual origin of the signal was (some speculated that they could be "little green men", i.e. aliens that were sending these signals), what Jocelyn Bell had found was the very first pulsar, which we now refer to as PSR B1919+21 (Hewish et al., 1968). In the following years, a few more pulsating sources with very similar signal properties were found, in particular more pulsars were identified, such as the Vela (Large et al., 1968) and the Crab pulsars (Staelin & Reifenstein, 1968; Comella et al., 1969), associated with known supernova remnants. From their characteristics, it soon became clear that such a fast periodic emission could only be produced by extremely compact objects that were rotating very fast. In particular, as put forward by Gold (1968), only a rotating NS could explain all the phenomenology seen in the observed sources, including, among other things, their association with supernova remnants. The term *pulsar*, short for PULSating stAR, was then coined to describe these objects. The discovery of pulsars was monumental, as it confirmed the existence of neutron stars and provided evidence for their properties, more than 30 years after they had been theorized.

As of today, more than 3600 pulsars have been discovered and cataloged, according to the ATNF pulsar database[1] (Manchester et al., 2005). The discovery of such a large number of pulsars was possible thanks to numerous radio telescopes that, over the decades, conducted extensive surveys aimed at expanding the total known pulsar population (e.g. Manchester et al., 2001; Keith et al., 2010; Barr et al., 2013). Despite this, the precise mechanism behind the radio emission of pulsars remains a mystery, even fifty years after their initial discovery.

1.2 Formation of pulsars

As we saw earlier, a pulsar is a particular neutron star. In order to understand how a pulsar is formed, we therefore need to understand how a NS can be produced, which in turn depends on the evolution of the progenitor star. The evolution of a star is now a well-understood process, which is governed by the balance between gravity and nuclear forces. And, it is now well established that a neutron star is the end result of the evolution of a massive $(8\ M_\odot < M < 25\ M_\odot)$ main sequence star.

Indeed, a typical star, like our Sun, spends the vast majority of its life in a state called "main sequence", during which it maintains equilibrium against gravitational collapse through the outward radiative pressure generated by nuclear fusion (Vogt, 1926; Russell, 1931). This stage involves the conversion of hydrogen into helium in the core, a process called *proton-proton reaction*, which releases the energy that also provides the star's luminosity. This nuclear fusion generates a radiative pressure that counterbalances the gravitational pull due to the mass of the star itself, which would make the star collapse on itself if not contrasted by an opposing force. The total time that a star spends in its main sequence depends solely on its mass: more massive stars consume their nuclear fuel at a much faster rate than stars of smaller mass, and will therefore spend much less time in their main sequence than lighter stars. For example, our Sun, which weighs 1 solar mass, will spend a total of ~ 10 Gyr in its

[1] https://www.atnf.csiro.au/research/pulsar/psrcat

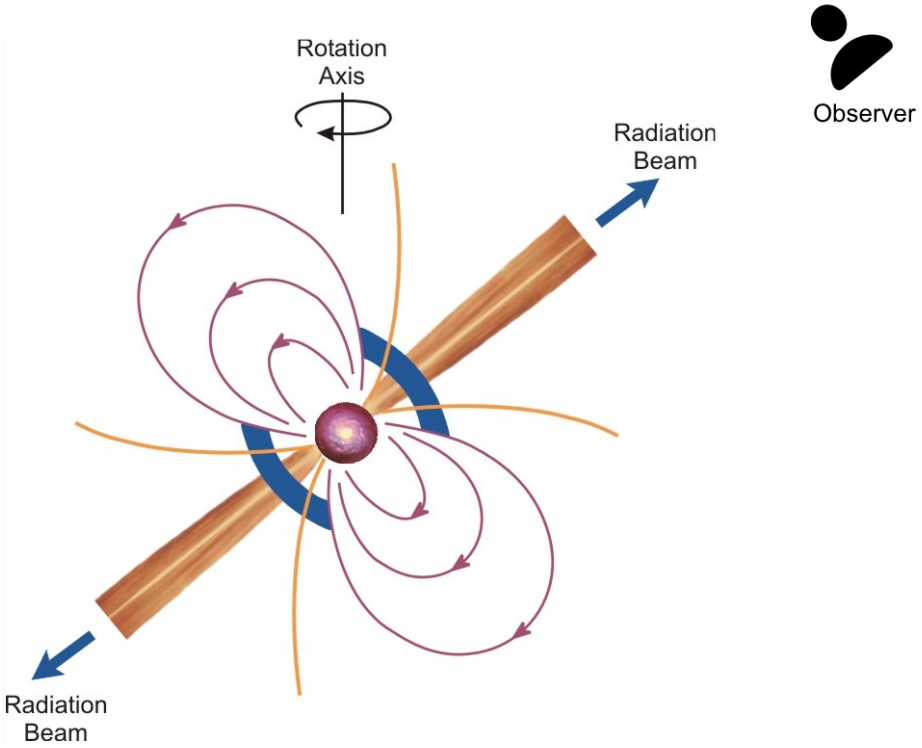

Figure 1.1. Schematic representation of a radio pulsar. Figure adapted from NRAO (https://www.nrao.edu/pr/2002/3c58/pulsars/pulsardiagram.jpg).

main sequence phase. On the other hand, a star with ten times the mass of the Sun, will spend just ~ 20 Myr in its main sequence phase.

When all the hydrogen is turned into helium, the star will leave its main sequence phase and its core will shrink, causing its temperature to rise. When this temperature becomes high enough, the fusion of helium will start to take place. This process releases energy that causes the star to expand, entering the so-called giant phase. For stars lighter than ~ 8 $M_\odot$, once the helium is also depleted, the star will not have enough mass to trigger the fusion of heavier elements. In that case, the star then will shed its outer layers and form a planetary nebula, leaving behind a *white dwarf* (WD). On the other hand, if the mass of the star is larger than ~ 8 $M_\odot$, a new contraction of the core occurs, resulting in the heating and fusion of heavier elements, such as carbon, neon and oxygen, within a series of concentric shells, in each of which a different element burns. This cycle continues, for the most massive stars, until the burning of iron (^{56}Fe). Contrary to previous fusion reaction, the fusion of ^{56}Fe is an endothermic process, that is, it requires energy to be provided from the outside, in order for the process to happen. This means that the fusion of iron does not have any energy release associated. As a consequence, there is no outward pressure to counteract gravity, hence the star can no longer sustain itself, eventually collapsing. This event results in a tremendous explosion, called a core-collapse supernova, during which about 10^{10} times the luminosity of the Sun is released (Arnett, 1996). The envelope of the star is violently ejected, forming a so-called *supernova remnant* (SNR), while the core implodes.

If the mass of the core exceeds the Chandrasekhar mass ($\simeq 1.44\,\mathrm{M}_\odot$; Chandrasekhar 1931, 1935), the collapse will continue until the matter is confined within a radius of ~ 10 km (Lattimer & Prakash, 2001). Under such conditions, the density can reach $\sim 10^9\,\mathrm{kg\,m^{-3}}$ and, when this occurs, protons and electrons are forced to merge through electron capture, forming neutrons and releasing a burst of neutrinos, a process called *inverse-β decay*. The neutrons so formed arrange themselves in a lattice where quantum phenomena occur. In particular, as neutrons are a gas of fermions, a quantum degeneracy pressure builds up, and the latter is strong enough to contrast gravity and therefore to keep the star as a stable sphere of just a few kilometres across: that is what we call a *neutron star*.

1.3 Pulsar properties

A full understanding of the whole pulsar phenomenon, in particular in regards to the exact mechanisms that powers the pulsar emission, is far from being obtained. Notwithstanding, many characteristics of pulsars can still be excellently explained starting from a very simple model where the pulsar is assumed to be a neutron star, endowed with a dipolar magnetic field, that spins in a vacuum.

This model, originally proposed by Goldreich & Julian (1969) and further improved over the years, is sufficient to derive useful analytical expressions that relate some key properties of a pulsar to observable (and in most cases, easily measurable) quantities: the spin period, P, and the first and second time derivatives of the latter, $\dot{P}$ and $\ddot{P}$.

1.3.1 Dipole radiation and spin-down

Let us consider a dipolar magnetic field with a magnetic moment $\mathbf{m}$, misaligned by an angle α_m with respect to the rotation axis of the neutron star, $\mathbf{S}$. The magnetic field spins around the rotation axis with an angular frequency Ω. It can be shown, through classic electrodynamics (e.g. Jackson, 1962), that such a spinning magnetic field will radiate power in the form of electromagnetic waves at a rate of:

$$\dot{E}_\mathrm{dipole} = \frac{2}{3}\frac{|\mathbf{m}|^2\Omega^4\sin^2\alpha_\mathrm{m}}{c^3}\,, \tag{1.1}$$

On the other hand, we know that the pulsar emission is ultimately powered by the neutron star's rotational kinetic energy:

$$E_\mathrm{rot} = \frac{1}{2}\mathcal{I}\,\Omega^2\,, \tag{1.2}$$

where $\mathcal{I}$ is the NS moment of inertia, which is assumed to be $10^{45}\ \mathrm{g\,cm^2}$. The rate of energy loss, also referred to as *spin-down luminosity*, L_sd, is obtained by taking the time derivative of E_rot:

$$L_\mathrm{sd} = -\frac{\mathrm{d}}{\mathrm{d}t}\left(\frac{1}{2}\mathcal{I}\,\Omega^2\right) = -\mathcal{I}\,\Omega\,\dot{\Omega} = 4\pi^2\,\mathcal{I}\,\dot{P}P^{-3}\,. \tag{1.3}$$

By equating Eq. (1.3) to Eq. (1.1), we can therefore derive the pulsar spin-down

rate:

$$\dot{\Omega} = -\left(\frac{2|\mathbf{m}|^2 \sin^2 \alpha_{\rm m}}{3\mathcal{I}\, c^3}\right)\Omega^3 \,. \tag{1.4}$$

which, as we can see, is proportional to the third power of the rotational frequency. This, however, assumes a perfectly dipolar magnetic field and only dipole radiation as the only emission process taking place. If one wants to account for possible deviations from the model of a perfect dipole in a vacuum, a more general form of Eq. (1.4) would be written as:

$$\dot{\Omega} = -K\Omega^n \,, \tag{1.5}$$

where K is a constant and n is called the *braking index*. The latter is relevant as its value depends on the underlying processes that power the pulsar emission: differentiating Eq. (1.5) with respect to time and by using it again to eliminate the constant K, one obtains:

$$n = \frac{f\ddot{f}}{\dot{f}^2} \,. \tag{1.6}$$

As can be seen, the braking index can be obtained by just measuring the spin frequency and its first two time derivatives. However, while f and $\dot{f}$ are typically very easy to measure, this is not the case for $\ddot{f}$, whose measurement is often contaminated by timing noise (particularly for slow pulsars) or it is simply too small to be measured.

1.3.2 Age

Let us take Eq. (1.5) and write it in terms of P and $\dot{P}$:

$$\dot{P} \equiv \frac{{\rm d}P}{{\rm d}t} = KP^{(2-n)} \quad \Rightarrow\ P^{(n-2)}{\rm d}P = K{\rm d}t \,. \tag{1.7}$$

We can now integrate both members, assuming $n \neq 1$, along the whole lifetime of the pulsar, that is, from its birth ($t = 0$) to the present time $\tau_{\rm p}$:

$$\int_{P_0}^{P} P^{(n-2)}{\rm d}P = K\int_0^{\tau_{\rm p}} {\rm d}t \,, \tag{1.8}$$

where $P_0 \equiv P(t = 0)$ is the pulsar spin period at birth. Solving the integrals, we find:

$$\tau_{\rm p} = \frac{P}{(n-1)\dot{P}}\left[1 - \left(\frac{P_0}{P}\right)^{n-1}\right] . \tag{1.9}$$

Now, by further assuming that the pulsar spin period today is much larger than its value at birth ($P_0 \ll P$) and that the only emission mechanism is pure dipole braking ($n = 3$), Eq. (1.9) becomes:

$$\tau_{\rm p}(P_0 \ll P; n = 3) \equiv \tau_{\rm c} = \frac{P}{2\dot{P}} \quad . \tag{1.10}$$

which defines what is referred to as the *characteristic age* of the pulsar. This should be considered only as an order-of-magnitude estimate of the real age of the pulsar. However, in some noteworthy cases, such as that of the Crab pulsar, the characteristic age turns out to be about 1200 years, strikingly close to the real age of the pulsar,

which is known to be born in the year 1054 AD, when the supernova explosion of the progenitor star was widely observed on Earth and recorded by Chinese astronomers.

1.3.3 Magnetic field

Another physical quantity that can be easily estimated is the pulsar's surface magnetic field.

Knowing that the strength of a dipolar magnetic field scales as:

$$B(r) \propto \frac{|\mathbf{m}|}{r^3}\,. \tag{1.11}$$

where r is the distance and, again, assuming that the only emission mechanism is pure dipole braking ($n = 3$), we can use Eq. (1.4) to express $|\mathbf{m}|$ as a function of P and $\dot{P}$. In this way, the magnetic field at the surface of a neutron star of radius R is simply:

$$B_{\rm s} \equiv B(r=R) = \sqrt{\frac{3c^3}{8\pi^2}\frac{\mathcal{I}}{R^6\,\sin^2\alpha_{\rm m}}P\dot{P}} \simeq \left(\frac{\dot{P}}{10^{-15}}\right)^{1/2} \times \left(\frac{P}{\rm s}\right)^{1/2} \times 10^{12}\ {\rm G}\,, \tag{1.12}$$

where, typically, it is assumed $R \sim 10$ km, $\mathcal{I} \simeq 10^{45}$ g cm^2 and $\alpha_{\rm m} = 90$ deg.

1.3.4 Emitted spectrum

Pulsars are very weak radio sources, with typical pulsed mean flux densities of the order of the 10^{-3}–10^{-5} Jy, when observed at radio frequencies around 1 GHz. However, pulsars have been observed across a very wide range of radio frequencies, which go from a few tens of MHz to as much as 291 GHz (Torne et al., 2017), and their luminosity vary significantly as a function of the observing frequency. In fact, different studies (e.g., Maron et al. 2000) have measured the flux density at different radio frequencies of a large sample of pulsars, showing that their dependency can be, in most cases, described by a simple power-law:

$$S_{\rm mean}(\nu) \propto \nu^{\xi}\,, \tag{1.13}$$

with the spectral index, ξ, being measured $\xi \simeq -1.8 \pm 0.2$ across the whole population (Maron et al., 2000), regardless of the pulsar type (Kramer et al., 1998; Toscano et al., 1998), with the sole exception of magnetars, whose spectra are often remarkably flat (e.g., Camilo et al. 2008). A small fraction of pulsars, however, show more complex spectra. For instance, some pulsars require a two-component power-law to fit their spectrum (Sieber, 1973), while others show a spectral turn-over at a frequency that is typically in the range between 100 MHz and 1 GHz (Kijak et al., 2011; Rajwade et al., 2016).

1.4 Interstellar medium and its effects

The electromagnetic waves produced by a pulsar transverse regions in our Galaxy that are permeated by the interstellar medium (ISM) before they arrive to Earth. A

number of physical effects arise from the crossing of this path. These effects will modify the emitted radiation in a variety of ways such as dispersion, scintillation, scattering and Faraday rotation (Lorimer & Kramer, 2004). The effects of dispersion and Faraday rotation can be understood through the adoption of an homogeneous plasma model. Scintillation and scattering, on the other hand, require a more realistic model of inhomogeneous gas which can give rise to turbulence phenomena. In this work, we will be mainly concerned with the effects of dispersion and, to a lesser extent, scattering. In the following, we will discuss these two effects in more detail.

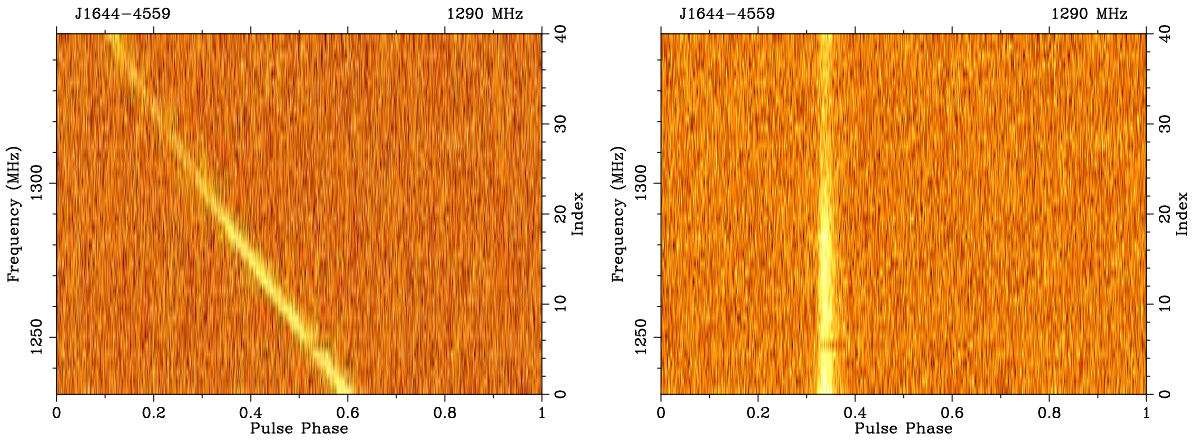

Figure 1.2. Left panel: dispersion effect in the signal of the 455-ms pulsar B1641-45 within 120 MHz of bandwidth between the frequencies of 1230 MHz and 1350 MHz. The DM of the pulsar is 478.66 $\mathrm{pc\ cm^{-3}}$. The delay in the arrival time of the pulses between the top and the bottom of the band is 222 ms. Right panel: same observation after being de-dispersed.

1.4.1 Dispersion

The first (and most relevant for this thesis work) interstellar medium effect is called *dispersion*. This is the phenomenon by which electromagnetic waves propagate at different speed, depending on their frequency, when passing through a medium that contains free electrons. The ISM very often has an ionized component, which makes it a dispersive medium.

In a vacuum, electromagnetic waves travel at the speed of light, $c = 299792458$ m/s, regardless of their frequency ν. However, if the same radiation travels through a dispersive medium, its propagation speed, v, will be lower by a factor $n(\nu)$, referred to as *refractive index*, that depends on the frequency of the radiation:

$$v(\nu) = n(\nu)\, c\,. \tag{1.14}$$

The refractive index is always smaller than 1 and it in turn depends on the physical properties of the medium. If we ignore higher order terms and corrections due to the magnetic field, the refractive index of the ionized ISM can be expressed as (e.g. Lorimer & Kramer, 2004):

$$n(\nu) = \sqrt{1 - \left(\frac{\nu_\mathrm{p}}{\nu}\right)^2}\quad . \tag{1.15}$$

where ν_p is called *plasma frequency* and is defined as:

$$\nu_\mathrm{p} = \sqrt{\frac{e^2 n_\mathrm{e}}{\pi m_\mathrm{e}}} \simeq 8.5 \text{ kHz} \left(\frac{n_\mathrm{e}}{\mathrm{cm}^{-3}}\right)^{1/2} . \tag{1.16}$$

Here n_e is the electron number density of the plasma, whereas e and m_e are the charge and the mass of the electron, respectively.

From Eq. (1.15) we can easily deduce that, in a dispersive medium, electromagnetic waves with higher frequencies move faster those at lower frequencies. As a result, when observing a pulsar within a given observing band, the pulsed signal at high frequencies will arrive earlier than the same signal at low frequencies. We can also note that, in the limit of $\nu \to \infty$, the refractive index $n(\nu) \to 1$ and the speed is the same as in a vacuum ($v = c$). On the other hand, if $\nu < \nu_\mathrm{p}$, Eq. (1.15) cannot be solved: physically, this means that an electromagnetic wave at such low frequency cannot propagate at all in that dispersive medium.

We can use Eq. (1.14) to quantify the delay $\Delta t_{(\nu,\infty)}$ between the arrival times of an electromagnetic wave of frequency ν and another one of infinite frequency:

$$\Delta t_{(\nu,\infty)} = \left[\int_0^d \frac{\mathrm{d}l}{v_\mathrm{g}(\nu)}\right] - \frac{d}{c} , \tag{1.17}$$

The integral is calculated along the optical path from the pulsar to Earth and d is the distance between them.

In the vast majority of cases, the frequency at which pulsars are observed are much higher than the plasma frequency of the ionized ISM, that is $\nu \gg \nu_\mathrm{p}$. Under this condition, it is possible to get and approximate formula for the dispersion relation (Eq. 1.15) using a first-order Taylor expansion. Plugging the latter it into Eq. (1.17), one gets:

$$\Delta t_{(\nu,\infty)} \simeq \frac{1}{c}\int_0^d \left[1 + \frac{1}{2}\frac{\nu_\mathrm{p}^2}{\nu^2}\right]\mathrm{d}l - \frac{d}{c} = \frac{e^2}{2\pi m_\mathrm{e} c}\frac{1}{\nu^2}\int_0^d n_\mathrm{e}\,\mathrm{d}l \equiv \mathcal{D}\cdot\frac{\mathrm{DM}}{\nu^2} \quad . \tag{1.18}$$

Here $\mathcal{D} \doteq e^2/(2\pi m_\mathrm{e} c)$ is called *dispersion constant*, while:

$$\mathrm{DM} \doteq \int_0^d n_\mathrm{e}\,\mathrm{d}l\,. \tag{1.19}$$

is called *dispersion measure*. The latter quantity is extremely important for pulsar astronomers, as it measures the free electron content along the line of sight from the pulsar to the observer, providing an indirect way of estimating the distance of the pulsar, as we shall see in the remainder of this thesis.

Also, the DM is a quantity that is always easily measurable for any pulsar, particularly if the latter is observed at relatively low frequencies ($\lesssim 2$ GHz). Indeed, from Eq. (1.18), we can deduce that a straightforward way to measure the DM is by measuring the difference $\Delta t_{(\nu_1,\nu_2)}$ in the arrival time of the pulsar signal at two given frequencies, ν_1 and ν_2 (with $\nu_1 < \nu_2$):

$$\Delta t_{(\nu_1,\nu_2)} = \frac{e^2}{2\pi m_\mathrm{e} c}\cdot\left(\frac{1}{\nu_1^2} - \frac{1}{\nu_2^2}\right)\cdot\mathrm{DM}. \tag{1.20}$$

Once the DM is determined, one can integrate Eq. (1.19) to estimate the distance of the pulsar, provided that the electron number density distribution, $n_e(l)$ is known. As of today, there are at least two models, namely the NE2001 model (Cordes & Lazio, 2002a, 2003) and the YMW16 model (Yao et al., 2016), that map the electron content distribution of our Galaxy, providing estimates of the pulsar distance, with a typical relative uncertainty of $\sim 10 - 50\%$, given the DM and the sky location of the pulsar. Clearly, the inverse is also possible: if we have an independent way of determining the distance to a pulsar, we can use the measured DM to derive the electron content along the line of sight to the pulsar. In fact, this technique is the the one used to calibrate the Galactic electron content models like the NE2001 and the YMW16, which improve as more and more pulsars have their distance independently measured.

1.4.2 Scattering

Another important interstellar medium effect is *scattering*. This is due to the inhomogeneities of our Galaxy ISM. The irregularities in the density of free electrons alter the refractive index locally encountered by the electromagnetic wave. Consequently, the paths of the rays deviate from a straight line, leading to increased travel times. This means that, at any specific frequency, while the bulk of the radiation reaches the observer at the same time, some other portion will be delayed creating an extended "tail" in the pulse profile we detect. The scattering effect was initially described by Scheuer (1968), which proposed the so-called *thin-screen model*. This model presumes that the density irregularities follow a Kolmogorov spectrum and are contained within a thin layer located between the pulsar and the observer. Under these basic premises, it has been demonstrated (e.g. Lorimer & Kramer 2004) that the intensity of a pulse over time is given by:

$$I(t) \propto e^{-\Delta t/\tau_s},$$

where Δt represents the time delay caused by the extended path travelled by the radiation. Thus, the pulse profile we observe from a pulsar is essentially the intrinsic pulse shape convolved with a one-sided exponential function. This function has a characteristic timescale τ_s, which is inversely proportional to the fourth power of the frequency:

$$\tau_s \propto \nu^{-4}.$$

As a result, at low frequencies (< 1 GHz), scattering can be important, potentially leading to the complete smearing of the pulsar's signal, depending on the characteristics of the scattering environment.

1.5 Pulsar populations

As of June 2024, more than 3600 pulsars are known, according to the ATNF pulsar catalogue[2] (version 2.2.0, Manchester et al. 2005). Almost all of the known pulsars (precisely, 96.6%) are visibile in the radio band of the electromagnetic spectrum, whereas the remaining 3.4% are only observed at other wavelengths (most often in the X-rays or γ-rays).

[2] https://www.atnf.csiro.au/research/pulsar/psrcat

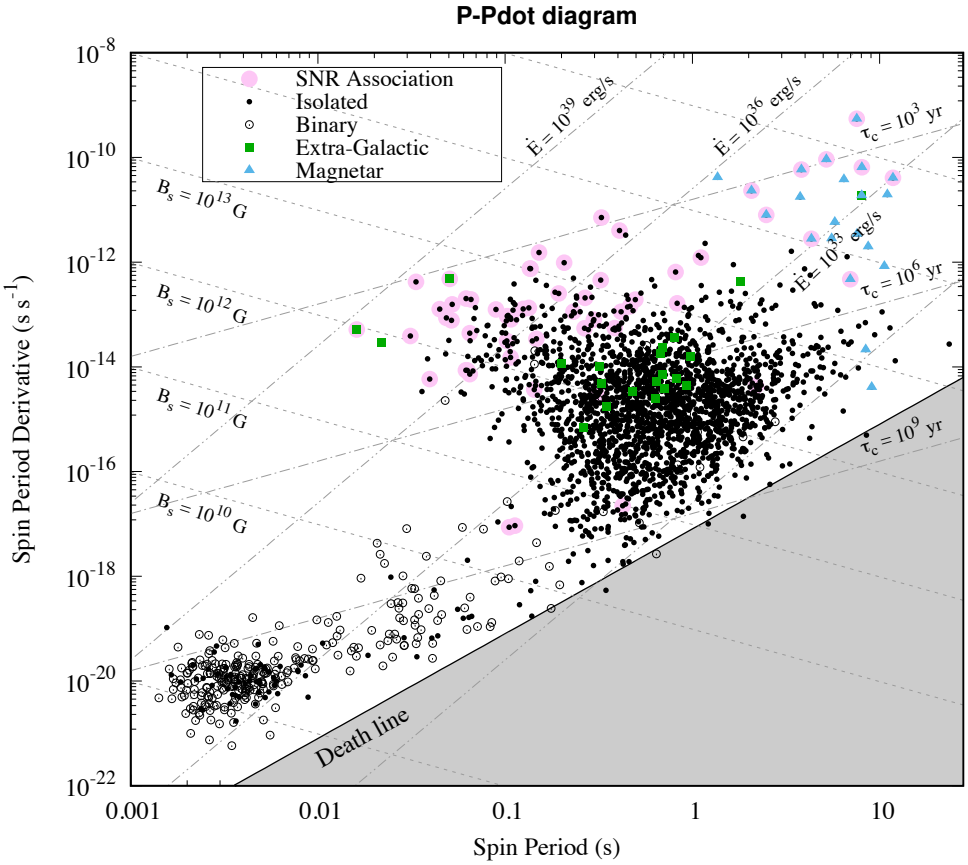

Figure 1.3. P-$\dot{P}$ diagram for the currently known pulsar population.

The whole known pulsar population is extremely diverse, therefore it is common to refer to different classes of pulsars, depending on their characteristics. As we saw in the previous sections, several key properties of pulsars can be derived from the value of their spin period and and spin period derivative. For this reason, the different pulsar populations are often identified within the so-called P-$\dot{P}$ diagram, where, as the name suggests, pulsars are placed according to the measured values of these two quantities. A P-$\dot{P}$ diagram of the currently known pulsar population is shown in Figure 1.3.

In the remainder of this section, we will discuss the main sub-population of pulsars that are relevant for this thesis, using the P-$\dot{P}$ diagram as a visual help.

1.5.1 Ordinary and young pulsars

The vast majority of the pulsars known have a spin period and a spin period derivative that place them in a large cluster in the center of the P-$\dot{P}$ diagram. Specifically, they have periods that range between a few hundred milliseconds to a few seconds, and $\dot{P}$ values of $\sim 10^{-12}$–10^{-17}. These imply typical characteristic ages in the range 10^5–10^9 yr and surface magnetic field strengths of $\sim 10^{11} - 10^{13}$ G.

Ordinary pulsars are direct descendant of newly-born pulsars (also referred to as *young pulsars*), which are those that have have very small ages of $\lesssim 10^5$ yr, and are

often found associated with supernova remnants. Because, at birth, pulsars typically have very high ($\gtrsim 10^{-15}$) spin-down rates, they slow down quite rapidly over time, "quickly" becoming the ordinary pulsars that we see today.

Ordinary pulsars are in almost all cases isolated objects. For this reason, they almost always continue to spin-down indefinitely, describing a trajectory, in the P-$\dot{P}$ diagram, that goes towards higher periods and smaller period derivatives. This process continues until the pulsar crosses the so-called *death-line* (Chen & Ruderman, 1993), which defines an area in the P-$\dot{P}$ diagram where the spin-down energy of the neutron star is not anymore sufficient to sustain the radio emission and, hence, the pulsar becomes undetectable. Only if some other external processes intervene (see Section 1.5.3) can the pulsar emission be re-activated.

1.5.2 Magnetars

Magnetars (see, e.g., Kaspi & Beloborodov 2017 for a recent review) are a special type of young pulsars, characterized by extremely small characteristic ages (which can be as short as just ~ 240 years, see Esposito et al. 2020), unusually high surface magnetic fields (typically $\gtrsim 10^{14}$ G), and relatively long spin periods of $2-15$ seconds. To date, 30 such objects are known[3]. The key property, from which magnetars are named, is that their emission mechanism is primarily powered by the decay of their ultra-strong magnetic field (Duncan & Thompson, 1992). For this reason, their emission properties are quite different from that of the typical pulsars: the vast majority of them exhibit X-ray emission (often also manifested through recursive "outbursts"), and a small fraction also γ-ray emission. Only 7 out of the 30 known magnetars are known to also emit in the radio band of the spectrum (Olausen & Kaspi, 2014b), and such emission is often erratic, periodically appearing and disappearing (e.g. Camilo et al. 2016), and showing a flat or sometimes even inverted spectrum, which in some cases makes them detectable even at very high ($\gg 10$ GHz) radio frequencies (Torne et al., 2017). As we shall see in Chapter 4, searching for the radio pulsations from an X-ray magnetar was one of the main motivations for part of the work done in the context of this thesis.

1.5.3 Recycled pulsars

Even if a pulsar naturally slows down, eventually crossing the death line and turning off its emission, there is still a possibility where the pulsar can spin up and re-activate the emission. This can happen if the pulsar is part of a binary system, where the companion is a normal star.

In this situation, the companion star can evolve, eventually expanding in size, up to the point where its outer layers fall under the gravitational influence of the neutron star. When this happens, it is said that the companion star is filling its Roche Lobe, and the matter starts flowing from the companion star to the pulsar, thus transferring mass and angular momentum to the neutron star. As a consequence of this process, which is referred to as *recycling* (Bhattacharya & van den Heuvel, 1991; Tauris & van den Heuvel, 2006), the neutron star increases its mass and, most importantly, rotates faster and faster as more and more angular momentum is transferred (e.g.

[3] https://www.physics.mcgill.ca/~pulsar/magnetar/main.html

Radhakrishnan & Srinivasan, 1982; Podsiadlowski et al., 2002; Papitto et al., 2013). The duration of the recycling process can vary from millions to billions of years, depending on the mass of the companion star. For binary systems where the companion star is light ($\lesssim 1\ M_\odot$), the process can last for billions of years, a time sufficient to make the neutron star spin at a rate of hundreds of times per second (or, equivalently, rotate once every few milliseconds). If the companion star is instead massive ($> 1\ M_\odot$), then its evolution, and consequent mass transfer will occur over much short time scales of just millions of years, therefore leaving only a partially recycled neutron star. In any case, the recycling process and the consequent neutron star spin-up allows the radio emission mechanism to be re-activated, and the pulsar to be again detectable. On the other hand, the accretion of matter also causes a quenching of the magnetic field, which becomes orders of magnitude weaker than that of normal pulsars, reaching typical values of $\sim 10^8$ G. As a result, their spin-down rate also sharply decreases to values of the order of 10^{-20}. By virtue of these characteristics, these pulsars are also called *millisecond pulsars* (MSPs) and occupy the bottom-left part of the P-$\dot{P}$ diagram.

Given the way they form, all recycled pulsars should be part of binary systems. However, this is not always the case. In fact, excluding pulsars in globular clusters, where binary systems can be disrupted by gravitational interactions with other stars (see Section 1.6.1), there is a significant fraction of millisecond pulsars in our Galaxy that are found to be isolated, and their origin is still matter of debate.

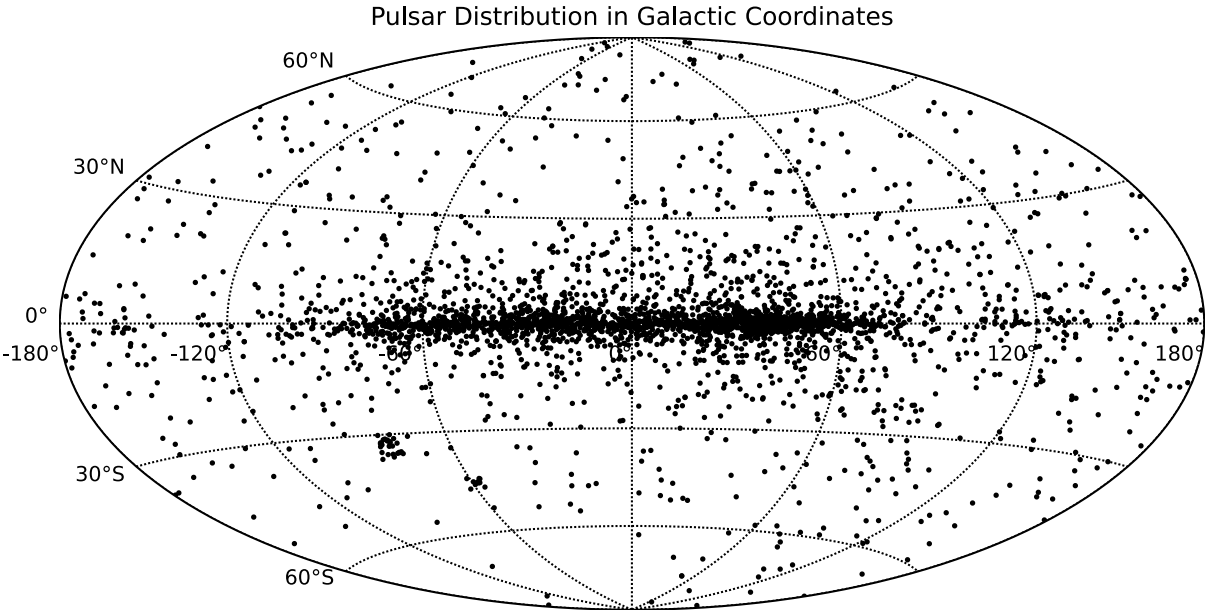

Figure 1.4. Position of all known pulsars (black dots), as per the ATNF Pulsar Catalog v2.2.0, in Galactic coordinates in a Hammer-Aitoff projection.

1.6 Distribution of pulsars

All of the pulsars that we currently know are located in our Galaxy or in the immediate proximity of it. In fact, over 90% of the ~ 3600 pulsars known are located in the plane of the Milky Way (see Fig. 1.4). This is a direct consequence of the way neutron stars

(and, hence, pulsars) are born. Indeed, as the Galactic plane, and in particular its spiral arms, are the cradle where new stars (particularly the massive ones) form, this is also the place where neutron stars will also be born as a result of the supernova explosion of such stars. While the majority will be found very close to the Galactic plane, (over 60% are located within a Galactic latitude range of $-5 < b < +5$ deg), a fraction of them are found farther out. This is because the supernova explosion of a massive star can at times be asymmetric, resulting in a "kick" imparted to the neutron star due to conservation of linear momentum. This will make the pulsar be thrown away at high speed (typically a few hundred km/s) and, depending on the kick direction and how much time elapsed, will eventually place it far away from the Galactic plane. In fact, one can estimate a pulsar's age through its *kinematic age*, i.e., by measuring its 3D-velocity and re-constructing its trajectory, deriving how much time it took for the pulsar to move from the Galactic plane to its current position (e.g., Noutsos et al. 2013).

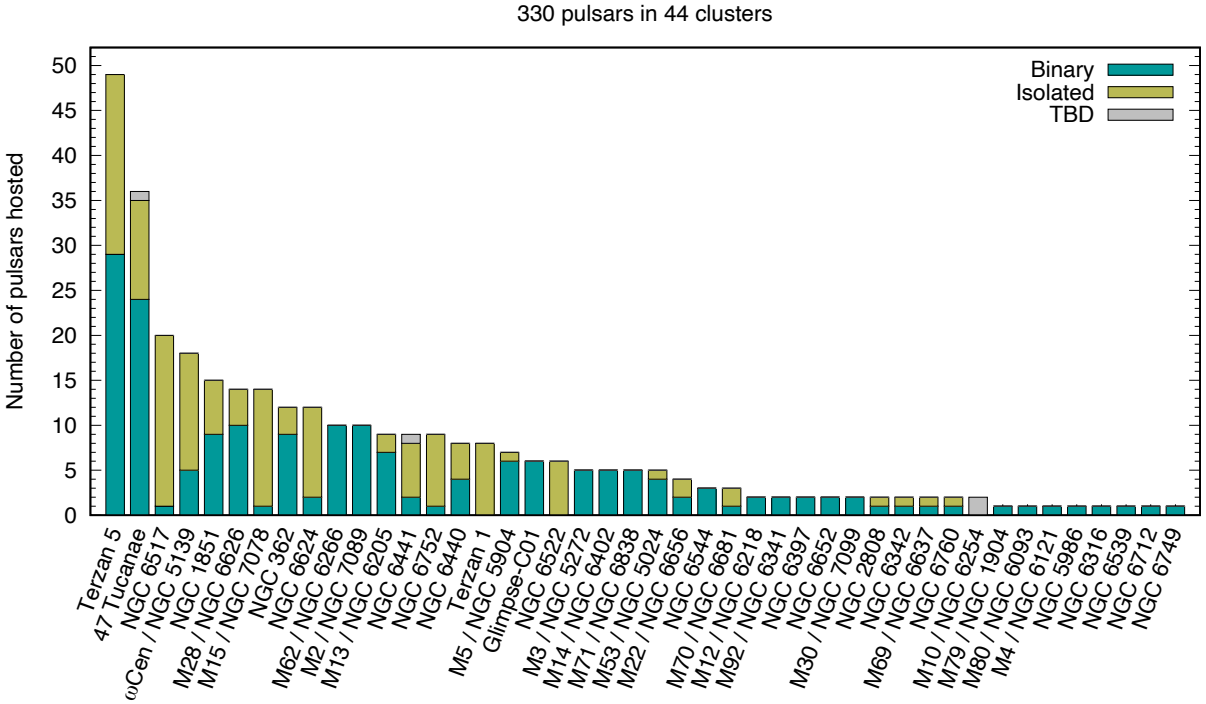

Figure 1.5. Histogram of the 330 pulsars in GCs currently known as function of host cluster. Image credit: Alessandro Ridolfi.

1.6.1 Pulsars in globular clusters

Globular clusters (GCs) are spherical agglomerations of 10^4 to 10^6 stars, which are bound together by their mutual gravity, within a typical volume of a few parsecs across. These stellar systems are found both in the bulge and in the halo of our Galaxy, and are among the most ancient structures that are known in the universe. Indeed, even though their origin is still matter of debate, their typical ages are $10 - 12$ Gyr, comparable to age of the universe. This is evident from the lack of gas and of any form of ongoing star formation. In fact, all the stars that compose a GC show clear signs of

being all born together, with their current differences being explained by the different stellar evolution, which in turn solely depend on the initial mass of the stars.

Given these premises, it is easy to understand that, in a GC, all of the massive stars have already evolved and reached the end of their lives. Therefore, the more massive stars (> 4 $M_\odot$) will have left stellar-mass black holes and neutron stars, while the lighter one (< 4 $M_\odot$) will have produced white dwarfs. The only stars that can still be in their main sequence phase are those with very low masses ($\lesssim 1$ $M_\odot$), stars similar or lighter than our Sun, whose evolution occurs over time scales of > 10 Gyr. For this reason, GCs are rich in neutron stars and, therefore, are among the most prolific places to target when searching for pulsars.

Another key property of GCs is their very high stellar density. Near the cores of GCs, latter can reach values of up $10^5 - 10^6$ stars per cubic parsec, which is many orders of magnitude higher than the typical values that characterize the Galactic plane. Because of these crowded environments, several interesting phenomena occur in GCs. First of all, the high stellar density promotes the gravitational interactions among the stars. By repeatedly passing close to other bodies several times within their lifetime, stars can exchange their kinetic energies, which is over time being equally distributed across all stars and all locations within the cluster. With all the stars having similar kinetic energy, the more massive stars will then have slower velocities than the lighter stars. This leads to major changes to the cluster structure, as the lighter stars will be much more likely to be flung towards the outer regions of the GCs, whereas the most massive objects (namely neutron stars and black hole) will sink toward the center. This phenomenon, which is referred to as *mass segregration* (**?**), is reason why the vast majority of pulsars (which are neutron stars) in GCs are found to be in the innermost regions of their host cluster.

Another consequence of the high stellar density is the fact that binary systems can easily form (but also disrupt) as the result of a close encounter between stars. In particular, what is relevant for pulsar astronomy, is the fact that while the majority of isolated pulsars formed in the cluster eventually become undetectable due to their spin-down, a fraction of them can instead be recycled. Indeed, a "dead" neutron star can easily acquire a low-mass star companion (for instance, via tidal capture; Fabian et al. 1975; Press & Teukolsky 1977) and being recycled by it for billions of years, eventually becoming a millisecond pulsar. On the other hand, when a third body gravitationally interacts with such a binary, further outcomes are possible. One possibility is the *exchange interaction* scenario, which happens when a binary system composed by a pulsar and a low-mass star (such as, e.g. a He WD) encounters a heavier star. When this happens, the most likely result is that the lighter star is ejected from the system and replaced by the heavier one. In the process, the binary system is likely to acquire a large eccentricity and to be flung towards the outskirts of the GC, due to the recoil produced by the interaction. Alternatively, the chaotic three-body encounter can lead to the disruption of the binary, leaving an isolated recycled or partially recycled pulsar. Also, these processes can obviously happen multiple times to a single neutron star.

As the standard evolutionary path of stars can easily be interrupted, perturbed or completely twisted, the resulting population of pulsars in GCs is very different for that of the Milky Way. At the time of writing, 330 pulsars are known to reside in 44

different GCs[4]. Among these pulsars, more than 80% are recycled, compared to just about 10% in the Galactic field. Moreover, several pulsars and binary systems show exotic properties that would not be possible to find in the Galactic plane. Among these are ultra-fast-spinning pulsars (Hessels et al., 2006), highly eccentric binary MSP pulsar systems (Ridolfi et al., 2021; Balakrishnan et al., 2023) as well as potential pulsar-stellar mass black hole systems (Barr et al., 2024).

The presence of pulsars with such extraordinary characteristics is certainly the main scientific driver for many pulsar searching projects, including the one done in the context of this thesis.

1.6.2 Extra-galactic pulsars

Even though 99% of the known pulsars are located in the Milky Way, there are a few pulsars that are found just outside of it. Specifically, 25 pulsars are currently known in the Large Magellanic Cloud (including the most luminous pulsar known; Wang et al. 2022) and another 9 in the Small Magellanic Cloud (Manchester et al., 2006), with further searches currently ongoing (Carli et al., 2024). Although it is certain that pulsars are also present in other galaxies (simply because they are the direct descendant of massive stars), their intrinsic faintness, combined with the very large distances, prevent us from detecting them outside a few tens of kpc, with our current available sensitivity.

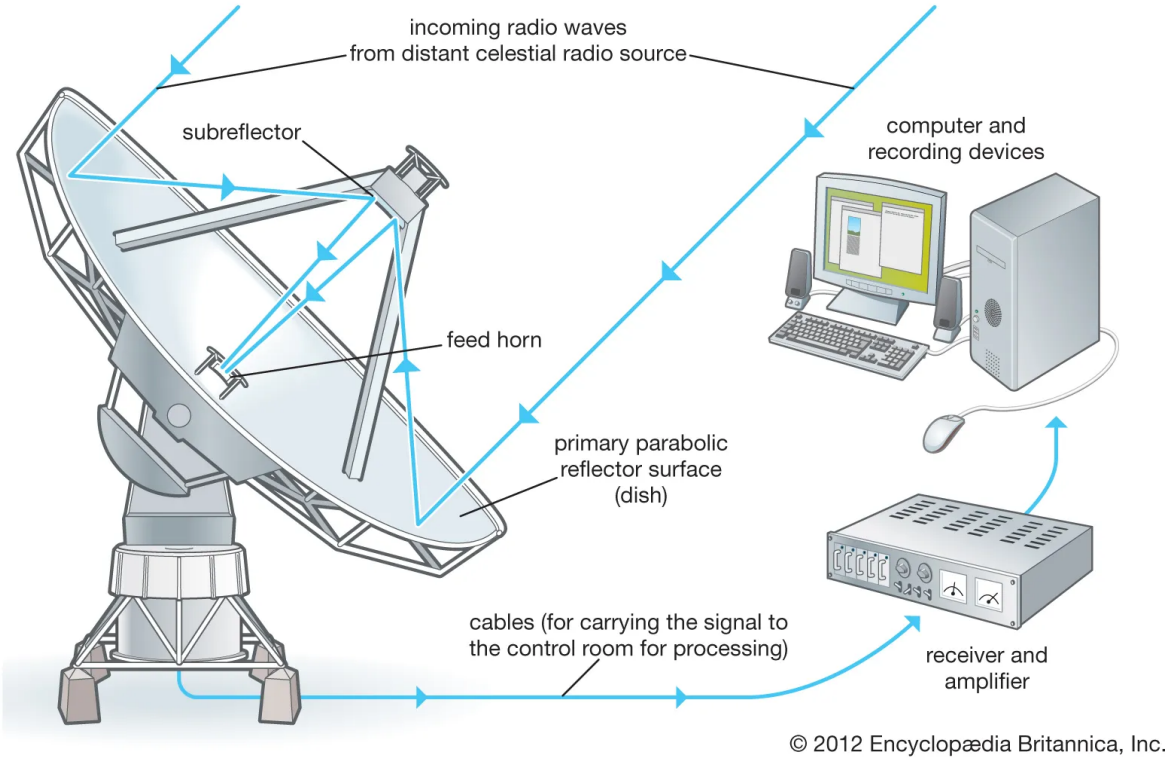

Figure 1.6. Scheme of a traditional single-dish radio telescope. Credits: Encyclopedia Britannica.

[4] https://www3.mpifr-bonn.mpg.de/staff/pfreire/GCpsr.html

1.7 Radio telescopes and pulsar observations

The most common way through which pulsars are studied is by observing them with radio telescopes. In the following section we will describe, in a very simplified fashion, the main elements that characterize a modern radio telescope.

A radio telescope is an instrument that is capable of collecting electromagnetic radiation in the radio band of the spectrum.

In its classic, and most common, conception, a radio telescope comprises a main reflector (most often, but not always, parabolic in shape) through which the electromagnetic waves coming from a distant source (which we can approximate as located at infinity) gets reflected and focused to one point, which is the telescope's primary focus. Here the radiation can be either further reflected by a secondary mirror, or directly collected by a device called *front-end* (or *receiver*). The latter converts the incoming electromagnetic waves having a frequency within a given range (called *observing band*, which is determined by the receiver design) into electric voltages. The resulting signal is further amplified using cryogenically-cooled amplifiers, in order to minimize the thermal noise and increase the sensitivity, and filtered so as to exclude unwanted frequencies outside the range of interest, which may also be contaminated by radio frequency interference (RFI) due to human activities. The signal is then carried through cables to the so-called *backend*, which is the actual data acquisition system. The backend, which can be composed of electronic boards as well as by normal computers, first digitizes the raw voltages with the aid of analogue-to-digital converters. The digitized signal is then further processed in such a way that the observing band is split into several smaller "slices" (or, more properly, *frequency channels*), and the channelized data is eventually recorded onto disk by some attached computing machine, in a specific file format that is suitable for later analyses by the astronomers. Some examples of single-dish radio telescopes that are used to study pulsars are the 64-m "Murriyang" radio telescope near Parkes, Australia, the 64-m Sardinia Radio Telescope in Italy, the 100-m Effelsberg radio telescope in Germany. Currently, the largest single-dish radio telescope on the planet is the Five-hundred-metre Spherical Aperture Telescope (or FAST, for short) radio telescope in the province of Guizhou in China. As its name suggests, its main reflector is 500 metres in diameter, and it has been built within a natural depression of the karst-dominated landscape of the area.

Single-dish radio telescopes have very large reflectors of tens to hundreds of meters across because, as can be intuitively understood, the larger the dish, the higher the sensitivity and, thus, our ability to detect the feeblest astrophysical signals. However, as one can also easily understand, building huge single-dish radio telescopes beyond a certain size becomes extremely costly, challenging from a technical and mechanical standpoint, and it comes with several compromises, such as being unable to steer the telescope. Notwithstanding, thanks to technological advances, it now possible to combine the signal of several, much smaller telescopes, so as to make them work together as if they were a single, very sensitive telescope. The technique used for this is called *beamforming* (e.g. Chen et al. 2021), and makes the construction of highly sensitive telescopes much easier from a mechanical standpoint, shifting the complexity (and, often times, the costs) to the computational side of things. Telescopes that combine the signals of several antennas together are referred to as *interferometers*. For this reason, the majority of the recently-built high-sensitive radio telescopes are

in fact interferometers composed by an array of antennas (tens to hundreds), as well as by some high-performance computing facility, which is required to beamform and further process the signals from all the antennas in real time. Examples of modern telescopes with an interferometric design that are relevant for pulsar science are, e.g., the MeerKAT radio telescope array in South Africa (which is composed by 64 13.5-m dishes, each 13.5-m in diameter), the LOFAR radio telescope in the Netherlands (composed of thousands of low-frequency dipole antennas, van Haarlem et al. 2013), and the Giant Metrewave Radio Telescope (GMRT) in India (made of 30 dishes, each 45 meters across), but several more could be mentioned.

For this thesis, we will be using data taken both with a single dish telescope, namely the Parkes radio telescope, as well as with an interferometer, namely the MeerKAT radio telescope.

1.8 The many scientific applications of pulsars

By virtue of their rich phenomenology, and in particular of their outstanding rotational stability, pulsars can be regarded and used as extremely precise cosmic clocks. This, together with the large variety of pulsar type and binary system types, enables a plethora of scientific applications in physics, astrophysics and several other areas of research. For this reason, since the discovery of the first pulsar, astronomers have been conducting surveys aimed at expanding the total sample of known pulsars, and this is happening still today.

In the following, we briefly discuss some of the major scientific applications for which pulsars are used.

1.8.1 Study of the interstellar medium

One the easiest quantity that is possible to measure when a pulsar is discovered is its dispersion measure (DM). As we saw in Section 1.4.1, the latter is an indirect measurement of the free electron number density along the line of sight from the observer to the pulsar. By measuring the DM for a large number of pulsars, in combinations with independent measurements of the distance to the pulsar (e.g., Deller et al., 2012), it is possible to construct detailed maps of the whole electron content of our Galaxy (Cordes & Lazio 2002a; Schnitzeler 2012; Yao et al. 2016). The latter can then be used, among other things, to infer the distance of a newly found pulsar, given its DM AND

1.8.2 Tests of gravity and equations of state

When a pulsar is found orbiting another star, it is possible to use the former to probe the gravitational field produced by the latter. This allows pulsar astronomers to conduct extremely precise gravity tests in the strong-field regime. In particular, if at least three post-Keplerian (PK) effects (such as the periastron advance in eccentric orbits, the orbital decay due to the emission of gravitational waves, or the time dilation and gravitational redshift due to the curvature of space-time) are measured, it is possible to test General Relativity (GR) as well as alternative theories of gravity (Freire et al., 2012). The most notable example of a binary pulsar where these kind of experiments

are possible is the Double Pulsar (Burgay et al., 2003; Lyne et al., 2004), the only system composed by two pulsars, which revolve about each other in a very tight orbit every 2.4 hours. With the Double Pulsar, it has recently been possible to validate the predictions of GR at a level of 1.3^{-4} with 95% confidence (Kramer et al., 2021).

Besides testing gravity, the measurement of at least two PK parameters give access to the precise measurement of the individual masses of the pulsar and the companion. As the exact equation of state of neutron stars is still not known, measuring the masses of pulsars, allows us to rule out all those equations of states that imply a maximum neutron star mass lower than the measured value (e.g. Antoniadis et al., 2013).

1.8.3 Detection of ultra-low-frequency gravitational waves

One of the most fascinating applications of pulsars is the detection of gravitational waves (GWs). Predicted by Einstein's theory of General Relativity in 1915, the first proof of the existence of these tiny space-time ripples was obtained in 1974 by measuring the orbital decay in the very first binary pulsar known, PSR B1913+16, also known as the Hulse-Taylor pulsar (Hulse & Taylor, 1975), which was worth the 1993 Nobel prize in physics. Another ~ 40 years were necessary to have the first direct detection of GWs through the use of the LIGO ground-based interferometers (Abbott et al., 2016).

Both of these experiments were detecting high-frequency GWs emitted by binary systems during their inspiral and merger phases. The current next challenge is to try and reveal those GWs emitted by merging supermassive black hole binaries. Because of the much longer time-scales that characterize supemassive binary systems, the frequency of the emitted GWs is extremely small, of the order of 10^{-9} Hz. Their detection is possible by correlating the signals coming from an ensemble of tens of highly stable millisecond pulsars located in different directions in the sky, an experiment referred to as Pulsar Timing Array (PTA, e.g. Manchester 2013). The latter requires the follow-up of these MSPs for several decades. For this purpose, many radio telescopes and several large PTA collaborations across the world are currently involve in this huge endeavor. It is expected that first high-significance detection of nHz GWs from PTA experiment will be possibile within the current decade (Falxa et al., 2023).

1.8.4 Stellar and binary evolution

The discovery of the Hulse-Taylor binary pulsar was important because it proved the existence of GWs, but also because it raised the question on how such a system could have form, from a stellar evolution standpoint. As more and more pulsars in binary systems were found with different companions types and different characteristics of the orbit (such as double-neutron star systems, triple systems, pulsar-WD systems, etc.), the need to explain their origin within a coherent picture became more and more challenging. Today, the majority of the binary pulsar system types known have been successfully explained by stellar evolution models (Tauris et al., 2000, 2017). Also, the recycling model, which explains the formation of MSPs as direct descendant of LMXBs, has now been amply confirmed by the discoveries of transitional MSPs, pulsars that swing between a rotation-powered state where they are visibile in the radio band, to

an accretion-powered state where they are visible in the X-ray (Archibald et al., 2009; Papitto et al., 2013). Notwithstanding, there are still some open issues. One of these is, for example, the existence of isolated MSPs in the Galactic field, which cannot be explained by our current evolutionary models.

In addition to binary pulsars, the study of individual pulsars can also be important for study of stellar evolution. Specifically, the measurement of the space velocity of a pulsar, in particular in combination with it polarimetry properties, can return crucial information about the kick undergone by the pulsar at birth, in turn providing insights into the physics of supernova explosions (Noutsos et al., 2008).

1.8.5 Study of globular clusters

Once a sufficient number of pulsars are discovered in a globular cluster, it is possible to use the pulsars to study the host cluster, enabling a number of interesting experiments. For example, by measuring higher-order spin period derivatives of several pulsars, it is possible to probe the gravitational field of the cluster (e.g. Freire et al., 2017). This also allows to put constraints of the possible presence of non-luminous matter at the center of the cluster, such as that of an intermediate-mass black hole, or of an ensemble of stellar-mass black holes (e.g. Prager et al., 2016; Abbate et al., 2019). By precisely measuring the DMs and the positions of the pulsars, one can reveal the presence of a possible ionized intra-cluster medium (Freire et al., 2001; Abbate et al., 2018). If the polarimetric properties of the pulsars are also known, it may also be possible to constrain the presence of an intra-cluster magnetic field (Ho et al., 2014; Abbate et al., 2020; Martsen et al., 2022).

Chapter 2

Time-series analyses and techniques for radio pulsar searching

As we have discussed in the previous chapter, radio pulsars are outstanding tools with which one can carry out extremely high-precision experiments in a plethora of scientific areas. For this reason, since the discovery of the first pulsar, astronomers have carried out several surveys, aimed at expanding the total known pulsar population. These surveys make use of a wide range of analysis techniques for time-series data, tailored to detect the highly coherent periodic signals emitted by pulsars. In this chapter, we delve into the details of radio pulsar searching. We discuss the methods that allow us to reveal the existence of a coherent periodic signal in the data, with virtually no prior information at our disposal. While doing so, we will also examine the numerous challenges that make the detection of such signals difficult, particularly in modern datasets.

2.1 The basics of how to find a pulsar

As previously mentioned, the radio signal of a pulsar consists of a train of pulses that are emitted in an extremely regular fashion, at a rate that corresponds to the spin rate of the NS (Fig. 2.1). Because the NS spin rate is extremely stable (at least over sufficiently short time scales, such as the few hours of a typical single observation), this stability is reflected in the periodicity of the pulse train. The single pulses of radio emission, however, are in most cases too weak to be individually detected in the data, and they will be hidden by the overall noise (Fig. 2.2), which is produced by the several sources, both astrophysical and human-made. Obviously, the periodicity of the signal is unknown prior to its discovery. Therefore, the problem is to find a way to reveal the underlying periodic signal in the presence of noisy data. The most suitable mathematical tool to detect any periodicities underlying a time series is the Fourier Transform. So, in principle, discovering a pulsar means finding prominent peaks in the Fourier power spectrum. However, this is easier said than done. Indeed, a number of complications add up to the problem and must be addressed to be successful in reveal the pulsations. For instance, as we always observe pulsars within a certain range of radio frequencies (see Section 1.7), the signal will be dispersed across the different frequency channels according to the DM associated with the pulsar, which is also unknown. This effect must be corrected before trying to reveal the periodicity, hence the data must be searched over a range of de-dedispersion trial DM values. To complicate things further, modern data is very often highly contaminated by human-made interference (RFI), which have to be removed or highly suppressed before searching

for the astrophysical signals. For these and other reasons, the whole procedure that leads to the discovery of a pulsar is not as straightforward as it may seem at first. In the following, we will describe all the main steps involved in a typical pulsar searching analysis.

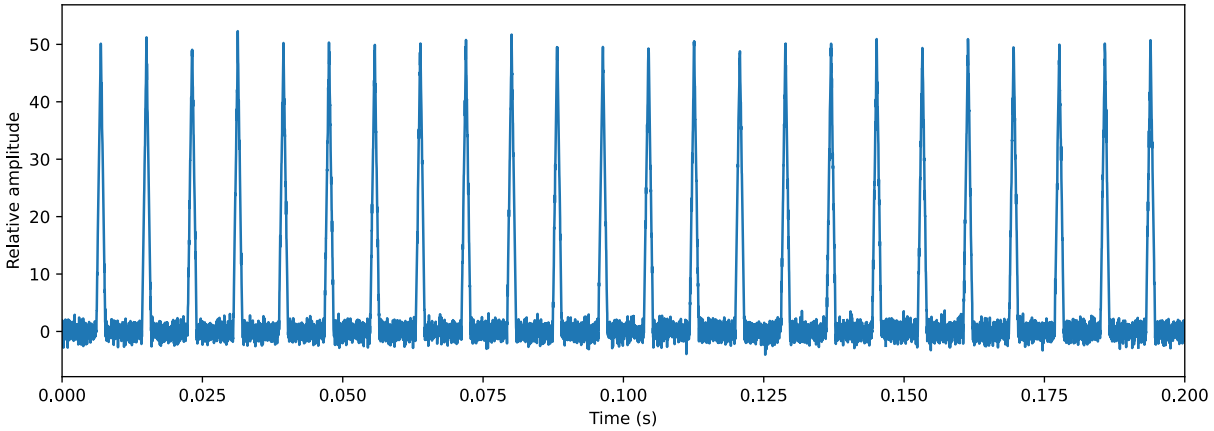

Figure 2.1. Simulated signal emitted by an isolated pulsar having a spin period of 8.13 ms (or, equivalently, spinning at 123 Hz). In this example, the individual pulse are much brighter than the underlying noise.

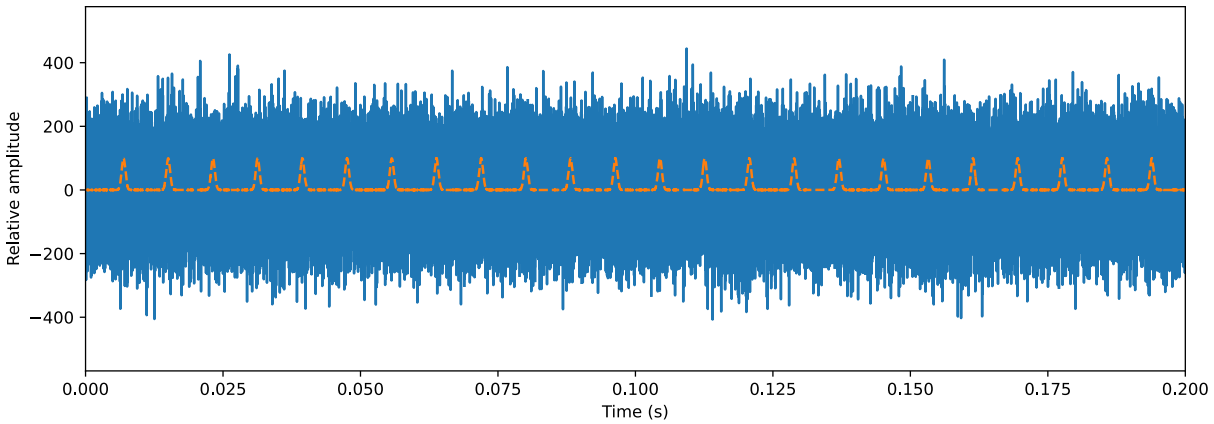

Figure 2.2. Schematic representation of a more realistic case in which the intensity of single pulses of the pulsar signal (orange dotted line) is lower than the background noise (blue line). Under this condition, which is the most common, the individual pulses are not directly detectable.

2.2 A realistic pulsar searching pipeline

Fig. 2.4 show the general scheme of a typical pulsar searching pipeline. In the following, we will go through all the steps involved.

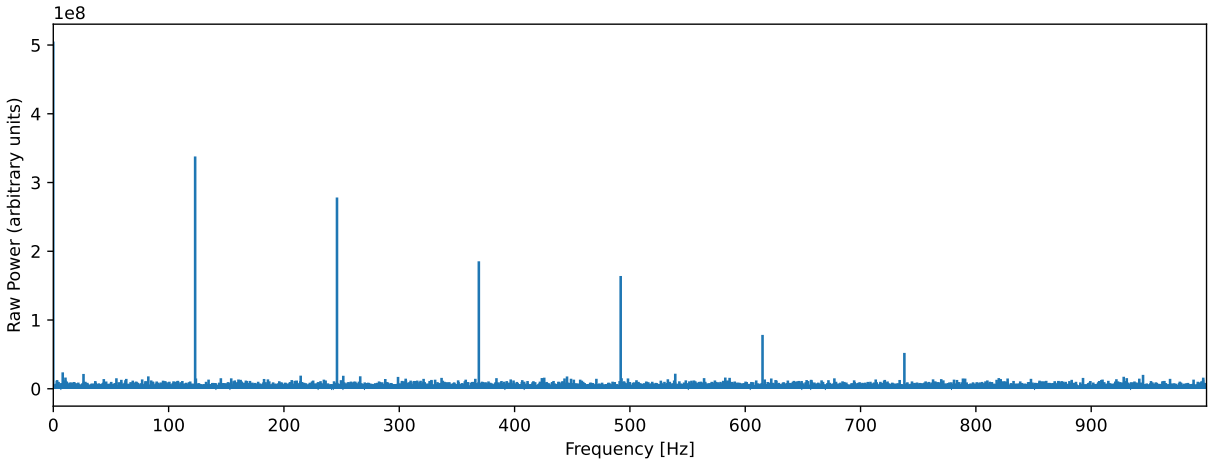

Figure 2.3. Fourier spectrum of the simulated 123-Hz pulsar signal shown in Fig. 2.1. Because of the spiky shape of the individual pulses, peaks of power are present at several multiples of the fundamental frequency (the so-called *harmonics*).

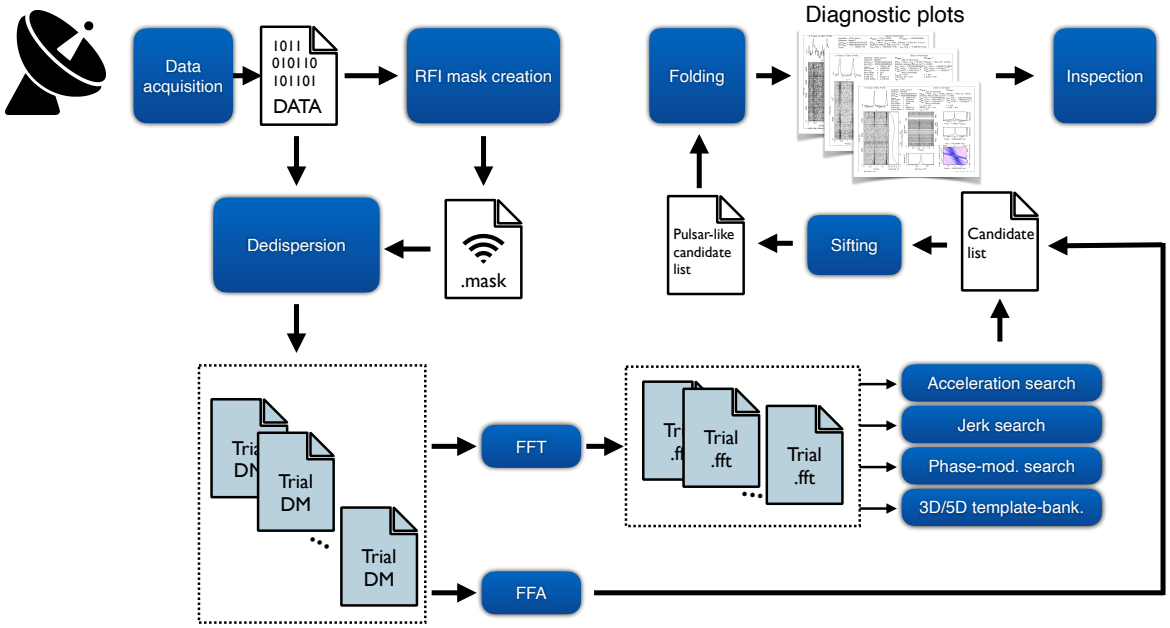

Figure 2.4. Sketch of a typical modern pulsar searching pipeline.

2.2.1 Data acquisition

When searching for new pulsars, the first and most obvious step required is the acquisition of the data. This consists in pointing a radio telescope at a specific area of the sky and collect the radiation coming from that particular direction for a given amount of time (referred to as *integration time*). Depending on the way the area of the sky is selected, the search can be either *targeted* or *blind*. In the former case, the telescope is aimed at specific points or areas where it is expected to find pulsars: typical examples are supernova remnants, pulsar wind nebulae, globular cluster, unidentified γ-ray sources etc. In the latter case, the telescope covers a certain area uniformly with a given number of pointings, each of them with the same dwell time.

When designing a search, besides choosing the target, one has to decide the observational set up. For single-dish telescopes, this includes the receiver, which in turn determines the central observing frequency and total bandwidth, and the backend, which allows the acquisition of the data with certain modes and/or characteristics (such as the time resolution, the number of frequency channels etc.). For interferometer telescopes, an additional parameter to choose is how many and which antennas will be used for the observation. The latter choice will in turn determine the total telescope gain (i.e., its "raw" sensitivity) and the size of the beam(s) on the sky, which will obviously impact the total number of pointings (and, hence, the total observing time) needed to survey the selected sky area. Last but not least, the integration time is another key parameter, and is often a trade-off between the total number of observing hours available to conduct the search, and the need to achieve a certain sensitivity. The latter can be calculated, given the observing parameters and the telescope characteristics, using the so-called *radiometer equation* adapted for pulsars (Dewey et al., 1984; Lorimer & Kramer, 2004):

$$S_{\rm mean} = \frac{({\rm S/N})\,\zeta\,T_{\rm sys}}{\mathcal{G}\sqrt{n_{\rm pol}\,\Delta t_{\rm obs}\,\Delta\nu}}\sqrt{\frac{W}{P-W}}. \tag{2.1}$$

This equations provides the minimum mean flux density, $S_{\rm mean}$, that a pulsar must have to be detected with a given signal-to-noise ratio (S/N), when observed for a time $\Delta t_{\rm obs}$. The other parameters that play a role in the equation are the telescope gain, $\mathcal{G}$, the total system temperature, $T_{\rm sys}$, the number of acquired polarizations, $n_{\rm pol}$, the effective observed bandwidth, $\Delta\nu$, the pulsar spin period, P and its pulse width, W, as well as a correction factor, ζ, that accounts for sensitivity losses due to the digitization and other possible causes. Because targeted searches typically cover a far smaller sky area than blind survey, they can often have much longer integration, resulting in deeper (i.e., more sensitive) searches being possible with a given telescope / observing set-up.

The signal so captured by the radio telescope is then digitized and stored in a so-called "search-mode" file format, typically the *filterbank* proprietary file format of the `SIGPROC`[1] pulsar searching software (Lorimer, 2011), or the more modern PSRFITS file format (Hotan et al., 2004a). Regardless of the exact format, a search-mode data file is composed by a header, which contains all the necessary information to correctly read the file, and by the actual data. The latter is essentially the full observing bandpass,

[1] https://sigproc.sourceforge.net/

split into a number of frequency channels (typically hundreds or thousands), recorded once every sampling time interval (typically of the order of few tens of microseconds), This very high time resolution is retained so as to be able to resolve the pulses of even the fastest MSPs, allowing their possible discovery. The fine channelization of the bandpass is instead required to de-disperse the data over a wide range of DM trial values (see Section 1.4.1), as well as to effectively remove narrow-band RFI present in the data (see Section 2.2.2).

2.2.2 RFI mitigation

In addition to the radio wave coming from the sky location pointed, a radio telescope also picks a large number of other signals produced by humans on the Earth. All these unwanted signals that are nevertheless collected and, therefore, present in the recorded data, are referred to as *radio frequency interference* (RFI). These can be manifest themselves in the recorded data in many ways, showing up in a great variety of forms: they can be persistent, temporary, or even bursty; they can be broad-band or narrow-band; and, they can be stable, slowly-varying or even changing very fast.

As can be easily understood, this signals can significantly hamper our ability to detect pulsars, particularly if we want to discover new ones, where we have little to no information about the pulsr signal that we are about to reveal.

Until the end of the previous century, RFI were present in very small portions of the radio band, and were therefore only a marginal problem that could be solved by simply excluding those frequency channels or time intervals where the interference signals were present. In the last few decades, however, the use of wireless telecommunication systems and satellites has exponentially increased, with more and more protocols and systems occupying larger and larger portions of the radio band of the electromagnetic spectrum. At the same time, modern radio telescope receiving systems often have very large observing bandwidth of several hundreds of MHz or even a few GHz (e.g. Hobbs et al. 2020), therefore increasing the likelihood of collecting radio waves in frequency ranges contaminated by human-made signals. These two things combined have made RFI an increasingly concerning issue for radio observations. Astronomers have therefore been forced to devise clever strategies to mitigate the impact of RFI on radio-astronomical observations, properly detecting and flagging polluted pieces data, without also filtering out the possible astrophysical signal of interest. Such techniques have rapidly developed over the last few years, and include the implementation of sophisticated mathematical methods, both in the time-domain and in frequency domain (e.g. Akeret et al. 2017; Maan et al. 2021; Morello et al. 2022). With the diffusion of multi-beams observing systems, both in single-dish and interferometric telescopes, spatial filtering RFI excision techniques have also started to develop (e.g. Kocz et al., 2012).

2.2.3 Search planning

After the RFI are removed or mitigated from the data, the next step is to plan the search strategy.

First, as the dispersion measures of the yet-to-be-discovered pulsars are obviously unknown, one has to decide which DM range to search. In blind all-sky surveys, one

usually wants to find any possible detectable pulsar along the line of sight. For this reason, it is common to search over a wide range of DM values, from ~ 0 pc cm^{-3}(to target close-by pulsars), up to a value that corresponds to the maximum distance that one wants to explore. The NE2001 and/or YMW16 models for the Galactic electron content are typically used to determine the latter value. On the other hand, there are cases in which the expected DM of the pulsar is roughly known. This is the case, e.g., of those globular clusters: as all the pulsars in a GC are confined within a volume of just a few pc, they basically all share the same distance from Earth and the same direction in the sky. Moreover, GCs contain very little to no ionized intra-cluster gas. As a consequence, the DMs of all the pulsars are expected to be very close to one another, and the small differences (typically of the order of a fewpc cm^{-3}) are solely due to the slightly different directions of lines of sight to the different pulsars. Therefore, if at least one pulsar is known in a GC, its DM will be very close to the DM of any other pulsar present in the cluster, and it is sufficient to explore a small range of DMs around that value to discover more pulsars in the GC.

Another important aspect to decide is which search algorithms to apply. This in turns depends on which types of pulsars and binary systems one wants to target and also how much computational power is available and how much time one can afford for the processing. We will review the main pulsar searching algorithms, with their characteristics and limitations, in Section 2.3.

2.2.4 De-dispersion (+ barycentering)

As explained in Section 1.4.1, the dispersion effect make the the signal of a pulsar arrive at the telescope at different times across the observing band. If this effect is not corrected, the pulses emitted by the pulsar can be significantly broadened or completely smeared out, resulting in sharply reduced sensitivity or even the inability to detect the signal.

Searching a given DM range means de-dispersing the data at a series of DM values across that range. After applying the appropriate shifts to each frequency channel, the frequency channels are summed together, producing a *de-dispersed time series*, which is basically a light-curve encompassing whole observing band, for each DM trial value. Clearly, when exploring a given DM range, it is important to choose an appropriate DM step size. This is because one wants to minimize the total number of de-dispersion trials (to minimize the total processing time needed to carry out the search), while also not lose sensitivity in case the true DM of the pulsars falls between two steps (and therefore no de-dispersion trial is optimal for that pulsar).

The optimal DM step size $\Delta\mathrm{DM}$ can be calculated once the observing parameters are fixed. The i-th trial DM value can be expressed as (Lorimer & Kramer, 2004):

$$\mathrm{DM}_i = 1.205 \times 10^{-7}\ \mathrm{pc\ cm^{-3}} (i-1)\, t_{\mathrm{samp}}\, (\nu^3/\Delta\nu), \tag{2.2}$$

where t_{samp} is expressed in ms and ν and $\Delta\nu$ in MHz.

For each DM trial value, the corresponding de-dispersed time series is also *barycentered*, that is, it is referred to the Solar System barycenter. This allows pulsar astronomers to refer all the periodicities found to an inertial frame of reference, and therefore be able to directly compare signals found in observations taken in different

times of the year (as the motion of the Earth around the Sun, and its consequent Doppler effect, is removed).

2.2.5 Periodicity search

Once all the RFI-cleaned, barycentered, de-dispersed time series are produced, one or more search algorithms are applied to each of them in search of underlying periodicities in the data. These algorithms can work either in the time domain or in the frequency domain.

2.2.5.1 Frequency-domain algorithms

The most powerful and widespread mathematical tool to detect any periodicities underlying a time series is the Fourier Transform (FT). The latter exploits the Fourier theorem, which states that any function can be described as the superposition of a number of sinusoidal signals, each with an appropriate amplitude, frequency and phase. The FT is the mathematical tool that can perform such a decomposition on the original function, returning the amplitudes $\mathcal{A}_i$ and phases ϕ_i of all the sinusoids of frequency f_i that make up the latter. The squares of the amplitudes, called *Fourier powers*, are then plotted as a function of the corresponding frequency of the sinusoid, forming the so-called *power spectrum*. Because the signal emitted by a pulsar has an intrinsic periodicity, while noise does not, the sinusoids with the same periodicity as that of the pulsar signal, will have a much larger amplitude (and, hence, power, defined as the square of the amplitude) compared to all the other sinusoidal components, and will therefore easily stand out in the Fourier domain.

In real world, the original functions (i.e. time series that have been de-dispersed, as outlined in Section 2.2.4) are composed of discrete, evenly spaced data points. Therefore the FT is performed with its discrete implementation, called Discrete Fourier Transform (DFT, see e.g. Press et al., 1992). The computational demand for performing a DFT on a time series with N data points is on the order of $\mathcal{O}(N^2)$, which becomes computationally intensive for lengthy data sets, challenging even the capabilities of contemporary computers. To address this issue, the Fast Fourier Transform (FFT) algorithm is employed (see Cooley & Tukey, 1965), which is a highly efficient version of the DFT, scaling at an operational complexity of $\mathcal{O}(N \log N)$.

It is important to note that, although the signal from a pulsar is periodic, it is typically far from being a perfectly sinusoidal function. Instead, it manifests as a train of pulses with varying degrees of complexity in shape. In the Fourier domain, this translates to a spectrum where the signal's power is distributed among the fundamental frequency and its harmonics, that is, the integer multiples and submultiples of the fundamental frequency (Fig. 2.3). This distribution is more pronounced when the pulse duty cycle is smaller. To properly recover the entire power of the pulsar signal, a process known as *harmonic summing* is commonly employed: copies of the Fourier spectrum, each scaled by an integer factor, are generated and then added to the original spectrum. This technique ensures that peaks related by harmonics are combined, thereby enhancing the pulsar signal's power relative to the noise level. Typically, this method involves adding up to 32 harmonics.

2.2.5.2 Time-domain algorithms

Another class of periodicity search algorithms are those that operate directly in the time domain. That is, the de-dispersed time series is not Fourier transformed, but the underlying periodicity is sought with different methods. The primary example of time-domain periodicity search algorithm in pulsar astronomy is the Fast Folding Algorithm (or FFA). In a nutshell, the latter try to split the time series into segments of different trial length (i.e. different trial spin periods), sums the segments coherently in phase and measures the S/N of the pulse profile so obtained. A periodogram, with S/N vs trial period data, is then inspected in search for prominent peaks. A more extensive description of the FFA algorithm is given in Section 2.3.2.1.

2.2.6 Sifting

After searching through all the de-dispersed time series (with either time or frequency domain techniques) one is left with a list containing the spin-period, its detection SNR, and the associated DM trial. These are what we call *candidates*. Even if the strongest RFI were previously removed from the data, modern observations can still contain a large number of human-made signals that eluded the filtering, which can result in thousands of spurious candidates. It is therefore crucial to find ways to recognize these, and substantially reduce the total number of candidates. Fortunately, there are different ways to achieve this. For example, for a real pulsar signal, which is broad-band, the same periodicity is often detected in multiple adjacent DM trial values, with the S/N varying as a function of trial DM, peaking at the value that is closest to the real one. This is one criterion by which promising candidates are selected and duplicate detections are grouped together. All of this process, aimed at significantly reducing the final number of candidates, is known as *sifting*.

2.2.7 Folding

After sifting, we end up with the list of the most promising candidate. The next step is *folding* the candidates. Folding consists in taking the original observation, de-dispersing the frequency channels at the candidate DM, and then splitting it into time segments with lengths of the candidate period, finally producing four-dimensional data-cubes consisting of time, frequency, rotational phase and power of a signal.

2.2.8 Candidate inspection

From the folded data cube, a number of one-dimensional or two-dimensional projections are produced, resulting in graphs that show, among other things, the integrated pulse profile, the pulse amplitude as a function of pulse phase and time and as a function of pulse phase and frequency, the S/N as a function of trial DM etc. All of these graphs are put together to produce an overall diagnostic plot, which can be viewed to determine whether the candidate signal is in fact astrophysical in nature or not.

For example, pulsar signals are broad-band, while RFI are often (but not always) narrow-band; pulsar signals usually have one or multiple peaks per period, with a narrow or broad duty cycle ranges, whereas RFI signals tend to be more sinusoidal in shape (compare Figs. 2.5 and 2.6). Also, the S/N of a pulsar signal is expected to

peak at a non-zero DM, as it crosses ionized interstellar medium during its path to Earth, contrary to RFI, which are terrestrial in nature.

In the past, and partly also at present, all the candidate diagnostic plots were reviewed by eye by the astronomer. However, as modern surveys can easily produce thousands or even millions of candidates per observing run, it has become practically unfeasible to do this manually. For this reason, pulsar astronomers now often resort to machine-learning based software to automatically evaluate the goodness of the plots, drastically reducing the total number of plots that need visual inspection (e.g. Lee et al., 2013; Morello et al., 2014; Zhu et al., 2014).

If the candidate passes all the checks and the visual inspection, it can be regarded as a potential pulsar, which can then be re-observed for its ultimate confirmation.

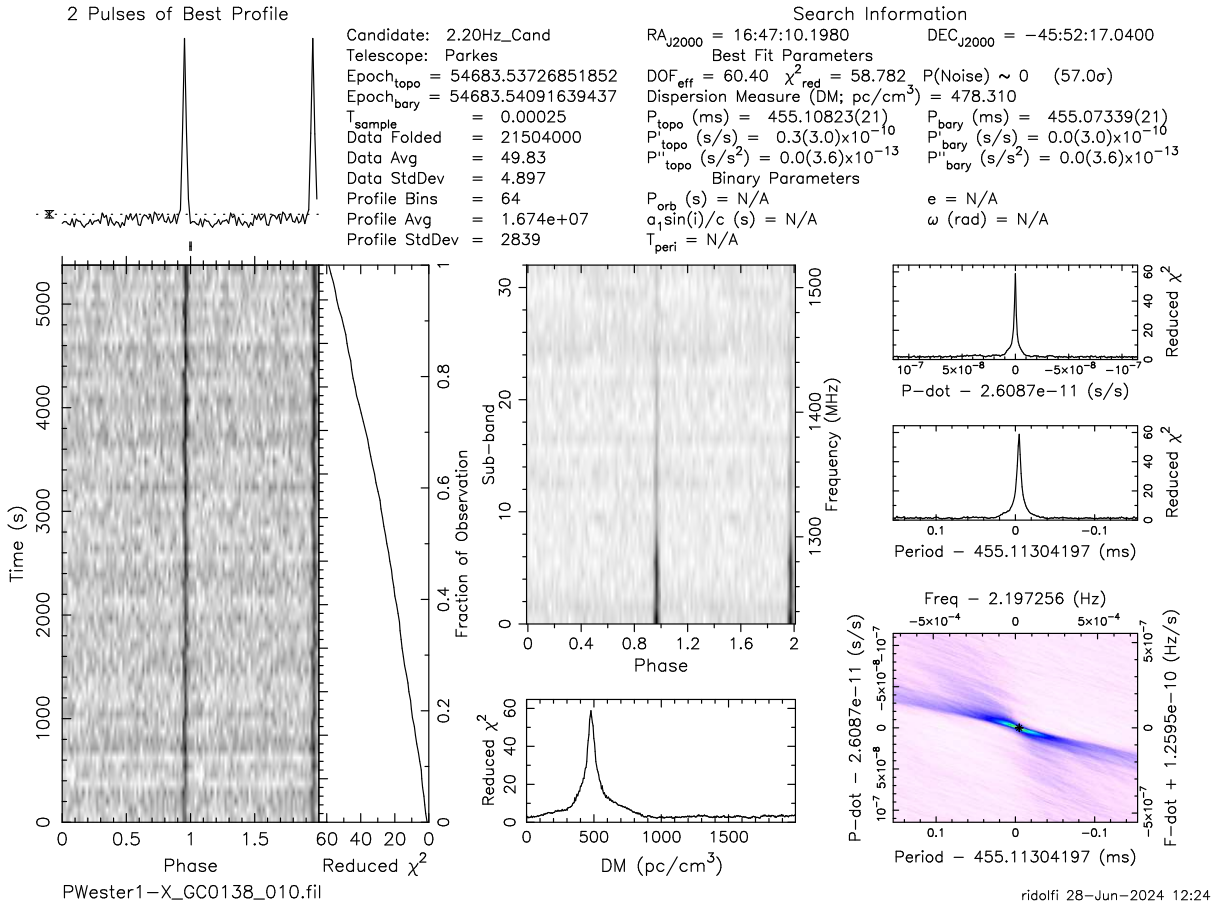

Figure 2.5. Example of diagnostic plot produced with PRESTO showing the signal of a real pulsar (PSR B1641−45)

2.3 State of the art of pulsar searching algorithms

After going through all the major steps that characterize a modern pulsar searching pipeline, we hereby focus on the state of the art of periodicity search algorithms.

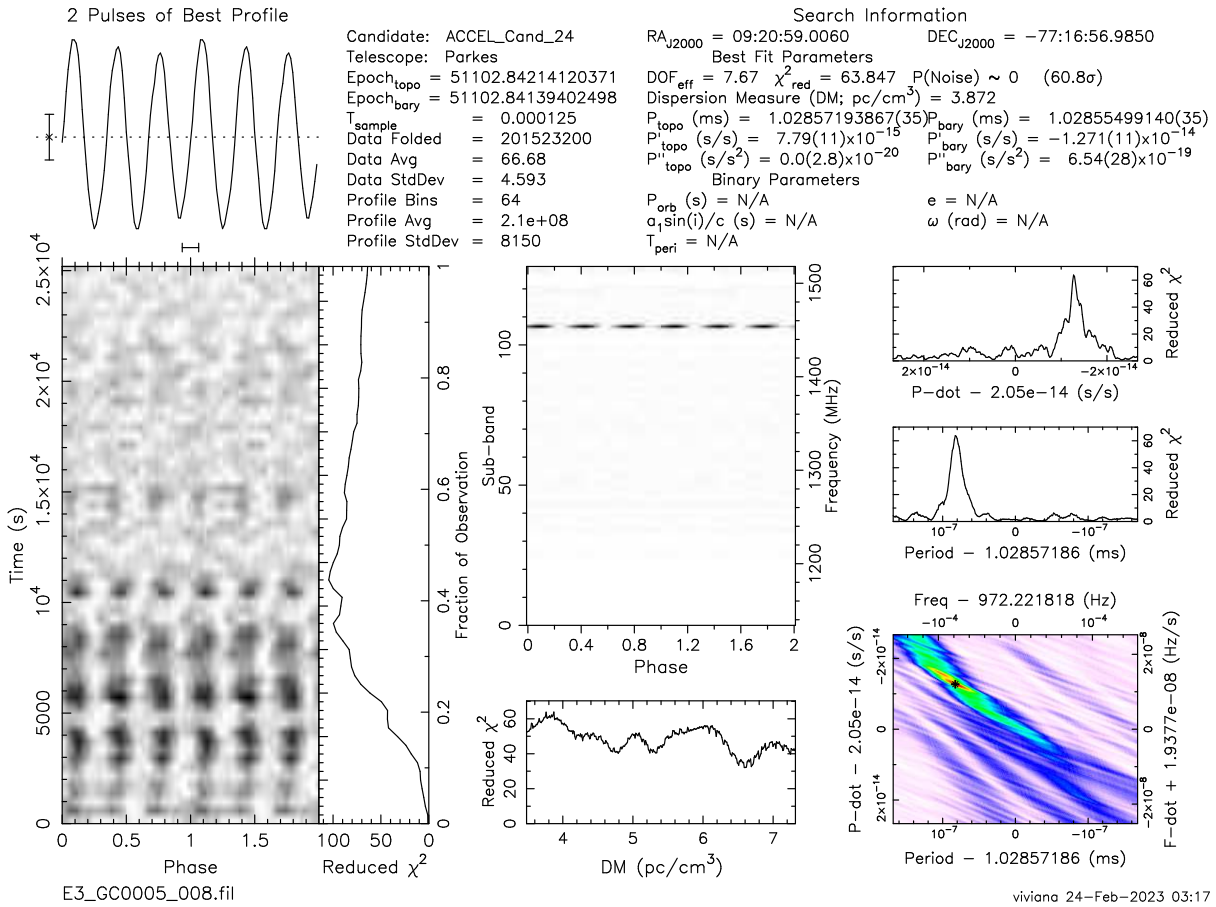

Figure 2.6. Example of diagnostic plot produced with PRESTO showing a narrow-band RFI signal.

2.3.1 Detecting pulsar in binary systems

The search pipeline that we described in the previous section assumed that the pulsars to be discovered be isolated. However, when a pulsar is part of a binary system, the detection of its signal becomes more challenging. The reason for this is that, in this case, the neutron star constantly undergoes time-dependent acceleration due to the orbital motion. The projection of such acceleration along the line of sight in turn causes a time-varying observed spin period and spin period derivative within a single observation: this is nothing else that a time-varying Doppler effect, due to a time-varying projected velocity of the pulsar along our line of sight during the observation. The observed spin period and its derivative can therefore be expressed as:

$$P_{\rm obs}(t) = P\left[1 + \frac{v_l(t)}{c}\right]; \qquad \dot{P}_{\rm obs}(t) = P\,\frac{a_l(t)}{c}\,, \tag{2.3}$$

where P and $\dot{P}$ are the intrinsic spin period and spin period derivative, $P_{\rm obs}$ and $\dot{P}_{\rm obs}$ the observed ones, $v_l(t)$ and $a_l(t)$ the pulsar velocity and acceleration component projected along the line of sight, respectively.

In frequency-domain search methods, as a consequence of a time-varying per-

ceived spin period (and therefore, a time-varying spin frequency), the Fourier power associated with the signal will be spread across multiple bins in the power spectrum, with the effects being larger for larger accelerations. As the power is spread across many Fourier bins, if the signal is not strong enough, it may not stand out from the noise, but rather stay buried in it, remaining undetected. Therefore, one need a way to account for such effect in order to recover the pulsar signal.

Over the decades, several techniques have been developed for this purpose. In the following, we review the major techniques currently used to recover the signal of pulsars within binary systems.

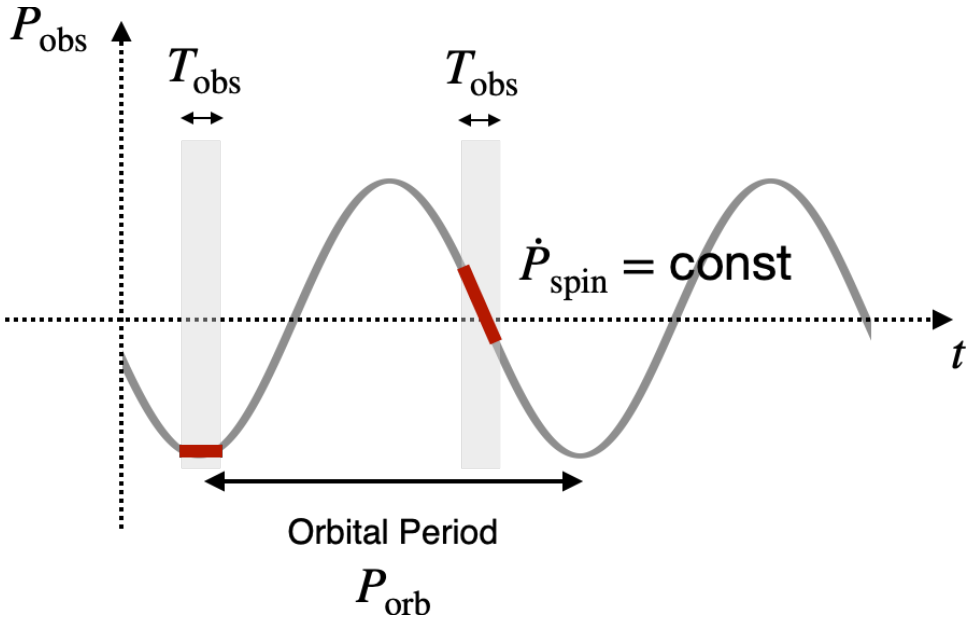

Figure 2.7. Schematic representation of the "10% rule" of acceleration search. In the plot, we show the sinusoidal modulation of the observed spin period, $P_{\rm obs}$, of a pulsar in a circular binary orbit, over more than a full cycle. If an observation (here shown as the grey shaded area) covers less than 10% of the orbital cycle, then the observed variation of $P_{\rm obs}$ during the observation, regardless of the orbital phase interval covered, can nicely be approximated with a line (red line); that is, the observed spin period derivative, $\dot{P}_{\rm spin}$ can be considered as constant throughout the observation. This is the assumption under which the *acceleration search* technique works.

2.3.1.1 Acceleration search

The *acceleration search* is the most widespread technique used to discover pulsars in binary systems. In a nutshell, it assumes that the acceleration component along the line of sight undergone by the pulsar be constant throughout the observation, and corrects for the effect. As we shall see in the following, this is valid only under certain assumptions.

Let us start from the $P_{\rm obs}(t)$ expression of Eq. (2.3). This can be expressed as a Taylor series expansion (e.g., Johnston & Kulkarni 1991):

$$v_l(t) = \dot{v}_l(0)t + \frac{\ddot{v}_l(0)}{2!}t^2 + \frac{\dddot{v}_l(0)}{3!}t^3 + \mathcal{O}(t^4) \tag{2.4}$$

where we recall that v_l is the line-of-sight component of the pulsar's velocity. If we make the assumption that, during the observation, the Doppler modulation is caused only by a constant acceleration, Eq. (2.4) reduces to:

$$v_l(t) = \dot{v}_l(0)\, t = a_l\, t \tag{2.5}$$

where a_l is the acceleration component along the line of sight, and not the total acceleration.

In order for this assumption to be valid, the length of the observation must be substantially shorter than the orbital period of the binary system, P_b. This can be intuitively understood looking at Figure 2.7. The latter schematically shows the observed spin period of a pulsar in a circular binary orbit, which has a sinusoidal dependency as a function of time, as a result of the time-varying projection of the velocity along the line of sight. If the observation length T_obs is short enough compared to the orbital period P_b, the sinusoidal function that describes the spin period modulation can effectively be approximated with a line (that is, $\dot{P}_\mathrm{obs}(t) \propto a_l(t) = \text{const}$) in any section of the orbit. As a general rule of thumb, for a circular orbit, this approximation can effectively hold valid if $T_\mathrm{obs} \lesssim P_\mathrm{b}/10$. This is what is commonly referred to as the "10% rule" in the pulsar astronomy jargon.

If this is the case, the acceleration search techniques consists in correcting for the constant acceleration undergone by the pulsar during the observation. This can be done either in the time domain or in the Fourier domain. The two methods, although sharing the same principles, work differently:

- The *time-domain acceleration search* (or TDAS) method accounts for the Doppler effect due to the orbit by re-sampling the time series. In essence, it shifts the samples in time applying anticipations or delays according to the assumed constant acceleration. Mathematically, these time shifts can be expressed as

$$\mathcal{T}(t) = \mathcal{T}(0)\left(1 + \frac{a_l \cdot t}{c}\right) \tag{2.6}$$

  where $\mathcal{T}(t)$ is a time interval in the pulsar frame, $\mathcal{T}(0)$ is a normalization factor and c is the speed of light. After the resampling (which can be done, e.g., through a simple linear interpolation Middleditch & Kristian 1984), the pulsar signal will look like as if the pulsar were in fact isolated, and we can later apply our standard Fourier or time-domain detection techniques for isolated pulsars.

- The *Fourier-domain acceleration search* (or FDAS) does not work on the time series, rather on on its power spectrum after a FT is applied. It is possible to show that, for a pulsar of spin period P, a constant line-of-sight acceleration a_l will cause the power of the fundamental and higher harmonics f the pulsar signal to spread across a number of Fourier bins that can be expressed as (Ransom et al., 2002):

$$z = T_\mathrm{obs}^2 \frac{a_l \cdot h}{cP}. \tag{2.7}$$

  where h is the harmonic number. This equation is used to generate templates for different values of z, with which a matched filtering in the Fourier domain

is performed. The template that best fits the spectral signature of the binary-modulated signal of the pulsar will then be used to retrieve the corresponding acceleration of the pulsar and, therefore, derive the corresponding P and $Pdot$ observed in that particular observation.

Clearly, in both implementations, the constant acceleration a_l is unknown a-priori, and therefore is a parameter that has to be searched over a sensible range. Notwithstanding, the problem of detecting the signal of a pulsar in a binary system is essentially reduced to a one-dimensional problem, and it is therefore relatively cheap from a computational standpoint.[2]. On top of that, some acceleration search implementations can now exploit the high level of parallelization provided by modern Graphics Processing Units (GPUs), making the algorithm extremely fast when running on GPUs. All of this makes acceleration search still the fastest method available to search for binary pulsars. Because of this, despite its main limitation of being effective only with pulsars in sufficiently wide orbits, acceleration search is still the most popular binary pulsar search technique used by astronomers.

2.3.1.2 Jerk search

The *jerk search* algorithm is an extension of the acceleration search that also includes the time derivative of the acceleration, $\dot{a}_l$. This basically means considering an additional term in the Taylor expansion of Eq. (2.4). The line-of-sight component of the pulsar's velocity will therefore be expressed as:

$$v_l(t) = a_l\, t + \frac{j_l \cdot t^2}{2} \tag{2.8}$$

where j_l is the time derivative of the line-of-sight acceleration and is called *jerk*. In jerk search, the orbital modulation of the pulsar spin period is therefore approximated with a parabola, rather a line. This means that the validity of the approximation can be extended to observation lengths that are up to 15-20% of the orbital period. Therefore, for a certain observation of a given length, jerk search can detect pulsars that are part of tighter orbits, when compared to acceleration search. The price to pay for this increased effectiveness is the higher dimensionality of the problem, as we now have two unknown parameters (a_l and j_l) that must be searched. This implies much longer processing times for jerk searches with respect to acceleration searches.

Exactly like acceleration search, jerk search can be implemented both in the time domain and in the frequency domain. At the time of writing, the only implementation available is Fourier-based and has been developed by Andersen & Ransom (2018) within the `PRESTO` pulsar searching software, where the z parameter is now accompanied by its time derivative $\dot{z} = w$, which is related to the jerk as:

$$w = T_{\rm obs}^3 \frac{j_l \cdot h}{cP}. \tag{2.9}$$

[2]The FDAS implementations are usually much more computationally efficient that TDAS implementations. Indeed, while the former require only a single FFT to be done on a time series, the later require an FFT operation for each acceleration trial value applied, for each de-dispersed time series.

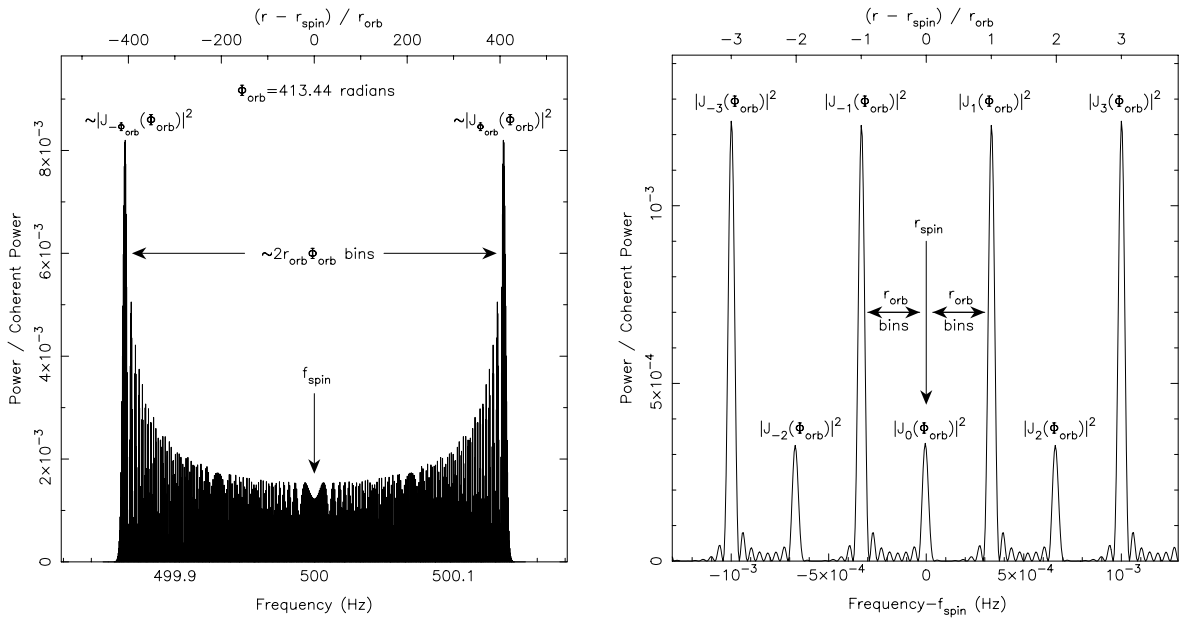

Figure 2.8. Fourier response of a simulated signal emitted by a 2-ms pulsar in a 50-minute circular orbit, for an 8-h observation. As can be seen in the left panel, the Doppler-modulated signal produces the typical "horned-shaped" response in the Fourier spectrum. In the right panel, it is shown how the individual peaks are equally spaced by $r_{\rm orb} = T_{\rm obs}/P_{\rm b}$ Fourier bins, where $T_{\rm obs}$ is the observation length and $P_{\rm b}$ is the orbital period. Figure taken from Ransom et al. (2003).

2.3.1.3 "Phase-modulation" (or "side-band") search.

The acceleration and jerk search methods have proved to be very effective at finding binary pulsar in relatively wide orbits, with hundreds of discoveries made with these techniques (e.g. D'Amico et al., 2001; Ridolfi et al., 2021; Douglas et al., 2022). As discussed in the previous sections, however, their efficacy decreases sharply when the observation searched is longer than 10% of the orbital period in the case of the acceleration search, or than $\sim 15 - 20\%$ in the case of the jerk search. Therefore, finding pulsars in ultra-compact binary systems, where the observation length is comparable or even much larger than the orbital period, requires the use of different methods. One of these is the so-called *phase-modulation* or *sideband* search, a Fourier-domain method independently developed by Jouteux et al. (2002) and Ransom et al. (2003). The phase-modulation search complements the use of the acceleration and jerk searches, by targeting pulsars in binary systems with $T_{\rm obs} \gtrsim 1.5 P_{\rm b}$; that is, all those binary systems for which the observation covered more than one orbit and a half. The efficacy of the phase-modulation search technique also increases as the ratio $T_{\rm obs}/P_{\rm b}$ increases: in other words, the larger the number of orbits that the observation covers, the higher the sensitivity. In the following, we provide some more in-depth description of the method, following the derivation of Ransom et al. (2003)and considering only the case of circular orbits. The latter choice is made both for the sake of simplicity and also because ultra-compact binaries are, for the most part, expected to be circular.

Let us consider a pulsar of intrinsic spin period P (and, hence, spin frequency $f_{\rm spin} = 1/P$) in a circular orbit of period $P_{\rm b}$ (orbital frequency $f_{\rm b} = 1/P_{\rm b}$), being observed for a time $T_{\rm obs} \gtrsim 1.5 P_{\rm b}$.

The signal coming from the pulsar, as seen from a distant observer, will be Doppler-modulated by the orbital motion, and will therefore be seen with the train of pulses being "squeezed" and "stretched" periodically in a sinusoidal fashion, due to the longer or shorter distance that light has to travel from the pulsar to the observer, depending on the position of the pulsar along its orbit. The fundamental harmonic, as sampled by the telescope, can be described as:

$$n(t) = \mathcal{A} \cos \left[2\pi \frac{(t - t_0)}{P} + \phi_{\rm spin} + \underbrace{\Phi_{\rm orb} \cos \left(2\pi \frac{(t - t_0)}{P_{\rm b}} + \phi_{\rm orb} \right)}_{\text{orbital modulation term}} \right] \tag{2.10}$$

where t_0 is the start time of the observation; $\mathcal{A}$ and $\phi_{\rm spin}$ are the amplitude and phase of the pulses; $\Phi_{\rm orb}$ and $\phi_{\rm orb}$ are the amplitude and phase of the orbital modulation.

Now, it can be shown (Ransom et al., 2003) that the Fourier transform of the phase-modulated signal of Equation 2.10 is equivalent to the Fourier transform of a series of cosinusoids, at frequencies (referred to as *sidebands*) that are centered at the pulsar spin frequency and are spaced from latter by $m\, r_{\rm orb}$ Fourier bins, where $r_{\rm orb} = T_{\rm obs}/P_{\rm b}$ is the number of orbits covered by the observation and $m \in \mathbb{Z}$. The amplitudes of the sidebands show a characteristic "horned shaped" trend (see Fig. 2.8), and their exact value depend on the orbital characteristics. In any case these amplitudes decrease sharply for sidebands separated by more than $r_{\rm orb}\Phi_{\rm orb}$ bins from the intrinsic spin frequency of the pulsar.

As the peaks in the power spectrum are equally spaced by $r_{\rm orb}$ bins, these can in turn be seen as a periodic signal: this periodicity can be revealed by performing a local "mini-FFT" in the power spectrum, obtaining the value of $r_{\rm orb}$ and, consequently, the rough value of the binary orbital period. Although this operation can be performed very quickly, obtaining a refined value for $P_{\rm b}$, as well as the other two orbital parameters (the projected size of the orbit, $x_{\rm p}$, and the epoch of passage at the ascending node, $T_{\rm asc}$) is a much more computationally intensive task. This is because, in order to do that, one has to search the three-dimensional orbital parameters space ($P_{\rm b}, x_{\rm p}, T_{\rm asc}$) within a sensible range of values. For each triplet of parameters, a template of the "horned-shaped" Fourier response is generated and matched-filtered and evaluated against the actual power spectrum. This has to be done for all the potential candidate binary pulsars detected with the "mini-FFT". This makes the phase-modulation search method extremely computationally demanding, requiring several hours on a modern machine to search just a single de-dispersed time series. Therefore the application of this search method to actual surveys has been extremely limited, and restricted to very specific cases.

2.3.1.4 Full Keplerian Template Bank search

Another method to discover binary pulsars in compact orbits is the *full Keplerian template bank search* (Balakrishnan et al., 2022). The idea is to convolve the data with a large number of simulated templates (or, a *bank*) of pulsar signals modulated by the

motion along a binary orbit. The latter is fully modelled using 5 Keplerian parameters, namely: the projected semi-major axis, $x_{\rm p}$; the eccentricity, e; the longitude of periastron, ω; the mean angular velocity, $\Omega_{\rm orb}$; the initial orbital phase, $\alpha_{\rm orb}$. In addition to the five Keplerian orbital parameters, the intrinsic spin frequency of the pulsar, $f_{\rm spin}$ is needed to generate a model (template) of the binary pulsar signal. Overall, a 6-dimensional parameter space $\{x_{\rm p}, e, \Omega_{\rm orb}, \alpha_{\rm orb}, f_{\rm spin}\}$ must therefore be searched. For each point in this space, a pulsar signal template is generated and matched filtered to the data through a convolution process. Therefore an optimal coverage of this parameter space is also key to minimize the computational cost. The full Keplerian template bank search is technically the most effective method to reveal pulsars in compact binary systems with any possible orbital characteristics. However, the high dimensionality of the parameter space makes this method the most computationally intensive one to search for binary pulsars, even after accounting for the GPU support of its current implementation (https://github.com/vishnubk/5D_Peasoup, Balakrishnan et al. 2022). Therefore the Keplerian template bank algorithm will likely applicable only through large-scale high-performance-computing facilities.

A simplified version of the 5D-Keplerian template bank search is its version for circular orbits, where the Keplerian parameters are reduced to three. Such an implementation currently finds application within the Einstein@Home project[3] (Allen et al., 2013; Knispel et al., 2013), which is a platform for volunteer distributed computing, where real astronomical data is processed thanks to the computing power "donated" by the volunteers.

2.3.2 Improved algorithms for isolated pulsars

Binary pulsars, and in particular binary MSPs, have historically been among the most desired targets of pulsar astronomers carrying out searches. This is primarily because pulsars in binaries enable a number of experiments that it is not possible to perform with isolated pulsars. Moreover, it has been long thought that our ability to find single pulsars was essentially limited only by our sensitivity, while binary pulsars required sophisticated techniques, as we just saw. For this reason, most efforts have historically gone to the development of algorithms to discover pulsars in binary systems. In the recent years, however, the discovery of extremely slow pulsars with spin periods well above 10 seconds (Tan et al., 2018; Morello et al., 2020a) have shown that there are several objects with extremely long spin periods that may have been missed by most surveys. This has led astronomers to further develop or improve techniques better tailored to reveal isolated pulsars, particularly those with very long periods. In the following we review two main search techniques now commonly used for this purpose.

2.3.2.1 The Fast Folding Algorithm

The Fourier Transform and its FFT implementation has historically been the most widespread method employed in the search for pulsars, as it was successfully used in numerous large-scale surveys. Notwithstanding, the FFT has a number of drawbacks. For instance, the current implementations of FFT search methods are only capable of incoherently summing a limited number of harmonics (typically 16 or 32),

[3] https://einsteinathome.org

which can greatly reduce the capability of detecting periodic signals with very small duty cycles. Also, FFT methods are highly susceptible to red noise, which can notably diminish their ability to detect pulsars with long rotational periods, particularly those exceeding ~ 1 second (which are all concentrated in the $\sim 0-1$ Hz region of the power spectrum). Indeed, Lazarus et al. (2015) demonstrated that the actual sensitivity reached by the Pulsar Arecibo L-band Feed Array (PALFA) survey was significantly lower than what predicted by the radiometer equation, particularly for pulsars with periods longer than approximately 100 milliseconds. If not properly taken into account, these limitations can potentially induce a significant selection bias, distorting our understanding of the true pulsar population. Additionally, the detection of slow-spinning pulsars is typically much more heavily affected by the presence of RFI. An alternative approach to the Fourier Transform is the direct folding of the time series using a number of trial rotational periods, and inspect the resulting folded profiles. A computationally efficient implementation of this technique is the so-called fast-folding algorithm (FFA), originally put forward by Staelin (1969) and recently implemented in modern pieces of software by Cameron et al. (2017), Parent et al. (2018) and Morello et al. (2020b). The FFA is very efficient at folding a time series with multiple trial periods by cleverly avoiding redundant summations and storing partial results for later recall as needed. Notably, the FFA's processing speed increases when it folds data over extended periods. This is because the required number of additions during the folding sequence is proportional to $O(N \log_2(N/p))$, where N represents the total sample count in the dataset, and p denotes the initial trial period for folding, measured in sample units. Consequently, with a constant N, as p grows, the addition operations diminish, thereby enhancing the FFA's efficiency for longer periods. Additionally, even though the FFA is not completely immune to red noise, it is a phase-coherent method, therefore being intrinsically more sensitive that FFT-based techniques. The FFA has been successfully used to discovery two slow-spinning pulsars in the globular cluster M15 (Zhou et al., 2024).

2.3.2.2 Stack search

Another way to increase the sensitivity to isolated pulsars is by using the *stack search* techniques. The latter exploits the facts that the spin period of an isolated pulsar, when referred to the Solar System Barycenter, is constant over a long period of time (with the intrinsic spin-down playing a role only over very long time scales). As a consequence, the power of the pulsar signal in the Fourier spectrum is expected to be located always at the Fourier frequency. Therefore, one can add together several power spectra obtained from different observations of the same target to obtain a "stacked" spectrum were the powers associated with isolated pulsars are boosted. As this method only uses the Fourier powers, ignoring the phase, it is in fact an incoherent method. As a result, the Fourier significance of the pulsar signal will grow as $T_{\rm obs}^{\rm tot}/\sqrt{T_{\rm obs}^{\rm tot}} \sim \sqrt{T_{\rm obs}^{\rm tot}}$, where $T_{\rm obs}^{\rm tot}$ is the total integration time of all the observations whose spectra are stacked. Clearly, this method is not particularly useful for large scale surveys, where a single sky region is typically observed a couple of times at most. Rather, it is very effective for targets that are observed repeatedly, like globular clusters. Indeed, the stack search technique has been fruitfully used to discover isolated pulsars in the globular clusters 47 Tucanae (Pan et al., 2016) and Terzan 5

(Cadelano et al., 2018).

2.3.3 Single pulse search

All the previous methods are based on the assumption that the signal coming from the pulsar is persistent in time, that is, that we get a pulse at every rotation of the neutron star. However, that are classes of pulsars, such as the Rotating Radio Transients (McLaughlin et al., 2006) and the "nulling" pulsars, that are known to emit their pulses sporadically or only for limited periods of time. Applying periodicity search methods to these sources is therefore largely ineffective, and a different searching approach is thus required. This led to the development of *single-pulse* search algorithms. The latter essentially tries to detect individual bright pulses by applying a matched-filtering algorithm to a de-dispersed time series, looking for statistically significant "events". The method, originally devised to look for transient pulsars, has led to the serendipitous discovery of a new class of transient sources of extra-galactic origin, which we now refer to as *Fast Radio Bursts* (Lorimer et al., 2007). Given its cheap computational cost, the single-pulse search is nowadays commonly included in the majority of large-scale pulsar surveys.

CHAPTER 3

Applications to globular cluster data taken with southern radio telescopes

3.1 Introduction

As discussed in Section 1.6.1, among the best places where to search for pulsars are globular clusters (GCs). This is because these stellar aggregations are known to harbor a wealth of pulsars in a very compact region of the sky. Furthermore, the pulsars that are found in globular clusters often exhibit properties that are extreme or exotic, enabling new and peculiar studies that would not be possible with Galactic field pulsars. For these reasons, over the decades, several telescopes have conducted surveys aimed at finding pulsars in GCs. As a result, hundreds of observations have been taken and hundreds of pulsars have been discovered.

In this Chapter, we apply some of the search methods previously described to look for pulsars in 10 selected globular clusters, using observations taken with two major radio telescopes in the southern hemisphere: the Australian "Murriyang" radio telescope, and the South African MeerKAT radio telescope.

3.1.1 Pulsars in globular clusters at the "Murriyang" radio telescope

The "Murriyang" radio telescope (Fig. 3.1) is a single parabolic dish with a diameter of 64 meters, operating within the Parkes Observatory, which is situated about 20 km north of the town of Parkes, New South Wales, Australia. Since its first commissioning in 1961, the Parkes Observatory has proved to be one of the most successful radio facilities ever built: besides having a major role in historical human achievements (such as the Apollo 11 moon landing), over the decades it has been pivotal for numerous outstanding scientific breakthrough, such as the discovery of the first quasar 3C 273 (Hazard et al., 1963), as well as of the first Fast Radio Burst (Lorimer et al., 2007). Its contribution to pulsar astronomy has also been paramount, with over 1000 pulsars discovered, including PSR J0737−3039A/B, the only double-pulsar system known (Burgay et al., 2003).

The "Murriyang" telescope has also been one of the most active radio facilities for the study of pulsars in globular clusters: the Parkes Globular Cluster survey (PKSGC, Possenti et al. 2003), which started in the late 90's, observed tens of globular clusters, giving a major contribution to the first wave of pulsar discoveries in these stellar systems. Even today, thanks to upgraded instrumentation, the Parkes Observatory continues to have a primary role in the discovery and follow-up of pulsars in several GCs (e.g. Dai et al., 2020; Zhang et al., 2020).

Figure 3.1. The 64-m single-dish "Murriyang" radio telescope near Parkes, Australia. Photo credit: Alessandro Ridolfi (2012).

Figure 3.2. View of nine of the 64 antennas that compose the MeerKAT radio telescope array. Photo credit: Alessandro Ridolfi (2018).

3.1.2 Pulsars in globular clusters at the MeerKAT radio telescope

The MeerKAT radio telescope (Fig. 3.2; Jonas & MeerKAT Team 2016; Camilo 2018) is the most sensitive cm-wavelength telescope of the southern hemisphere. It is located in the Karoo desert, in the Northern Cape province of South Africa. Contrary to the Parkes radio telescope, MeerKAT is not a single-dish telescope. Rather, it is an interferometer composed by 64 antennas, each having a diameter of 13.5 metres, spread within an area of 4 km in radius. The signals from all the antennas are combined together so as to work as if they were a single telescope with a collecting area as large as the sum of the collecting area of all the individual antennas. MeerKAT is also the precursor to the SKA1-mid telescope (Dewdney et al., 2009), which will be an enhanced version of MeerKAT: over the coming years, more dishes will be added and, eventually, a total of 197 antennas will compose the array, turning MeerKAT into SKA1-mid.

Since it began operations in 2018, the MeerKAT telescope has been devoted to a large number of scientific objectives, which are pursued through the execution of 10 Large Survey Projects (LSPs). These are 5-year-long observing programmes, each dedicated to a specific theme. Among the 10 LSPs approved at MeerKAT, TRAPUM[1] ("TRansients and PUlsars with MeerKAT" Stappers & Kramer 2016) is one of two dedicated to pulsars. The main scientific objectives of TRAPUM are the increase of the total known population of Galactic and extra-Galactic pulsars, the discovery of peculiar pulsars and binary systems, and the discovery of transient radio sources. This is achieved by means of targeted observations of supernova remnants, pulsar wind nebulae, unidentified Fermi γ-ray sources, nearby galaxies, and globular clusters. The TRAPUM globular cluster pulsar survey, which started in 2020 (e.g., Douglas et al., 2022) and is still ongoing, carries out deep, repeated observations of more than 30 GCs, in search for the faintest and most extreme pulsars. As of June 2024, TRAPUM has discovered more than 220 pulsars[2], over 90 of which in GCs.

3.2 Observations

The dataset analyzed in the context of this thesis consisted of 20 observations, carried out with the Parkes and MeerKAT radio telescopes, of 10 selected southern globular clusters with no pulsars previously known to be residing in them: these are E3, ESO 452, NGC 288, NGC 3021, NGC 4372, NGC 4590, NGC 4833, NGC 5286, NGC 6541 and NGC 6584. All the selected clusters have declinations lower than -26 deg, hence the majority are only observable from the Parkes and MeerKAT sites, being inaccessible from any other high-sensitivity cm-wavelength radio telescopes. We selected GCs that, to our knowledge, have so far only been observed at Parkes and not already deeply searched with modern software and high-performance-computing facilities. In addition, we restricted our sample to only those GCs that were not among the targets of the TRAPUM GC pulsar survey at MeerKAT. The sole exception to this is represented by NGC 6541, a core-collapsed cluster, observed both with MeerKAT and Parkes, whose observations have all been searched in the context of this thesis. The list of the searched GCs with their main characteristics is reported in Table 3.1, while

[1] https://trapum.org
[2] https://trapum.org/discoveries

their positions in Galactic coordinates are displayed in Fig. 3.4. Optical images of all the clusters are shown in Fig. 3.3.

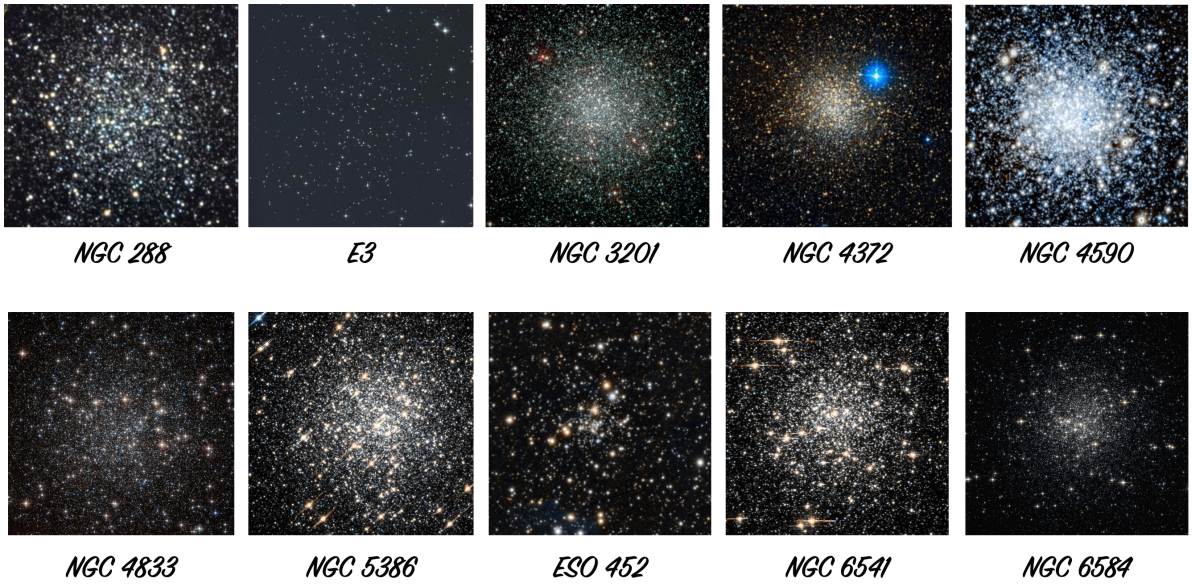

Figure 3.3. Optical images of the 10 globular clusters searched in the context of this thesis. Image credits: NGC 288: Wikisky; E3: HST; NGC 3201: ESO; NGC 4372: Bernhard Hubl; NGC 4590 and ESO 452: PanSTARRS DR1; NGC 4833: ESA/Hubble; NGC 5286 and NGC 6541: Hubble Legacy Archive; NGC 6584: NASA/HST.

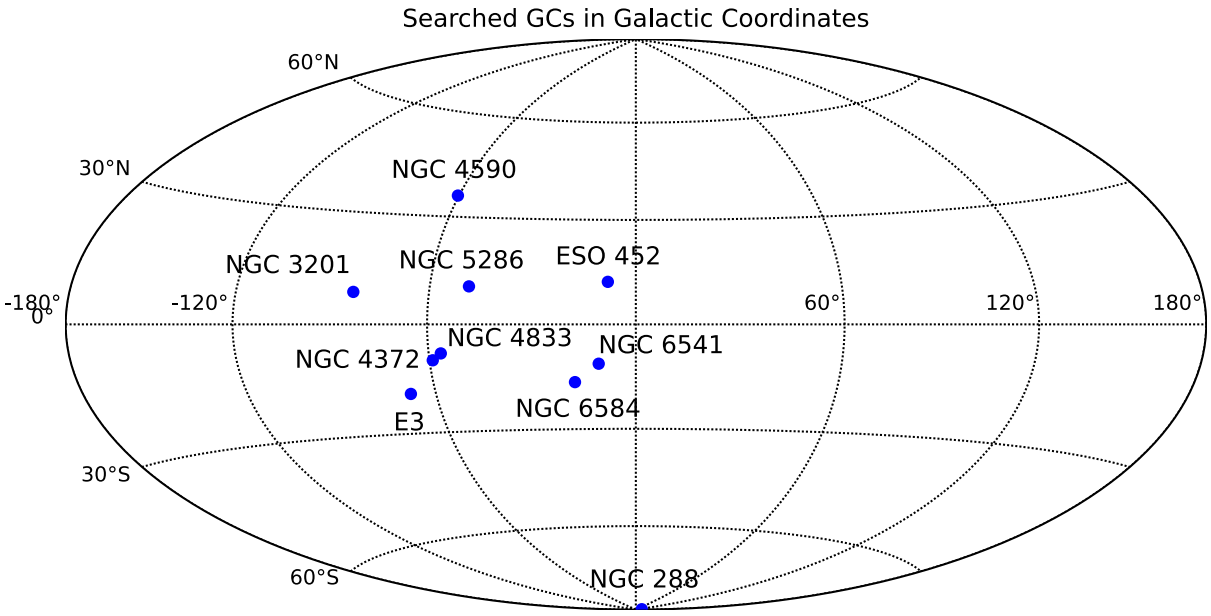

Figure 3.4. Location of the 10 globular clusters searched, in Galactic coordinates.

Table 3.1. List of the globular clusters searched in the context of this thesis. α: Right Ascension of the nominal cluster center; δ: Declination of the nominal cluster center; r_c: core radius, defined as the distance from the core at which the cluster surface brightness is half of its central value; r_h: half-light radius, defined as the radius at which half of the total light of the globular is emitted; $\mathcal{C}$: cluster concentration, defined as $\mathcal{C} = \log(r_t/r_c)$, where r_t, called *tidal radius*, is the distance from the cluster center at which the gravitational field of the host galaxy becomes more important than the self gravity of the cluster; d: cluster distance; $DM_{NE2001\ /\ YMW16}$: dispersion measure associated with the cluster, as predicted by the NE2001 and YMW16 Galactic electron density model, respectively.

Cluster	α (J2000)	δ (J2000)	r_c (arcmin)	r_h (arcmin)	$\mathcal{C}$	d (kpc)	$DM_{NE2001\ /\ YMW16}$ (pc cm^{-3})
NGC 288	00:52:45.24	−26:34:57.4	1.35	2.23	0.99	8.9	28 / 18
E3	09:20:57.07	−77:16:54.8	1.87	2.10	0.75	8.1	99 / 113
NGC 3201	10:17:36.82	−46:24:44.9	1.30	3.10	1.29	4.9	141 / 353
NGC 4372	12:25:45.40	−72:39:32.4	1.75	3.91	1.3	5.8	173 / 159
NGC 4590 (M68)	12:39:27.98	−26:44:38.6	0.58	1.51	1.41	10.3	52 / 41
NGC 4833	12:59:33.92	−70:52:35.4	1.00	2.41	1.25	6.6	210 / 170
NGC 5286	13:46:26.81	−51:22:27.3	0.28	0.73	1.41	11.7	208 / 146
ESO 452	16:39:25.45	−28 23:55.3	0.50	0.50	1.00	8.3	182 / 105
NGC 6541	18:08:02.36	−43:42:53.6	0.18	1.06	1.86 (cc)	7.5	195 / 108
NGC 6584	18:18:37.60	−52:12:56.8	0.26	0.73	1.47	13.5	138 / 93

3.2.1 The Parkes dataset

The Parkes dataset comprises a total of 19 observations, split among the ten selected GCs. These observations were all carried out as part of the PKSGC survey, which aimed at searching for pulsars in virtually all the GCs visible from the Parkes site. All of the 19 observations, except one, were taken using the central beam of the Parkes Multi-beam receiver (Staveley-Smith et al., 1996) and the Analogue FilterBank (AFB) backend with two different configurations. In one configuration, the central frequency was set to 1326 MHz, and the observing bandwidth to 384 MHz, divided into 128, 3-MHz wide frequency channels. In the other configuration, the central frequency was set to 1390 MHz, and the observing bandwidth to 256 MHz, divided into 512, 0.5-MHz wide frequency channels. The beam size on the sky (full-width at half maximum) of these observations is approximately 14 arcmin, sufficient to encompass much more than the half-light radius of all the clusters. A single observation of NGC 288 was taken with another receiver, at a central frequency of 2934 MHz. In this case, the observing bandwidth was 576 MHz, divided into 192 channels, resulting in 3-MHz wide frequency channels. The beam size of this observation is about 7 arcmin, still sufficient to cover the half-light radius of NGC 288. All the observations were acquired in total intensity mode, with 1 bit per sample and a sampling time that ranged between 50 and 125 μs. All the observations, with their parameters, are listed in Table 3.2.

3.2.2 The MeerKAT dataset

The MeerKAT dataset consists of a single, 2-hour-long observation of the core-collapsed cluster NGC 6541. The observation was carried out on 26 July 2023 with the MeerKAT L-band (856–1712 MHz) receivers, using 60 antennas. The data were acquired using the Filterbanking Beamformer User Supplied Equipment (FBFUSE) and the Acceler-

ated Pulsar Search User Supplied Equipment (APSUSE) computing clusters as backends, which, together, constitute the data-taking system of the TRAPUM project (Barr, 2018). FBFUSE is used to synthesize a large number of tied-array beams on the sky, by correlating the signals coming from all the MeerKAT antennas (Chen et al., 2021). In our case, the observation recorded 36, partially overlapping, tied-array beams, each being about ~ 9 arcsec in size. Altogether, the tied-array beams formed a tiling, which covered an area of approximately 0.5 arcmin in radius around the nominal center of the cluster (Fig. 3.5). This was sufficient to cover well beyond the core radius of NGC 6541, and approximately half of the half-light radius of the cluster: within this area our sensitivity was the highest. Along with the tied-array beams, an additional incoherent beam was recorded: this has the advantage of covering a much larger area of the sky (about 0.5 degrees in radius), but its sensitivity is about 8 times lower than that of the tied-array beams[3]. All the beams were recorded with the APSUSE cluster as total-intensity, 8-bit digitized, filterbank search-mode files. The total observing bandwidth of 856 MHz, centered at 1284 MHz, was split into 4096 channels and recorded every 153 μs. The details of the positions, sizes and properties of all the recorded beams are reported in Table 3.3.

3.2.3 Sensitivity

As outlined above, our dataset is composed of observations made with different telescopes, different set-ups, and different integration times. Therefore, our sensitivity (and therefore our ability to find faint pulsars) varies from observation to observation. We can calculate the sensitivity of our searches by means of the radiometer equation (Eq. 2.1), using the parameters of each individual observation and of the telescope used. For the Parkes observations taken with the multi-beam receiver, we use $G = 0.735$ KJy^{-1}, $T_{\rm sys} = 23$ K, $\xi = 1.1$, whereas for the MeerKAT observation, where 60 antennas were used, we use $G = 2.625$ KJy^{-1}, $T_{\rm sys} = 26$ K, $\xi = 1.1$. For our calculations, we assume S/N = 10 and an intrinsic pulse duty cycle, W/P, of 8%. The *effective* duty cycle, however, will be affected by the intra-channel dispersion (which in turn depends on the DM and on the width of the frequency channels) and by potential scattering (see Lorimer & Kramer 2004). This will cause a degradation in the sensitivity: the larger the assumed DM and size of the frequency channels, the larger the penalty in sensitivity, which is more severe for the fastest-spinning pulsars, as their pulse duty cycle increases sharply when smearing effects are at play. When accounting for all of these effects, one can get a sensitivity curve that shows the minimum detectable mean flux density as a function of the spin period of the pulsar. In Fig. 3.6 we show the best sensitivity curve (i.e., we consider only the longest, and therefore most sensitive, observation when multiple observations with similar setups were made for a given cluster) for each of the 10 globular clusters searched in this work. When calculating the sensitivity curve, we assume the associated DM to be the higher value between the two predictions made by the NE2001 and YMW16 models. As can be seen, with the Parkes data, the minimum detectable mean flux density for slowly-rotating ($P \gtrsim 100$ ms) pulsars ranges between ~ 63 μJy (for the 46-minute ob-

[3]This is because the sensitivity of a tied-array beams scales linearly with the number of antennas used, while the sensitivity of an incoherent beam only scales with the square root of the number of antennas used.

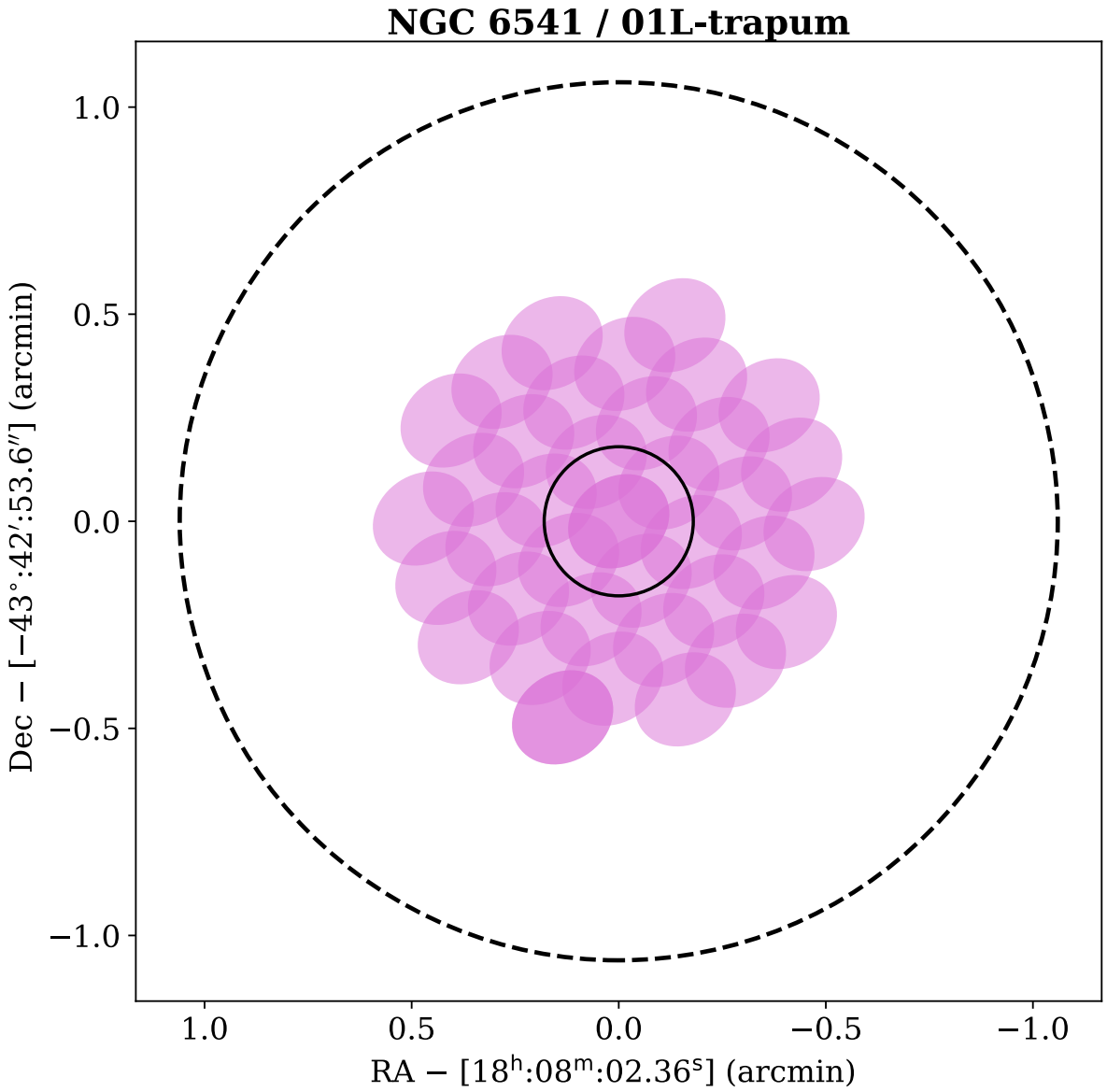

Figure 3.5. Tiling of the TRAPUM observation of NGC 6541 taken on 2023 July 26. The pink ellipses represent the tied-array beams contours at the 50 per cent of their boresight power. The outer dashed circle and the inner solid circle show the half-light radius (at 1.06 arcmin from the nominal cluster centre) and core radius (at 0.18 arcmin from the nominal cluster centre) of NGC 6541, respectively.

Table 3.2. Table listing all the observations of the 10 different globular clusters searched in the context of this thesis. $T_{\rm obs}$: observation length; $f_{\rm c}$: central frequency; Δf: observing bandwidth; $N_{\rm chan}$: number of frequency channels; Δf_c: channel bandwidth; $t_{\rm samp}$: sampling time; $N_{\rm beams}$: number of tied-array beams on the sky.

Cluster	Telescope	Start Date and Time (UTC)	$T_{\rm obs}$ (min)	$f_{\rm c}$ (MHz)	Δf (MHz)	$N_{\rm chan}$	Δf_c (MHz)	$t_{\rm samp}$ (μs)	$N_{\rm beams}$
NGC 288	Parkes	1998-10-17 14:39	64	1326	384	128	3.00	125	1
	Parkes	1998-10-17 16:03	211	1326	384	128	3.00	125	1
	Parkes	2004-02-15 07:11	140	2934	576	192	3.00	125	1
E3	Parkes	1998-10-16 20:12	420	1326	384	128	3.00	125	1
	Parkes	2002-07-28 06:04	140	1390	256	512	0.50	125	1
NGC 3201	Parkes	1998-10-17 19:12	214	1326	384	128	3.00	125	1
	Parkes	1998-10-17 20:57	177	1326	384	128	3.00	50	1
	Parkes	2000-07-22 23:30	140	1390	256	512	0.50	125	1
NGC 4372	Parkes	2000-07-23 01:53	140	1390	256	512	0.50	125	1
NGC 4590	Parkes	2002-07-31 07:12	140	1390	256	512	0.50	125	1
NGC 4833	Parkes	2001-03-09 14:11	70	1390	256	512	0.50	125	1
NGC 5286	Parkes	2002-07-22 06:22	140	1390	256	512	0.50	125	1
	Parkes	2006-10-07 01:04	113	1390	256	512	0.50	100	1
ESO 452	Parkes	2002-08-01 08:44	140	1390	256	512	0.50	125	1
NGC 6541	Parkes	1999-12-09 23:49	140	1390	256	512	0.50	125	1
	Parkes	2000-12-05 06:45	70	1390	256	512	0.50	125	1
	Parkes	2000-12-07 07:24	46	1390	256	512	0.50	80	1
	Parkes	2000-12-08 23:19	70	1390	256	512	0.50	125	1
	MeerKAT	2023-07-26 00:28	120	1284	856	4096	0.209	153	37
NGC 6584	Parkes	2002-07-28 14:04	140	1390	256	512	0.50	125	1

servation of NGC 4833) and ~ 21 μJy (for the 7-hour observation of E3). These values rapidly increase for pulsars with shorter spin periods because of the pulse broadening effects coming at play due to the finite width of the frequency channels and predicted scattering. With the MeerKAT data, thanks to the much higher telescope gain, larger observing bandwidth and much finer channelization, the minimum detectable mean flux density is lower than 10 μJy for pulsars with $P > 5$ ms, and it is always lower than 20 μJy for any pulsar with $P > 1$ ms.

3.3 Data analysis

As a first step in the data analysis, we devised the search strategy. Firstly, we determined the DM range to search using the NE2001 and YWM16 electron density models (see Section 1.4.1) as implemented in the PyGEDM[4] software (Price et al., 2021). For each cluster, we inputed the equatorial coordinates and the distance as reported in the Harris Catalog of globular clusters[5] (Harris, 2010) obtaining two predicted DM values.

[4] https://apps.datacentral.org.au/pygedm
[5] https://physics.mcmaster.ca/~harris/mwgc.dat

Table 3.3. Table listing the parameters of the 37 beams recorded for the MeerKAT observation of NGC 6541 taken on 26 July 2023. Beam I-000 is the incoherent beam. Beams C-0xx are coherent (tied-array) beams. $\alpha_{\rm beam}$, $\delta_{\rm beam}$: beam boresight coordinates (Right Ascension and Declination); $\mathcal{D}_{\rm x}^{\rm beam}$,$\mathcal{D}_{\rm y}^{\rm beam}$: beam sizes (major and minor axis) at half power; $T_{\rm obs}$: observation length; f_c: central frequency; Δf: observing bandwidth; $N_{\rm chan}$: number of frequency channels; Δf_c: channel bandwidth; $t_{\rm samp}$: sampling time.

NGC 6541 - MeerKAT observation									
Beam id	$\alpha_{\rm beam}$ (J2000)	$\delta_{\rm beam}$ (J2000)	$\mathcal{D}_{\rm x}^{\rm beam}$,$\mathcal{D}_{\rm y}^{\rm beam}$	$T_{\rm obs}$ (min)	f_c (MHz)	Δf (MHz)	$N_{\rm chan}$	Δf_c (MHz)	$t_{\rm samp}$ (μs)
I-000	18:08:02.36	−43:42:53.6	(1.08°,1.08°)	120	1284	856	4096	0.209	153
C-000	18:08:02.36	−43:42:53.6	(10″,8″)	120	1284	856	4096	0.209	153
C-001	18:08:01.39	−43:42:56.6	(10″,8″)	120	1284	856	4096	0.209	153
C-002	18:08:03.33	−43:42:50.6	(10″,8″)	120	1284	856	4096	0.209	153
C-003	18:08:00.42	−43:42:59.6	(10″,8″)	120	1284	856	4096	0.209	153
C-004	18:08:04.30	−43:42:47.6	(10″,8″)	120	1284	856	4096	0.209	153
C-005	18:08:01.69	−43:42:48.0	(10″,8″)	120	1284	856	4096	0.209	153
C-006	18:08:02.66	−43:42:45.0	(10″,8″)	120	1284	856	4096	0.209	153
C-007	18:08:00.72	−43:42:51.0	(10″,8″)	120	1284	856	4096	0.209	153
C-008	18:08:03.63	−43:42:42.0	(10″,8″)	120	1284	856	4096	0.209	153
C-009	18:07:59.75	−43:42:54.0	(10″,8″)	120	1284	856	4096	0.209	153
C-010	18:08:04.60	−43:42:39.0	(10″,8″)	120	1284	856	4096	0.209	153
C-011	18:08:02.06	−43:43:02.2	(10″,8″)	120	1284	856	4096	0.209	153
C-012	18:08:03.03	−43:42:59.2	(10″,8″)	120	1284	856	4096	0.209	153
C-013	18:08:01.09	−43:43:05.2	(10″,8″)	120	1284	856	4096	0.209	153
C-014	18:08:04.00	−43:42:56.2	(10″,8″)	120	1284	856	4096	0.209	153
C-015	18:08:00.12	−43:43:08.2	(10″,8″)	120	1284	856	4096	0.209	153
C-016	18:08:04.97	−43:42:53.2	(10″,8″)	120	1284	856	4096	0.209	153
C-017	18:08:01.99	−43:42:39.4	(10″,8″)	120	1284	856	4096	0.209	153
C-018	18:08:01.02	−43:42:42.4	(10″,8″)	120	1284	856	4096	0.209	153
C-019	18:08:02.96	−43:42:36.4	(10″,8″)	120	1284	856	4096	0.209	153
C-020	18:08:00.05	−43:42:45.4	(10″,8″)	120	1284	856	4096	0.209	153
C-021	18:08:03.92	−43:42:33.4	(10″,8″)	120	1284	856	4096	0.209	153
C-022	18:08:02.73	−43:43:07.8	(10″,8″)	120	1284	856	4096	0.209	153
C-023	18:08:01.76	−43:43:10.8	(10″,8″)	120	1284	856	4096	0.209	153
C-024	18:08:03.70	−43:43:04.8	(10″,8″)	120	1284	856	4096	0.209	153
C-025	18:08:00.80	−43:43:13.8	(10″,8″)	120	1284	856	4096	0.209	153
C-026	18:08:04.67	−43:43:01.8	(10″,8″)	120	1284	856	4096	0.209	153
C-027	18:08:01.32	−43:42:33.8	(10″,8″)	120	1284	856	4096	0.209	153
C-028	18:08:02.28	−43:42:30.8	(10″,8″)	120	1284	856	4096	0.209	153
C-029	18:08:00.35	−43:42:36.8	(10″,8″)	120	1284	856	4096	0.209	153
C-030	18:08:03.25	−43:42:27.8	(10″,8″)	120	1284	856	4096	0.209	153
C-031	18:08:02.44	−43:43:16.4	(10″,8″)	120	1284	856	4096	0.209	153
C-032	18:08:03.41	−43:43:13.4	(10″,8″)	120	1284	856	4096	0.209	153
C-033	18:08:01.47	−43:43:19.4	(10″,8″)	120	1284	856	4096	0.209	153
C-034	18:08:04.37	−43:43:10.4	(10″,8″)	120	1284	856	4096	0.209	153
C-035	18:08:01.61	−43:42:25.2	(10″,8″)	120	1284	856	4096	0.209	153

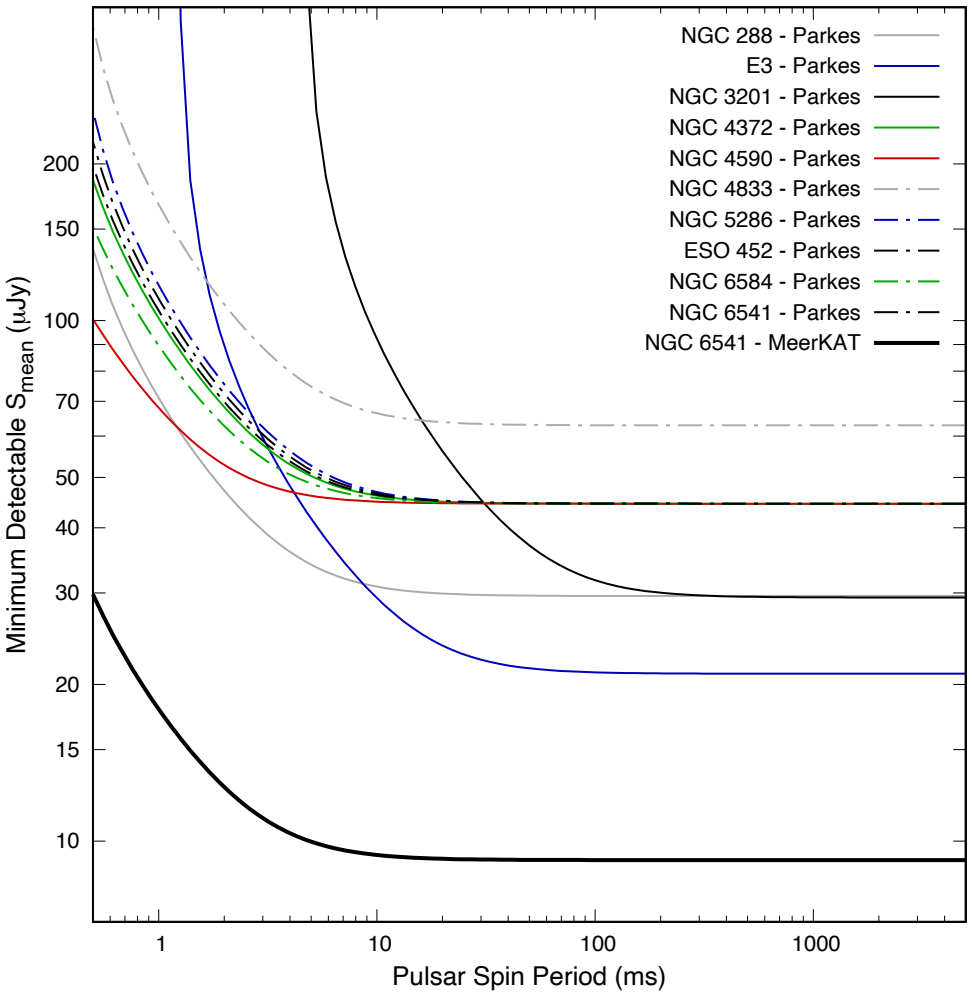

Figure 3.6. Sensitivity curves for the longest observation of each globular cluster searched in the context of this thesis. The curves are calculated assuming the predicted value for the DM as given by the NE2001 model (see Table 3.1)

.

The search for the latter was then conservatively performed across a DM range from zero to about double the value of the higher between the DMs returned by the two models. Once the DM range to search for each cluster was established, an RFI mask for every single observation was created using the `rfifind` routine of the PRESTO[6] pulsar searching package (Ransom, 2011). As for the search itself, we decided to restrict ourselves to Fourier-domain techniques, and to include acceleration and jerk searches. This choice is justified as it is a good trade-off between having reasonably fast processing times, and being sensitive to fast-spinning pulsars in fairly compact binaries, which are abundant in globular clusters. The application of additional methods, more suitable to find ultra-compact binary pulsars (such as the phase-modulation search and the 5D Keplerian template banking search), would have required much longer processing times, incompatible with the time frame of this work.

[6] https://github.com/scottransom/presto

The actual pulsar search analysis was carried out with PULSAR_MINER[7] (Ridolfi et al., 2021), an automated pipeline based on PRESTO and its GPU-optimized variant (PRESTO_ON_GPU[8]), which allows to perform Fourier-domain searches, including acceleration and jerk searches. The processing was done on a 14-node high-performance-computing cluster recently installed at the INAF – Osservatorio Astronomico di Cagliari. All nodes are powered by dual 16-core/32-thread AMD Epyc "Milan" CPUs, while 6 nodes also feature two NVIDIA A40 GPUs, which we exploited for the acceleration search part of the analysis.

With PULSAR_MINER, each observation is first summed in frequency, ignoring the RFI-polluted frequency channels and time intervals indicated in the previously made mask, to produce a 0-DM time series. The latter is then Fourier transformed, and the resulting power spectrum is scanned in search of prominent peaks. These will indicate the presence of low-level periodic signals of terrestrial origin (the so-called *birdies*), whose frequencies are then stored in a "zaplist file" so as to be ignored in the later analysis. Then, an optimal de-dispersion scheme is calculated using the `DDplan.py` routine of PRESTO: given the parameters of the observation (i.e., central frequency, observing bandwidth, number of frequency channels and sampling time interval), `DDplan.py` returns the best DM trial step sizes to use across the whole DM range to be searched, allowing for the minimization of the number of computations without losing sensitivity.

Using this plan, the `prepsubband` routine is run on the observation in combination with the corresponding RFI mask to generate cleaned, barycentered (i.e. referred to the Solar System barycenter) de-dispersed time series for each DM trial value. Each of these is then Fourier transformed with the `realfft` routine and the slow time-varying effects of possible red noise are mitigated by running the `rednoise` routine. All these steps produce (mostly) RFI-free, de-reddered power spectra, one for each DM trial. These are then searched using PRESTO's `accelsearch` routine. The latter performs a matched filtering in the Fourier domain and can seek signals coming from both isolated and binary pulsars. To specify exactly what types of pulsars to target, `accelsearch` accepts two input parameters: `-zmax` and `-wmax`. The `-zmax` parameter defines the maximum allowed spectral drift, in terms of number of Fourier bins, due to linear acceleration undergone because of a binary motion, for the highest harmonic considered. Therefore, when `-zmax` equals to 0, no possible spectral drift is considered, meaning that only isolated pulsars will be searched. On the other hand, if `-zmax` is greater than zero, a possible binary motion, under the linear acceleration approximation ("acceleration search", see Section 2.3.1.1) can be accounted for. The larger the `-zmax` value, the larger the allowed linear acceleration, but also the longer the computational time required. Therefore, the `-zmax` value must be chosen as a trade-off between acceptable processing time and maximum linear acceleration to be sensitive to. For our searches, we let PULSAR_MINER run `accelsearch` with both `-zmax` = 0, to target isolated pulsars, and `-zmax`=200, to target binary pulsars. In both cases the highest number of harmonics considered was 8. In addition to acceleration search, we carried out jerk search. The latter is enabled when the `-wmax` is greater than 0. In our case, the parameters used where `-zmax`=100, `-wmax`=300 and up to 4 harmonics

[7] https://github.com/alex88ridolfi/PULSAR_MINER
[8] https://github.com/jintaoluo/presto2_on_gpu

were considered.

As we explained in Section 2.3.1.1, the acceleration search is effective only when $T_{\rm obs} \lesssim 0.1\,P_{\rm b}$, while the jerk search works well as long as $T_{\rm obs} \lesssim 0.2\,P_{\rm b}$. As all the observations in our dataset were longer than 45 minutes, with most of them being longer than 2 hours, our ability to detect binary pulsars would in principle be restricted to orbits at least five times longer than the length of the observation (i.e. orbits longer 3.75 hours in the best case, longer than 10 hours for most cases). In order to be sensitive to even more compact orbits and make our sensitivity to binary orbits more uniform across all the observations, we enabled a "segmented search" in `PULSAR_MINER`: each observation was first searched in its full length, and then split into segments of lengths (whenever applicable) of 120, 60, 30 and 15 minutes, and each segment was searched individually. This strategy allowed us to be sensitive to potential binary pulsars with orbits as short as about 15 min $\times\, 10 = 150$ min with the acceleration search and about 15 min $\times\, 5 = 75$ min with the jerk search. This ability comes at the expense of a higher minimum mean flux density that the pulsar must have to be detected, due to the shorter integration time of the segments. After each segment is searched, all the candidate periodicities that are found to have a Fourier significance higher than 4σ are grouped together and sifted according to several criteria (see Section 2.2.6), and written onto a final candidates list file. All the sifted candidates are then folded by running the `prepfold` routine on the raw data, using the nominal DM and period of the candidate, and applying the RFI mask to ignore bad channels and time intervals. The routine also optimizes the folding parameters so as to maximize the S/N of the resulting integrated pulse profile and produces a diagnostic plot for each candidate. As a result of our searches, a number of the order of a few hundred to a few thousands of candidate plots per observation were produced. Although high, the number is still manageable and no particular additional filtering was needed. All the plots were therefore inspected visually.

3.4 Results

As a result of the search of all the globular clusters, a total of about 24700 candidates were produced. After the detailed scrutiny of all the relative diagnostic plots, we selected 56 of them as promising candidate pulsars. The details of such selected candidates are listed in Table 3.4, while their diagnostic plots are shown in Appendix A.

As can be seen from the Table, the vast majority of the candidate pulsars are MSPs (which we regard here as those with spin periods shorter than 10 ms), whereas six are potential mildly recycled pulsars (with $10 < P < 37$ ms) and one is a possible slow pulsar ($P = 311$ ms)

Among the candidates, 22 candidates have been detected with no significant acceleration, indicating that the putative pulsar would be isolated, or in a very wide orbit that has an orbital period much longer than the segment where the pulsar was found. On the other hand, the other 34 were detected with a significant line-of-sight acceleration, with nominal absolute values that range between 0.10 to as much as 99 $\mathrm{m\,s^{-2}}$. These values are perfectly reasonable for the kind of (possibly eccentric) binary pulsars that can be found in a GC. Even the highest detected line-of-sight ac-

Table 3.4. List of the 56 most promising pulsar candidates found in the 10 different globular clusters searched in the context of this thesis. For each candidate, we list where the candidate was found (in order: the host cluster; the date of the observation; the beam, if applicable; the segment length; the segment number) as well as its properties (in order: the candidate spin period; the candidate spin period derivative, if applicable; the candidate second spin period derivative, if applicable; the candidate DM; the corresponding candidate linear acceleration; the candidate significance).

Cluster	Obs. date	Beam number	Seg. length	Seg. #	P (ms)	$\dot{P}$ (10^{-10})	$\ddot{P}$ (s^{-1})	DM (pc cm^{-3})	a_l (m s^{-2})	σ
E3	28 Jul 2002	-	full	0	6.290	0.213	0	96.3	1.02	6.6
NGC 288	17 Oct 1998	-	30 m	2	3.018	0	0	27.7	0	5.6
NGC 288	17 Oct 1998	-	30 m	6	4.174	0	0	43.4	0	5.4
NGC 288	17 Oct 1998	-	60 m	2	3.092	0	0	56.5	0	9.5
NGC 3201	22 Jul 2000	-	full	0	5.628	0	0	201.6	0	6.6
NGC 3201	22 Jul 2000	-	30 m	0	3.089	1.35	0	197.8	13.11	6.6
NGC 3201	23 Jul 2000	-	15 m	3	2.806	0	0	32.9	0	7.1
NGC 3201	23 Jul 2000	-	15 m	4	8.717	-5.16	0	173.6	−17.73	5.5
NGC 3201	23 Jul 2000	-	30 m	2	5.942	0.22	0	109.6	1.10	6.9
NGC 4372	23 Jul 2000	-	30 m	1	9.595	0	0	251.0	0	6.2
NGC 4372	23 Jul 2000	-	30 m	0	5.422	0	0	34.5	0	7.7
NGC 4372	23 Jul 2000	-	30 m	0	3.502	0.63	0	135.2	5.35	6.5
NGC 4372	23 Jul 2000	-	30 m	0	2.768	0	0	121.2	0	6.2
NGC 4372	23 Jul 2000	-	30 m	0	2.407	0	0	272.1	0	6.6
NGC 4372	23 Jul 2000	-	30 m	3	37.262	0	0	202.1	0	7.3
NGC 4372	23 Jul 2000	-	15 m	3	6.552	0	0	320.7	0	5.3
NGC 4372	23 Jul 2000	-	60 m	0	5.083	0.49	0	247.9	2.90	6.4
NGC 4372	23 Jul 2000	-	60 m	0	5.850	1.52	0	256.9	7.78	6.0
NGC 4372	23 Jul 2000	-	15 m	0	4.795	5.06	0	268.8	31.62	6.5
NGC 4590	31 Jul 2002	-	60 m	1	5.162	0.06	0	99.1	0.35	9.9
NGC 4590	31 Jul 2002	-	30 m	0	5.080	1.88	0	20.8	11.11	7.3
NGC 4590	31 Jul 2002	-	full	0	8.945	0.09	0	96.9	0.30	6.4
NGC 4833	9 Mar 2001	-	full	0	8.363	0	0	180.1	0	6.7
NGC 4833	9 Mar 2001	-	full	0	12.022	0	0	379.8	0	6.9
NGC 5286	7 Oct 2006	-	60 m	0	5.133	0	0	53.2	0	6.9
NGC 5286	7 Oct 2006	-	60 m	1	7.083	1.00	0	135.5	4.22	5.9
NGC 5286	7 Oct 2006	-	60 m	1	7.941	0	0	137.2	0	6.3
ESO 452	1 Aug 2002	-	15 m	1	7.334	−0.70	0	179.2	−2.87	6.5
ESO 452	1 Aug 2002	-	30 m	0	4.261	0	0	237.8	0	8.7
ESO 452	1 Aug 2002	-	30 m	2	3.352	0	0	124.7	0	10.3
ESO 452	1 Aug 2002	-	30 m	3	6.881	0	0	171.7	0	9.6
ESO 452	1 Aug 2002	-	full	0	4.635	0.008	0	173.7	0.05	10.1
ESO 452	1 Aug 2002	-	full	0	3.248	−0.10	0	242.0	−0.92	11.2
NGC 6541	9 Dec 1999	-	60 m	0	3.056	−0.06	0	119.4	−0.60	6.4
NGC 6541	9 Dec 1999	-	15 m	0	3.137	4.75	0	297.0	45.43	5.2
NGC 6541	9 Dec 1999	-	full	0	7.205	0.17	0	305.4	0.71	6.7
NGC 6541	5 Dec 2000	-	15 m	0	9.804	32.5	0	286.1	99.31	6.1
NGC 6541	5 Dec 2000	-	full	0	3.014	0	0	306.6	0	6.2
NGC 6541	5 Dec 2000	-	full	0	6.161	0.47	0	297.3	2.30	6.0
NGC 6541	8 Dec 2000	-	full	0	311.010	−590	0	63.5	−56.86	10.1
NGC 6541	8 Dec 2000	-	full	0	14.123	−6.47	0	303.3	−13.74	6.6
NGC 6541	8 Dec 2000	-	full	0	3.130	−0.07	0	170.3	−0.68	6.4
NGC 6541	8 Dec 2000	-	full	0	7.979	1.68	0	306.3	6.31	6.8
NGC 6541	8 Dec 2000	-	15 m	0	15.373	−12.3	0	318.5	−24.02	6.3
NGC 6541	8 Dec 2000	-	full	0	3.569	−0.33	0	175.4	−2.78	7.4
NGC 6541	26 Jul 2023	C-001	full	0	4.136	0	0	257.9	0	4.2
NGC 6541	26 Jul 2023	C-001	full	0	11.003	−0.038	0	574.2	−0.10	5.3
NGC 6541	26 Jul 2023	C-004	full	0	7.136	−0.210	0	314.1	−0.88	4.8
NGC 6541	26 Jul 2023	C-005	full	0	5.373	0.07	0	190.0	0.41	5.1
NGC 6541	26 Jul 2023	C-005	full	0	9.773	−0.35	0	515.9	−1.07	4.8
NGC 6541	26 Jul 2023	C-013	full	0	7.179	0.05	0	173.2	0.20	4.8
NGC 6541	26 Jul 2023	C-028	full	0	6.357	0.28	0	495.1	1.32	5.2
NGC 6541	26 Jul 2023	C-031	full	0	11.166	0	0	120.0	0	5.0
NGC 6541	26 Jul 2023	C-032	full	0	6.591	0	0	107.9	0	6.0
NGC 6584	28 Jul 2002	-	30 m	0	6.060	−4.11	0	194.4	−20.34	6.3
NGC 6584	28 Jul 2002	-	30 m	3	7.228	−3.32	0	191.9	−13.77	5.3

celeration of 99.31 m s^{-2} is still well within the maximum absolute acceleration known for a binary pulsar system (which is 684 m s^{-2}, for the double-neutron star system PSR J1757−1854, Cameron et al. 2018). We also note that none of the selected candidates showed any non-zero second spin period derivative (jerk).

Lastly, we can see that the significance of all the candidates is between $\sim 4 - 11\sigma$, with the majority being $\lesssim 7\sigma$.

3.5 Discussion and future work

If all the selected promising candidates found were real, the proportions among the different types of pulsars (MSPs versus mildly recycled versus slow, as well as isolated pulsars versus binary pulsars) would not be surprising. Rather, they would be in very good agreement with the broader GC pulsar population. However, the low significance of the candidates prevents us from claiming the discovery of any pulsars in the searched clusters. Any of the candidate pulsars found would require an additional detection of the same periodicity, at the same DM, in a different observation, in order to be confirmed. However, for half of the GCs searched (specifically, NGC 4372, NGC 4590, NGC 4833, ESO 452, and NGC 6584), only a single observation was available, therefore, it was not possible to confirm any of their candidates. For the other five GCs, multiple observations were available and searched, but none of the candidate pulsars found were seen in more than one observation. One possibility is, obviously, that those candidates are not real pulsars. Alternatively, the non-detection of at least some of these candidates in additional observations of the same cluster could be due to a few other reasons, such as: a) the different integration times, which give different sensitivities, for the different observations; b) for the pulsars in binary systems, unfavorable orbital phases, where the pulsar could be eclipsed or could have too high a line-of-sight acceleration or jerk, which could not be accounted for; c) for the candidates with low nominal DM (< 100 pc cm^{-3}), scintillation could boost or suppress the pulsar signal in different observations. All of these explanations, although unlikely, are anyway possible and apply to the Parkes observations, where the observing set-up, and therefore the sensitivity, is very similar across all the observations of the clusters.

Different considerations are needed for the core-collapsed cluster NGC 6541, as it was observed with both the Parkes and MeerKAT telescopes. In this case, given the much superior sensitivity of the South African telescope over the Australian one, one could expect the candidates found in the Parkes observations to show up, and much brighter, also in the MeerKAT observation. However, the latter covered a much smaller area on the sky than the former (~ 1 arcmin vs ~ 14 arcmin in diameter). Therefore, it is possible that some pulsars found in the Parkes data fall outside the tied-array beam tiling of the MeerKAT observation. In fact, other core-collapsed GCs (e.g. NGC 6752, M15), have pulsars that are located in the very outskirts of the cluster, as a result of being flung because of a gravitational interaction with other stars in the dense cluster core. In this regard, one might argue that those pulsars would anyway show up in the incoherent beam (C-000), which covers about ~ 1 deg in diameter. However, the sensitivity of the incoherent beam is slightly lower than that of the Parkes data, and much more severely affected by RFI than the tied-array beams. Therefore, given that

all the candidates found in the Parkes observation of NGC 6541 are very faint and therefore have low significance, it would not be surprising if they were not detected in the coherent MeerKAT beam, even though they were real.

Given all of this, the only way to confirm or refute the candidates presented here, is to re-observe the clusters with either the Parkes or the MeerKAT telescope. If re-observed at Parkes, one would be able to use the new Ultra-Wideband-Low receiver (UWL, Hobbs et al. 2020), which covers the 0.7-4.0 GHz frequency range. This would provide a much larger bandwidth than our searched observations, allowing us to have higher sensitivity while still being able to observe a sky area of several arcminutes in diameter, therefore covering well the half-light radius of all clusters. Re-observing the clusters with MeerKAT and its L-band (856-1712 MHz) receivers, will obviously give the advantage of the much higher (up to $\sim 4-6\times$) sensitivity. However, given the interferometric nature of MeerKAT, it would be very important, for the future observations, to be able to synthesize hundreds of tied-array beams on the sky, so as to cover an area of few arcmin in radius, so as to encompass at least the half-light radius.

If none of the candidates are confirmed, nor other new pulsars are found even after re-observing the GCs with Parkes/UWL or with MeerKAT, we see three possible explanations:

1. The pulsars are missed because the searching algorithms used are not effective against the characteristics of the pulsars.

2. All the potentially detectable pulsars (i.e. those with their beams pointing towards the Earth) in these clusters have mean flux densities below the minimum detectable threshold. In other words, the pulsars are too faint, and require more sensitive telescopes or longer integration times to be detected.

3. None of the pulsars in these cluster have their beam pointing towards the Earth, hence none of them will ever be detectable.

The second scenario is what we regard as the most likely. In fact, this has been the case for a few GCs, most notably for the globular cluster Omega Centauri. Indeed, the latter was searched for pulsars at Parkes for about two decades, with no success. However, as soon as the more sensitive UWL receiver was installed and used, five pulsars were found with Parkes (Dai et al., 2020), and a further 13 were later discovered with MeerKAT (Chen et al., 2023).

Notwithstanding, scenario 1 is also very much possible, if not even likely. Indeed, the recent discovery of a MSP in a record-breaking orbit of just 53 minutes in the globular cluster M71 (PSR J1953+1844E, Pan et al. 2023) has once again demonstrated that pulsars in ultra-compact ($P_\mathrm{b} \lesssim 2$ h) binary systems exist and are likely common in GCs. The detection of such a compact binary pulsar was possible thanks to the extremely high gain of 16 K Jy^{-1} of the FAST telescope: having a huge instantaneous sensitivity allowed the successful application of acceleration search algorithms to data segments as short as 5 minutes (Han et al., 2021) while still being sensitive down to $S_\mathrm{mean} \sim 20$ μJy for pulsar with $P \sim 5$ ms. In the absence of FAST and its outstanding sensitivity, systems like PSR J1953+1844E could still be easily discovered by applying the more advanced searching techniques that we reviewed in Chapter 2, such as the phase-modulation search and/or the 3D/5D Keplerian template banking search.

Similarly, a few pulsars with unusually long periods ($\gtrsim 2$ s) were also found by FAST in the globular cluster M15 (Zhou et al., 2024), showing that slow pulsars in globular clusters may be more common than previously thought. However, as discussed in the previous chapter, the very long period pulsars are usually difficult to detect with traditional Fourier-domain methods, as they are more heavily impacted by the presence of red noise and RFI. In this case, an FFA algorithm is more indicated for search for them.

In light of these considerations, the application of the aforementioned more sophisticated algorithms will also be a crucial part of possible future work relative to the ten globular clusters searched here. One major obstacle to this is the processing time needed, which, in many cases, can be prohibitively long, particularly with modern datasets, and even if using high-performance-computing facilities. Another key aspect and possible future work (which would be beneficial for the whole pulsar community, and not only for those searching for pulsars in GCs) is therefore the further optimization and speed-up of (at least some of) the searching algorithms reviewed in this thesis. This could be achieved by making some of the codes be able to exploit GPUs, better utilize the multiple CPU threads available, and, most importantly, finding cleverer ways to explore the parameter space to search or to do the computations. This obviously requires some major effort on the development side of things. However, it is clear that such an endeavour is worthwhile, as it will have a major impact in our ability to process data quickly. This is something that is becoming a more and more important aspect, and that will be even more pressing in the era of big data and computational astrophysics that the new generation of radio telescopes, such as the SKA, are set to bring.

Chapter 4

Applications to young massive clusters: the case of Westerlund 1

This chapter is based on the article titled *"Serendipitous Discovery of a 431 ms Pulsar in the Background of Westerlund 1"*, which is published in *Universe* (Piga, V.; Burgay, M.; Possenti, A.; Ridolfi, A.; Pilia, M.; Rea, N.; Perna, R.; Colpi, M.; Israel, G. Serendipitous Discovery of a 431 ms Pulsar in the Background of Westerlund 1. Universe 2024, 10, 274, DOI: https://doi.org/10.3390/universe10070274).

4.1 Introduction

Young Massive Star Clusters (YMCs) are very dense agglomerations of young stars, conventionally defined as those clusters with ages smaller than 100 Myr and masses of $\gtrsim 10^4$ $M_\odot$ (Portegies Zwart et al., 2010). Several YMCs are found in the Local Group, and they are most common in starburst and interacting galaxies.

With a total mass in the range of $(44 - 57) \times 10^3$ $M_\odot$ (Andersen et al., 2017), Westerlund 1 (Westerlund, 1961; Clark et al., 2005) is the most massive YMC of the Local Group. The cluster is located in our Galaxy, in the Ara Constellation, with center coordinates at Right Ascension $\alpha = 16{:}47{:}04.00$ and Declination $\delta = -45°51'04''.9$ (Clark et al., 2005), corresponding to a Galactic longitude of $l = 339.55°$ and Galactic latitude of $b = -0.40°$. It is also relatively nearby, with an estimated distance of 4.05 ± 0.20 kpc (Navarete et al., 2022), which makes it a relatively easy target to study, when compared to other YMCs. Westerlund 1 has been extensively observed at various wavelengths over time (optical and X-ray images of the cluster are shown in Fig. 4.1). Among these, X-ray observations made with *Chandra* in 2005, revealed that the cluster is the host of a bright X-ray source, dubbed CXOU J164710.2−455216 (henceforth, CXOU J1647), which was identified as a magnetar spinning once every 10.61 seconds (Muno et al., 2006). In September 2006, CXOU J1647 experienced an X-ray outburst (Krimm et al., 2006), where its luminosity increased by a factor of 100 in just a few days (Muno et al., 2007). The discovery of CXOU J1647 triggered searches for the possible pulsed radio emission produced by the source: a multi-year monitoring campaign of CXOU J1647 was therefore initiated at the "Murriyang" radio telescope near Parkes, Australia, where observations were carried out between 2006 and 2010 with an approximately bi-monthly cadence.

In this Chapter, we report on the searches originally made to uncover the potential radio pulsations emitted by CXOU J1647. We also re-process the entire Parkes data set of Westerlund 1, blindly searching for radio pulsations, as well as for single pulses, potentially coming from CXOU J1647 and any possible other pulsars. The re-processing was motivated by the significantly more efficient pulsar searching algorithms and much larger computing power available today, and, for the single-pulse

search part, by the recent discovery of Fast Radio Burst-like signals from the Galactic magnetar SGR 1935+2154 (Mereghetti et al., 2020).

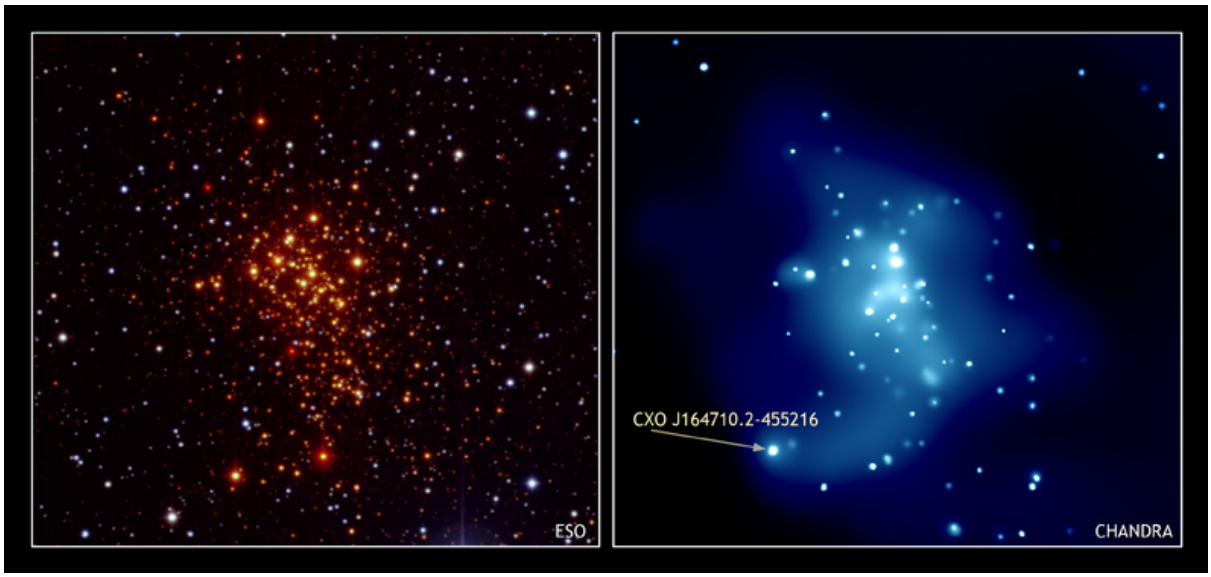

Figure 4.1. Images of the young massive cluster Westerlund 1 as seen in visible light (left) and in the X-rays (right panel). In the latter, the position of the X-ray magnetar CXOU J164710.2−455216 is indicated. Image credit: NASA/CXC/UCLA/M.Muno et al.

4.2 Observations

The dataset used for this work consists of 83 observations acquired between September 2005 and February 2010 with the Australian 64-m "Murriyang" Parkes radio telescope. Their durations varied from 18 to 280 minutes. In addition to the multi-year follow-up campaign made to search for the radio pulsations of CXOU J1647, the dataset includes one observation of Westerlund 1 made in 2005 (prior to the discovery of the magnetar), which was part of a pilot survey aimed at YMCs. The vast majority of the observations were taken with the central beam of the Parkes 21cm Multi-Beam receiver (Staveley-Smith et al., 1996), pointed at the location of the magnetar with the exception of the first observation, which was pointed at the nominal center of Westerlund 1. The central frequency used with the multi-beam receiver was either 1374 or 1390 MHz. About one-fourth of the observations were taken with "H-OH" receiver, at a central frequency of 1518 MHz, while a handful of observations were carried out with other single-beam receivers, which had higher central frequencies of ∼2.2 and ∼3.2 GHz. The total bandwidths used ranged between 256 MHz and 1152 MHz divided into 96, 192, 384 or 512 channels, 1-bit digitized in total-intensity only, with sampling intervals ranging between 125 and 750 μs. All the observations used in this work and their parameters are listed in Table 4.1.

Table 4.1. List of Parkes observations of the open cluster Westerlund 1 analyzed for this work. All of them were acquired using the Analogue Filterbank (AFB) backend. $\Delta t_{\rm obs}$: observation length; $f_{\rm c}$: central observing frequency; Δf: observing bandwidth; $N_{\rm chan}$: number of frequency channels; $t_{\rm samp}$: sampling time.

Start Date and Time (UTC)	$\Delta t_{\rm obs}$ (min)	$f_{\rm c}$ (MHz)	Δf (MHz)	$N_{\rm chan}$	$t_{\rm samp}$ (μs)
2005-09-07 06:02	280	1390	256	512	750
2006-08-14 10:06	70	1390	256	512	125
2006-09-28 04:51	248	1390	256	512	200
2006-10-02 01:29	119	1390	256	512	250
2006-11-10 23:06	60	1374	288	96	250
2006-12-24 04:03	59	1518	576	192	250
2006-12-24 05:04	55	1518	576	192	250
2006-12-26 03:41	45	1518	576	192	250
2006-12-27 01:46	59	1518	576	192	250
2006-12-27 04:45	58	1518	576	192	250
2006-12-28 01:13	59	1518	576	192	250
2006-12-28 23:22	59	1518	576	192	250
2006-12-29 00:22	59	1518	576	192	250
2007-01-06 01:14	100	2233	576	192	250
2007-01-06 02:55	100	2233	576	192	250
2007-01-14 02:07	18	1518	576	192	250
2007-01-14 02:26	59	1518	576	192	250
2007-01-15 01:15	47	1518	576	192	250
2007-01-22 17:32	59	1518	576	192	250
2007-01-22 18:33	59	1518	576	192	250
2007-02-14 22:14	59	1518	576	192	250
2007-02-15 15:58	40	1518	576	192	250
2007-02-16 01:36	41	1518	576	192	250
2007-02-21 19:18	90	3222	1152	384	250
2007-04-14 19:56	53	1518	576	192	250
2007-04-14 20:50	59	1518	576	192	250
2007-05-03 19:17	53	1518	576	192	250
2007-05-03 20:11	59	1518	576	192	250
2007-05-20 18:35	53	1374	288	96	250
2007-05-20 19:29	48	1374	288	96	250
2007-06-06 16:57	53	1374	288	96	250
2007-06-06 17:51	53	1374	288	96	250
2007-07-14 06:38	53	1374	288	96	250
2007-07-14 07:31	56	1374	288	96	250
2007-07-18 07:11	60	1374	288	96	250
2007-07-19 06:02	60	1374	288	96	250
2007-07-21 08:24	60	1374	288	96	250
2007-07-21 12:52	60	1374	288	96	250
2007-07-21 15:21	51	1374	288	96	250
2007-08-15 07:56	53	1374	288	96	250
2007-08-15 08:49	60	1374	288	96	250
2007-09-19 09:18	53	1374	288	96	250
2007-09-19 10:11	60	1374	288	96	250
2007-10-21 04:10	53	1374	288	96	250
2007-10-21 05:09	180	1374	288	96	250
2007-10-21 23:47	89	1374	288	96	250
2007-10-22 05:36	144	1374	288	96	250
2007-10-23 00:01	119	1374	288	96	250
2007-10-23 05:02	180	1374	288	96	250
2007-10-24 00:02	89	1374	288	96	250
2007-10-24 07:12	50	1374	288	96	250
2007-10-24 23:41	60	1374	288	96	250
2007-10-26 23:39	50	1374	288	96	250
2007-11-01 03:09	54	1374	288	96	250
2007-11-19 23:43	60	1374	288	96	250
2007-12-06 05:16	28	1390	256	512	250
2007-12-06 05:51	80	1390	256	512	250
2008-01-04 03:01	53	1374	288	96	250
2008-01-04 03:55	31	1374	288	96	250
2008-01-04 04:27	49	1374	288	96	250
2008-01-10 04:09	44	1374	288	96	250
2008-01-29 00:39	104	1374	288	96	250
2008-01-29 02:24	50	1374	288	96	250
2008-02-02 00:40	104	1374	288	96	250
2008-02-26 23:10	60	1374	288	96	250
2008-02-27 00:17	50	1374	288	96	250
2008-04-05 13:33	75	1374	288	96	250
2008-05-07 19:42	75	1374	288	96	250
2008-05-31 18:06	78	1374	288	96	250
2008-06-30 14:14	81	1374	288	96	250
2008-08-05 12:53	89	1374	288	96	250
2008-09-08 12:11	47	1374	288	96	250
2008-10-18 09:19	61	1374	288	96	250
2008-12-19 03:36	81	1374	288	96	250
2009-01-18 01:29	92	1374	288	96	250
2009-02-14 01:22	70	1374	288	96	250
2009-03-17 20:08	81	1374	288	96	250
2009-04-12 20:22	68	1374	288	96	250
2009-06-07 08:49	70	1374	288	96	250
2009-09-24 08:14	89	1374	288	96	250
2009-10-09 08:08	82	1374	288	96	250
2009-12-01 23:37	89	1374	288	96	250
2010-02-02 18:59	80	1374	288	96	250

4.3 Data Analyses and Results

4.3.1 Initial searches of radio pulsations from the magnetar

With the aim of finding radio pulsations from CXOU J1647, the data targeting the magnetar were folded, shortly after each observing run, using the X-ray ephemerides published in Israel et al. (2007) and a nominal dispersion measure (DM) of 300 pc/cm^3. This initial value was derived using the estimated distance to the cluster and the NE2001 Galactic electron density model (Cordes & Lazio, 2002b). Data archives with 1024 profile bins were created using the `DSPSR`[1] software (van Straten & Bailes, 2011), with time sub-integrations of 120 seconds and keeping all the frequency channels. This allowed us to search over the unknown DM, up to twice the nominal value, without any loss of sensitivity, and to search $\pm$ 1 ms around the nominal X-ray period (largely encompassing the X-ray ephemeris uncertainties for all our observing epochs) with a maximum broadening of the pulse in the individual sub-integrations compatible with a single time bin. We did this using the `PDMP` routine of the `PSRCHIVE`[2] software package (Hotan et al., 2004b; van Straten et al., 2012), running it six times over adjacent DM ranges of 100 pc cm^{-3} each. We also carried out a basic blind search spanning the same DM range as for the above targeted search (0 to 600 pc/cm^3) with `SIGPROC` (Lorimer, 2011), which uses the Fast Fourier Transform (FFT) to reveal periodic signals in the data.

No radio pulsations compatible with the spin period of the magnetar were found with a flux density upper limit between 70 and 190 μJy at around 1.4 GHz, depending on the specific observation, and of 70 and 50 μJy respectively at 2.3 GHz and 3.2 GHz, conservatively assuming a 10% duty cycle and a pulsed signal-to-noise ratio (S/N) of 7.

4.3.2 Deep periodicity search

Compared to when the observations were taken, pulsar searching algorithms are now highly optimized and more computationally efficient. Moreover, the rapid technological advances have led to significantly increased computing power currently being at our disposal. All of this translates into a much larger parameter space that can be searched for a given dataset. Motivated by this possibility, we re-processed all the Westerlund 1 data using state-of-the-art pulsar searching software, based both on some of the Fourier-domain and time-domain methods that we described in Chapter 2.

First, we used the `rfifind` routine of the `PRESTO`[3] pulsar searching package (Ransom, 2011) to look for radio frequency interference (RFI) in each observation. With this, we created masks indicating those frequency channels and time intervals that were corrupted by RFI and that should therefore be ignored in the subsequent analyses. Then we determined the DM range to search using the PyGEDM[4] software (Price et al., 2021), based on the NE2001 (Cordes & Lazio, 2002b) and YWM16 (Yao et al., 2017) Galactic electron density models, by estimating the expected DM along the line

[1] `https://sourceforge.net/projects/dspsr`
[2] `https://psrchive.sourceforge.net`
[3] `https://github.com/scottransom/presto`
[4] `https://apps.datacentral.org.au/pygedm`

of sight towards Westerlund 1, at a distance of 4.05 kpc. The NE2001 and YWM16 models returned a predicted DM of ~ 307 and ~ 345 pc cm^{-3}, respectively. Given the much larger computing power at our disposal, we decided to search a significantly larger DM range, between 2 and 1500 pc cm^{-3}. Each observation was therefore de-dispersed using hundreds of DM trials (the exact number depended on the characteristics of each observation) in this range. Similarly to what we did for the ten globular clusters analyzed in the previous chapter, the periodicity search was first performed using `PULSAR_MINER`. For each de-dispersed time series, the pipeline performed a Fourier-domain search targeting both isolated and binary pulsars. The latter are targeted with an "acceleration search" algorithm, using `PRESTO`'s `accelsearch` routine, in which we allowed the pulsar spin frequency to drift up to 200 Fourier bins (using the `-zmax 200` option of `accelsearch`) due to the Doppler shift induced by the orbital motion. Each observation was searched in its full length, as well as, whenever possible, in shorter segments of 60, 30 and 15 minutes, so as to potentially be sensitive to binary pulsars with orbits as short as ~ 150 minutes.

On a second stage, we processed the data with `RIPTIDE`[5] (Morello et al., 2020b), a time-domain pulsar searching pipeline based on a highly optimized version of the Fast Folding Algorithm (FFA, Staelin (1969)). The FFA is significantly more sensitive than Fourier-domain methods for pulsars with long spin periods ($\gtrsim 1$ second). However, it cannot per se account for possible binary motions (unless one applies corrections to the data before running the FFA, see e.g. Wongphechauxsorn et al. (2024)). Therefore, in our case, it only targeted isolated pulsars. We ran `RIPTIDE` on all the cleaned and de-dispersed timeseries previously produced. For each observation, both pipelines produced diagnostic plots of potential pulsar candidates, which were visually inspected.

With both pipelines, we were able to easily re-detect PSR B1641−45, an extremely bright isolated pulsar with a spin period of 455 ms and a DM of 450 pc cm^{-3}, located at about 25 arcminutes from the nominal center of Westerlund 1 (therefore well outside the cluster), which was first discovered by Komesaroff et al. (1973). Despite being well outside the primary beam, its mean flux density was sufficient to allow a detection in all the observations. Its distance, constrained by HI absorption measurement (Frail & Weisberg, 1990), ranges in the 4.5 ± 0.4 kpc interval (Verbiest et al., 2012).

We also discovered a new long-period pulsar, named PSR J1646−4545, with a spin period of 431 ms, a DM of 1029 pc cm^{-3}, and no signs of acceleration, suggesting it being isolated. The pulsar was easily detected with high S/N by both pipelines in almost all the observations. Example diagnostic plots produced by the `PULSAR_MINER` and `RIPTIDE` pipelines showing the new pulsar are displayed in Figure 4.2 and 4.3, respectively. In Figure 4.4 we show a high-S/N integrated pulse profile of PSR J1646−4545, obtained by summing 24 bright detections at a central frequency of 1374 MHz. The pulse profile is broad, with a pulse width at half-maximum of ~ 78 ms, corresponding to about 18 per cent of the pulse period. This value is much larger than the typical duty cycles at half-maximum of non-recycled pulsars: according to the ATNF pulsar catalog[6], it is larger than that of 97 per cent of all pulsars with spin periods longer than 30 ms and surface magnetic field $B > 10^{11}$ G. The profile is also slightly asymmetric,

[5] https://github.com/v-morello/riptide

[6] https://www.atnf.csiro.au/research/pulsar/psrcat (v2.1.1)

with the trailing part hinting at scattering being at play.

4.3.3 Single pulse search

We also performed a single pulse search throughout the dataset to look for bright sporadic events such as bright single pulses emitted by pulsars, as well as potential fast radio bursts (Bailes, 2022; Petroff et al., 2022) that could serendipitously be present in our field of view or potentially linked to the magnetar. To do this, we searched each observation using the `Heimdall`[7] (Barsdell et al., 2012) software. An initial RFI flagging was done using a spectral-kurtosis algorithm (Nita & Hellbourg, 2020) provided by the `YOUR`[8] package (Aggarwal et al., 2020) and the noisiest channels found were parsed through `Heimdall` via the -zap_chans option. We then used `Heimdall` to search excesses in the DM range of $0 - 3000\,\mathrm{pc\,cm^{-3}}$, with a DM trial array sampled to have a S/N loss for each trial of 1%, and searched for events with a maximum boxcar width of 512 time bins. No evidence of single pulses/bursts has been found above a S/N threshold of 10.

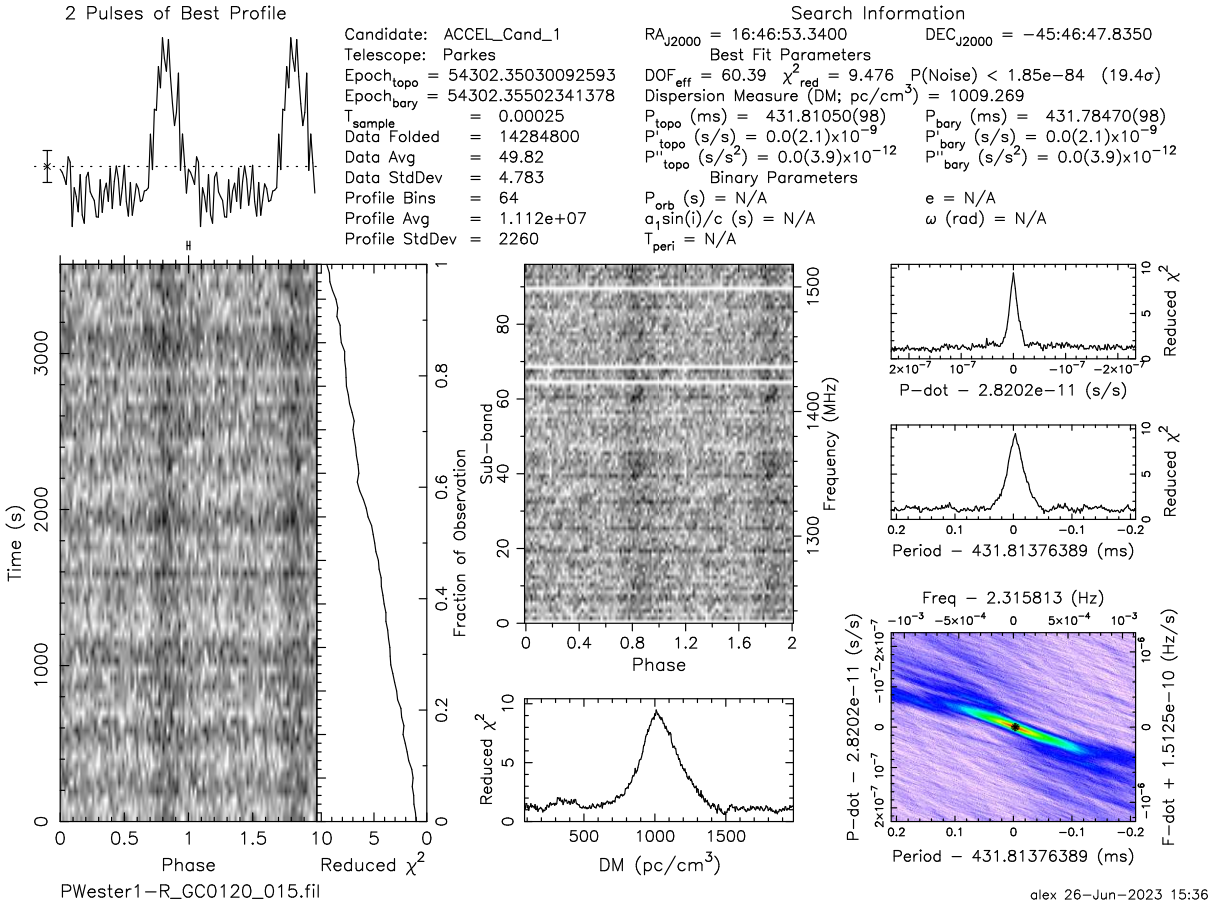

Figure 4.2. Diagnostic plot for the new 431-ms isolated pulsar PSR J1646−4545 as produced by the `PULSAR_MINER` Fourier-domain searching pipeline applied to the 2007 July 21 observation.

[7] https://sourceforge.net/projects/heimdall-astro
[8] https://github.com/thepetabyteproject/your

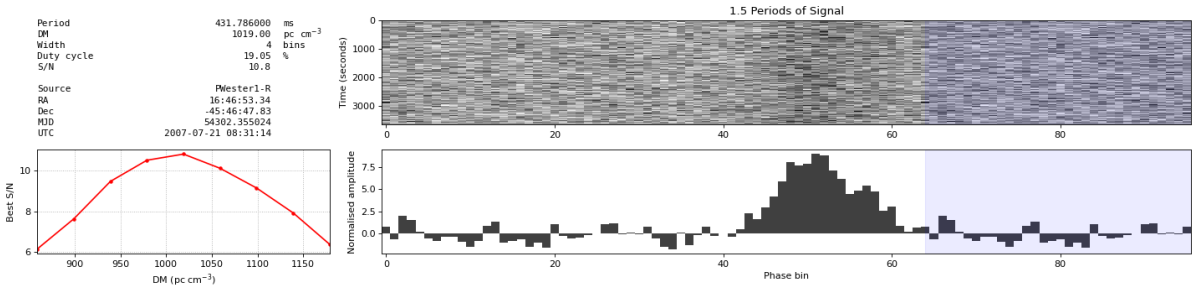

Figure 4.3. Diagnostic plot for the new 431-ms isolated pulsar PSR J1646−4545 as produced by the RIPTIDE FFA searching pipeline applied to the 2007 July 21 observation.

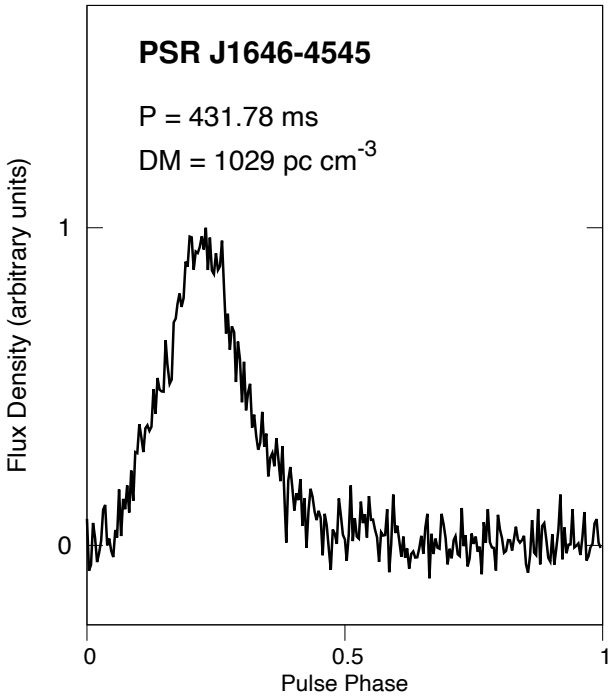

Figure 4.4. Integrated pulse profile of PSR J1646−4545 obtained by summing 24 bright detections of the pulsar at a central frequency of 1374 MHz and with a bandwidth of 288 MHz.

4.3.4 Timing of the new pulsar PSR J1646−4545

The new pulsar PSR J1646−4545 was clearly detected in 73 different observations, spanning more than 4 years. All these detections were processed with DSPSR and the PSRCHIVE software to obtain a total of 217 times of arrival (TOAs) across the whole time span covered by the data. We then used the TEMPO2[9] pulsar timing software (Edwards et al., 2006) to derive a phase-connected timing solution (see, e.g., Lorimer & Kramer 2004 for an introduction to pulsar timing). This allowed us to precisely measure the pulsar position, which locates it at ~ 5.97 arcmin north-west of the nominal center of Westerlund 1 (see Figure 4.5), and its first spin period derivative, which is $\dot{P} = 2.78(3) \times 10^{-16}$. All the parameters of the pulsar with their 1-σ uncertainties derived

[9] https://bitbucket.org/psrsoft/tempo2

with the TEMPO2 timing are reported in Table 4.2. The corresponding timing residuals are shown in Figure 4.6.

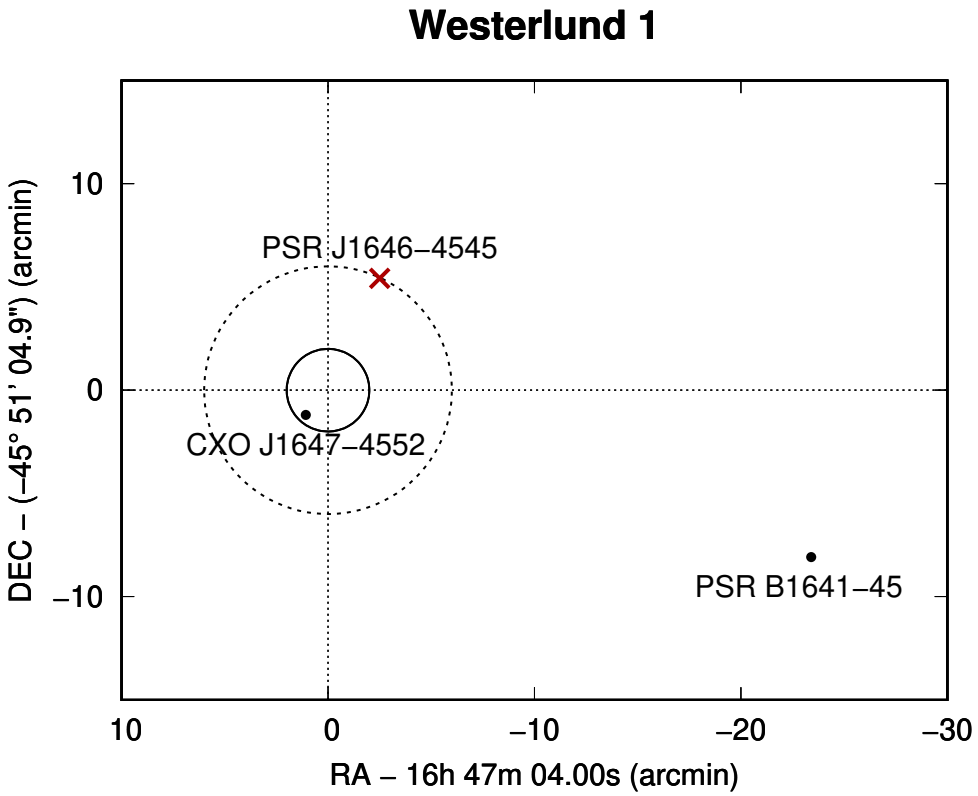

Figure 4.5. Position of the newly discovered PSR J1646−4545 (red cross) with respect to the nominal center of Westerlund 1 (intersection of the dotted lines) and to the positions of the X-ray magnetar CXOU J1647 and the radio pulsar PSR B1641−45 (black dots). The inner solid circle, at 2 arcmin, shows the effective radius of Westerlund 1, defined as the radius containing about 50 per cent of the Gaia-EDR3 sources belonging to the cluster (Navarete et al., 2022). The outer dashed circle, at 6 arcmin, contains about 75 per cent of the same sample.

4.4 Discussion

As outlined in the previous sections, our search observations, pointed at the X-ray magnetar CXOU J1647 in the young massive stellar cluster Westerlund 1, did not show any pulsed radio emission from the magnetar itself. However , they revealed one new pulsar, PSR J1646−4545, the parameters of which argue, for the most part, against its belonging to Westerlund 1. In the following, we thoroughly discuss this putative association and the implications of the lacking of any *bona fide* radio pulsars in the cluster.

4.4.1 The case of PSR J1646−4545

In order to discuss if PSR J1646−4545 belongs to Westerlund 1, we examine separately the three most relevant parameters resulting from the campaign run at the

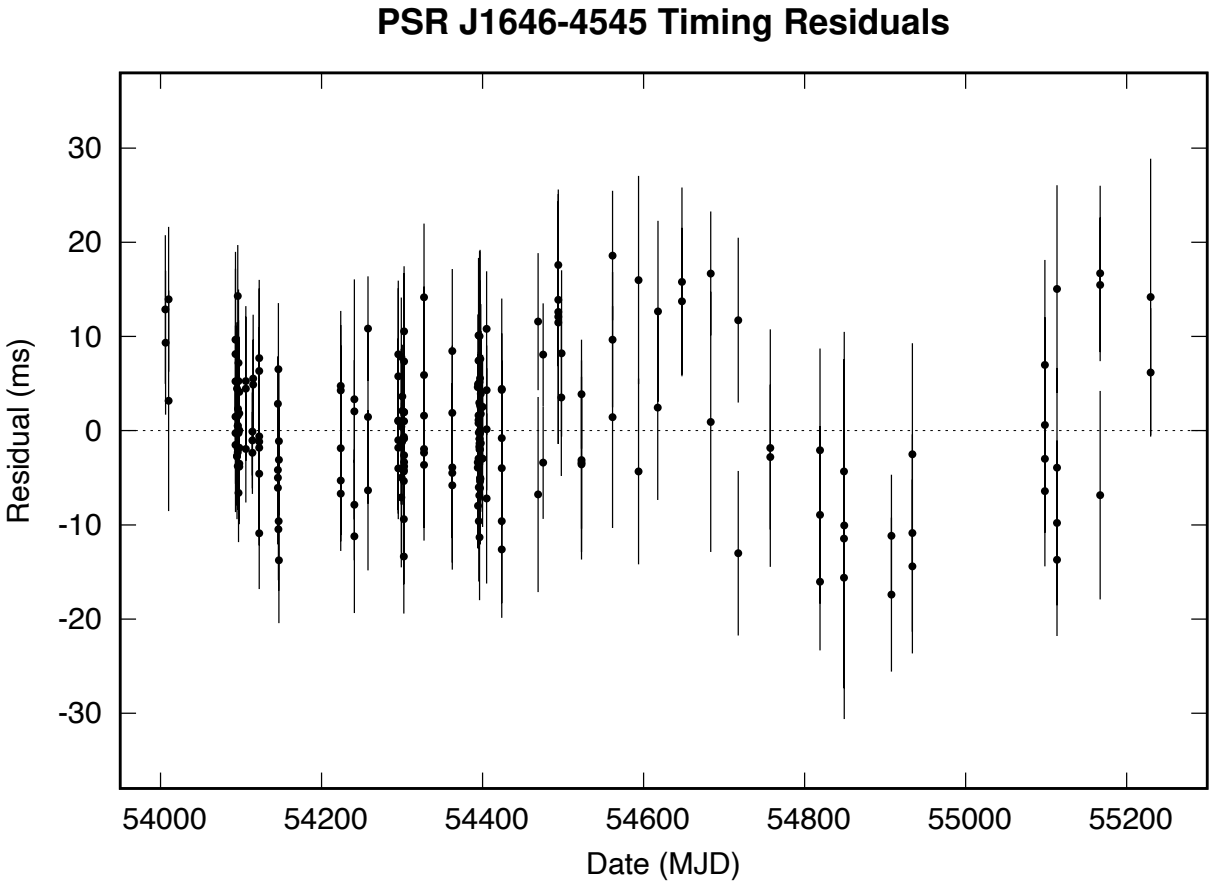

Figure 4.6. Timing residuals of PSR J1646−4545. The leftover unmodeled trend, visible in the residuals, is likely due to timing noise.

Murriyang radio telescope, namely the position, the dispersion measure, and the spin-down age of the pulsar.

4.4.1.1 The position of the pulsar

According to Navarete et al. (2022), the effective radius of Westerlund 1 is $r = 2'$, although stars belonging to the cluster can be found at least up to $6'$ from the center. Given that, the location of PSR J1646−4545 at ∼5.97 arcmin north-west of the nominal center of Westerlund 1 (Clark et al., 2005) is only marginally compatibile with its belonging to the cluster. Because of its relatively long spin period and the large rms of the timing solution, no measurement of the proper motion has been possible for PSR J1646−4545 to date. This prevents us from directly inferring if the neutron star could have significantly traveled from the position of the original supernova to the current location. However, at the GAIA3 distance of 4.05 ± 0.20 kpc, $6'$ corresponds to 7.0 ± 0.4 pc; thus, even a small kick velocity at birth of just ~ 10 km/s would have allowed PSR J1646−4545 to easily move from the center of Westerlund 1 to the outskirts of the cluster in less than ~ 1 Myr (the upper limit for the age of the cluster being about ten times larger, see later). It should also be noted that the aforementioned value of r was somehow biased towards the high-mass tail (up to tens of solar

Pulsar	PSR J1646−4545
Right Ascension, α (J2000)	16:46:49.66(4)
Declination, δ (J2000)	−45:45:39.8(8)
Spin Frequency, f (s^{-1})	2.3159744218(2)
1st Spin Frequency derivative, $\dot{f}$ (Hz s^{-2})	$-1.49(1)\times10^{-15}$
2nd Spin Frequency derivative, $\ddot{f}$ (Hz s^{-3})	$3.0(5)\times10^{-24}$
Reference Epoch (MJD)	54217.000
Start of Timing Data (MJD)	54006.245
End of Timing Data (MJD)	55229.834
Dispersion Measure, DM (pc cm^{-3}) ...	1029(3)
Solar System Ephemeris	DE421
Terrestrial Time Standard	UTC(NIST)
Time Units	TDB
Number of TOAs	217
Residuals RMS (ms)	6.7
Derived Parameters	
Spin Period, P (s)	0.43178369786(3)
1st Spin Period derivative, $\dot{P}$ (s s^{-1}) ...	$2.78(3)\times10^{-16}$
Spin Down Age, $\tau_{\rm p}$ (Myr)	24.6
Surface Magnetic Field, $B_{\rm s}$ (G)	3.51×10^{11}
Spin-down Luminosity, $\dot{E}$ (erg s^{-1})	1.36×10^{32}

Table 4.2. Timing parameters for PSR J1646−4545 as derived by the phase-connected timing solution obtained in this work. All the quoted uncertainties on the last digits (in parentheses) are 1σ.

masses) in the distribution of the stellar content of this young cluster (Navarete et al., 2022), while relatively lower-mass stars, alike PSR J1646−4545 (the mass of which is expected in the ∼1-2 $M_\odot$ range[10]), might be found at even larger radius from the center. Moreover, it has been suggested (Gennaro et al., 2017) that Westerlund 1 did not experience any mass segregation at birth, and at origin had a similar or larger size than currently seen; this could support the presence of a neutron star at the offset position of PSR J1646−4545.

At the moment, PSR J1646−4545 is the closest known pulsar to the Westerlund 1 center, being four times closer than the 2nd ranked, PSR B1641−45 (see Section 4.3). According to the ATNF pulsar catalog, in the area of the sky surrounding Westerlund 1, the surface density of previously discovered radio pulsars (none of which expected to be associated with Westerlund 1) is in the range 1-3 deg^{-2}. In particular it is 2.4 deg^{-2} in a circle of radius 1.5 deg from the Westerlund 1 center, while looking at a wider rectangular strip of 9 deg (in RAJ) and thickness 3 deg (in DecJ) centered at same position as above, one gets a lower value[11] of 1.4 deg^{-2}. Taking these numbers at face value, there is a chance probability of $\sim 2\%$ of finding a pulsar unrelated to Westerlund 1 within $6'$ from its center. However, it is worth noting that this probability must be taken cautiously, since this results from the combination of various pulsar surveys

[10] https://www3.mpifr-bonn.mpg.de/staff/pfreire/NS_masses.html

[11] These surface densities are typical of sky regions chosen in the Galactic disk and including the Galactic center (i.e. Galactic longitude $-90 < l < +90$). For instance, the surface density is 2.4 deg^{-2} within [−1;+1] deg in Galactic latitude and 1.0 deg^{-2} within [−3;+3] deg.

performed in the area, each with its own search parameters, which are different with respect to the search experiment presented in this paper.

4.4.1.2 The dispersion measure of the pulsar

Another observable that can be used to investigate the association of PSR J1646−4545 with Westerlund 1 is the value of its DM, which is 1029 ± 3 pc cm^{-3}. The mean of the DMs for the known pulsars within 1.5 deg from the center of Westerlund 1 is 463 pc cm^{-3}, with a standard deviation of 177 pc cm^{-3}. There are two outliers in this population, with DM values of 718 pc cm^{-3} and 925 pc cm^{-3}. As reported in Section 4.3, according to the NE2001 and YMW16 models, the predicted DMs for a pulsar included in Westerlund 1 are 307.6 pc cm^{-3} and 344.6 pc cm^{-3}, respectively (for the distance of 4.05 kpc); in this context we also note that the second closest pulsar to the center of Westerlund 1, PSR B1641−45, has a distance measured via HI absorption (i.e. independently from its DM value of 450 pc cm^{-3}) and that was used to calibrate the YMW16 model in that area of the sky, lending additional reliability to the prediction of this model. The measured DM for PSR J1646−4545 would imply a distance of 10.4 kpc and 6.3 kpc for the NE2001 and YMW16 model, respectively. All in all, these considerations all strongly point adversely to the membership of PSR J1646−4545 to the cluster.

However, since Westerlund 1 is the most massive YMC in the Local Group (see Section 4.1), one may wonder if the high wind losses from the young star population could sustain an intra-cluster gas dense enough to explain the excess DM of ∼700 pc cm^{-3} of PSR J1646−4545 with respect to the predictions. Indeed, a set of concatenated ATCA observations made at 5.5 GHz and 9 GHz (Andrews et al., 2019), and an observing campaign carried out at 3 mm with ALMA (Fenech et al., 2018), both aimed to imaging the central region of Westerlund 1, revealed diffuse emission over $\sim 0.3'$ scales (corresponding to linear scales of ~ 0.3 pc), as well as the presence of several much more compact clouds without an optical counterpart[12]. For a gas cloud projected along the line-of-sight to the pulsar with a size of $s \sim 0.3$ pc and a gas ionization fraction $\chi = n_e/n_{\rm H}$ (where n_e is the free electron number density and $n_{\rm H}$ is the hydrogen equivalent number density), the excess DM would imply a number density $n_{\rm H} = (\Delta{\rm DM})/(s\chi) \sim 2.3 \times 10^3$ cm$^{-3}/\chi$. For small χ, the implied $n_{\rm H} \gtrsim 10^5$ cm^{-3} goes well beyond what is seen in observed gas clouds[13].

4.4.1.3 The age of the pulsar

From the combination of P and $\dot{P}$, it is possible to infer the so-called *spin-down age* of a pulsar, as $\tau_{\rm p} = P/(2\dot{P})$ (see Section 1.3.2). For most of the ordinary pulsars (i.e. those not "recycled" in a binary system), $\tau_{\rm p}$ can be used as a proxy for the real age of the underlying neutron star (see e.g. Lorimer & Kramer 2004), although with large errors, especially for relatively old objects (>Myr). For PSR J1646−4545 the spin-down age is $\tau_{\rm p} \sim 25$ Myr.

[12]Unfortunately, none of the mentioned observing campaigns covered the position of the pulsar and thus it is not possible to constrain the presence of any cloud along the line of sight to PSR J1646−4545.

[13]Such high $n_{\rm H}$ might be comparable to that recently predicted for the molecular gas retained in young star clusters (e.g. Silich et al. (2023)), but the offset position of PSR J1646−4545 also does not favor this hypothesis.

The age of Westerlund 1 has been long debated and its value often reviewed. Early observations indicated a very young age of 4 ± 1 Myr (Muno et al. (2006) and reference therein). More recently, the observation of several giant and supergiant stars, led Rocha et al. (2022) to suggest that multiple episodes of star formation, closely spaced in time, occurred in Westerlund 1, the oldest of which is dating back to no more than $\sim$ 12 Myr ago. Similar considerations have also been developed by Navarete et al. (2022) via the use of Binary Population and Spectral Synthesis (BPASS) models for the red supergiants with solar abundance, and by Beasor et al. (2023). Given these results, $\tau_{\rm p}$ is at least twice larger than the estimated age of Westerlund 1.

On the other hand, $\tau_{\rm p}$ coincides with the pulsar age only under the following hypotheses: *(i)* applicability of the formula for the magneto-dipole emission in a vacuum (see Lorimer & Kramer 2004); *(ii)* a non-decaying magnetic field; and *(iii)* an initial spin rate much higher than the measured one. Relaxing some of these commonly adopted assumptions can easily produce a factor of 2 (or more) shorter true age than the measured $\tau_{\rm p}$. In particular, in the case of point (ii), if we take into account some magnetic field evolution (Ronchi et al. 2022; Graber et al. 2023), the age estimate of the pulsar would reduce substantially and would be compatible with being even as short as 1 Myr: see the result of a detailed calculation of the evolution reported in Figure 4.7.

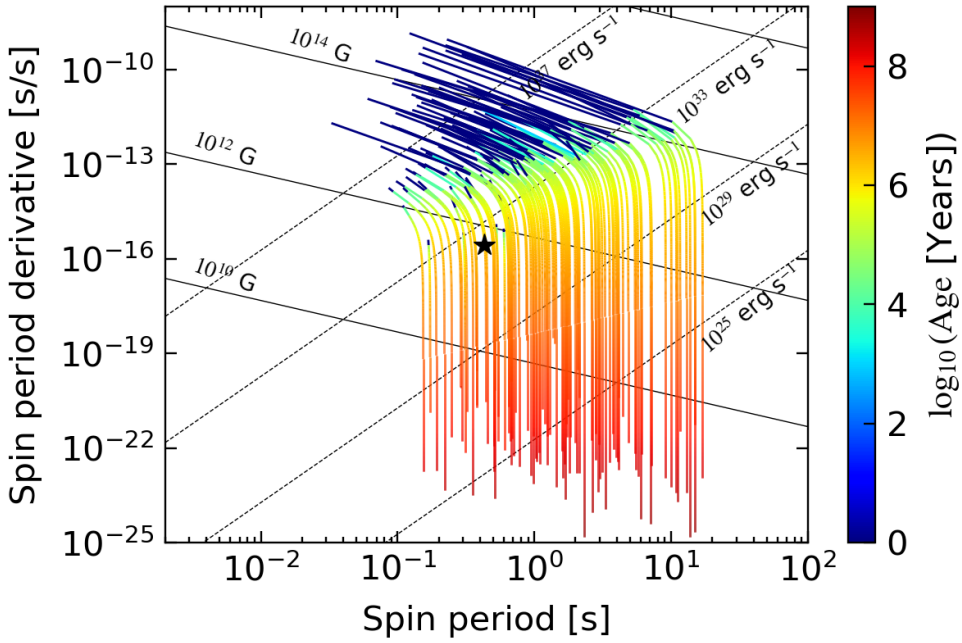

Figure 4.7. Evolution of synthetic pulsars in the P-$\dot{P}$ diagram over 1 Gyr, taking into account B-field evolution (adapted from Michele Ronchi's PhD thesis; see also Ronchi et al. (2022); Graber et al. (2023)) The black star indicates the position of PSR J1646−4545 in the diagram.

4.4.2 No radio pulsars in Westerlund 1

The absence of pulsed radio emission from the magnetar CXOU J1647 is not surprising *per se.* Over a total sample of about 30 catalogued magnetars, only 6 showed

transient phases of regular and/or bursty radio emission so far[14]. However, the lacking of any ordinary radio pulsars in Westerlund 1, in combination with the presence of a highly magnetized neutron star[15], deserves some considerations, which we develop in the following.

As reported in Section 4.3, our deepest observations of Westerlund 1 reached a flux density sensitivity limit of $S_{\rm lim} \sim 70$ μJy at 1.4 GHz. Given the distance $d \sim 4.05$ kpc of the open cluster (see Section 4.1), this translates into a pseudo-luminosity upper limit for any possible pulsar hosted in Westerlund 1 of $L_{\rm lim} = S_{\rm lim} d^2 \sim 1.15$ mJy kpc^2. According to the ATNF database, $\sim 80\%$ of the radio pulsars with a catalogued pseudo-luminosity L_{1400} at 1.4 GHz, have $L_{1400} > L_{\rm lim}$. This percentage progressively increases if one restricts the sample to only radio pulsars younger than the age of Westerlund 1 (see above): e.g. it becomes $\sim 84\%$ for pulsars younger than 12 Myr, and then grows to more than 90% for pulsars younger than 6 Myr. Assuming that the observed radio pulsar pseudo-luminosity distribution function (as derived from the ATNF database) is applicable to Westerlund 1, this means that our search might have only missed ordinary pulsars in Westerlund 1 that are at the faintest end of the pulsar pseudo-luminosity function at 1400 MHz. Provided that they have a radio beam that points towards us, these faint sources (if any) could be detected with deeper searches at more sensitive radio telescopes.

Alternatively, given the large sampled fraction of the pseudo-luminosity distribution, one can ascribe our null result to the complete absence of active ordinary pulsars currently hosted in Westerlund 1. This could be simply understood as due to the young age of the open cluster (see Section 4.4.1.3): i.e. the stars belonging to Westerlund 1 might not have had yet the time to produce any neutron stars, and, in turn, any radio pulsars. On the other hand, we know that Westerlund 1 hosts at least one neutron star, the magnetar CXOU J1647. In order to reconcile these two contrasting considerations, one needs to invoke the occurrence of some peculiar evolutionary factor, capable to sustain an earlier formation of neutron stars with a very high magnetic field.

In particular, the case for a massive progenitor star has been since long proposed (and supported by population synthesis calculations, e.g. Olausen & Kaspi (2014a) and references therein) in the framework of the so-called *fossil scenario* (e.g. Ruderman 1972) for the formation of magnetars. If this holds true, magnetars should be more massive than the neutron stars underlying the ordinary radio pulsars (a characteristic which could not be tested yet). On the other hand, the magnetars' progenitors should evolve off the main sequence earlier than the stars leading to the formation of ordinary radio pulsars. The peculiar case of Westerlund 1, which hosts one magnetar and no known radio pulsars, thus seems to support the second prediction of this model.

[14] https://www.physics.mcgill.ca/ pulsar/magnetar/main.html

[15] The association of CXOU J1647 with Westerlund 1 was discussed by Muno et al. (2006) on the basis of its very close sky position with respect to the center of the cluster. They found a 0.03 per cent chance probability of finding a X-ray pulsar so close to the center of Westerlund 1. If we restrict ourselves to only magnetars with X-ray emission that are located within 2 degrees from the Galactic plane, we find an even lower chance probability of 0.0037 per cent. If CXOU J1647 were in fact not associated to Westerlund 1, then the estimate of the minimum progenitor mass given in Muno et al. (2006), $\sim 35 - 40$ M$_\odot$, should also be revised.

4.5 Conclusions

In this work, we have reported on a series of pulsar search observations, pointed at the X-ray magnetar CXOU J1647, included in the open stellar cluster Westerlund 1. The main observational results are:

- no pulsed radio emission from the magnetar CXOU J1647 was detected;
- a new ordinary pulsar, PSR J1646−4545, was discovered at the rim of the cluster. This fact, together with the measured dispersion measure and the age of the pulsar, strongly suggests that PSR J1646−4545 is a pulsar located in the background of Westerlund 1;
- despite the search sampled a large portion of the pulsar pseudo-luminosity function, no pulsars were discovered in Westerlund 1.

The presence of the magnetar CXOU J1647 in Westerlund 1 has also been discussed in view of the absence of *bona fide* pulsars in the same cluster. This might favor models for which the magnetars' progenitors are more massive than the progenitors of the ordinary pulsars.

Chapter 5

Summary and Outlook

5.1 Summary

In this thesis, we delved into the fascinating realm of radio pulsars. We started, in Chapter 1, by seeing how pulsars are remarkable astrophysical objects, discussing their phenomenology and how some of their fundamental characteristics, such as their age, magnetic field and spin-down luminosity, can be inferred from the simple measurement of the spin period and its first two time derivatives. We also saw how the extreme properties of pulsars make them outstanding tools with which to carry out a wide range of scientific experiments, among which are the study of stellar evolution, the tests of gravity theories, the study of ultra-dense matter, the detection of ultra-low-frequency gravitational waves, and more. Not all pulsars are the same, though. In this regard, we reviewed the main pulsar populations, highlighting their differences and discussing how the current properties of pulsars are a direct consequence of their evolution. The latter is influenced, among other things, by the environment where pulsars form and evolve. In particular, we outlined how the population of pulsars in the Galactic plane is substantially different from the one that can be found in globular clusters, and how the latter are host of a large number of millisecond pulsars, as well as of pulsars with extreme or exotic properties.

The discovery of the over 3600 pulsars known at present has been possible thanks to numerous surveys carried out with different radio telescopes, and thanks to the use of sophisticated searching techniques that have been developed over the decades. In Chapter 2, we showed how the intrinsic periodicity of the signals emitted by pulsars allows us to leverage the power of the Fourier Transform and use this as an outstanding mathematical tool with which to reveal the extremely faint pulsar signals, even in the presence of noisy data. However, things are often more complicated than this. For example, when a pulsar is part of a binary system, the orbital motion makes the application of the Fourier Transform much less straightforward, as the the periodicity of the pulsar signal is heavily influenced by the Doppler effect. On the other hand, when a pulsar has a long spin period, red noise and radio frequency interference can make the detection of its signal very difficult when using traditional Fourier-domain methods. Therefore, we reviewed and discussed all the major Fourier-domain and time-domain based pulsar searching algorithms, devised to overcome these difficulties, available today. We started with the most common (and so far most successful) method used to find binary pulsars: the *acceleration search*. Although the latter is limited by being effective only for binary pulsars with orbits at least ~ 10 times longer than the duration of the observation, it is relatively cheap in terms of the computational time needed, a fact that makes it easily applicable even when only small computing facilities are available. An extension of the acceleration search is the *jerk search*, which improves the efficacy of the algorithm with pulsars in more compact

orbits, at the cost of an increased dimensionality of the parameter space to search. For the ultra-compact binary pulsars, that is, those with orbital periods comparable to or shorter than the observation, the *phase-modulation* and *full-Keplerian template banking* search methods are the most effective, but their huge computational costs make their application to large datasets currently difficult, especially in the absence of high-performance-computing facilities. Other search techniques, such as the *fast-folding algorithm* (FFA) and the *stack search*, are more tailored to find isolated pulsars. Finally, we saw how the *single-pulse search* technique is suitable to detect transients pulsars as well as "burst-like" events, such as Fast Radio Bursts.

In Chapter 3, we applied some of the above search methods to a set of data of ten different globular clusters (E3, ESO 452, NGC 288, NGC 3021, NGC 4372, NGC 4590, NGC 4833, NGC 5286, NGC 6541 and NGC 6584) observed with the Parkes and the MeerKAT radio telescopes. In particular, we processed the data using a pulsar searching pipeline that implemented standard Fourier-domain searches, acceleration searches and jerk searches to all the observations. The latter two methods were applied to the full observations, as well as to shorter segments, so as to be also sensitive to possibly bright pulsars in orbits as short as ~ 2.5 h. As a result of our analysis, we identified 56 candidate pulsars across all the ten clusters. Among the candidates, 32 are detected with significant acceleration, indicating that they could be part of binary systems. All the candidates were detected with relatively low significance, hence, with the available data, we are currently unable to confirm any of them.

Similarly, in Chapter 4, we applied a few algorithms to search for radio pulsations in several observations of the young open cluster Westerlund 1, taken with the Parkes radio telescope. The searches were originally motivated by discovery of the 10.61-second X-ray magnetar CXOU J164710.2−455216, and the primary aim was to look for possible radio pulsations emitted by the latter. We extended the searches to target not only the possible pulsations coming from the magnetar, but also to any possible radio pulsars hosted by Westerlund 1, or in its direction. To this end, we applied standard Fourier-domain and acceleration search methods, as well as the Fast-Folding-Algorithm and single-pulse searches. Our analyses led to the serendipitous discovery of PSR J1646−4545, a 431-ms isolated pulsar with a DM of 1029 $\mathrm{pc\ cm^{-3}}$. As we were able to detect the pulsar in almost all the observations, we carried out a pulsar timing analysis, which allowed us to fully characterize the newly found pulsar, determining its position and spin-down rate. From these, we argued that the association of the pulsar with Westerlund 1, is highly unlikely. This hypothesis is supported by at least to pieces of evidence: a) the DM of PSR J1646−4545 being about three times the predicted value of the DM for Westerlund 1; b) the spin-down age of the pulsar, ~ 25 Myr, being at least two times the maximum age estimated for the cluster. We therefore concluded that PSR J1646−4545 is, in all likelihood, a Galactic field pulsar in the background of Westerlund 1. No other pulsars were found in the cluster from our searches.

5.2 Outlook

The results presented in this thesis leave room to a number of possible follow-up works. Here we briefly discuss the main ones.

5.2.1 Algorithm development and optimization

Even though pulsar searching algorithms have experienced significant development over the last few years, the main obstacle to their successful exploitation is still the large computational time required for their application. This problem is going to become more and more pressing in the near future, as new generation of radio telescopes, such as the SKA, are set produce, on a daily basis, tera-bytes (in some cases even peta-bytes) of data that will need to be analyzed either in real-time or, in the best case, over extremely short time scales. We therefore foresee the need for the further development and computational optimization of the majority of pulsar searching algorithms. Specifically, a first aspect that we consider very important, is the optimization of the sampling of the parameter space to search. Such issue is particularly severe for those algorithms that aim to reveal compact binary pulsars, due to the high dimensionality of the problem. This is unfortunate, as the latter systems, besides being scientifically very valuable, are likely abundant in globular clusters. Although some codes already implement clever, and efficient ways to explore multi-dimensional parameter spaces minimizing the computations, some other codes still make use a simple, uniform grid, which results in a prohibitively large number of computations needed to explore the whole space. We therefore encourage the development of optimal ways to explore multi-dimensional parameter spaces minimizing the computations in such algorithms. Another important point is related to the ability of exploiting the available hardware: as high-performance-computing facilities endowed with thousands of CPUs and GPUs are becoming more and more common and used in astrophysics, it is crucial that most of the codes used for pulsar searching be able to use all of the available resources efficiently. We particularly encourage the porting of the core searching codes from CPU to GPU, as the parallelized architecture of GPUs can result in speed-ups of the order of tens or even hundreds of times, when compared to CPUs, depending on the algorithm implementation.

5.2.2 Confirmation of globular cluster pulsar candidates

The 56 candidate pulsars in the ten globular clusters presented in this thesis could not be confirmed. Follow-up observations of these clusters are therefore necessary to either confirm or refute the candidates. Nine of the clusters searched are not in the target list of the TRAPUM globular cluster pulsar survey at MeerKAT. Therefore, until the official end of the project, slated for mid-2025, it is unlikely that these clusters will be observed with the South African telescope. Nevertheless, before resorting to the outstanding sensitivity of MeerKAT, we suggest that these clusters be re-observed with Parkes and its new Ultra-Wideband-Low receiver. The latter, covering a frequency range of 0.7-4.0 GHz, would guarantee a higher sensitivity as compared to the observations analyzed for this work, while retaining a comparable field of view on the sky. Computational resources permitting, we also encourage the application of some of the more sophisticated pulsar searching techniques review in this thesis to better target binary pulsars in compact orbits, which we may have missed with the simple acceleration and jerk searches done. If no pulsars are found with Parkes/UWL and the more advance algorithm, then future MeerKAT observations will likely be needed. In the case NGC 6541, for which MeerKAT data are already available, the application of other algorithms for compact binaries is also highly encouraged, before trying deeper

observations. We also point out that, if some of the candidate pulsars are confirmed via these methods, then the DM associated with their host clusters will then be known. This would make deeper searches for further pulsars in those clusters much easier to carry out in the future, as the DM range to explore will be much smaller and the new observations could be acquired with a much smaller number of channels, thanks to the known DM, resulting in much smaller files to search.

5.2.3 Deeper searches in Westerlund 1

As discussed earlier, there are currently no ordinary radio pulsars known in Westerlund 1. Regarding this, we argued that, if present, the ordinary pulsars in Westerlund 1 must all belong to the faintest end of the pulsar pseudo-luminosity function distribution at 1.4 GHz. Alternatively, there must be some mechanism that favored the formation of neutron stars with very high magnetic field (as proved by the magnetar) but not neutron stars with "regular" magnetic fields. The only way to test these hypotheses is to conduct more sensitive observations of Westerlund 1. In this respect, a single 2-hour-long observation with MeerKAT, using 60 antennas and the L-band receivers, would result in a minimum detectable mean flux density of ~ 10 μJy, which would improve our current best limit (70 μJy) by about a factor of seven.

Appendices

Appendix A: diagnostic plots of best candidate pulsars found in globular clusters

asfasfafs

A.1 Best candidate pulsars found in NGC 288

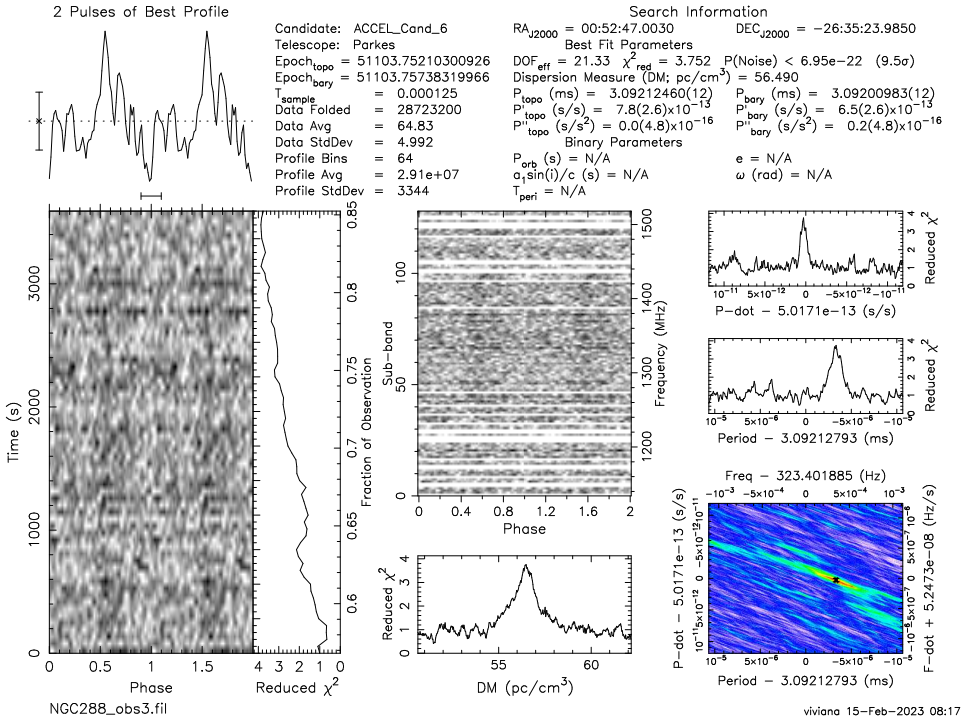

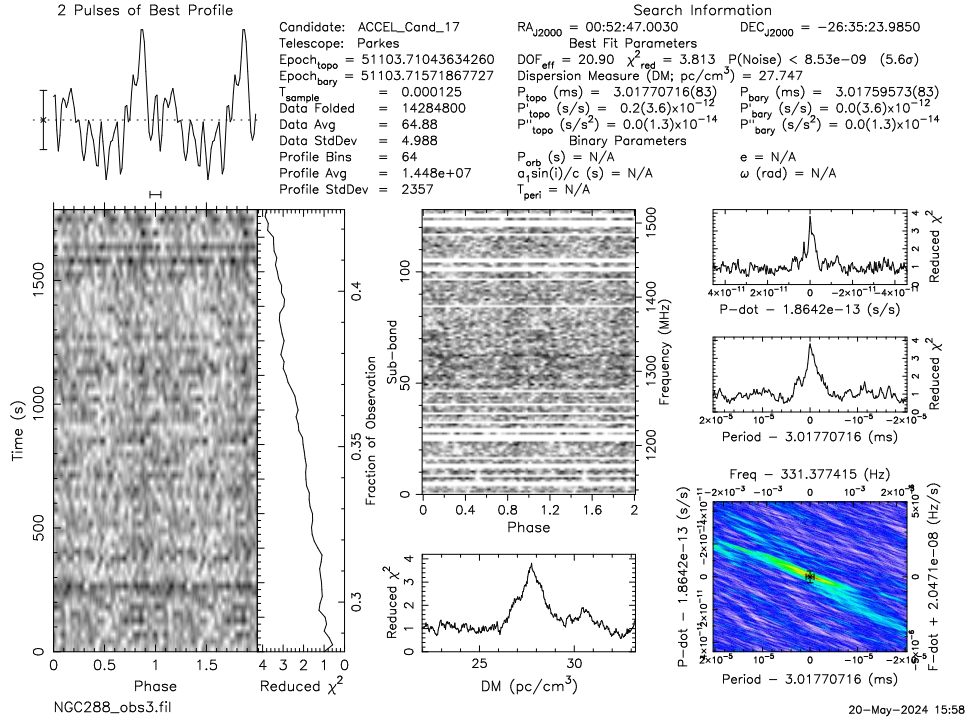
2 Pulses of Best Profile
Search Information
Candidate: ACCEL_Cand_17
Telescope: Parkes
Epoch_topo = 51103.71043634260
Epoch_bary = 51103.71571867727
T_sample = 0.000125
Data Folded = 14284800
Data Avg = 64.88
Data StdDev = 4.988
Profile Bins = 64
Profile Avg = 1.448e+07
Profile StdDev = 2357
RA_J2000 = 00:52:47.0030
DEC_J2000 = −26:35:23.9850
Best Fit Parameters
DOF_eff = 20.90 χ²_red = 3.813 P(Noise) < 8.53e−09 (5.6σ)
Dispersion Measure (DM; pc/cm³) = 27.747
P_topo (ms) = 3.01770716(83)
P_bary (ms) = 3.01759573(83)
P'_topo (s/s) = 0.2(3.6)x10⁻¹²
P'_bary (s/s) = 0.0(3.6)x10⁻¹²
P''_topo (s/s²) = 0.0(1.3)x10⁻¹⁴
P''_bary (s/s²) = 0.0(1.3)x10⁻¹⁴
Binary Parameters
P_orb (s) = N/A
e = N/A
a₁sin(i)/c (s) = N/A
ω (rad) = N/A
T_peri = N/A
Time (s)
Phase
Reduced χ²
Fraction of Observation
Sub-band
Frequency (MHz)
DM (pc/cm³)
P-dot − 1.8642e−13 (s/s)
Period − 3.01770716 (ms)
Freq − 331.377415 (Hz)
F-dot + 2.0471e−08 (Hz/s)
NGC288_obs3.fil
20−May−2024 15:58

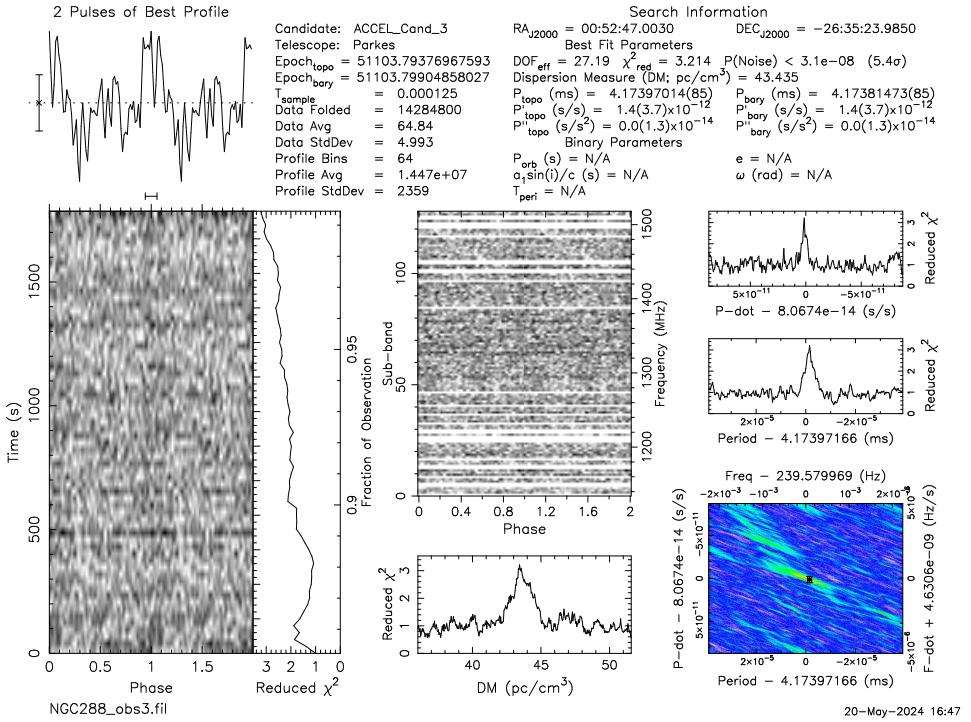
2 Pulses of Best Profile
Search Information
Candidate: ACCEL_Cand_3
Telescope: Parkes
Epoch_topo = 51103.79376967593
Epoch_bary = 51103.79904858027
T_sample = 0.000125
Data Folded = 14284800
Data Avg = 64.84
Data StdDev = 4.993
Profile Bins = 64
Profile Avg = 1.447e+07
Profile StdDev = 2359
RA_J2000 = 00:52:47.0030
DEC_J2000 = −26:35:23.9850
Best Fit Parameters
DOF_eff = 27.19 χ²_red = 3.214 P(Noise) < 3.1e−08 (5.4σ)
Dispersion Measure (DM; pc/cm³) = 43.435
P_topo (ms) = 4.17397014(85)
P_bary (ms) = 4.17381473(85)
P'_topo (s/s) = 1.4(3.7)x10⁻¹²
P'_bary (s/s) = 1.4(3.7)x10⁻¹²
P''_topo (s/s²) = 0.0(1.3)x10⁻¹⁴
P''_bary (s/s²) = 0.0(1.3)x10⁻¹⁴
Binary Parameters
P_orb (s) = N/A
e = N/A
a₁sin(i)/c (s) = N/A
ω (rad) = N/A
T_peri = N/A
Time (s)
Phase
Reduced χ²
Fraction of Observation
Sub-band
Frequency (MHz)
DM (pc/cm³)
P-dot − 8.0674e−14 (s/s)
Period − 4.17397166 (ms)
Freq − 239.579969 (Hz)
F-dot + 4.6306e−09 (Hz/s)
NGC288_obs3.fil
20−May−2024 16:47

A.2 Best candidate pulsars found in E3

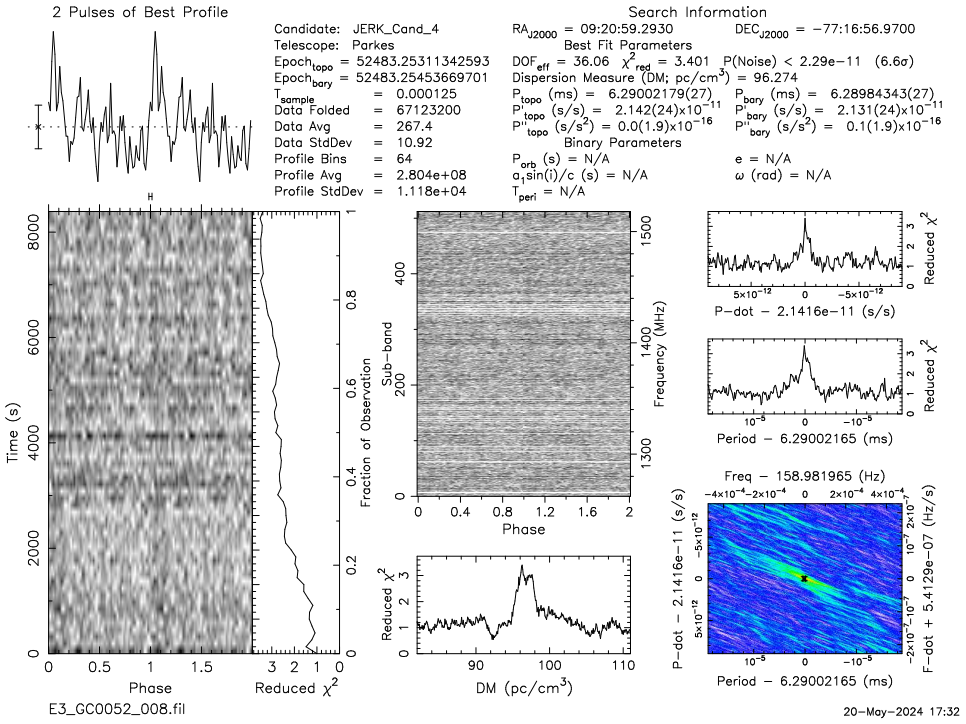

A.3 Best candidate pulsars found in NGC 3201

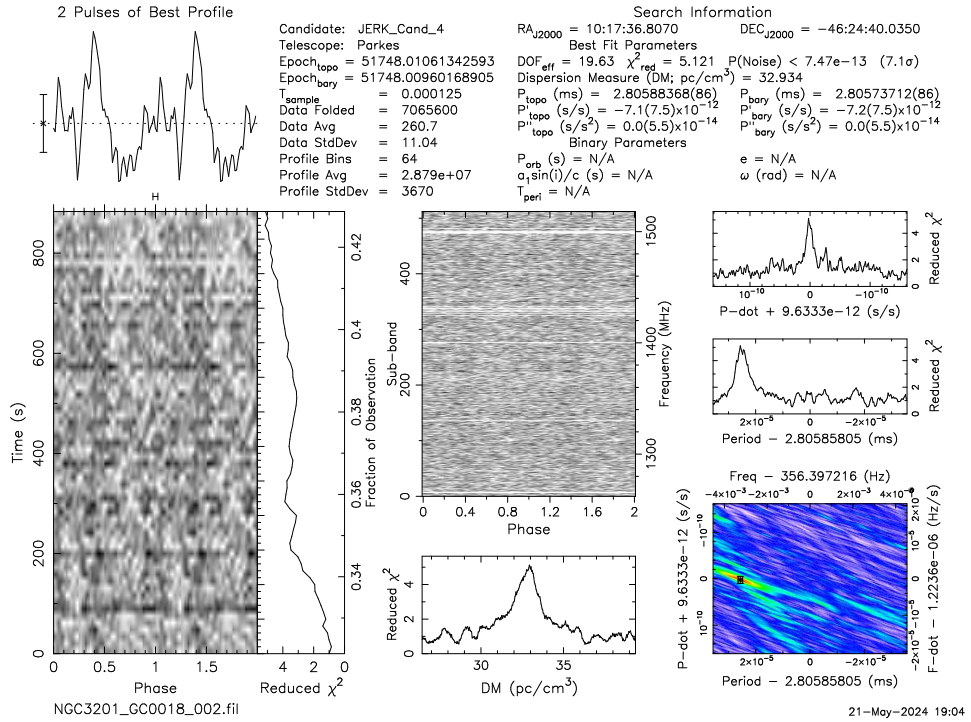

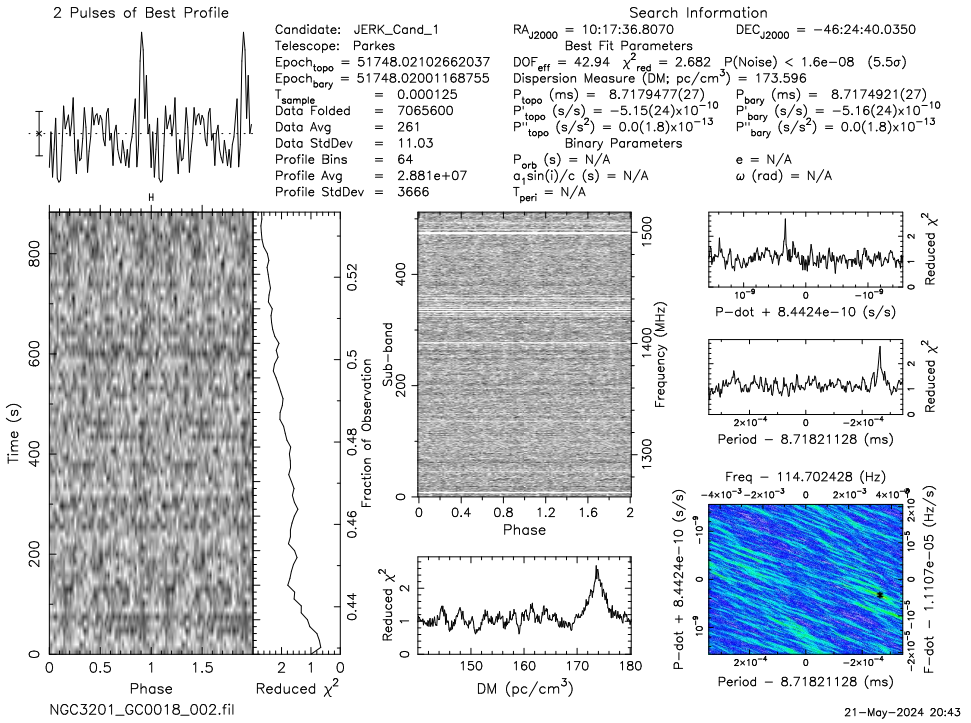

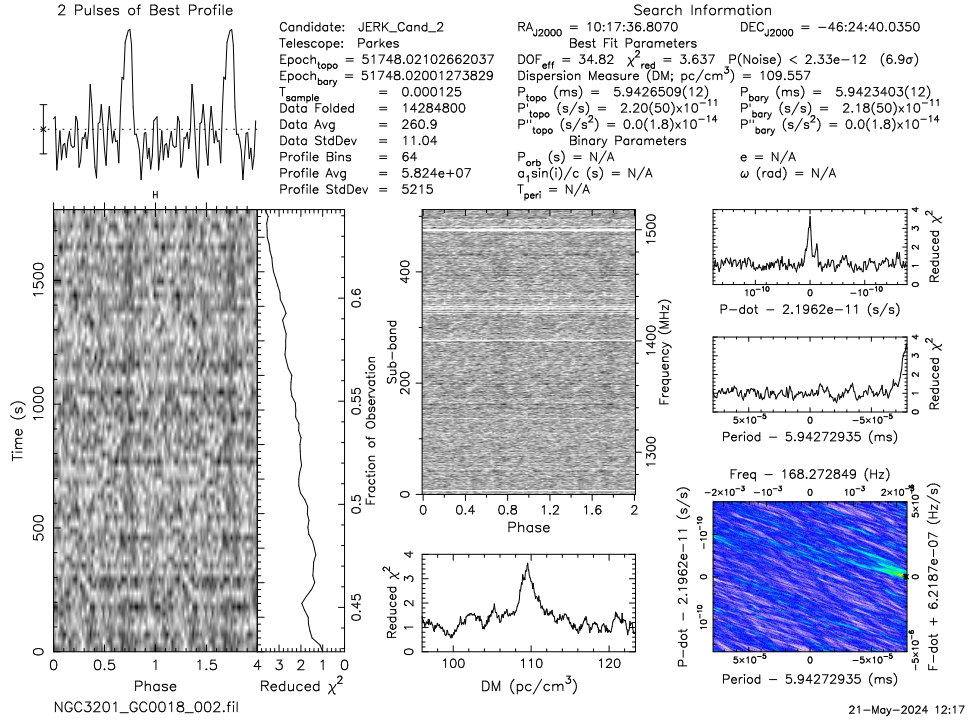
2 Pulses of Best Profile
Search Information
Candidate: JERK_Cand_2
Telescope: Parkes
Epoch_topo = 51748.02102662037
Epoch_bary = 51748.02001273829
T_sample = 0.000125
Data Folded = 14284800
Data Avg = 260.9
Data StdDev = 11.04
Profile Bins = 64
Profile Avg = 5.824e+07
Profile StdDev = 5215
RA_J2000 = 10:17:36.8070
DEC_J2000 = −46:24:40.0350
Best Fit Parameters
DOF_eff = 34.82 χ²_red = 3.637 P(Noise) < 2.33e−12 (6.9σ)
Dispersion Measure (DM; pc/cm³) = 109.557
P_topo (ms) = 5.9426509(12)
P_bary (ms) = 5.9423403(12)
P'_topo (s/s) = 2.20(50)x10⁻¹¹
P'_bary (s/s) = 2.18(50)x10⁻¹¹
P''_topo (s/s²) = 0.0(1.8)x10⁻¹⁴
P''_bary (s/s²) = 0.0(1.8)x10⁻¹⁴
Binary Parameters
P_orb (s) = N/A
e = N/A
a_1sin(i)/c (s) = N/A
ω (rad) = N/A
T_peri = N/A
Time (s)
Phase
Reduced χ²
Fraction of Observation
Sub-band
Frequency (MHz)
DM (pc/cm³)
P-dot − 2.1962e-11 (s/s)
Period − 5.94272935 (ms)
Freq − 168.272849 (Hz)
F-dot + 6.2187e-07 (Hz/s)
NGC3201_GC0018_002.fil
21−May−2024 12:17

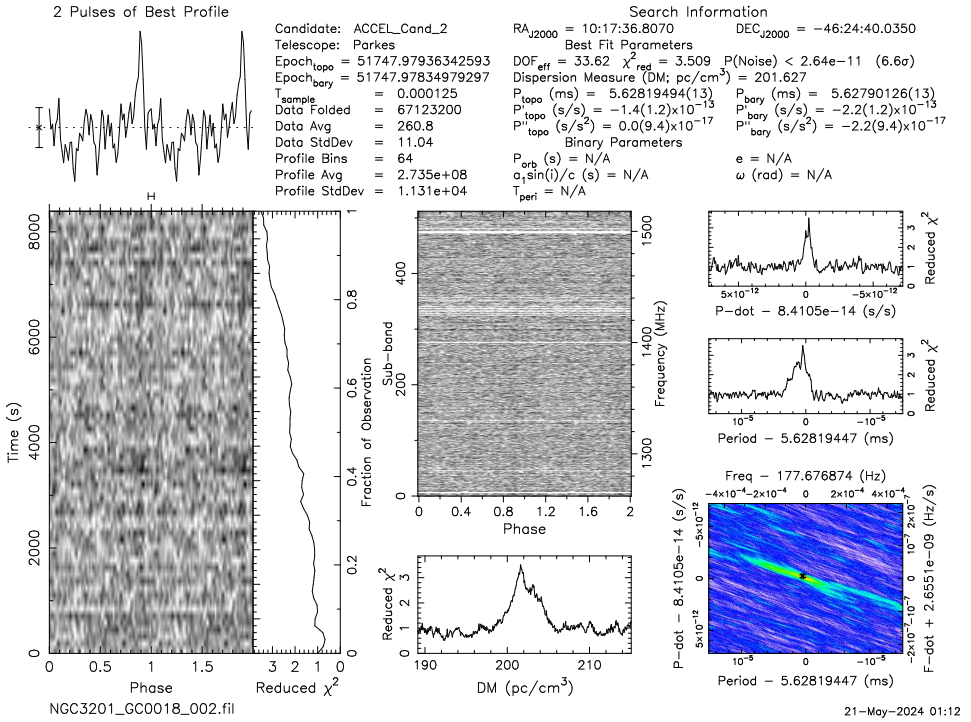
2 Pulses of Best Profile
Search Information
Candidate: ACCEL_Cand_2
Telescope: Parkes
Epoch_topo = 51747.97936342593
Epoch_bary = 51747.97834979297
T_sample = 0.000125
Data Folded = 67123200
Data Avg = 260.8
Data StdDev = 11.04
Profile Bins = 64
Profile Avg = 2.735e+08
Profile StdDev = 1.131e+04
RA_J2000 = 10:17:36.8070
DEC_J2000 = −46:24:40.0350
Best Fit Parameters
DOF_eff = 33.62 χ²_red = 3.509 P(Noise) < 2.64e−11 (6.6σ)
Dispersion Measure (DM; pc/cm³) = 201.627
P_topo (ms) = 5.62819494(13)
P_bary (ms) = 5.62790126(13)
P'_topo (s/s) = −1.4(1.2)x10⁻¹³
P'_bary (s/s) = −2.2(1.2)x10⁻¹³
P''_topo (s/s²) = 0.0(9.4)x10⁻¹⁷
P''_bary (s/s²) = −2.2(9.4)x10⁻¹⁷
Binary Parameters
P_orb (s) = N/A
e = N/A
a_1sin(i)/c (s) = N/A
ω (rad) = N/A
T_peri = N/A
Time (s)
Phase
Reduced χ²
Fraction of Observation
Sub-band
Frequency (MHz)
DM (pc/cm³)
P-dot − 8.4105e-14 (s/s)
Period − 5.62819447 (ms)
Freq − 177.676874 (Hz)
F-dot + 2.6551e-09 (Hz/s)
NGC3201_GC0018_002.fil
21−May−2024 01:12

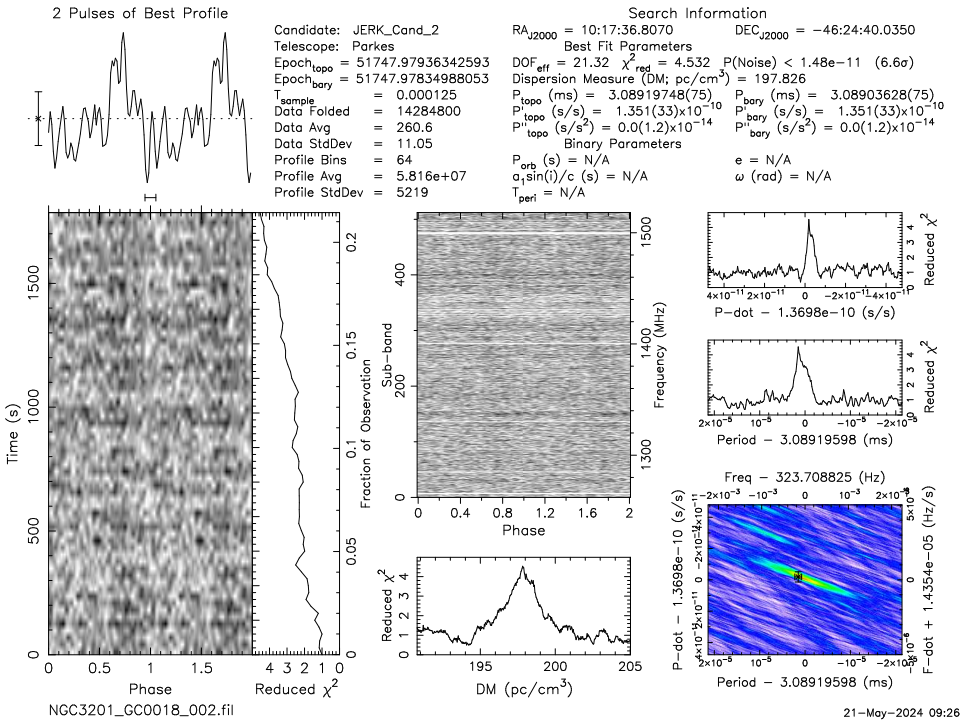
2 Pulses of Best Profile
Search Information
Candidate: JERK_Cand_2
Telescope: Parkes
Epoch_topo = 51747.97936342593
Epoch_bary = 51747.97834988053
T_sample = 0.000125
Data Folded = 14284800
Data Avg = 260.6
Data StdDev = 11.05
Profile Bins = 64
Profile Avg = 5.816e+07
Profile StdDev = 5219
RA_J2000 = 10:17:36.8070
DEC_J2000 = −46:24:40.0350
Best Fit Parameters
DOF_eff = 21.32 χ²_red = 4.532 P(Noise) < 1.48e−11 (6.6σ)
Dispersion Measure (DM; pc/cm³) = 197.826
P_topo (ms) = 3.08919748(75)
P'_topo (s/s) = 1.351(33)x10⁻¹⁰
P''_topo (s/s²) = 0.0(1.2)x10⁻¹⁴
P_bary (ms) = 3.08903628(75)
P'_bary (s/s) = 1.351(33)x10⁻¹⁰
P''_bary (s/s²) = 0.0(1.2)x10⁻¹⁴
Binary Parameters
P_orb (s) = N/A
e = N/A
a₁sin(i)/c (s) = N/A
ω (rad) = N/A
T_peri = N/A
Time (s)
Phase
Reduced χ²
Fraction of Observation
Sub-band
Frequency (MHz)
DM (pc/cm³)
P-dot − 1.3698e−10 (s/s)
Period − 3.08919598 (ms)
Freq − 323.708825 (Hz)
F-dot + 1.4354e−05 (Hz/s)
NGC3201_GC0018_002.fil
21−May−2024 09:26

A.4 Best candidate pulsars found in NGC 4372

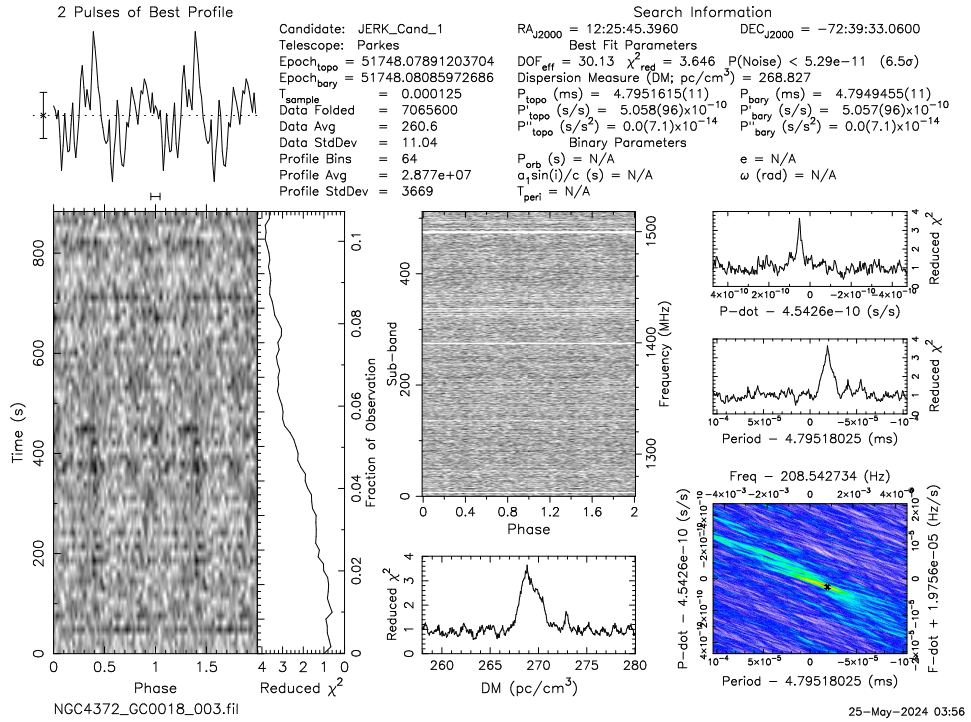

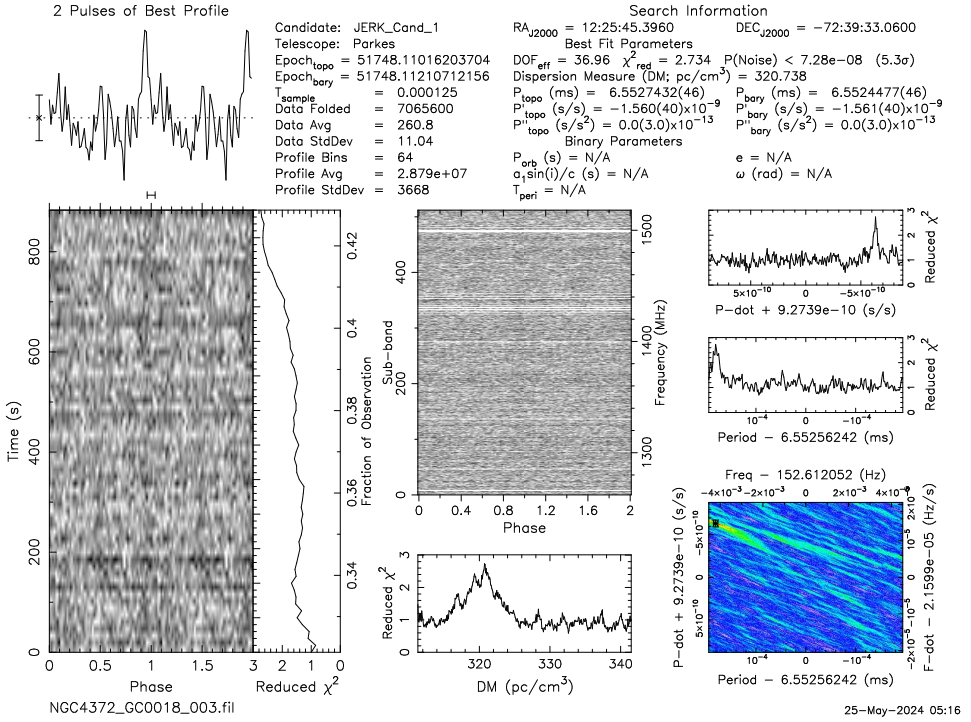

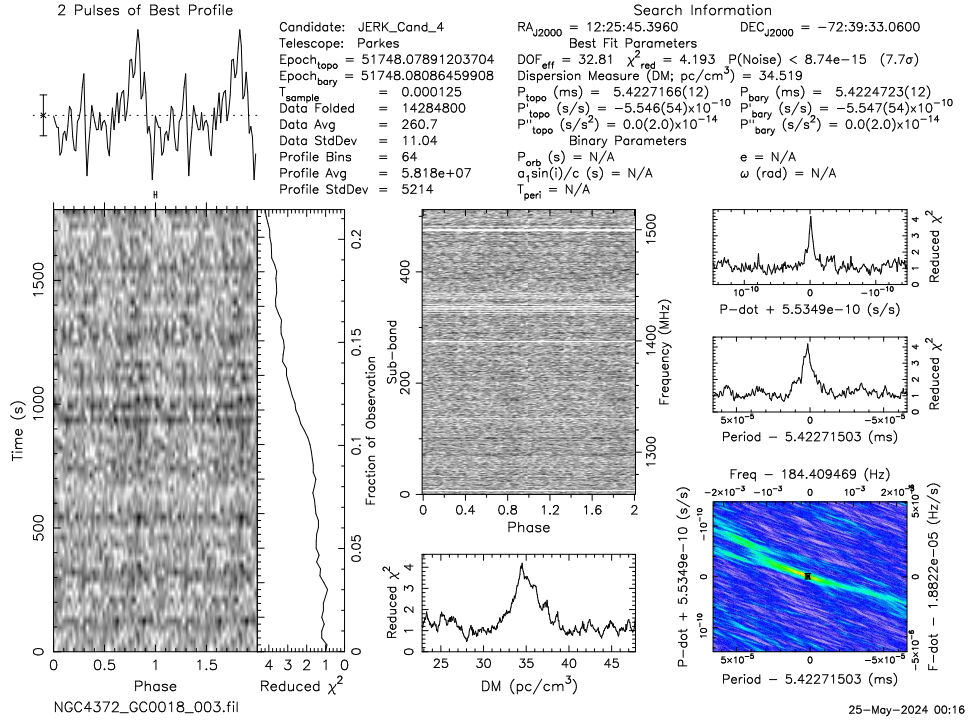
2 Pulses of Best Profile
Search Information
Candidate: JERK_Cand_4
Telescope: Parkes
Epoch_topo = 51748.07891203704
Epoch_bary = 51748.08086459908
T_sample = 0.000125
Data Folded = 14284800
Data Avg = 260.7
Data StdDev = 11.04
Profile Bins = 64
Profile Avg = 5.818e+07
Profile StdDev = 5214
RA_J2000 = 12:25:45.3960 DEC_J2000 = −72:39:33.0600
Best Fit Parameters
DOF_eff = 32.81 χ²_red = 4.193 P(Noise) < 8.74e−15 (7.7σ)
Dispersion Measure (DM; pc/cm³) = 34.519
P_topo (ms) = 5.4227166(12) P_bary (ms) = 5.4224723(12)
P'_topo (s/s) = −5.546(54)x10⁻¹⁰ P'_bary (s/s) = −5.547(54)x10⁻¹⁰
P''_topo (s/s²) = 0.0(2.0)x10⁻¹⁴ P''_bary (s/s²) = 0.0(2.0)x10⁻¹⁴
Binary Parameters
P_orb (s) = N/A e = N/A
a_1sin(i)/c (s) = N/A ω (rad) = N/A
T_peri = N/A
Time (s)
Phase
Reduced χ²
Fraction of Observation
Sub-band
Frequency (MHz)
DM (pc/cm³)
P-dot + 5.5349e−10 (s/s)
Period − 5.42271503 (ms)
Freq − 184.409469 (Hz)
F-dot − 1.8822e−05 (Hz/s)
NGC4372_GC0018_003.fil
25−May−2024 00:16

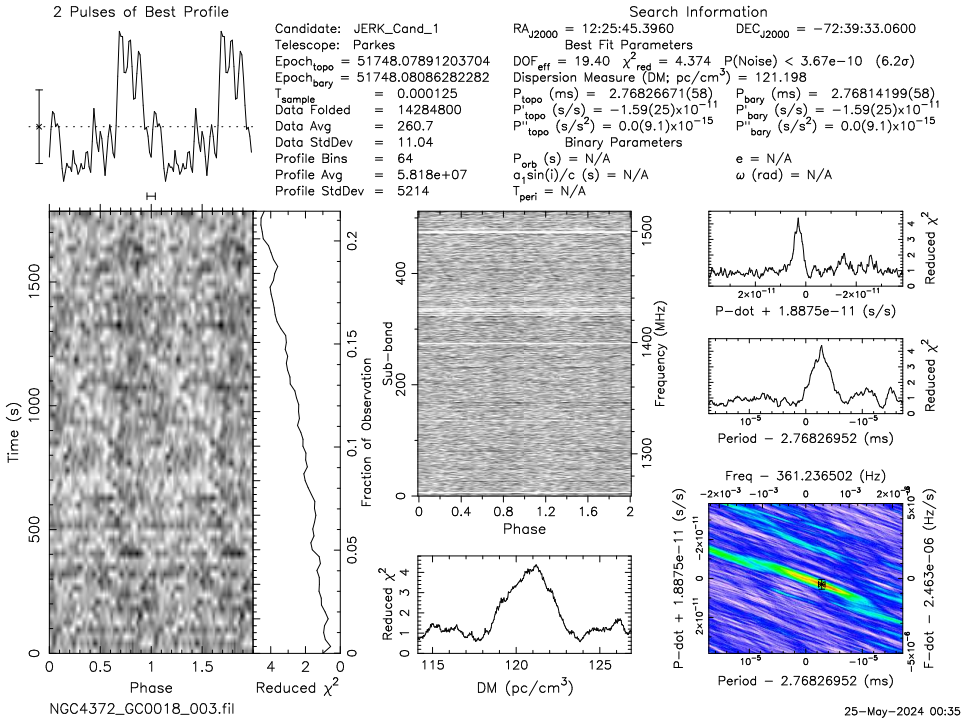
2 Pulses of Best Profile
Search Information
Candidate: JERK_Cand_1
Telescope: Parkes
Epoch_topo = 51748.07891203704
Epoch_bary = 51748.08086282282
T_sample = 0.000125
Data Folded = 14284800
Data Avg = 260.7
Data StdDev = 11.04
Profile Bins = 64
Profile Avg = 5.818e+07
Profile StdDev = 5214
RA_J2000 = 12:25:45.3960 DEC_J2000 = −72:39:33.0600
Best Fit Parameters
DOF_eff = 19.40 χ²_red = 4.374 P(Noise) < 3.67e−10 (6.2σ)
Dispersion Measure (DM; pc/cm³) = 121.198
P_topo (ms) = 2.76826671(58) P_bary (ms) = 2.76814199(58)
P'_topo (s/s) = −1.59(25)x10⁻¹¹ P'_bary (s/s) = −1.59(25)x10⁻¹¹
P''_topo (s/s²) = 0.0(9.1)x10⁻¹⁵ P''_bary (s/s²) = 0.0(9.1)x10⁻¹⁵
Binary Parameters
P_orb (s) = N/A e = N/A
a_1sin(i)/c (s) = N/A ω (rad) = N/A
T_peri = N/A
Time (s)
Phase
Reduced χ²
Fraction of Observation
Sub-band
Frequency (MHz)
DM (pc/cm³)
P-dot + 1.8875e−11 (s/s)
Period − 2.76826952 (ms)
Freq − 361.236502 (Hz)
F-dot − 2.463e−06 (Hz/s)
NGC4372_GC0018_003.fil
25−May−2024 00:35

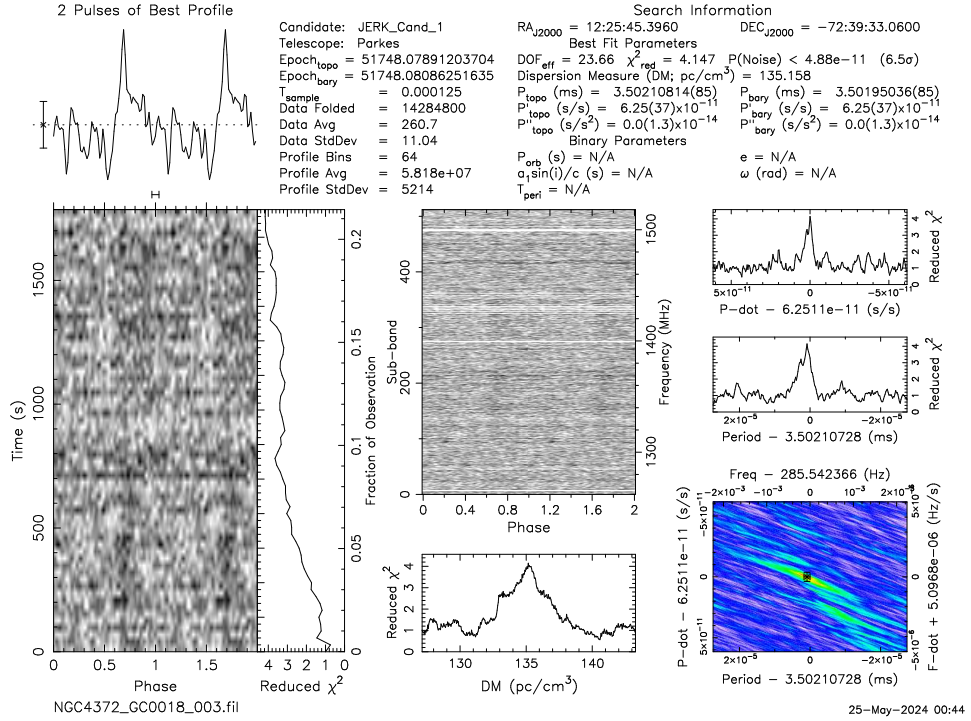
2 Pulses of Best Profile
Search Information
Candidate: JERK_Cand_1
Telescope: Parkes
Epoch_topo = 51748.07891203704
Epoch_bary = 51748.08086251635
T_sample = 0.000125
Data Folded = 14284800
Data Avg = 260.7
Data StdDev = 11.04
Profile Bins = 64
Profile Avg = 5.818e+07
Profile StdDev = 5214
RA_J2000 = 12:25:45.3960 DEC_J2000 = −72:39:33.0600
Best Fit Parameters
DOF_eff = 23.66 χ²_red = 4.147 P(Noise) < 4.88e−11 (6.5σ)
Dispersion Measure (DM; pc/cm³) = 135.158
P_topo (ms) = 3.50210814(85) P_bary (ms) = 3.50195036(85)
P'_topo (s/s) = 6.25(37)x10⁻¹¹ P'_bary (s/s) = 6.25(37)x10⁻¹¹
P''_topo (s/s²) = 0.0(1.3)x10⁻¹⁴ P''_bary (s/s²) = 0.0(1.3)x10⁻¹⁴
Binary Parameters
P_orb (s) = N/A e = N/A
a₁sin(i)/c (s) = N/A ω (rad) = N/A
T_peri = N/A
Time (s)
Phase
Reduced χ²
Fraction of Observation
Sub-band
Frequency (MHz)
DM (pc/cm³)
P-dot − 6.2511e−11 (s/s)
Period − 3.50210728 (ms)
Freq − 285.542366 (Hz)
F-dot + 5.0968e−06 (Hz/s)
NGC4372_GC0018_003.fil
25−May−2024 00:44

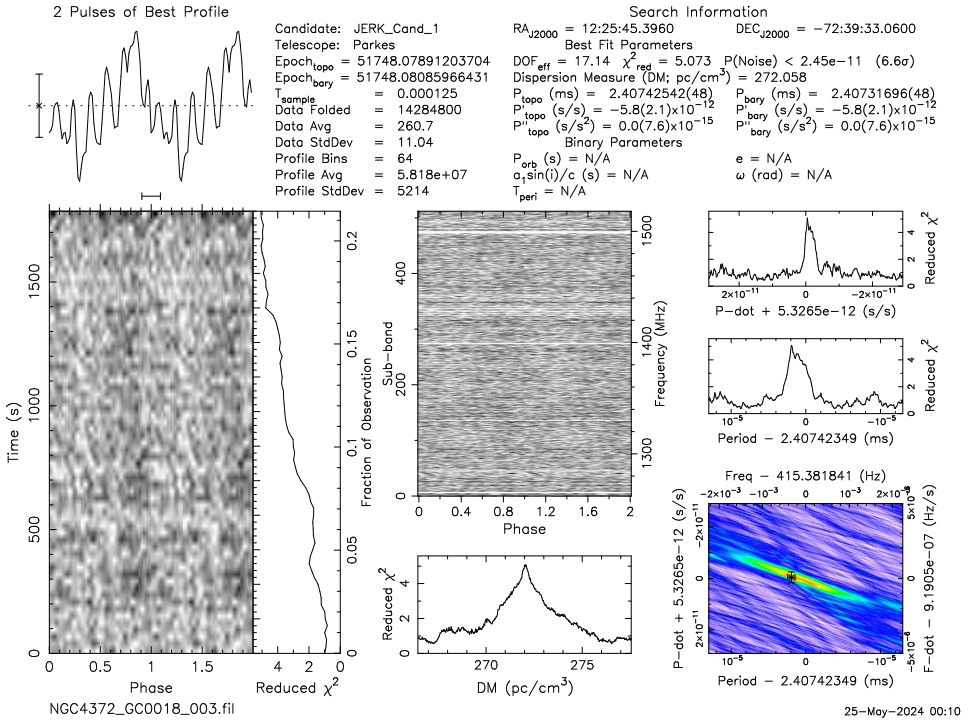
2 Pulses of Best Profile
Search Information
Candidate: JERK_Cand_1
Telescope: Parkes
Epoch_topo = 51748.07891203704
Epoch_bary = 51748.08085966431
T_sample = 0.000125
Data Folded = 14284800
Data Avg = 260.7
Data StdDev = 11.04
Profile Bins = 64
Profile Avg = 5.818e+07
Profile StdDev = 5214
RA_J2000 = 12:25:45.3960 DEC_J2000 = −72:39:33.0600
Best Fit Parameters
DOF_eff = 17.14 χ²_red = 5.073 P(Noise) < 2.45e−11 (6.6σ)
Dispersion Measure (DM; pc/cm³) = 272.058
P_topo (ms) = 2.40742542(48) P_bary (ms) = 2.40731696(48)
P'_topo (s/s) = −5.8(2.1)x10⁻¹² P'_bary (s/s) = −5.8(2.1)x10⁻¹²
P''_topo (s/s²) = 0.0(7.6)x10⁻¹⁵ P''_bary (s/s²) = 0.0(7.6)x10⁻¹⁵
Binary Parameters
P_orb (s) = N/A e = N/A
a₁sin(i)/c (s) = N/A ω (rad) = N/A
T_peri = N/A
Time (s)
Phase
Reduced χ²
Fraction of Observation
Sub-band
Frequency (MHz)
DM (pc/cm³)
P-dot + 5.3265e−12 (s/s)
Period − 2.40742349 (ms)
Freq − 415.381841 (Hz)
F-dot − 9.1905e−07 (Hz/s)
NGC4372_GC0018_003.fil
25−May−2024 00:10

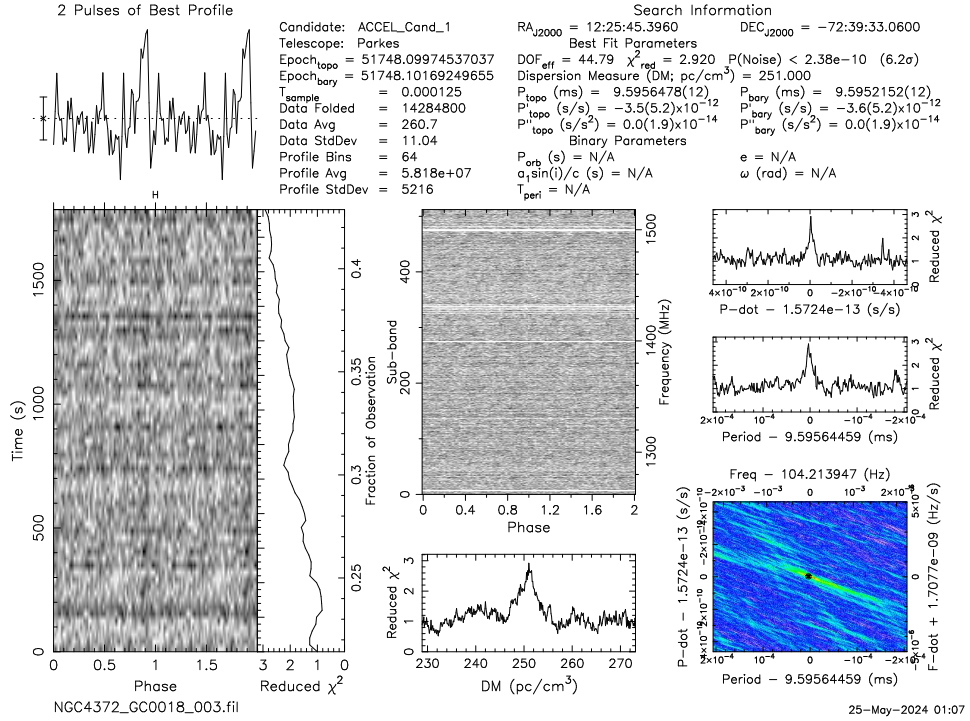
2 Pulses of Best Profile
Search Information
Candidate: ACCEL_Cand_1
Telescope: Parkes
Epoch_topo = 51748.09974537037
Epoch_bary = 51748.10169249655
T_sample = 0.000125
Data Folded = 14284800
Data Avg = 260.7
Data StdDev = 11.04
Profile Bins = 64
Profile Avg = 5.818e+07
Profile StdDev = 5216
RA_J2000 = 12:25:45.3960 DEC_J2000 = −72:39:33.0600
Best Fit Parameters
DOF_eff = 44.79 χ²_red = 2.920 P(Noise) < 2.38e−10 (6.2σ)
Dispersion Measure (DM; pc/cm³) = 251.000
P_topo (ms) = 9.5956478(12) P_bary (ms) = 9.5952152(12)
P'_topo (s/s) = −3.5(5.2)x10⁻¹² P'_bary (s/s) = −3.6(5.2)x10⁻¹²
P''_topo (s/s²) = 0.0(1.9)x10⁻¹⁴ P''_bary (s/s²) = 0.0(1.9)x10⁻¹⁴
Binary Parameters
P_orb (s) = N/A e = N/A
a_1sin(i)/c (s) = N/A ω (rad) = N/A
T_peri = N/A
Time (s)
Phase
Reduced χ²
Fraction of Observation
Sub-band
Frequency (MHz)
DM (pc/cm³)
P-dot − 1.5724e−13 (s/s)
Period − 9.59564459 (ms)
Freq − 104.213947 (Hz)
F-dot + 1.7077e−09 (Hz/s)
NGC4372_GC0018_003.fil
25−May−2024 01:07

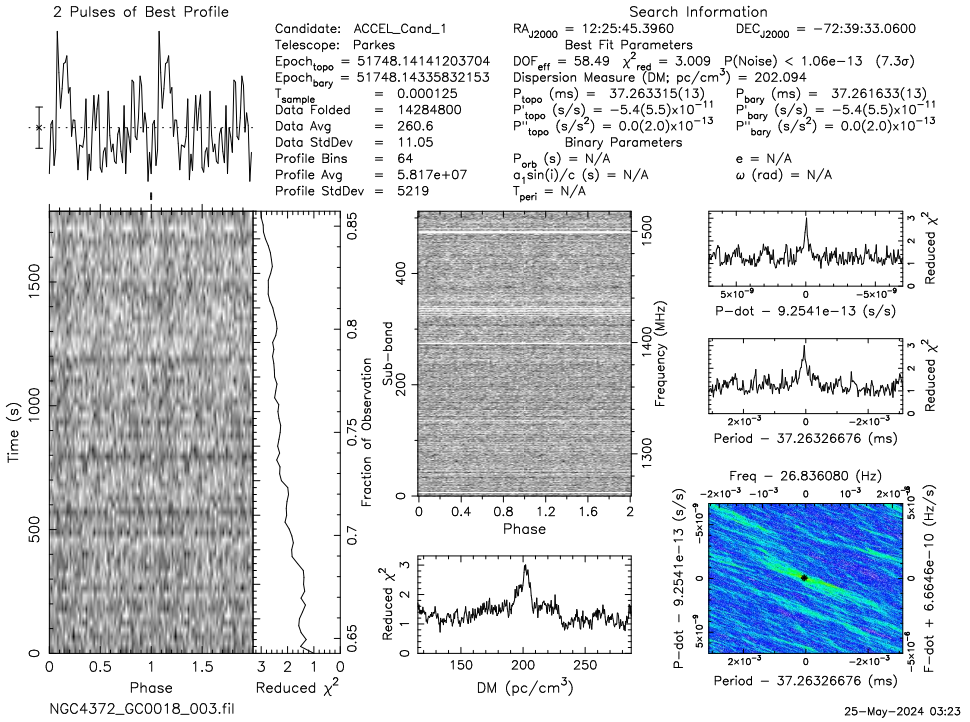
2 Pulses of Best Profile
Search Information
Candidate: ACCEL_Cand_1
Telescope: Parkes
Epoch_topo = 51748.14141203704
Epoch_bary = 51748.14335832153
T_sample = 0.000125
Data Folded = 14284800
Data Avg = 260.6
Data StdDev = 11.05
Profile Bins = 64
Profile Avg = 5.817e+07
Profile StdDev = 5219
RA_J2000 = 12:25:45.3960 DEC_J2000 = −72:39:33.0600
Best Fit Parameters
DOF_eff = 58.49 χ²_red = 3.009 P(Noise) < 1.06e−13 (7.3σ)
Dispersion Measure (DM; pc/cm³) = 202.094
P_topo (ms) = 37.263315(13) P_bary (ms) = 37.261633(13)
P'_topo (s/s) = −5.4(5.5)x10⁻¹¹ P'_bary (s/s) = −5.4(5.5)x10⁻¹¹
P''_topo (s/s²) = 0.0(2.0)x10⁻¹³ P''_bary (s/s²) = 0.0(2.0)x10⁻¹³
Binary Parameters
P_orb (s) = N/A e = N/A
a_1sin(i)/c (s) = N/A ω (rad) = N/A
T_peri = N/A
Time (s)
Phase
Reduced χ²
Fraction of Observation
Sub-band
Frequency (MHz)
DM (pc/cm³)
P-dot − 9.2541e−13 (s/s)
Period − 37.26326676 (ms)
Freq − 26.836080 (Hz)
F-dot + 6.6646e−10 (Hz/s)
NGC4372_GC0018_003.fil
25−May−2024 03:23

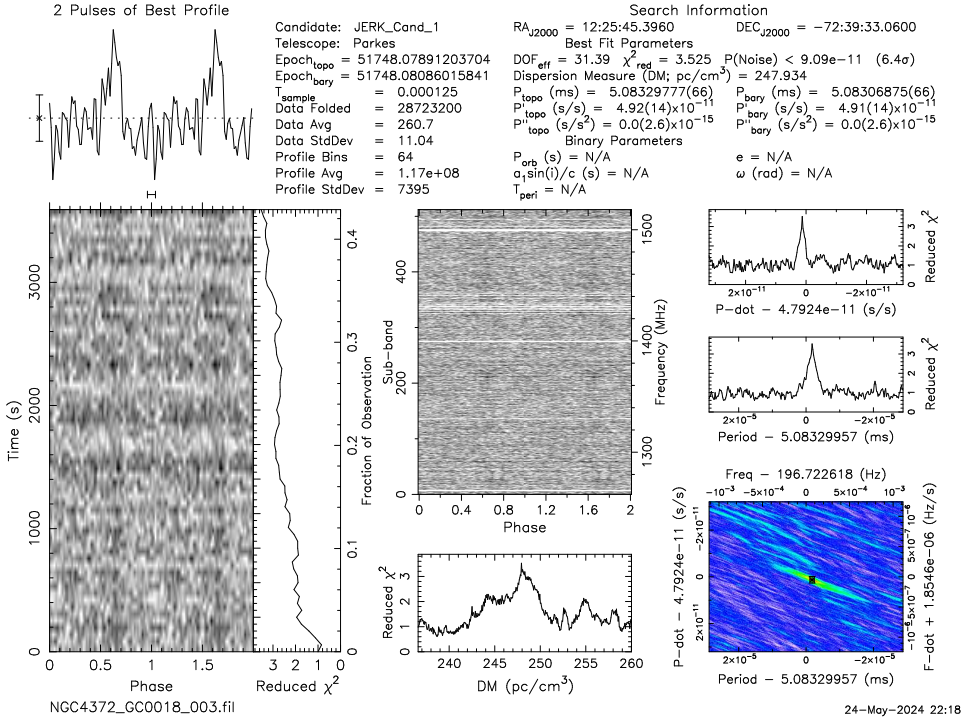
2 Pulses of Best Profile
Search Information
Candidate: JERK_Cand_1
Telescope: Parkes
Epoch_topo = 51748.07891203704
Epoch_bary = 51748.08086015841
T_sample = 0.000125
Data Folded = 28723200
Data Avg = 260.7
Data StdDev = 11.04
Profile Bins = 64
Profile Avg = 1.17e+08
Profile StdDev = 7395
RA_J2000 = 12:25:45.3960 DEC_J2000 = −72:39:33.0600
Best Fit Parameters
DOF_eff = 31.39 χ²_red = 3.525 P(Noise) < 9.09e−11 (6.4σ)
Dispersion Measure (DM; pc/cm³) = 247.934
P_topo (ms) = 5.08329777(66) P_bary (ms) = 5.08306875(66)
P'_topo (s/s) = 4.92(14)x10⁻¹¹ P'_bary (s/s) = 4.91(14)x10⁻¹¹
P''_topo (s/s²) = 0.0(2.6)x10⁻¹⁵ P''_bary (s/s²) = 0.0(2.6)x10⁻¹⁵
Binary Parameters
P_orb (s) = N/A e = N/A
a_1sin(i)/c (s) = N/A ω (rad) = N/A
T_peri = N/A
Time (s)
Phase
Reduced χ²
Fraction of Observation
Sub-band
Frequency (MHz)
DM (pc/cm³)
P-dot − 4.7924e−11 (s/s)
Period − 5.08329957 (ms)
Freq − 196.722618 (Hz)
F-dot + 1.8546e−06 (Hz/s)
NGC4372_GC0018_003.fil
24−May−2024 22:18

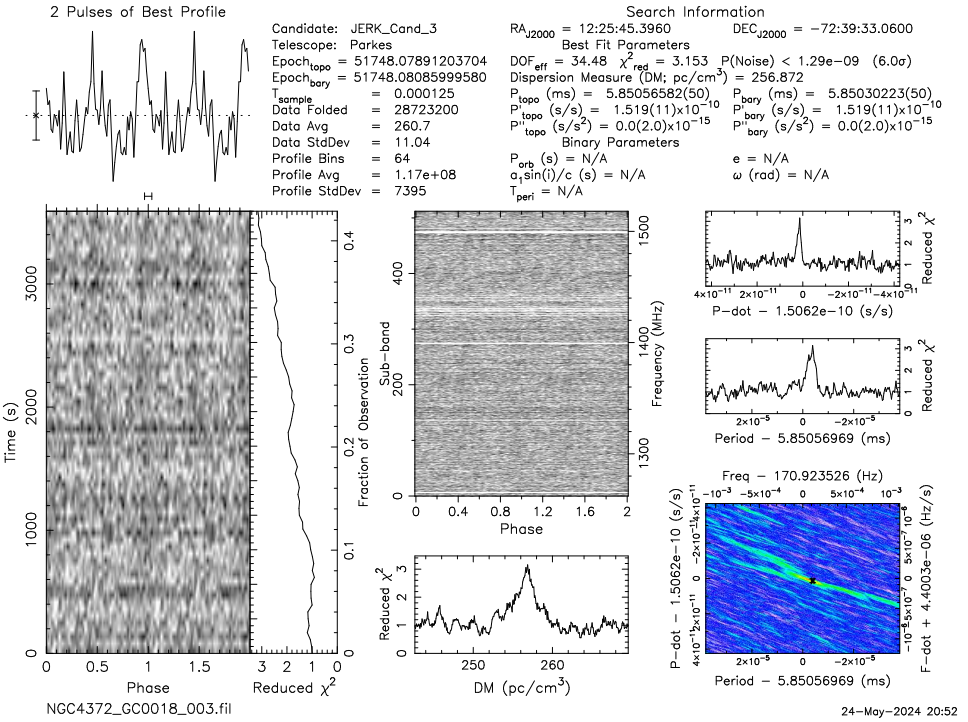
2 Pulses of Best Profile
Search Information
Candidate: JERK_Cand_3
Telescope: Parkes
Epoch_topo = 51748.07891203704
Epoch_bary = 51748.08085999580
T_sample = 0.000125
Data Folded = 28723200
Data Avg = 260.7
Data StdDev = 11.04
Profile Bins = 64
Profile Avg = 1.17e+08
Profile StdDev = 7395
RA_J2000 = 12:25:45.3960 DEC_J2000 = −72:39:33.0600
Best Fit Parameters
DOF_eff = 34.48 χ²_red = 3.153 P(Noise) < 1.29e−09 (6.0σ)
Dispersion Measure (DM; pc/cm³) = 256.872
P_topo (ms) = 5.85056582(50) P_bary (ms) = 5.85030223(50)
P'_topo (s/s) = 1.519(11)x10⁻¹⁰ P'_bary (s/s) = 1.519(11)x10⁻¹⁰
P''_topo (s/s²) = 0.0(2.0)x10⁻¹⁵ P''_bary (s/s²) = 0.0(2.0)x10⁻¹⁵
Binary Parameters
P_orb (s) = N/A e = N/A
a_1sin(i)/c (s) = N/A ω (rad) = N/A
T_peri = N/A
Time (s)
Phase
Reduced χ²
Fraction of Observation
Sub-band
Frequency (MHz)
DM (pc/cm³)
P-dot − 1.5062e−10 (s/s)
Period − 5.85056969 (ms)
Freq − 170.923526 (Hz)
F-dot + 4.4003e−06 (Hz/s)
NGC4372_GC0018_003.fil
24−May−2024 20:52

A.5 Best candidate pulsars found in NGC 4590

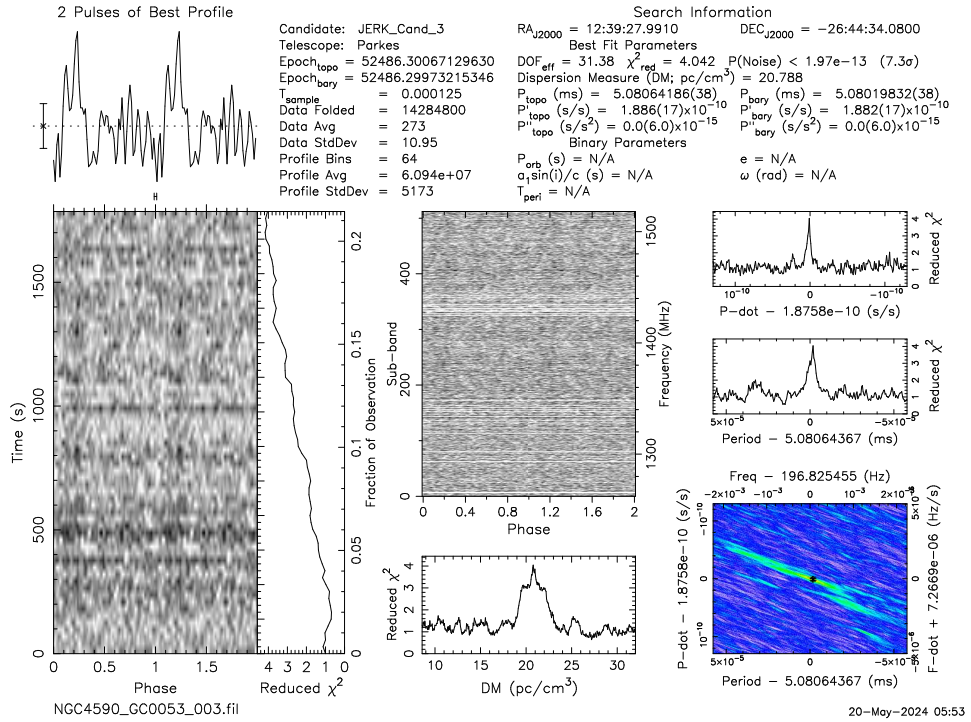

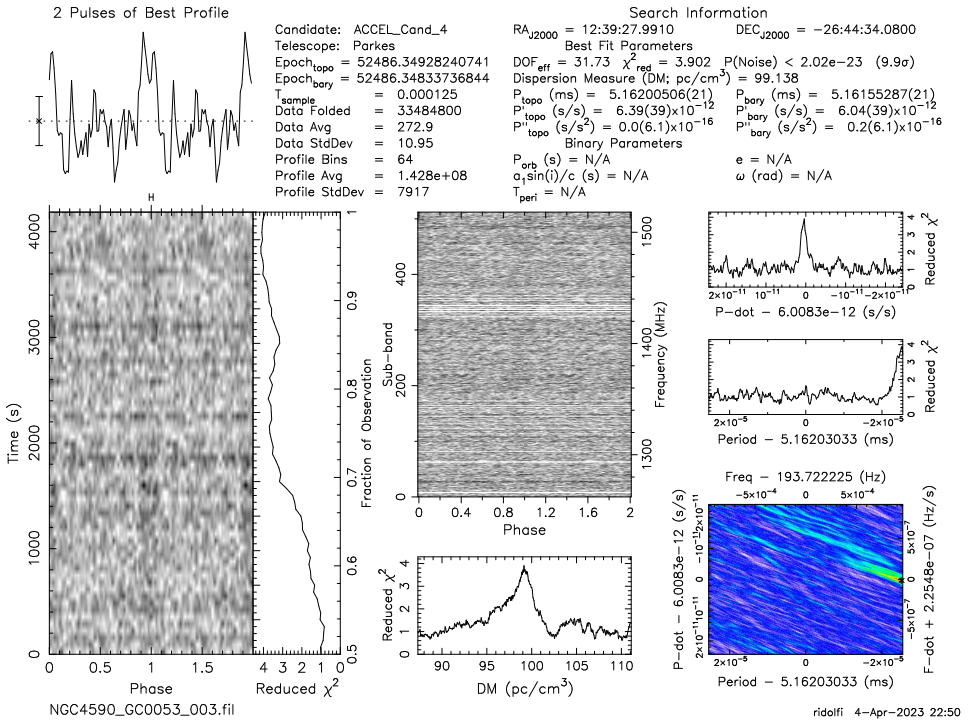

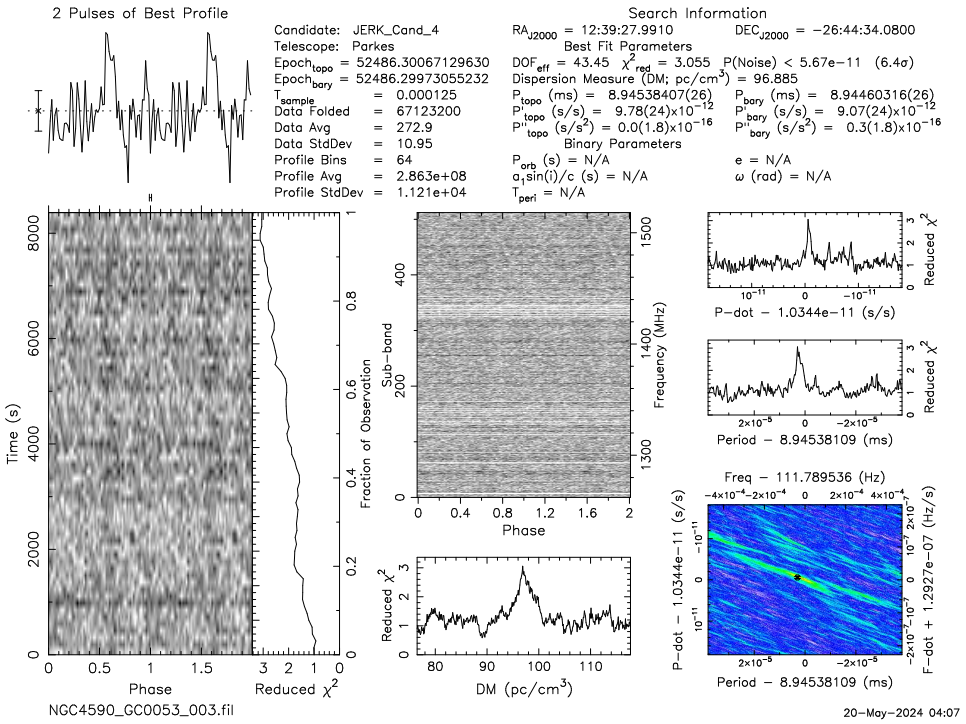
2 Pulses of Best Profile
Search Information
Candidate: JERK_Cand_4
Telescope: Parkes
Epoch_topo = 52486.30067129630
Epoch_bary = 52486.29973055232
T_sample = 0.000125
Data Folded = 67123200
Data Avg = 272.9
Data StdDev = 10.95
Profile Bins = 64
Profile Avg = 2.863e+08
Profile StdDev = 1.121e+04
RA_J2000 = 12:39:27.9910
DEC_J2000 = −26:44:34.0800
Best Fit Parameters
DOF_eff = 43.45 χ²_red = 3.055 P(Noise) < 5.67e−11 (6.4σ)
Dispersion Measure (DM; pc/cm³) = 96.885
P_topo (ms) = 8.94538407(26)
P_bary (ms) = 8.94460316(26)
P'_topo (s/s) = 9.78(24)x10⁻¹²
P'_bary (s/s) = 9.07(24)x10⁻¹²
P''_topo (s/s²) = 0.0(1.8)x10⁻¹⁶
P''_bary (s/s²) = 0.3(1.8)x10⁻¹⁶
Binary Parameters
P_orb (s) = N/A
e = N/A
a₁sin(i)/c (s) = N/A
ω (rad) = N/A
T_peri = N/A
Time (s)
Phase
Reduced χ²
Fraction of Observation
Sub-band
Frequency (MHz)
DM (pc/cm³)
P-dot − 1.0344e−11 (s/s)
Period − 8.94538109 (ms)
Freq − 111.789536 (Hz)
F-dot + 1.2927e−07 (Hz/s)
NGC4590_GC0053_003.fil
20−May−2024 04:07

A.6 Best candidate pulsars found in NGC 4833

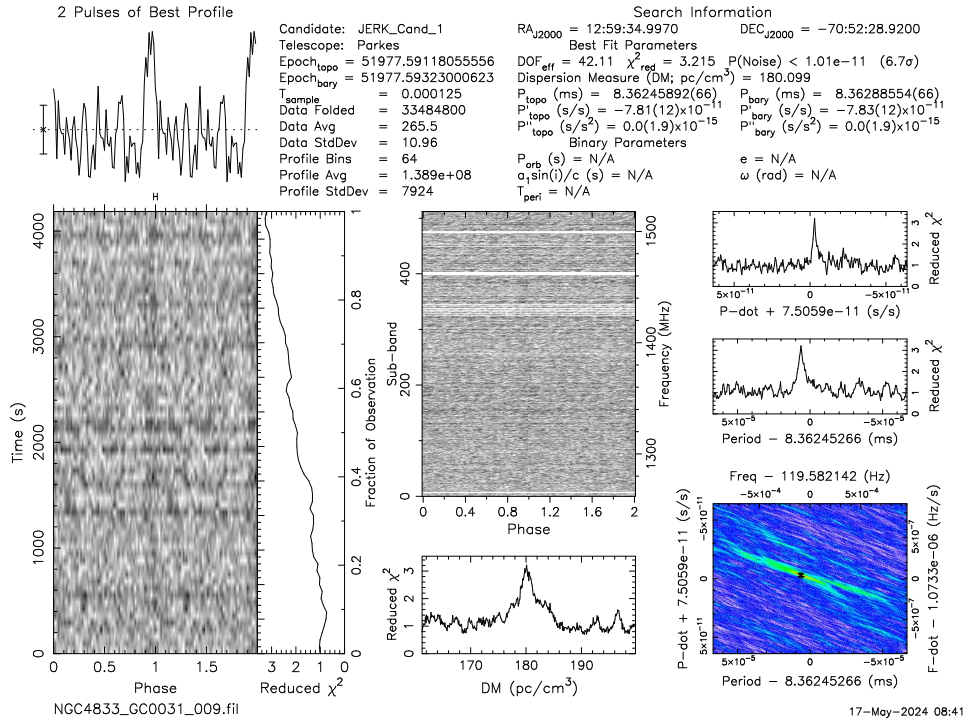

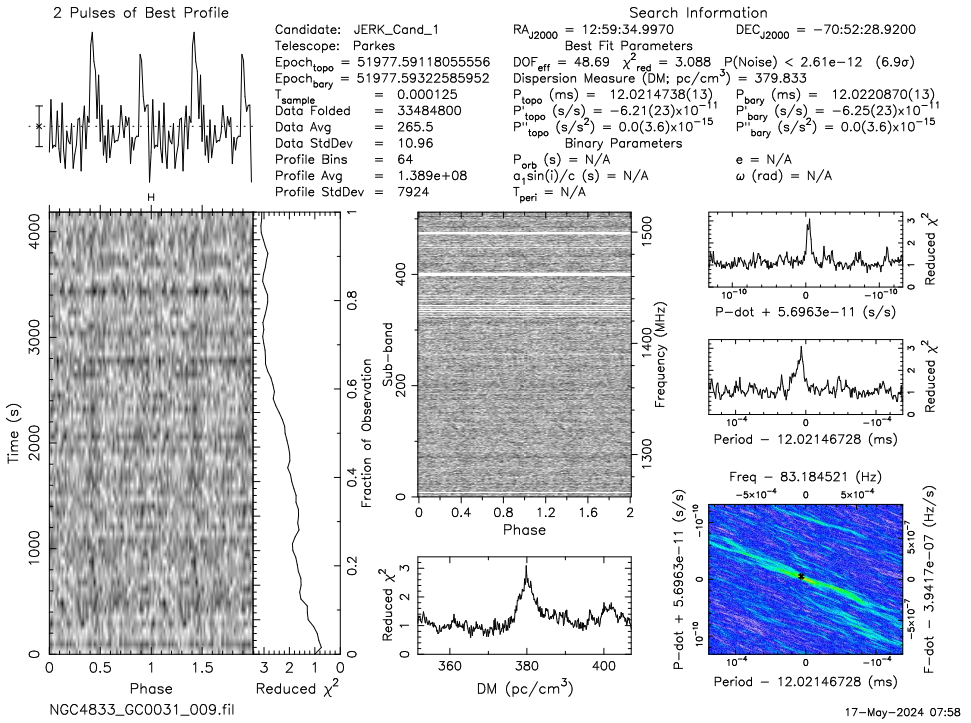

A.7 Best candidate pulsars found in NGC 5286

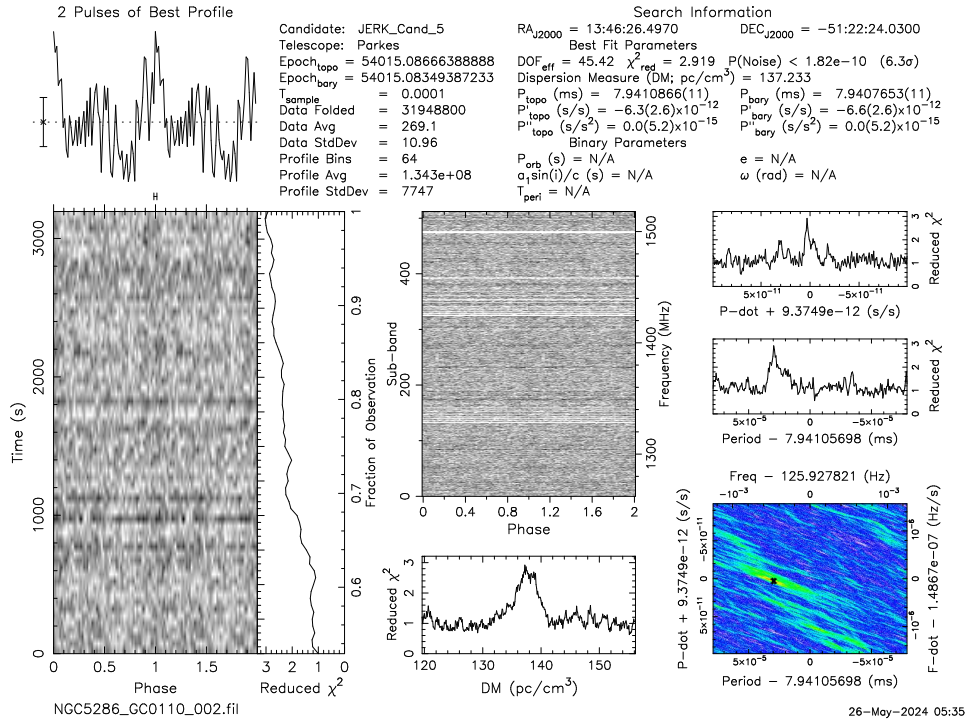

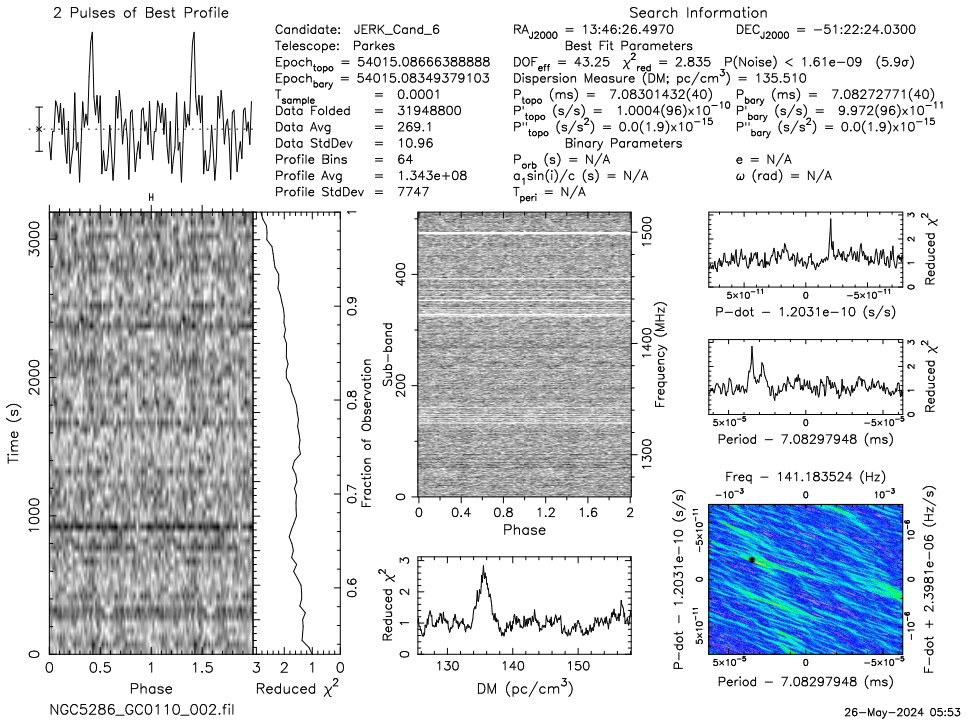

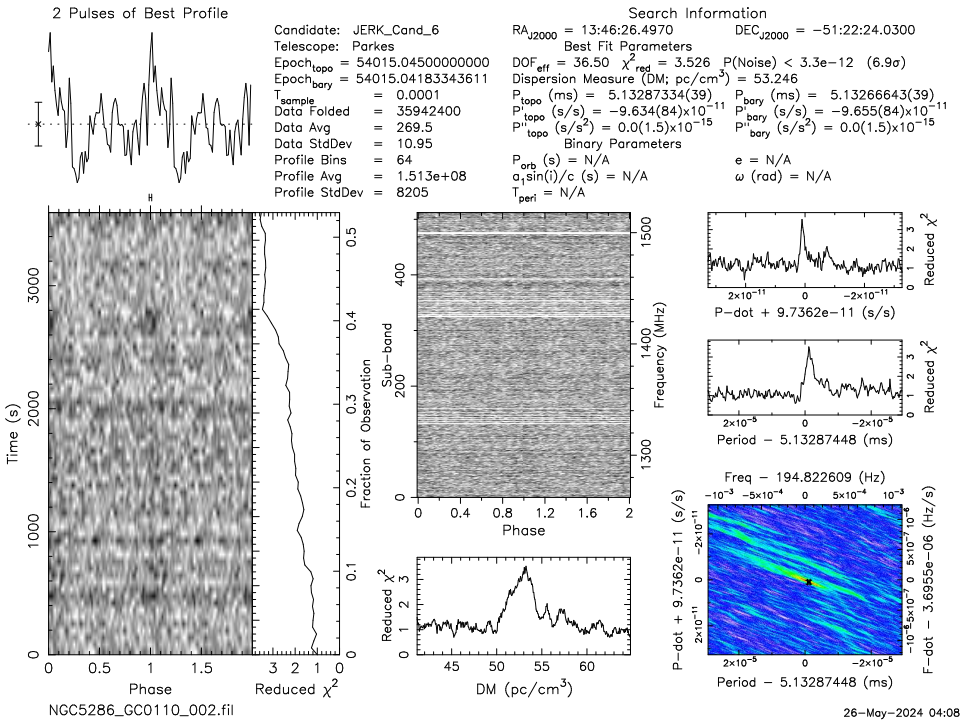
2 Pulses of Best Profile
Search Information
Candidate: JERK_Cand_6
Telescope: Parkes
Epoch_topo = 54015.04500000000
Epoch_bary = 54015.04183343611
T_sample = 0.0001
Data Folded = 35942400
Data Avg = 269.5
Data StdDev = 10.95
Profile Bins = 64
Profile Avg = 1.513e+08
Profile StdDev = 8205
RA_J2000 = 13:46:26.4970
DEC_J2000 = −51:22:24.0300
Best Fit Parameters
DOF_eff = 36.50 χ²_red = 3.526 P(Noise) < 3.3e−12 (6.9σ)
Dispersion Measure (DM; pc/cm³) = 53.246
P_topo (ms) = 5.13287334(39)
P_bary (ms) = 5.13266643(39)
P'_topo (s/s) = −9.634(84)x10⁻¹¹
P'_bary (s/s) = −9.655(84)x10⁻¹¹
P''_topo (s/s²) = 0.0(1.5)x10⁻¹⁵
P''_bary (s/s²) = 0.0(1.5)x10⁻¹⁵
Binary Parameters
P_orb (s) = N/A
e = N/A
a₁sin(i)/c (s) = N/A
ω (rad) = N/A
T_peri = N/A
Time (s)
Phase
Reduced χ²
Fraction of Observation
Sub-band
Frequency (MHz)
DM (pc/cm³)
P−dot + 9.7362e−11 (s/s)
Period − 5.13287448 (ms)
Freq − 194.822609 (Hz)
F−dot − 3.6955e−06 (Hz/s)
NGC5286_GC0110_002.fil
26−May−2024 04:08

A.8 Best candidate pulsars found in ESO 452

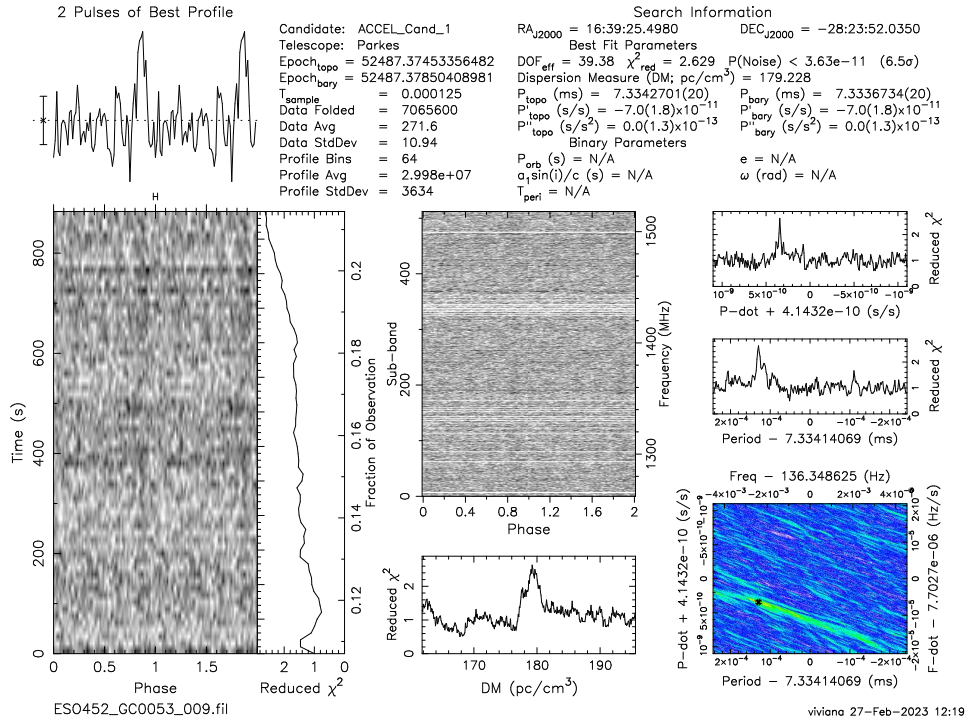

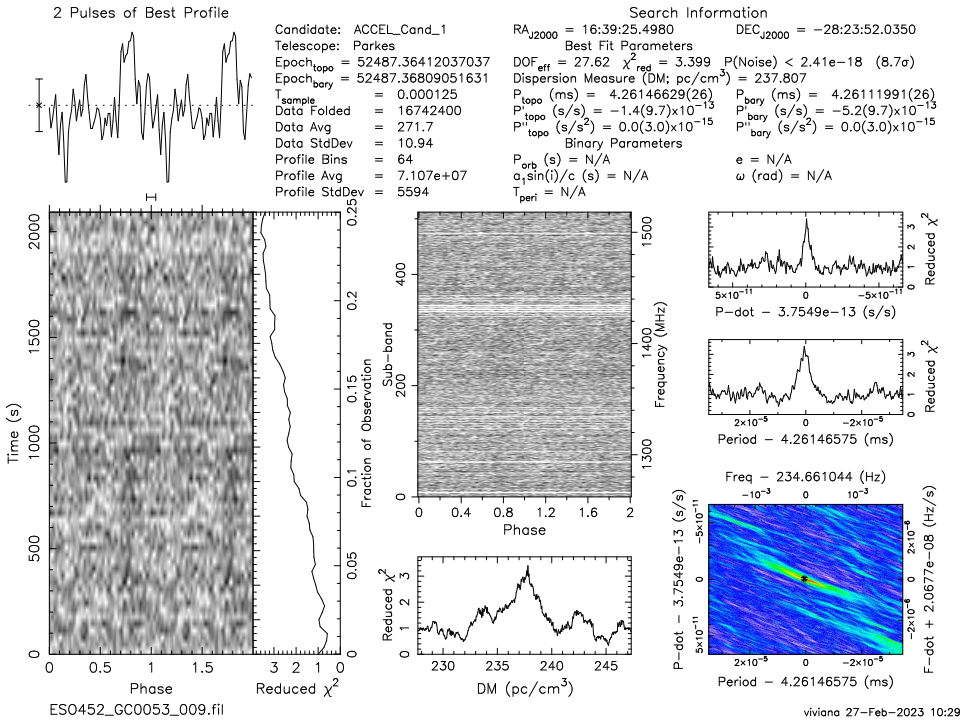

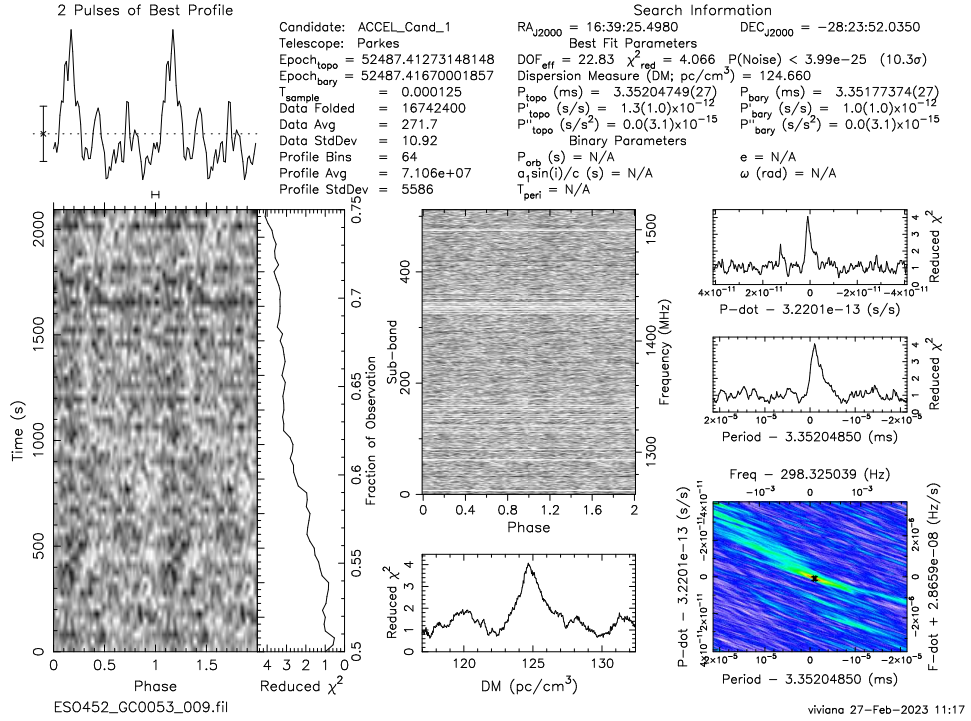
2 Pulses of Best Profile
Search Information
Candidate: ACCEL_Cand_1
Telescope: Parkes
Epoch_topo = 52487.41273148148
Epoch_bary = 52487.41670001857
T_sample = 0.000125
Data Folded = 16742400
Data Avg = 271.7
Data StdDev = 10.92
Profile Bins = 64
Profile Avg = 7.106e+07
Profile StdDev = 5586
RA_J2000 = 16:39:25.4980
DEC_J2000 = −28:23:52.0350
Best Fit Parameters
DOF_eff = 22.83 χ²_red = 4.066 P(Noise) < 3.99e−25 (10.3σ)
Dispersion Measure (DM; pc/cm³) = 124.660
P_topo (ms) = 3.35204749(27)
P_bary (ms) = 3.35177374(27)
P'_topo (s/s) = 1.3(1.0)x10⁻¹²
P'_bary (s/s) = 1.0(1.0)x10⁻¹²
P''_topo (s/s²) = 0.0(3.1)x10⁻¹⁵
P''_bary (s/s²) = 0.0(3.1)x10⁻¹⁵
Binary Parameters
P_orb (s) = N/A
e = N/A
a₁sin(i)/c (s) = N/A
ω (rad) = N/A
T_peri = N/A
Time (s)
Phase
Reduced χ²
Fraction of Observation
Sub-band
Frequency (MHz)
DM (pc/cm³)
P-dot − 3.2201e-13 (s/s)
Period − 3.35204850 (ms)
Freq − 298.325039 (Hz)
F-dot + 2.8659e-08 (Hz/s)
ES0452_GC0053_009.fil
viviana 27-Feb-2023 11:17

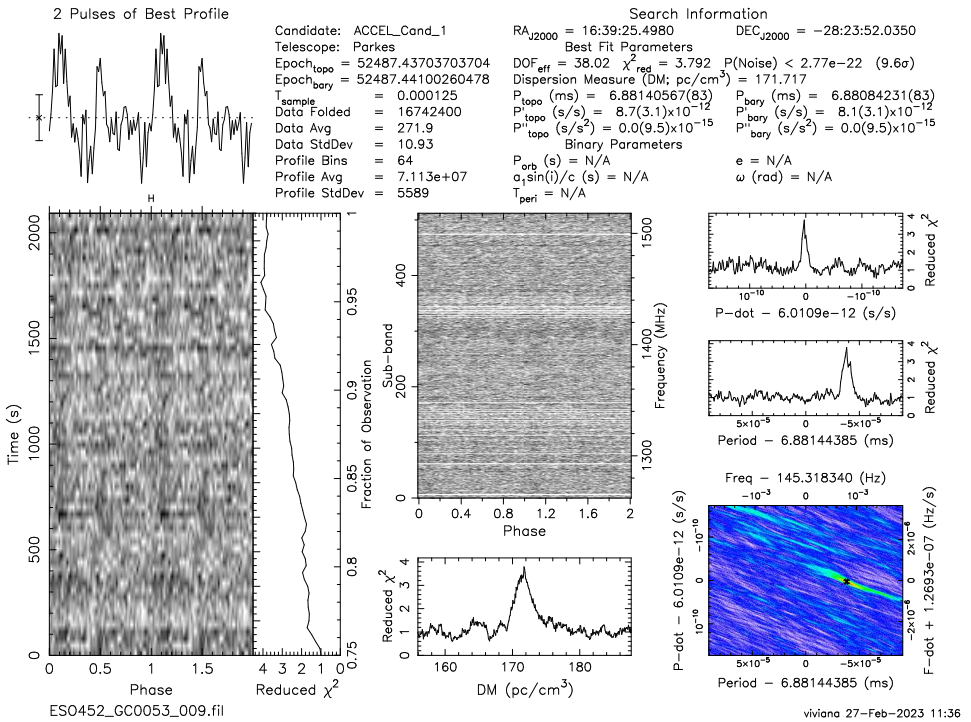
2 Pulses of Best Profile
Search Information
Candidate: ACCEL_Cand_1
Telescope: Parkes
Epoch_topo = 52487.43703703704
Epoch_bary = 52487.44100260478
T_sample = 0.000125
Data Folded = 16742400
Data Avg = 271.9
Data StdDev = 10.93
Profile Bins = 64
Profile Avg = 7.113e+07
Profile StdDev = 5589
RA_J2000 = 16:39:25.4980
DEC_J2000 = −28:23:52.0350
Best Fit Parameters
DOF_eff = 38.02 χ²_red = 3.792 P(Noise) < 2.77e−22 (9.6σ)
Dispersion Measure (DM; pc/cm³) = 171.717
P_topo (ms) = 6.88140567(83)
P_bary (ms) = 6.88084231(83)
P'_topo (s/s) = 8.7(3.1)x10⁻¹²
P'_bary (s/s) = 8.1(3.1)x10⁻¹²
P''_topo (s/s²) = 0.0(9.5)x10⁻¹⁵
P''_bary (s/s²) = 0.0(9.5)x10⁻¹⁵
Binary Parameters
P_orb (s) = N/A
e = N/A
a₁sin(i)/c (s) = N/A
ω (rad) = N/A
T_peri = N/A
Time (s)
Phase
Reduced χ²
Fraction of Observation
Sub-band
Frequency (MHz)
DM (pc/cm³)
P-dot − 6.0109e-12 (s/s)
Period − 6.88144385 (ms)
Freq − 145.318340 (Hz)
F-dot + 1.2693e-07 (Hz/s)
ES0452_GC0053_009.fil
viviana 27-Feb-2023 11:36

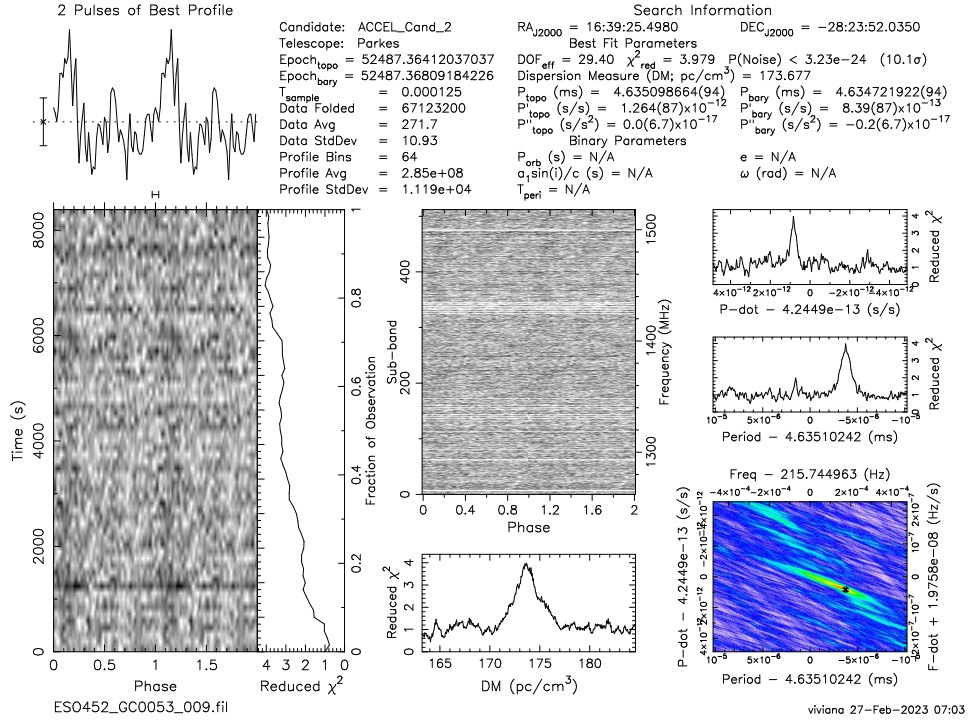
2 Pulses of Best Profile
Search Information
Candidate: ACCEL_Cand_2
Telescope: Parkes
Epoch_topo = 52487.36412037037
Epoch_bary = 52487.36809184226
T_sample = 0.000125
Data Folded = 67123200
Data Avg = 271.7
Data StdDev = 10.93
Profile Bins = 64
Profile Avg = 2.85e+08
Profile StdDev = 1.119e+04
RA_J2000 = 16:39:25.4980
DEC_J2000 = −28:23:52.0350
Best Fit Parameters
DOF_eff = 29.40 χ²_red = 3.979 P(Noise) < 3.23e−24 (10.1σ)
Dispersion Measure (DM; pc/cm³) = 173.677
P_topo (ms) = 4.635098664(94)
P_bary (ms) = 4.634721922(94)
P'_topo (s/s) = 1.264(87)x10⁻¹²
P'_bary (s/s) = 8.39(87)x10⁻¹³
P''_topo (s/s²) = 0.0(6.7)x10⁻¹⁷
P''_bary (s/s²) = −0.2(6.7)x10⁻¹⁷
Binary Parameters
P_orb (s) = N/A
e = N/A
a_1sin(i)/c (s) = N/A
ω (rad) = N/A
T_peri = N/A
Time (s)
Phase
Reduced χ²
Fraction of Observation
Sub-band
Frequency (MHz)
DM (pc/cm³)
P-dot − 4.2449e−13 (s/s)
F-dot + 1.9758e−08 (Hz/s)
Period − 4.63510242 (ms)
Freq − 215.744963 (Hz)
ES0452_GC0053_009.fil
viviana 27−Feb−2023 07:03

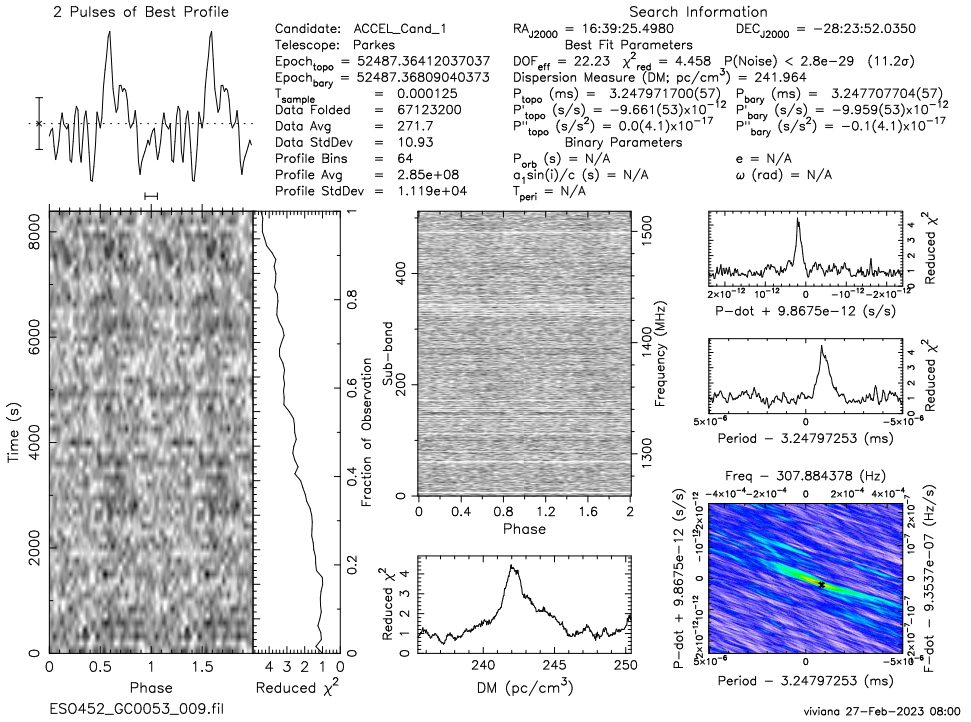
2 Pulses of Best Profile
Search Information
Candidate: ACCEL_Cand_1
Telescope: Parkes
Epoch_topo = 52487.36412037037
Epoch_bary = 52487.36809040373
T_sample = 0.000125
Data Folded = 67123200
Data Avg = 271.7
Data StdDev = 10.93
Profile Bins = 64
Profile Avg = 2.85e+08
Profile StdDev = 1.119e+04
RA_J2000 = 16:39:25.4980
DEC_J2000 = −28:23:52.0350
Best Fit Parameters
DOF_eff = 22.23 χ²_red = 4.458 P(Noise) < 2.8e−29 (11.2σ)
Dispersion Measure (DM; pc/cm³) = 241.964
P_topo (ms) = 3.247971700(57)
P_bary (ms) = 3.247707704(57)
P'_topo (s/s) = −9.661(53)x10⁻¹²
P'_bary (s/s) = −9.959(53)x10⁻¹²
P''_topo (s/s²) = 0.0(4.1)x10⁻¹⁷
P''_bary (s/s²) = −0.1(4.1)x10⁻¹⁷
Binary Parameters
P_orb (s) = N/A
e = N/A
a_1sin(i)/c (s) = N/A
ω (rad) = N/A
T_peri = N/A
Time (s)
Phase
Reduced χ²
Fraction of Observation
Sub-band
Frequency (MHz)
DM (pc/cm³)
P-dot + 9.8675e−12 (s/s)
F-dot − 9.3537e−07 (Hz/s)
Period − 3.24797253 (ms)
Freq − 307.884378 (Hz)
ES0452_GC0053_009.fil
viviana 27−Feb−2023 08:00

A.9 Best candidate pulsars found in NGC 6541

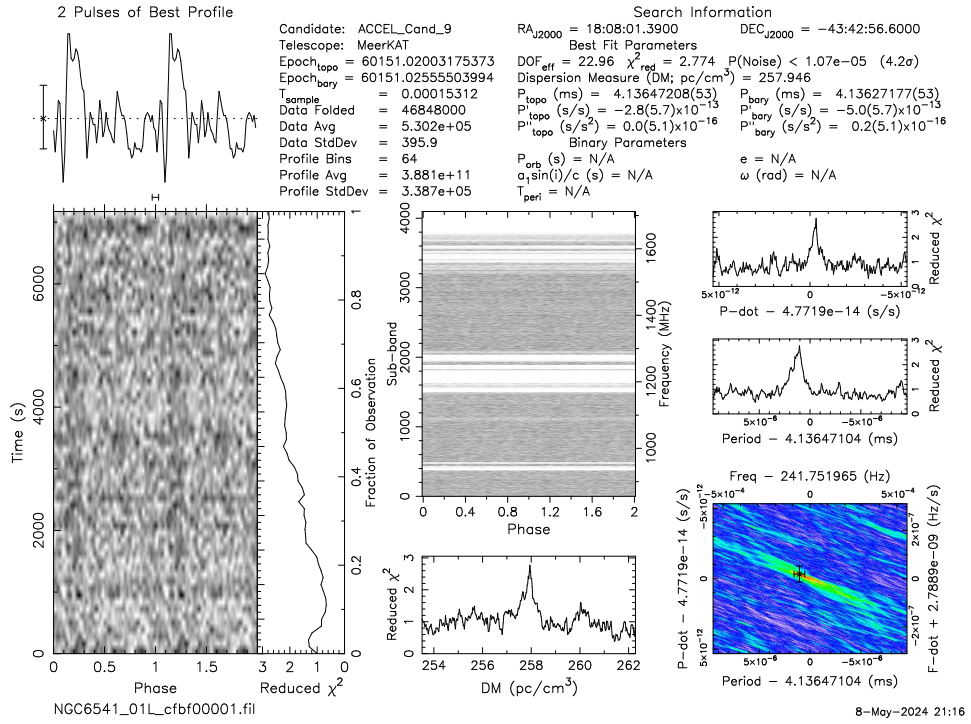

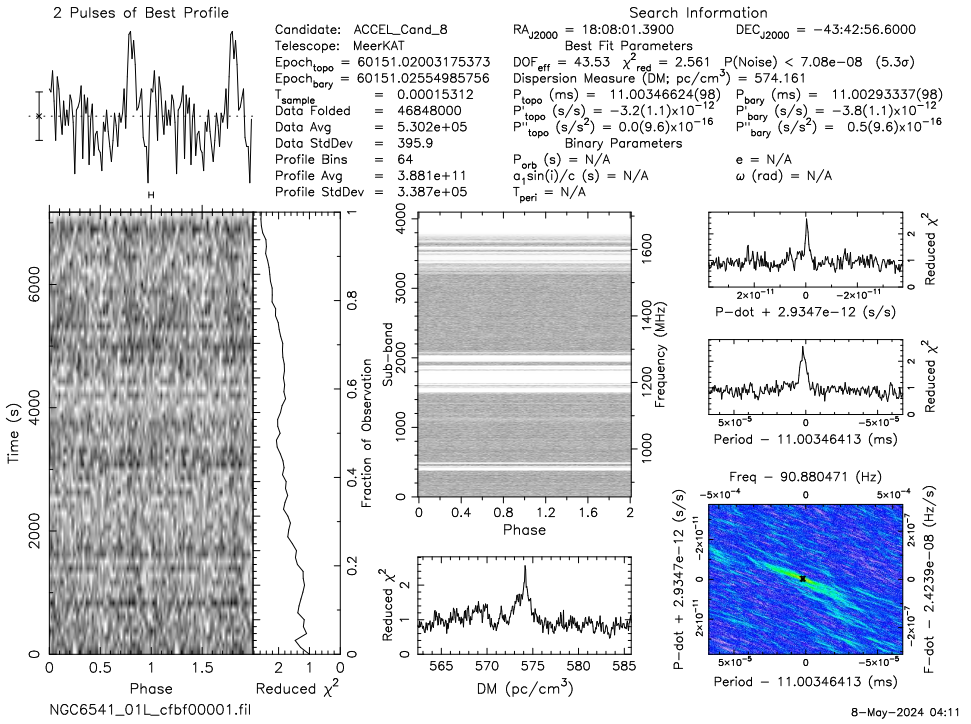

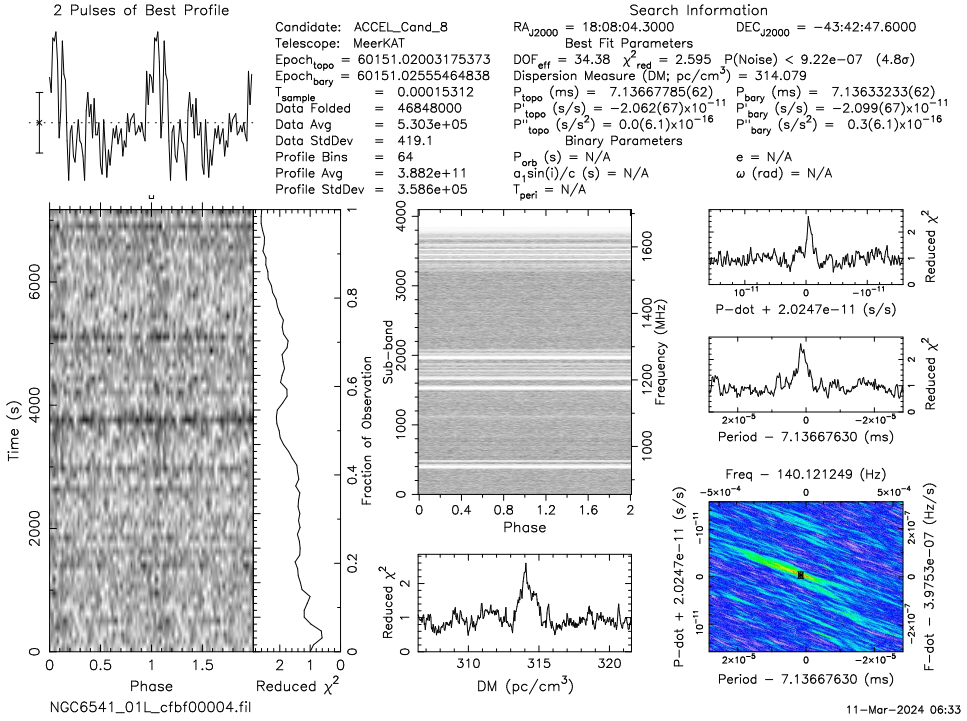
2 Pulses of Best Profile
Search Information
Candidate: ACCEL_Cand_8
Telescope: MeerKAT
Epoch_topo = 60151.02003175373
Epoch_bary = 60151.02555464838
T_sample = 0.00015312
Data Folded = 46848000
Data Avg = 5.303e+05
Data StdDev = 419.1
Profile Bins = 64
Profile Avg = 3.882e+11
Profile StdDev = 3.586e+05
RA_J2000 = 18:08:04.3000
DEC_J2000 = −43:42:47.6000
Best Fit Parameters
DOF_eff = 34.38 χ²_red = 2.595 P(Noise) < 9.22e−07 (4.8σ)
Dispersion Measure (DM; pc/cm³) = 314.079
P_topo (ms) = 7.13667785(62) P_bary (ms) = 7.13633233(62)
P'_topo (s/s) = −2.062(67)x10⁻¹¹ P'_bary (s/s) = −2.099(67)x10⁻¹¹
P''_topo (s/s²) = 0.0(6.1)x10⁻¹⁶ P''_bary (s/s²) = 0.3(6.1)x10⁻¹⁶
Binary Parameters
P_orb (s) = N/A e = N/A
a_1sin(i)/c (s) = N/A ω (rad) = N/A
T_peri = N/A
Time (s)
Phase
Reduced χ²
Fraction of Observation
Sub-band
Frequency (MHz)
DM (pc/cm³)
P−dot + 2.0247e−11 (s/s)
Period − 7.13667630 (ms)
Freq − 140.121249 (Hz)
F−dot − 3.9753e−07 (Hz/s)
NGC6541_01L_cfbf00004.fil
11−Mar−2024 06:33

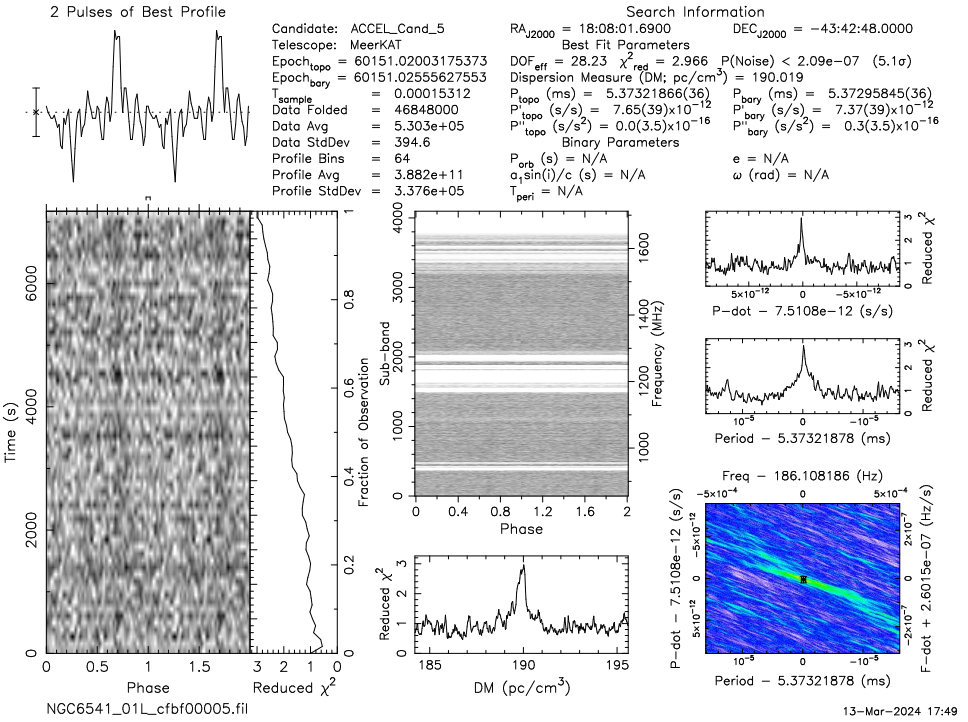
2 Pulses of Best Profile
Search Information
Candidate: ACCEL_Cand_5
Telescope: MeerKAT
Epoch_topo = 60151.02003175373
Epoch_bary = 60151.02555627553
T_sample = 0.00015312
Data Folded = 46848000
Data Avg = 5.303e+05
Data StdDev = 394.6
Profile Bins = 64
Profile Avg = 3.882e+11
Profile StdDev = 3.376e+05
RA_J2000 = 18:08:01.6900
DEC_J2000 = −43:42:48.0000
Best Fit Parameters
DOF_eff = 28.23 χ²_red = 2.966 P(Noise) < 2.09e−07 (5.1σ)
Dispersion Measure (DM; pc/cm³) = 190.019
P_topo (ms) = 5.37321866(36) P_bary (ms) = 5.37295845(36)
P'_topo (s/s) = 7.65(39)x10⁻¹² P'_bary (s/s) = 7.37(39)x10⁻¹²
P''_topo (s/s²) = 0.0(3.5)x10⁻¹⁶ P''_bary (s/s²) = 0.3(3.5)x10⁻¹⁶
Binary Parameters
P_orb (s) = N/A e = N/A
a_1sin(i)/c (s) = N/A ω (rad) = N/A
T_peri = N/A
Time (s)
Phase
Reduced χ²
Fraction of Observation
Sub-band
Frequency (MHz)
DM (pc/cm³)
P−dot − 7.5108e−12 (s/s)
Period − 5.37321878 (ms)
Freq − 186.108186 (Hz)
F−dot + 2.6015e−07 (Hz/s)
NGC6541_01L_cfbf00005.fil
13−Mar−2024 17:49

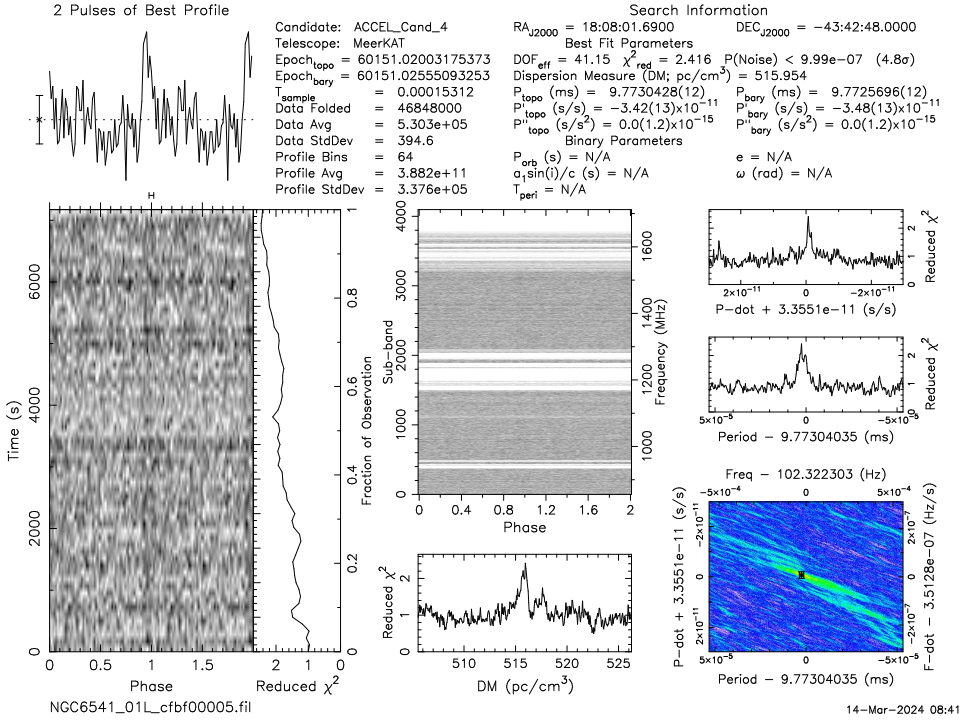
2 Pulses of Best Profile
Search Information
Candidate: ACCEL_Cand_4
Telescope: MeerKAT
Epoch_topo = 60151.02003175373
Epoch_bary = 60151.02555093253
T_sample = 0.00015312
Data Folded = 46848000
Data Avg = 5.303e+05
Data StdDev = 394.6
Profile Bins = 64
Profile Avg = 3.882e+11
Profile StdDev = 3.376e+05
RA_J2000 = 18:08:01.6900
DEC_J2000 = −43:42:48.0000
Best Fit Parameters
DOF_eff = 41.15 χ²_red = 2.416 P(Noise) < 9.99e−07 (4.8σ)
Dispersion Measure (DM; pc/cm³) = 515.954
P_topo (ms) = 9.7730428(12)
P_bary (ms) = 9.7725696(12)
P'_topo (s/s) = −3.42(13)x10⁻¹¹
P'_bary (s/s) = −3.48(13)x10⁻¹¹
P''_topo (s/s²) = 0.0(1.2)x10⁻¹⁵
P''_bary (s/s²) = 0.0(1.2)x10⁻¹⁵
Binary Parameters
P_orb (s) = N/A
e = N/A
a_1sin(i)/c (s) = N/A
ω (rad) = N/A
T_peri = N/A
Time (s)
Phase
Reduced χ²
Fraction of Observation
Sub-band
Frequency (MHz)
DM (pc/cm³)
P-dot + 3.3551e−11 (s/s)
Period − 9.77304035 (ms)
Freq − 102.322303 (Hz)
F-dot − 3.5128e−07 (Hz/s)
NGC6541_01L_cfbf00005.fil
14−Mar−2024 08:41

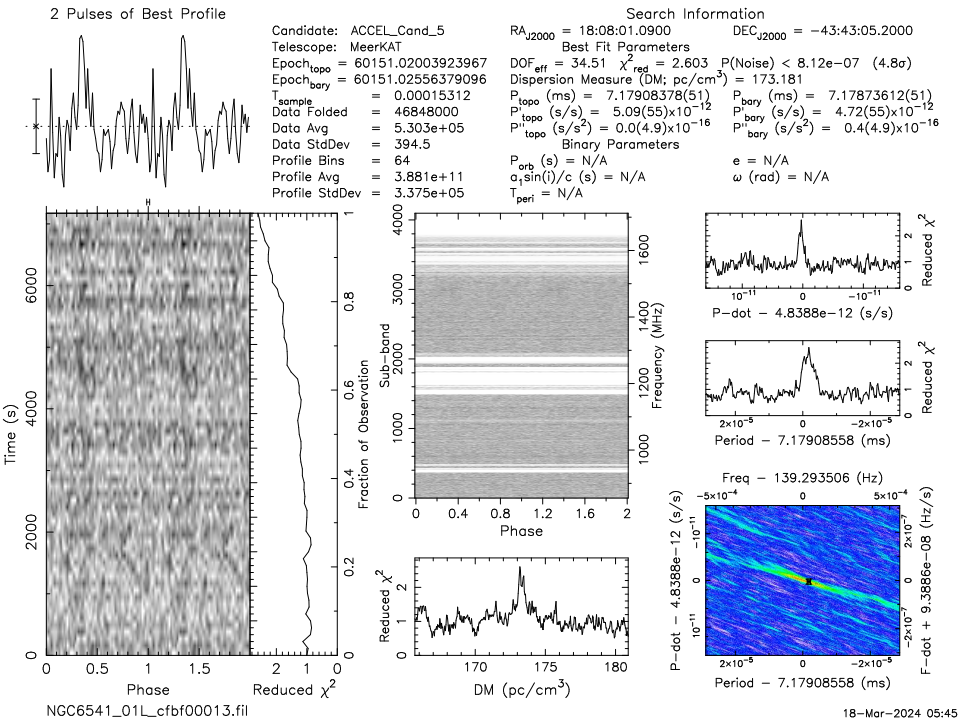
2 Pulses of Best Profile
Search Information
Candidate: ACCEL_Cand_5
Telescope: MeerKAT
Epoch_topo = 60151.02003923967
Epoch_bary = 60151.02556379096
T_sample = 0.00015312
Data Folded = 46848000
Data Avg = 5.303e+05
Data StdDev = 394.5
Profile Bins = 64
Profile Avg = 3.881e+11
Profile StdDev = 3.375e+05
RA_J2000 = 18:08:01.0900
DEC_J2000 = −43:43:05.2000
Best Fit Parameters
DOF_eff = 34.51 χ²_red = 2.603 P(Noise) < 8.12e−07 (4.8σ)
Dispersion Measure (DM; pc/cm³) = 173.181
P_topo (ms) = 7.17908378(51)
P_bary (ms) = 7.17873612(51)
P'_topo (s/s) = 5.09(55)x10⁻¹²
P'_bary (s/s) = 4.72(55)x10⁻¹²
P''_topo (s/s²) = 0.0(4.9)x10⁻¹⁶
P''_bary (s/s²) = 0.4(4.9)x10⁻¹⁶
Binary Parameters
P_orb (s) = N/A
e = N/A
a_1sin(i)/c (s) = N/A
ω (rad) = N/A
T_peri = N/A
Time (s)
Phase
Reduced χ²
Fraction of Observation
Sub-band
Frequency (MHz)
DM (pc/cm³)
P-dot − 4.8388e−12 (s/s)
Period − 7.17908558 (ms)
Freq − 139.293506 (Hz)
F-dot + 9.3886e−08 (Hz/s)
NGC6541_01L_cfbf00013.fil
18−Mar−2024 05:45

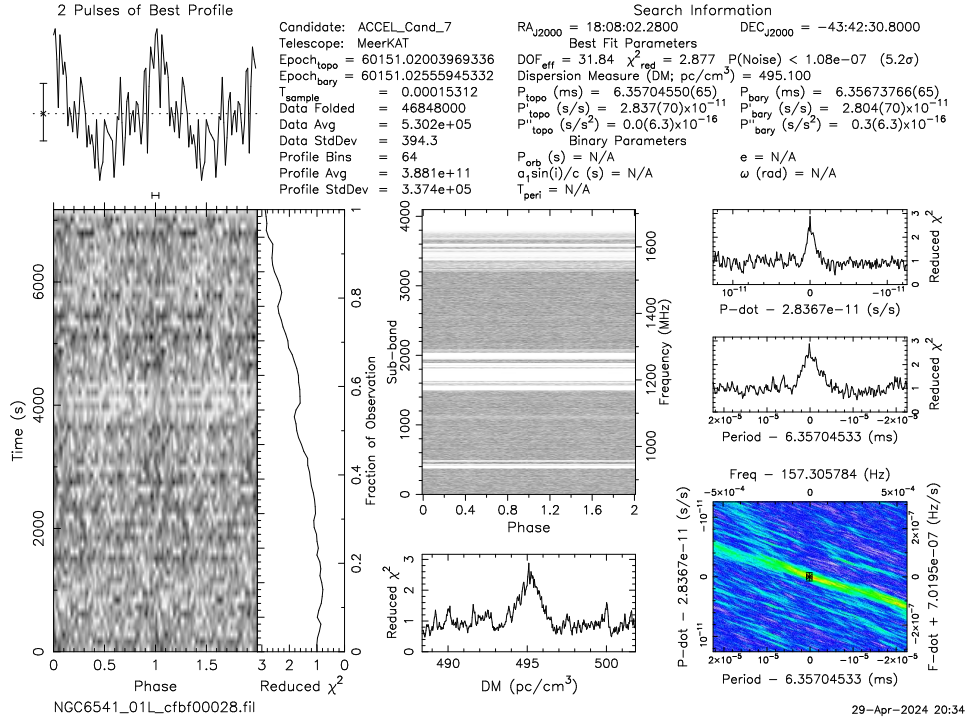
2 Pulses of Best Profile
Search Information
Candidate: ACCEL_Cand_7
Telescope: MeerKAT
Epoch_topo = 60151.02003969336
Epoch_bary = 60151.02555945332
T_sample = 0.00015312
Data Folded = 46848000
Data Avg = 5.302e+05
Data StdDev = 394.3
Profile Bins = 64
Profile Avg = 3.881e+11
Profile StdDev = 3.374e+05
RA_J2000 = 18:08:02.2800
DEC_J2000 = −43:42:30.8000
Best Fit Parameters
DOF_eff = 31.84 χ²_red = 2.877 P(Noise) < 1.08e−07 (5.2σ)
Dispersion Measure (DM; pc/cm³) = 495.100
P_topo (ms) = 6.35704550(65)
P_bary (ms) = 6.35673766(65)
P'_topo (s/s) = 2.837(70)x10⁻¹¹
P'_bary (s/s) = 2.804(70)x10⁻¹¹
P''_topo (s/s²) = 0.0(6.3)x10⁻¹⁶
P''_bary (s/s²) = 0.3(6.3)x10⁻¹⁶
Binary Parameters
P_orb (s) = N/A
e = N/A
a_1sin(i)/c (s) = N/A
ω (rad) = N/A
T_peri = N/A
Time (s)
Phase
Reduced χ²
Fraction of Observation
Sub-band
Frequency (MHz)
DM (pc/cm³)
P−dot − 2.8367e−11 (s/s)
Period − 6.35704533 (ms)
Freq − 157.305784 (Hz)
F−dot + 7.0195e−07 (Hz/s)
NGC6541_01L_cfbf00028.fil
29−Apr−2024 20:34

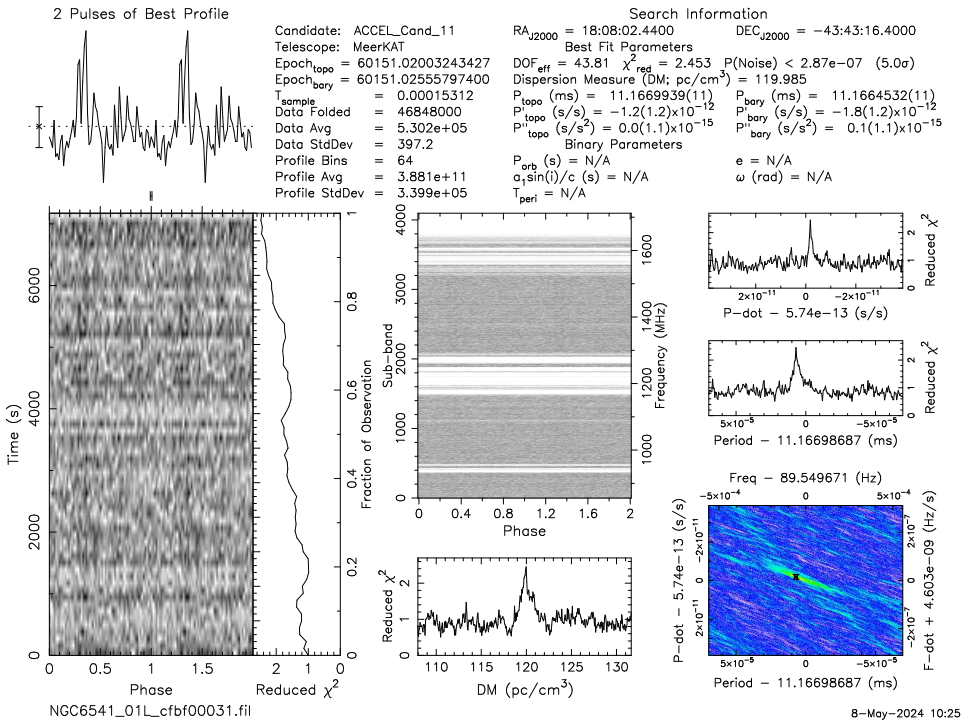
2 Pulses of Best Profile
Search Information
Candidate: ACCEL_Cand_11
Telescope: MeerKAT
Epoch_topo = 60151.02003243427
Epoch_bary = 60151.02555797400
T_sample = 0.00015312
Data Folded = 46848000
Data Avg = 5.302e+05
Data StdDev = 397.2
Profile Bins = 64
Profile Avg = 3.881e+11
Profile StdDev = 3.399e+05
RA_J2000 = 18:08:02.4400
DEC_J2000 = −43:43:16.4000
Best Fit Parameters
DOF_eff = 43.81 χ²_red = 2.453 P(Noise) < 2.87e−07 (5.0σ)
Dispersion Measure (DM; pc/cm³) = 119.985
P_topo (ms) = 11.1669939(11)
P_bary (ms) = 11.1664532(11)
P'_topo (s/s) = −1.2(1.2)x10⁻¹²
P'_bary (s/s) = −1.8(1.2)x10⁻¹²
P''_topo (s/s²) = 0.0(1.1)x10⁻¹⁵
P''_bary (s/s²) = 0.1(1.1)x10⁻¹⁵
Binary Parameters
P_orb (s) = N/A
e = N/A
a_1sin(i)/c (s) = N/A
ω (rad) = N/A
T_peri = N/A
Time (s)
Phase
Reduced χ²
Fraction of Observation
Sub-band
Frequency (MHz)
DM (pc/cm³)
P−dot − 5.74e−13 (s/s)
Period − 11.16698687 (ms)
Freq − 89.549671 (Hz)
F−dot + 4.603e−09 (Hz/s)
NGC6541_01L_cfbf00031.fil
8−May−2024 10:25

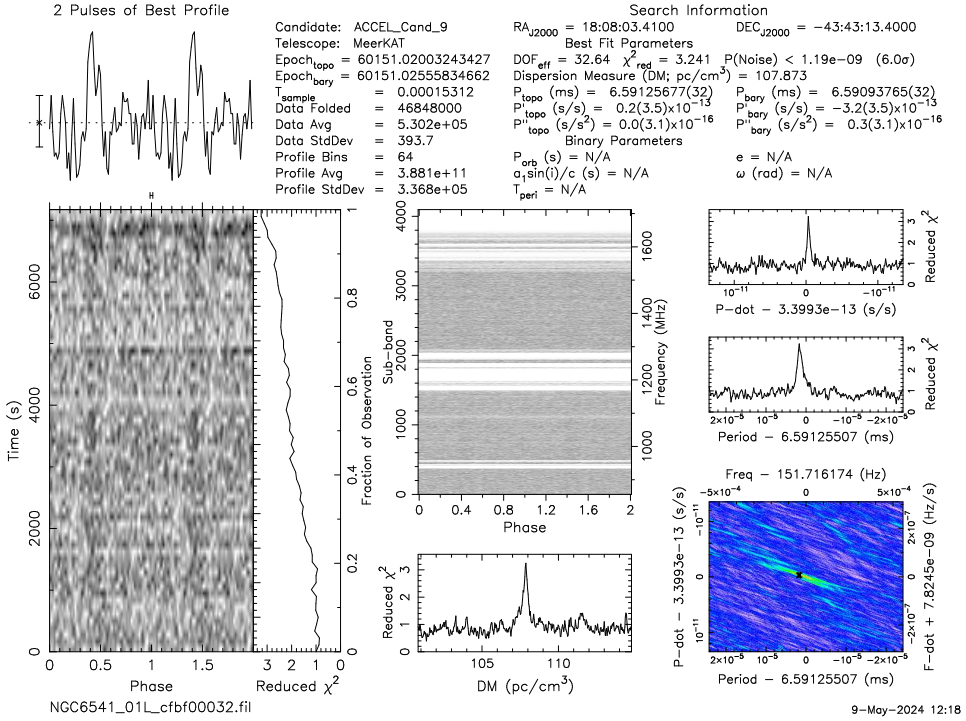
2 Pulses of Best Profile
Search Information
Candidate: ACCEL_Cand_9
Telescope: MeerKAT
Epoch_topo = 60151.02003243427
Epoch_bary = 60151.02555834662
T_sample = 0.00015312
Data Folded = 46848000
Data Avg = 5.302e+05
Data StdDev = 393.7
Profile Bins = 64
Profile Avg = 3.881e+11
Profile StdDev = 3.368e+05
RA_J2000 = 18:08:03.4100
DEC_J2000 = −43:43:13.4000
Best Fit Parameters
DOF_eff = 32.64 χ²_red = 3.241 P(Noise) < 1.19e−09 (6.0σ)
Dispersion Measure (DM; pc/cm³) = 107.873
P_topo (ms) = 6.59125677(32)
P_bary (ms) = 6.59093765(32)
P'_topo (s/s) = 0.2(3.5)x10⁻¹³
P'_bary (s/s) = −3.2(3.5)x10⁻¹³
P''_topo (s/s²) = 0.0(3.1)x10⁻¹⁶
P''_bary (s/s²) = 0.3(3.1)x10⁻¹⁶
Binary Parameters
P_orb (s) = N/A
e = N/A
a₁sin(i)/c (s) = N/A
ω (rad) = N/A
T_peri = N/A
Time (s)
Phase
Reduced χ²
Fraction of Observation
Sub-band
Frequency (MHz)
DM (pc/cm³)
P-dot − 3.3993e−13 (s/s)
Period − 6.59125507 (ms)
Freq − 151.716174 (Hz)
F-dot + 7.8245e−09 (Hz/s)
NGC6541_01L_cfbf00032.fil
9−May−2024 12:18

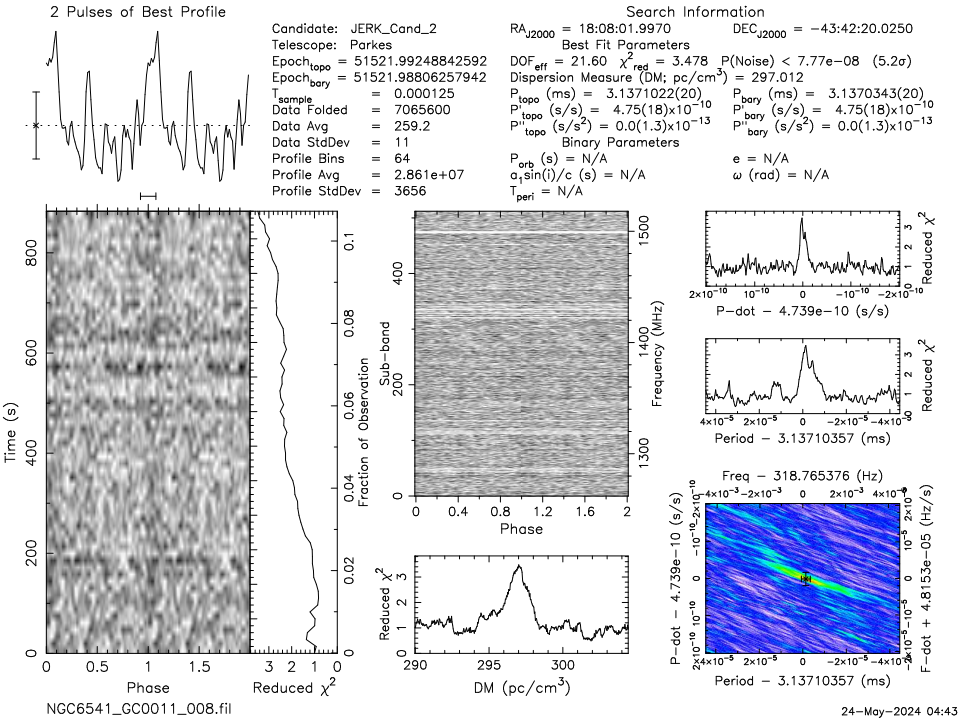
2 Pulses of Best Profile
Search Information
Candidate: JERK_Cand_2
Telescope: Parkes
Epoch_topo = 51521.99248842592
Epoch_bary = 51521.98806257942
T_sample = 0.000125
Data Folded = 7065600
Data Avg = 259.2
Data StdDev = 11
Profile Bins = 64
Profile Avg = 2.861e+07
Profile StdDev = 3656
RA_J2000 = 18:08:01.9970
DEC_J2000 = −43:42:20.0250
Best Fit Parameters
DOF_eff = 21.60 χ²_red = 3.478 P(Noise) < 7.77e−08 (5.2σ)
Dispersion Measure (DM; pc/cm³) = 297.012
P_topo (ms) = 3.1371022(20)
P_bary (ms) = 3.1370343(20)
P'_topo (s/s) = 4.75(18)x10⁻¹⁰
P'_bary (s/s) = 4.75(18)x10⁻¹⁰
P''_topo (s/s²) = 0.0(1.3)x10⁻¹³
P''_bary (s/s²) = 0.0(1.3)x10⁻¹³
Binary Parameters
P_orb (s) = N/A
e = N/A
a₁sin(i)/c (s) = N/A
ω (rad) = N/A
T_peri = N/A
Time (s)
Phase
Reduced χ²
Fraction of Observation
Sub-band
Frequency (MHz)
DM (pc/cm³)
P-dot − 4.739e−10 (s/s)
Period − 3.13710357 (ms)
Freq − 318.765376 (Hz)
F-dot + 4.8153e−05 (Hz/s)
NGC6541_GC0011_008.fil
24−May−2024 04:43

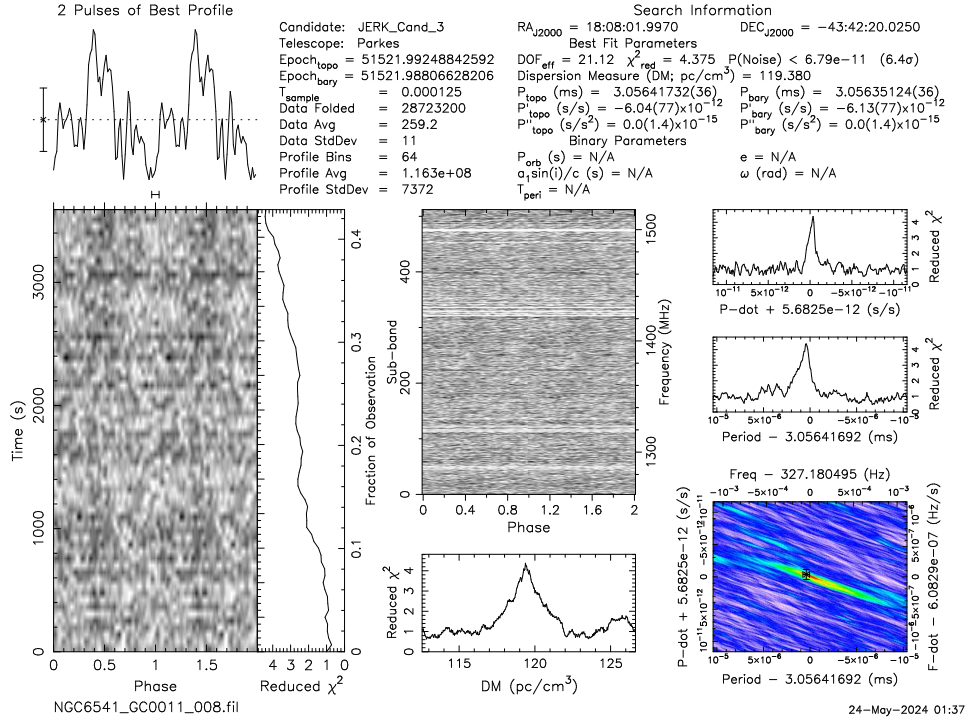
2 Pulses of Best Profile
Search Information
Candidate: JERK_Cand_3
Telescope: Parkes
Epoch_topo = 51521.99248842592
Epoch_bary = 51521.98806628206
T_sample = 0.000125
Data Folded = 28723200
Data Avg = 259.2
Data StdDev = 11
Profile Bins = 64
Profile Avg = 1.163e+08
Profile StdDev = 7372
RA_J2000 = 18:08:01.9970
DEC_J2000 = −43:42:20.0250
Best Fit Parameters
DOF_eff = 21.12 χ²_red = 4.375 P(Noise) < 6.79e−11 (6.4σ)
Dispersion Measure (DM; pc/cm³) = 119.380
P_topo (ms) = 3.05641732(36)
P_bary (ms) = 3.05635124(36)
P'_topo (s/s) = −6.04(77)x10⁻¹²
P'_bary (s/s) = −6.13(77)x10⁻¹²
P''_topo (s/s²) = 0.0(1.4)x10⁻¹⁵
P''_bary (s/s²) = 0.0(1.4)x10⁻¹⁵
Binary Parameters
P_orb (s) = N/A
e = N/A
a_1sin(i)/c (s) = N/A
ω (rad) = N/A
T_peri = N/A
Time (s)
Phase
Reduced χ²
Fraction of Observation
Sub-band
Frequency (MHz)
DM (pc/cm³)
P−dot + 5.6825e−12 (s/s)
Period − 3.05641692 (ms)
Freq − 327.180495 (Hz)
F−dot − 6.0829e−07 (Hz/s)
NGC6541_GC0011_008.fil
24−May−2024 01:37

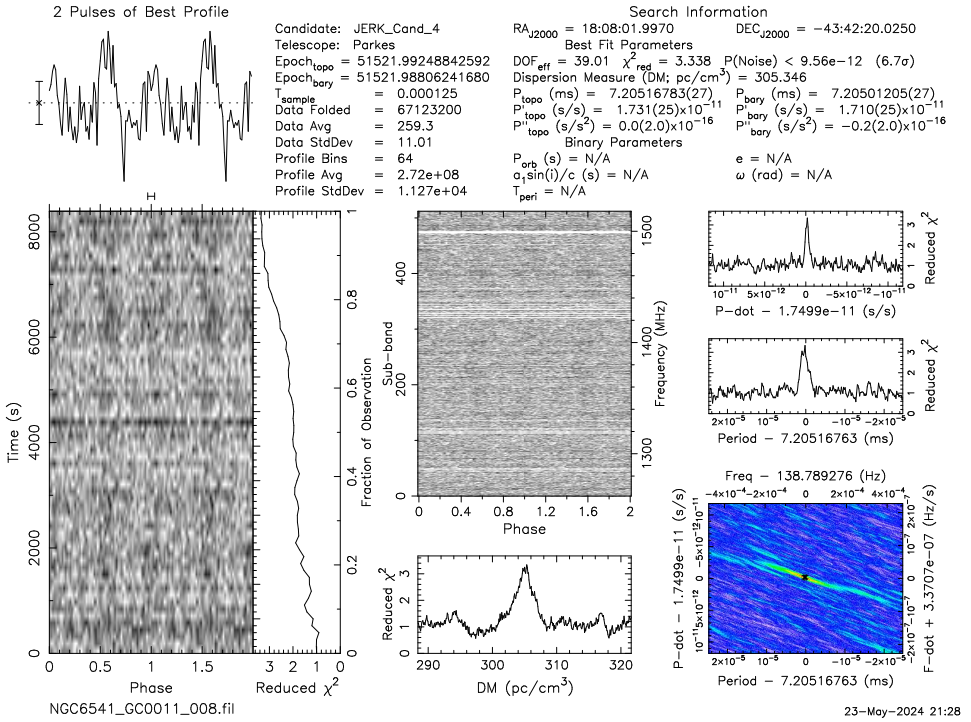
2 Pulses of Best Profile
Search Information
Candidate: JERK_Cand_4
Telescope: Parkes
Epoch_topo = 51521.99248842592
Epoch_bary = 51521.98806241680
T_sample = 0.000125
Data Folded = 67123200
Data Avg = 259.3
Data StdDev = 11.01
Profile Bins = 64
Profile Avg = 2.72e+08
Profile StdDev = 1.127e+04
RA_J2000 = 18:08:01.9970
DEC_J2000 = −43:42:20.0250
Best Fit Parameters
DOF_eff = 39.01 χ²_red = 3.338 P(Noise) < 9.56e−12 (6.7σ)
Dispersion Measure (DM; pc/cm³) = 305.346
P_topo (ms) = 7.20516783(27)
P_bary (ms) = 7.20501205(27)
P'_topo (s/s) = 1.731(25)x10⁻¹¹
P'_bary (s/s) = 1.710(25)x10⁻¹¹
P''_topo (s/s²) = 0.0(2.0)x10⁻¹⁶
P''_bary (s/s²) = −0.2(2.0)x10⁻¹⁶
Binary Parameters
P_orb (s) = N/A
e = N/A
a_1sin(i)/c (s) = N/A
ω (rad) = N/A
T_peri = N/A
Time (s)
Phase
Reduced χ²
Fraction of Observation
Sub-band
Frequency (MHz)
DM (pc/cm³)
P−dot − 1.7499e−11 (s/s)
Period − 7.20516763 (ms)
Freq − 138.789276 (Hz)
F−dot + 3.3707e−07 (Hz/s)
NGC6541_GC0011_008.fil
23−May−2024 21:28

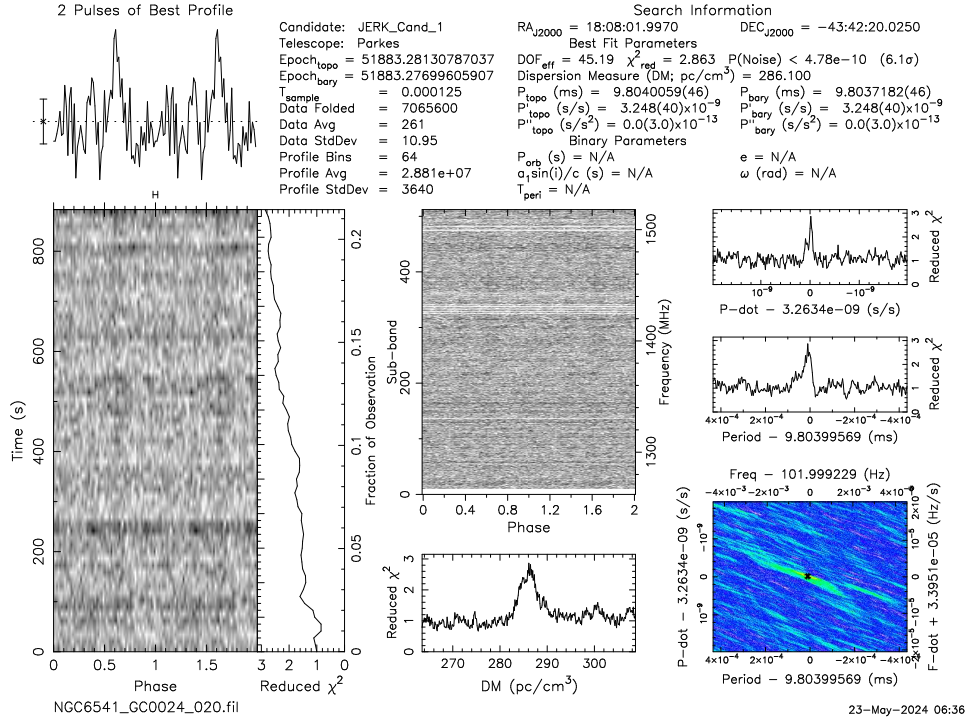
2 Pulses of Best Profile
Search Information
Candidate: JERK_Cand_1
Telescope: Parkes
Epoch_topo = 51883.28130787037
Epoch_bary = 51883.27699605907
T_sample = 0.000125
Data Folded = 7065600
Data Avg = 261
Data StdDev = 10.95
Profile Bins = 64
Profile Avg = 2.881e+07
Profile StdDev = 3640
RA_J2000 = 18:08:01.9970
DEC_J2000 = −43:42:20.0250
Best Fit Parameters
DOF_eff = 45.19 χ²_red = 2.863 P(Noise) < 4.78e−10 (6.1σ)
Dispersion Measure (DM; pc/cm³) = 286.100
P_topo (ms) = 9.8040059(46)
P_bary (ms) = 9.8037182(46)
P'_topo (s/s) = 3.248(40)x10⁻⁹
P'_bary (s/s) = 3.248(40)x10⁻⁹
P''_topo (s/s²) = 0.0(3.0)x10⁻¹³
P''_bary (s/s²) = 0.0(3.0)x10⁻¹³
Binary Parameters
P_orb (s) = N/A
e = N/A
a_1sin(i)/c (s) = N/A
ω (rad) = N/A
T_peri = N/A
Time (s)
Phase
Reduced χ²
Fraction of Observation
Sub-band
Frequency (MHz)
DM (pc/cm³)
P-dot − 3.2634e-09 (s/s)
Period − 9.80399569 (ms)
Freq − 101.999229 (Hz)
F-dot + 3.3951e-05 (Hz/s)
NGC6541_GC0024_020.fil
23-May-2024 06:36

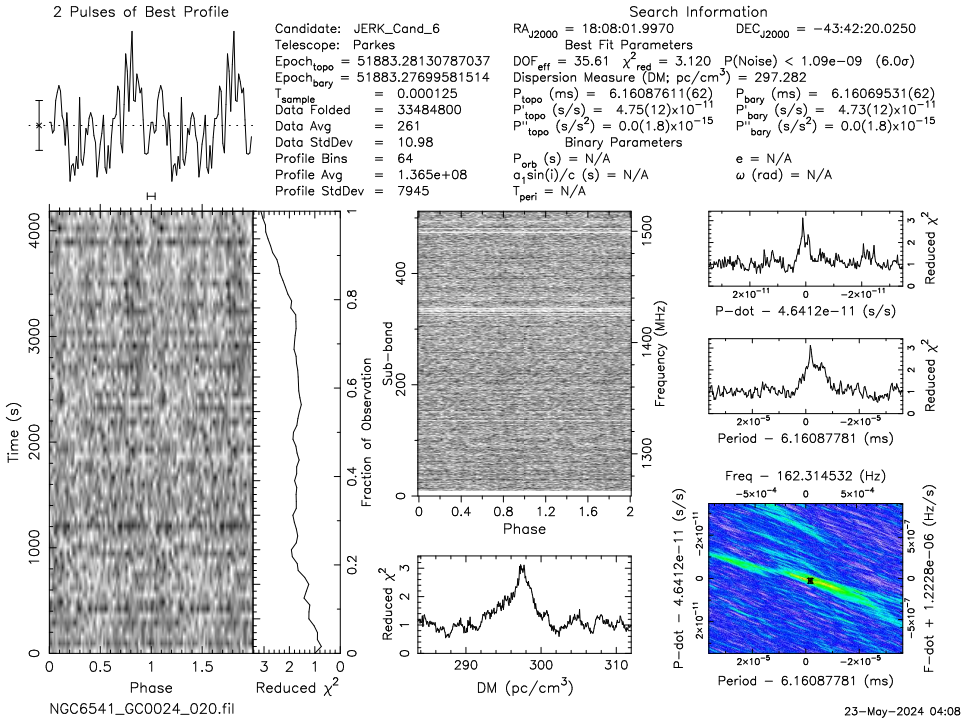
2 Pulses of Best Profile
Search Information
Candidate: JERK_Cand_6
Telescope: Parkes
Epoch_topo = 51883.28130787037
Epoch_bary = 51883.27699581514
T_sample = 0.000125
Data Folded = 33484800
Data Avg = 261
Data StdDev = 10.98
Profile Bins = 64
Profile Avg = 1.365e+08
Profile StdDev = 7945
RA_J2000 = 18:08:01.9970
DEC_J2000 = −43:42:20.0250
Best Fit Parameters
DOF_eff = 35.61 χ²_red = 3.120 P(Noise) < 1.09e−09 (6.0σ)
Dispersion Measure (DM; pc/cm³) = 297.282
P_topo (ms) = 6.16087611(62)
P_bary (ms) = 6.16069531(62)
P'_topo (s/s) = 4.75(12)x10⁻¹¹
P'_bary (s/s) = 4.73(12)x10⁻¹¹
P''_topo (s/s²) = 0.0(1.8)x10⁻¹⁵
P''_bary (s/s²) = 0.0(1.8)x10⁻¹⁵
Binary Parameters
P_orb (s) = N/A
e = N/A
a_1sin(i)/c (s) = N/A
ω (rad) = N/A
T_peri = N/A
Time (s)
Phase
Reduced χ²
Fraction of Observation
Sub-band
Frequency (MHz)
DM (pc/cm³)
P-dot − 4.6412e-11 (s/s)
Period − 6.16087781 (ms)
Freq − 162.314532 (Hz)
F-dot + 1.2228e-06 (Hz/s)
NGC6541_GC0024_020.fil
23-May-2024 04:08

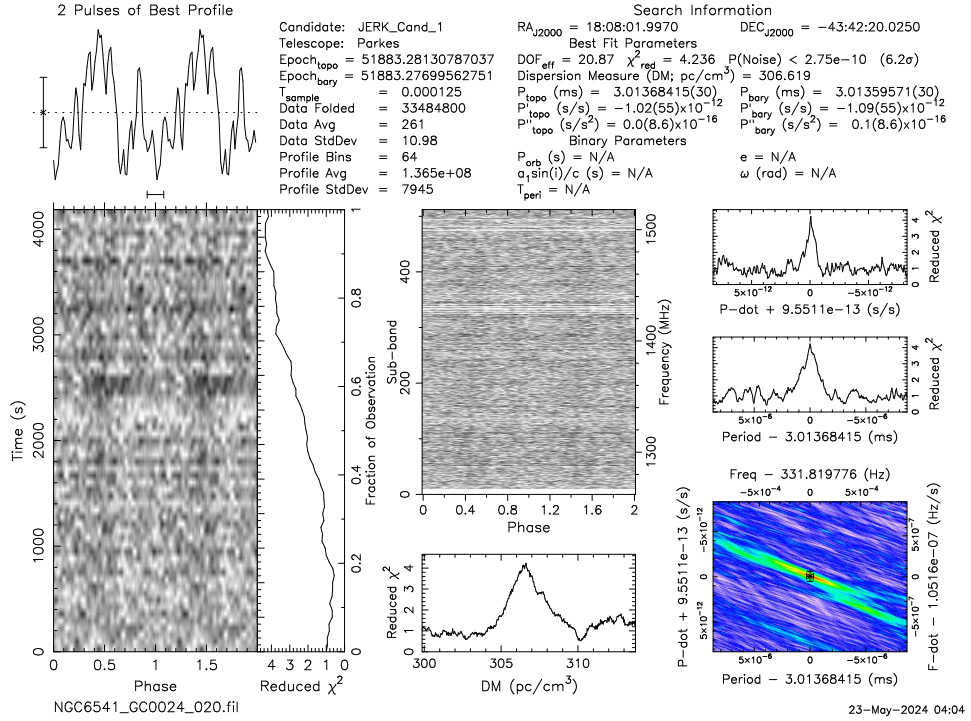
2 Pulses of Best Profile
Search Information
Candidate: JERK_Cand_1
Telescope: Parkes
Epoch_topo = 51883.28130787037
Epoch_bary = 51883.27699562751
T_sample = 0.000125
Data Folded = 33484800
Data Avg = 261
Data StdDev = 10.98
Profile Bins = 64
Profile Avg = 1.365e+08
Profile StdDev = 7945
RA_J2000 = 18:08:01.9970
DEC_J2000 = −43:42:20.0250
Best Fit Parameters
DOF_eff = 20.87 χ²_red = 4.236 P(Noise) < 2.75e−10 (6.2σ)
Dispersion Measure (DM; pc/cm³) = 306.619
P_topo (ms) = 3.01368415(30)
P_bary (ms) = 3.01359571(30)
P'_topo (s/s) = −1.02(55)x10⁻¹²
P'_bary (s/s) = −1.09(55)x10⁻¹²
P''_topo (s/s²) = 0.0(8.6)x10⁻¹⁶
P''_bary (s/s²) = 0.1(8.6)x10⁻¹⁶
Binary Parameters
P_orb (s) = N/A
e = N/A
a₁sin(i)/c (s) = N/A
ω (rad) = N/A
T_peri = N/A
Time (s)
Phase
Reduced χ²
Fraction of Observation
Sub-band
Frequency (MHz)
DM (pc/cm³)
P-dot + 9.5511e−13 (s/s)
Period − 3.01368415 (ms)
Freq − 331.819776 (Hz)
F-dot − 1.0516e−07 (Hz/s)
NGC6541_GC0024_020.fil
23−May−2024 04:04

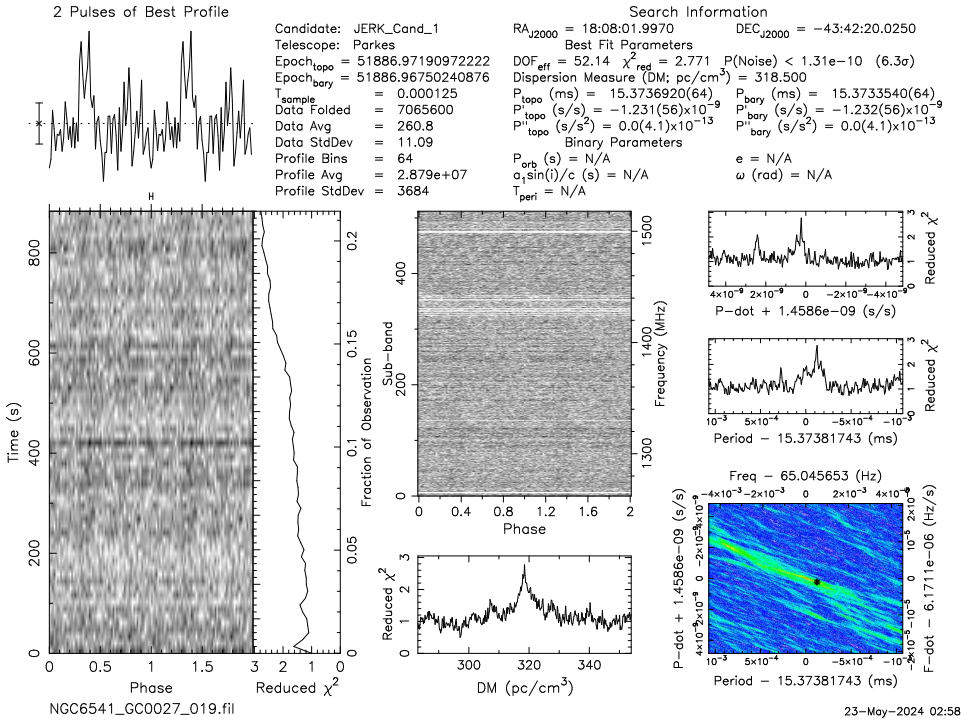
2 Pulses of Best Profile
Search Information
Candidate: JERK_Cand_1
Telescope: Parkes
Epoch_topo = 51886.97190972222
Epoch_bary = 51886.96750240876
T_sample = 0.000125
Data Folded = 7065600
Data Avg = 260.8
Data StdDev = 11.09
Profile Bins = 64
Profile Avg = 2.879e+07
Profile StdDev = 3684
RA_J2000 = 18:08:01.9970
DEC_J2000 = −43:42:20.0250
Best Fit Parameters
DOF_eff = 52.14 χ²_red = 2.771 P(Noise) < 1.31e−10 (6.3σ)
Dispersion Measure (DM; pc/cm³) = 318.500
P_topo (ms) = 15.3736920(64)
P_bary (ms) = 15.3733540(64)
P'_topo (s/s) = −1.231(56)x10⁻⁹
P'_bary (s/s) = −1.232(56)x10⁻⁹
P''_topo (s/s²) = 0.0(4.1)x10⁻¹³
P''_bary (s/s²) = 0.0(4.1)x10⁻¹³
Binary Parameters
P_orb (s) = N/A
e = N/A
a₁sin(i)/c (s) = N/A
ω (rad) = N/A
T_peri = N/A
Time (s)
Phase
Reduced χ²
Fraction of Observation
Sub-band
Frequency (MHz)
DM (pc/cm³)
P-dot + 1.4586e−09 (s/s)
Period − 15.37381743 (ms)
Freq − 65.045653 (Hz)
F-dot − 6.1711e−06 (Hz/s)
NGC6541_GC0027_019.fil
23−May−2024 02:58

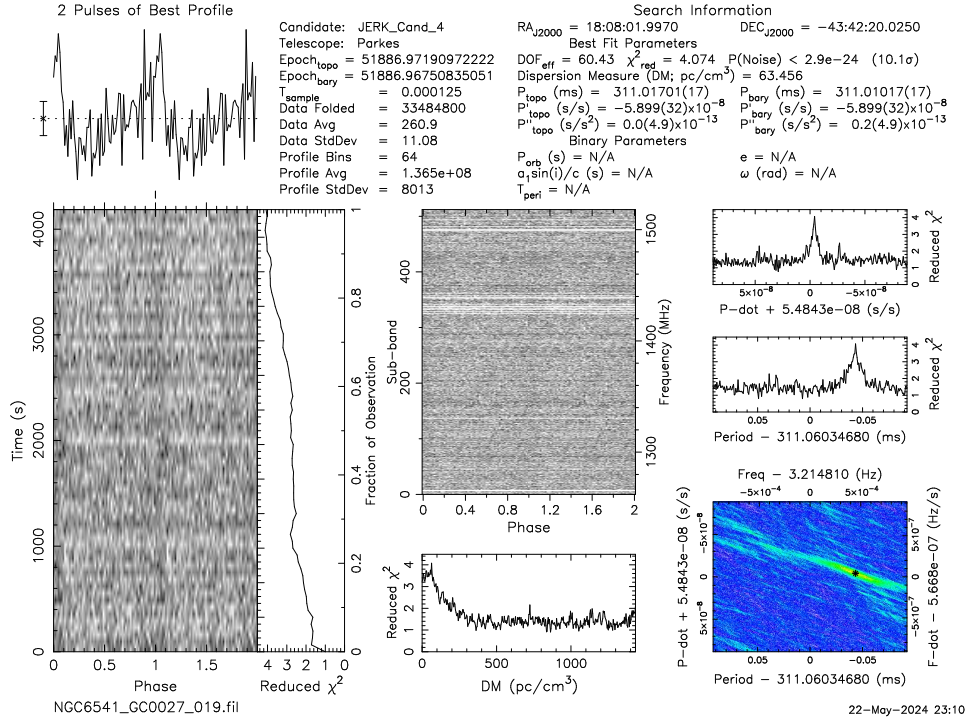
2 Pulses of Best Profile
Search Information
Candidate: JERK_Cand_4
Telescope: Parkes
Epoch_topo = 51886.97190972222
Epoch_bary = 51886.96750835051
T_sample = 0.000125
Data Folded = 33484800
Data Avg = 260.9
Data StdDev = 11.08
Profile Bins = 64
Profile Avg = 1.365e+08
Profile StdDev = 8013
RA_J2000 = 18:08:01.9970
DEC_J2000 = −43:42:20.0250
Best Fit Parameters
DOF_eff = 60.43 χ²_red = 4.074 P(Noise) < 2.9e−24 (10.1σ)
Dispersion Measure (DM; pc/cm³) = 63.456
P_topo (ms) = 311.01701(17)
P_bary (ms) = 311.01017(17)
P'_topo (s/s) = −5.899(32)x10⁻⁸
P'_bary (s/s) = −5.899(32)x10⁻⁸
P''_topo (s/s²) = 0.0(4.9)x10⁻¹³
P''_bary (s/s²) = 0.2(4.9)x10⁻¹³
Binary Parameters
P_orb (s) = N/A
e = N/A
a₁sin(i)/c (s) = N/A
ω (rad) = N/A
T_peri = N/A
Time (s)
Phase
Reduced χ²
Fraction of Observation
Sub-band
Frequency (MHz)
DM (pc/cm³)
P-dot + 5.4843e−08 (s/s)
Period − 311.06034680 (ms)
Freq − 3.214810 (Hz)
F-dot − 5.668e−07 (Hz/s)
NGC6541_GC0027_019.fil
22−May−2024 23:10

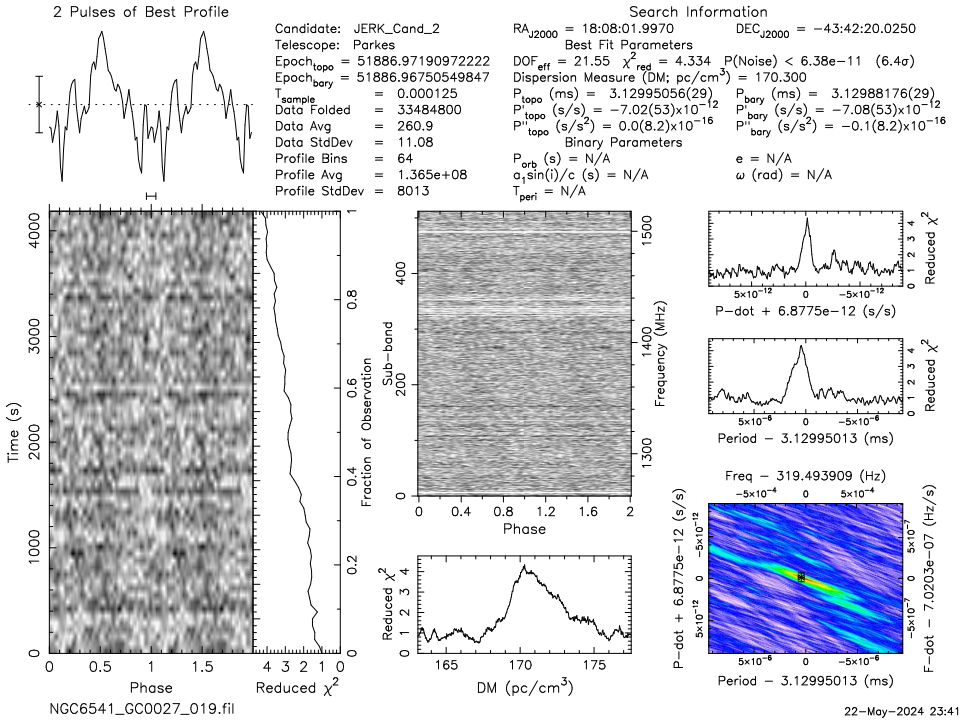
2 Pulses of Best Profile
Search Information
Candidate: JERK_Cand_2
Telescope: Parkes
Epoch_topo = 51886.97190972222
Epoch_bary = 51886.96750549847
T_sample = 0.000125
Data Folded = 33484800
Data Avg = 260.9
Data StdDev = 11.08
Profile Bins = 64
Profile Avg = 1.365e+08
Profile StdDev = 8013
RA_J2000 = 18:08:01.9970
DEC_J2000 = −43:42:20.0250
Best Fit Parameters
DOF_eff = 21.55 χ²_red = 4.334 P(Noise) < 6.38e−11 (6.4σ)
Dispersion Measure (DM; pc/cm³) = 170.300
P_topo (ms) = 3.12995056(29)
P_bary (ms) = 3.12988176(29)
P'_topo (s/s) = −7.02(53)x10⁻¹²
P'_bary (s/s) = −7.08(53)x10⁻¹²
P''_topo (s/s²) = 0.0(8.2)x10⁻¹⁶
P''_bary (s/s²) = −0.1(8.2)x10⁻¹⁶
Binary Parameters
P_orb (s) = N/A
e = N/A
a₁sin(i)/c (s) = N/A
ω (rad) = N/A
T_peri = N/A
Time (s)
Phase
Reduced χ²
Fraction of Observation
Sub-band
Frequency (MHz)
DM (pc/cm³)
P-dot + 6.8775e−12 (s/s)
Period − 3.12995013 (ms)
Freq − 319.493909 (Hz)
F-dot − 7.0203e−07 (Hz/s)
NGC6541_GC0027_019.fil
22−May−2024 23:41

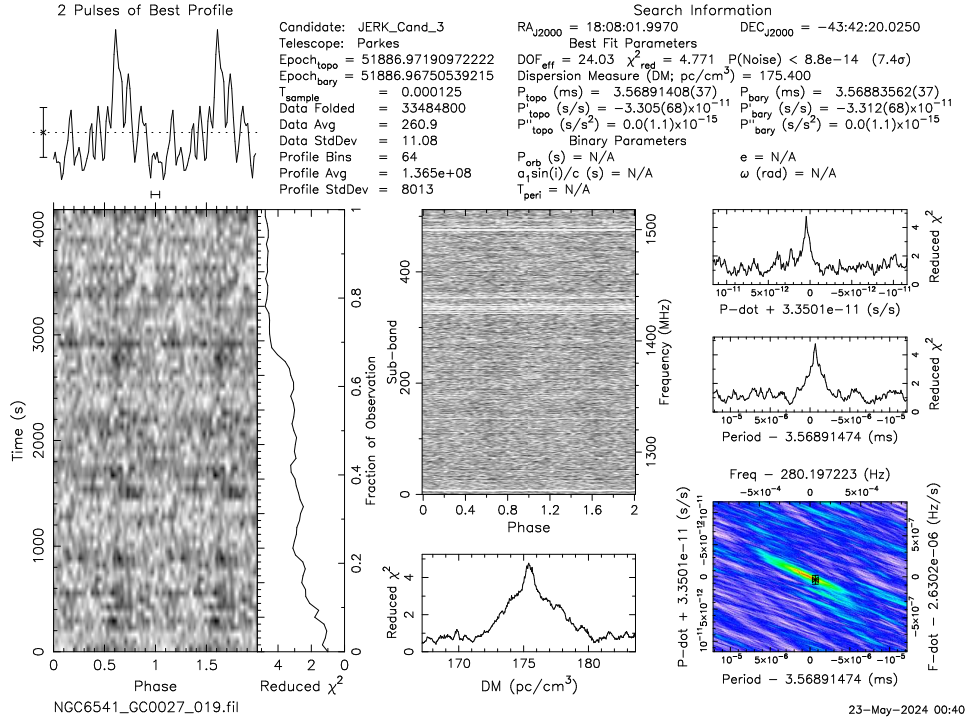
2 Pulses of Best Profile
Search Information
Candidate: JERK_Cand_3
Telescope: Parkes
Epoch_topo = 51886.97190972222
Epoch_bary = 51886.96750539215
T_sample = 0.000125
Data Folded = 33484800
Data Avg = 260.9
Data StdDev = 11.08
Profile Bins = 64
Profile Avg = 1.365e+08
Profile StdDev = 8013
RA_J2000 = 18:08:01.9970
DEC_J2000 = −43:42:20.0250
Best Fit Parameters
DOF_eff = 24.03 χ²_red = 4.771 P(Noise) < 8.8e−14 (7.4σ)
Dispersion Measure (DM; pc/cm³) = 175.400
P_topo (ms) = 3.56891408(37)
P_bary (ms) = 3.56883562(37)
P'_topo (s/s) = −3.305(68)x10⁻¹¹
P'_bary (s/s) = −3.312(68)x10⁻¹¹
P''_topo (s/s²) = 0.0(1.1)x10⁻¹⁵
P''_bary (s/s²) = 0.0(1.1)x10⁻¹⁵
Binary Parameters
P_orb (s) = N/A
e = N/A
a₁sin(i)/c (s) = N/A
ω (rad) = N/A
T_peri = N/A
Time (s)
Phase
Reduced χ²
Fraction of Observation
Sub-band
Frequency (MHz)
DM (pc/cm³)
P-dot + 3.3501e−11 (s/s)
Period − 3.56891474 (ms)
Freq − 280.197223 (Hz)
F-dot − 2.6302e−06 (Hz/s)
NGC6541_GC0027_019.fil
23−May−2024 00:40

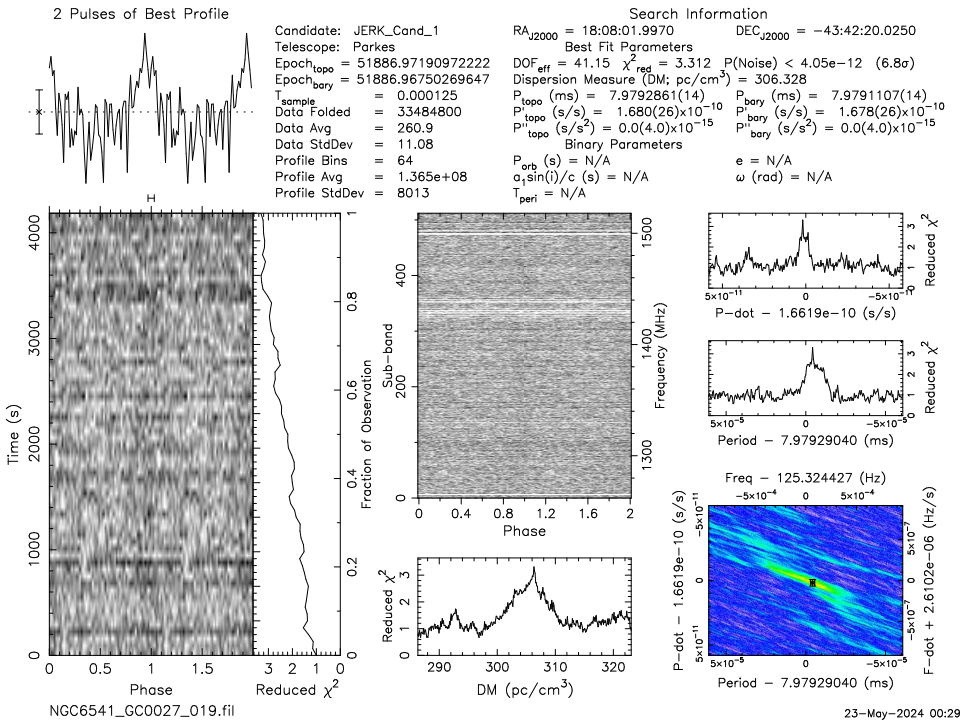
2 Pulses of Best Profile
Search Information
Candidate: JERK_Cand_1
Telescope: Parkes
Epoch_topo = 51886.97190972222
Epoch_bary = 51886.96750269647
T_sample = 0.000125
Data Folded = 33484800
Data Avg = 260.9
Data StdDev = 11.08
Profile Bins = 64
Profile Avg = 1.365e+08
Profile StdDev = 8013
RA_J2000 = 18:08:01.9970
DEC_J2000 = −43:42:20.0250
Best Fit Parameters
DOF_eff = 41.15 χ²_red = 3.312 P(Noise) < 4.05e−12 (6.8σ)
Dispersion Measure (DM; pc/cm³) = 306.328
P_topo (ms) = 7.9792861(14)
P_bary (ms) = 7.9791107(14)
P'_topo (s/s) = 1.680(26)x10⁻¹⁰
P'_bary (s/s) = 1.678(26)x10⁻¹⁰
P''_topo (s/s²) = 0.0(4.0)x10⁻¹⁵
P''_bary (s/s²) = 0.0(4.0)x10⁻¹⁵
Binary Parameters
P_orb (s) = N/A
e = N/A
a₁sin(i)/c (s) = N/A
ω (rad) = N/A
T_peri = N/A
Time (s)
Phase
Reduced χ²
Fraction of Observation
Sub-band
Frequency (MHz)
DM (pc/cm³)
P-dot − 1.6619e−10 (s/s)
Period − 7.97929040 (ms)
Freq − 125.324427 (Hz)
F-dot + 2.6102e−06 (Hz/s)
NGC6541_GC0027_019.fil
23−May−2024 00:29

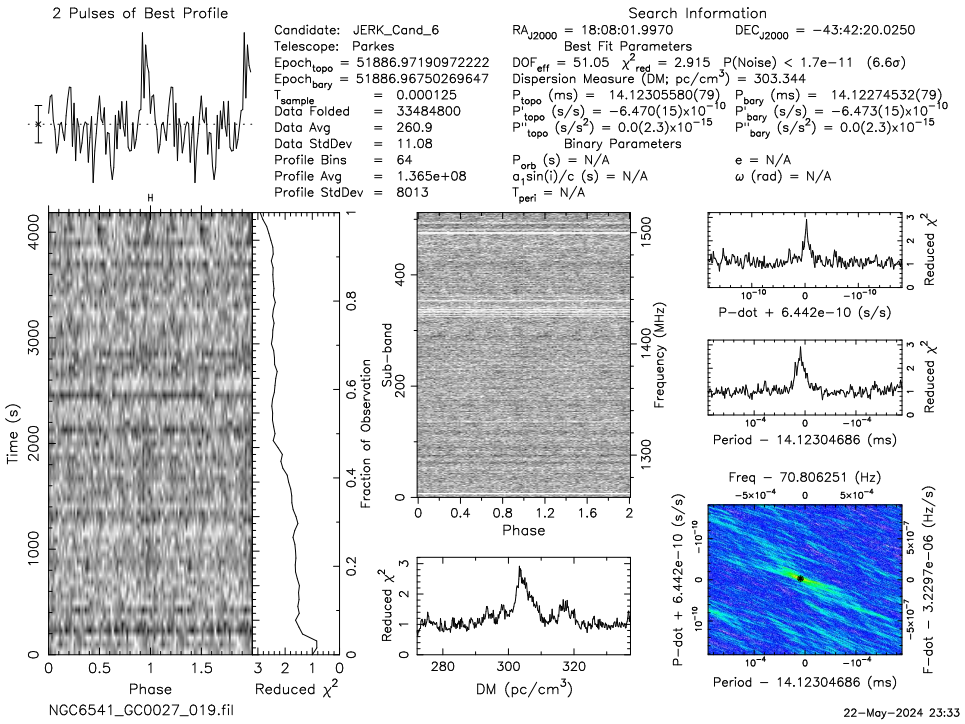
2 Pulses of Best Profile
Search Information
Candidate: JERK_Cand_6
Telescope: Parkes
Epoch_topo = 51886.97190972222
Epoch_bary = 51886.96750269647
T_sample = 0.000125
Data Folded = 33484800
Data Avg = 260.9
Data StdDev = 11.08
Profile Bins = 64
Profile Avg = 1.365e+08
Profile StdDev = 8013
RA_J2000 = 18:08:01.9970
DEC_J2000 = −43:42:20.0250
Best Fit Parameters
DOF_eff = 51.05 χ²_red = 2.915 P(Noise) < 1.7e−11 (6.6σ)
Dispersion Measure (DM; pc/cm³) = 303.344
P_topo (ms) = 14.12305580(79)
P_bary (ms) = 14.12274532(79)
P'_topo (s/s) = −6.470(15)x10⁻¹⁰
P'_bary (s/s) = −6.473(15)x10⁻¹⁰
P''_topo (s/s²) = 0.0(2.3)x10⁻¹⁵
P''_bary (s/s²) = 0.0(2.3)x10⁻¹⁵
Binary Parameters
P_orb (s) = N/A
e = N/A
a₁sin(i)/c (s) = N/A
ω (rad) = N/A
T_peri = N/A
Time (s)
Phase
Reduced χ²
Fraction of Observation
Sub-band
Frequency (MHz)
DM (pc/cm³)
P−dot + 6.442e−10 (s/s)
Period − 14.12304686 (ms)
Freq − 70.806251 (Hz)
F−dot − 3.2297e−06 (Hz/s)
NGC6541_GC0027_019.fil
22−May−2024 23:33

A.10 Best candidate pulsars found in NGC 6584

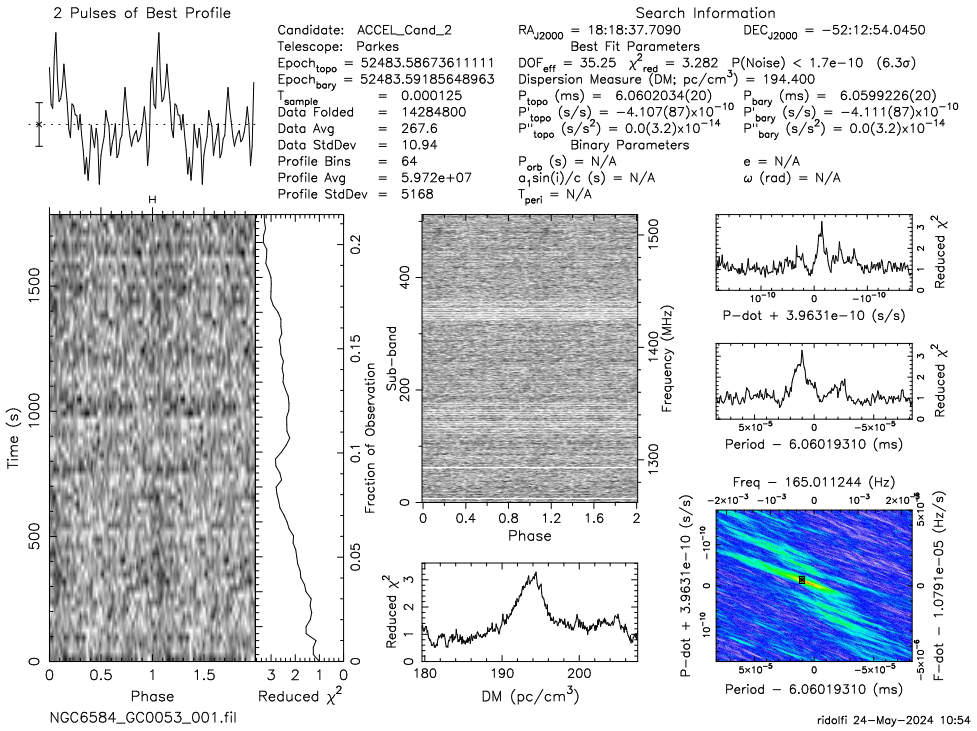

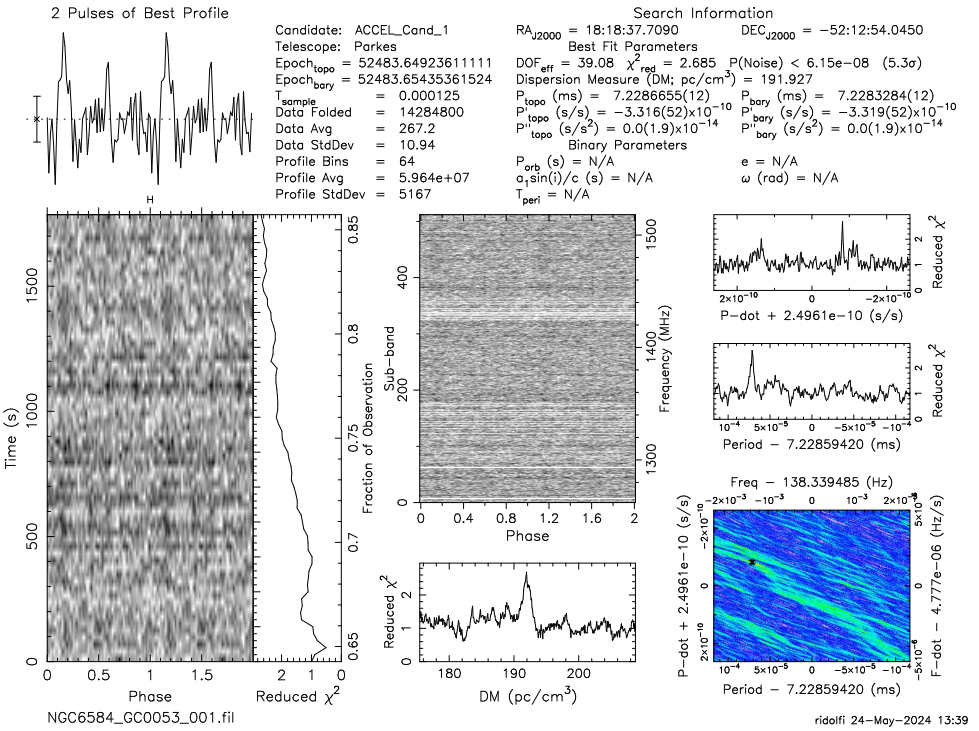

Bibliography

Abbate F., Possenti A., Ridolfi A., Freire P. C. C., Camilo F., Manchester R. N., D'Amico N., 2018, MNRAS, 481, 627 (Cited on page 29.)

Abbate F., Possenti A., Colpi M., Spera M., 2019, ApJ, 884, L9 (Cited on page 29.)

Abbate F., Possenti A., Tiburzi C., Barr E., van Straten W., Ridolfi A., Freire P., 2020, Nature Astronomy, 4, 704 (Cited on page 29.)

Abbott B. P., et al., 2016, Phys. Rev. Lett., 116, 061102 (Cited on page 28.)

Aggarwal K., et al., 2020, Journal of Open Source Software, 5, 2750 (Cited on page 70.)

Akeret J., Chang C., Lucchi A., Refregier A., 2017, Astronomy and Computing, 18, 35 (Cited on page 35.)

Allen B., et al., 2013, ApJ, 773, 91 (Cited on page 46.)

Andersen B. C., Ransom S. M., 2018, ApJ, 863, L13 (Cited on page 43.)

Andersen M., Gennaro M., Brandner W., Stolte A., de Marchi G., Meyer M. R., Zinnecker H., 2017, A&A, 602, A22 (Cited on page 65.)

Andrews H., Fenech D., Prinja R. K., Clark J. S., Hindson L., 2019, A&A, 632, A38 (Cited on page 75.)

Antoniadis J., et al., 2013, Science, 340, 448 (Cited on page 28.)

Archibald A. M., et al., 2009, Science, 324, 1411 (Cited on page 29.)

Arnett D., 1996, Supernovae and Nucleosynthesis (Cited on page 13.)

Baade W., Zwicky F., 1934, Proceedings of the National Academy of Science, 20, 259 (Cited on page 11.)

Bailes M., 2022, Science, 378, abj3043 (Cited on page 70.)

Balakrishnan V., Champion D., Barr E., Kramer M., Venkatraman Krishnan V., Eatough R. P., Sengar R., Bailes M., 2022, MNRAS, 511, 1265 (Cited on pages 45 and 46.)

Balakrishnan V., et al., 2023, ApJ, 942, L35 (Cited on page 25.)

Barr E. D., 2018, in Weltevrede P., Perera B. B. P., Preston L. L., Sanidas S., eds, Vol. 337, Pulsar Astrophysics the Next Fifty Years. pp 175–178, doi:10.1017/S1743921317009036 (Cited on page 54.)

Barr E. D., et al., 2013, MNRAS, 435, 2234 (Cited on page 12.)

Barr E. D., et al., 2024, Science, 383, 275 (Cited on page 25.)

Barsdell B. R., Bailes M., Barnes D. G., Fluke C. J., 2012, MNRAS, 422, 379 (Cited on page 70.)

Beasor E. R., Smith N., Andrews J. E., 2023, ApJ, 952, 113 (Cited on page 76.)

Bhattacharya D., van den Heuvel E. P. J., 1991, Phys. Rep., 203, 1 (Cited on page 21.)

Burgay M., et al., 2003, Nature, 426, 531 (Cited on pages 28 and 49.)

Cadelano M., Ransom S. M., Freire P. C. C., Ferraro F. R., Hessels J. W. T., Lanzoni B., Pallanca C., Stairs I. H., 2018, ApJ, 855, 125 (Cited on page 48.)

Cameron A. D., Barr E. D., Champion D. J., Kramer M., Zhu W. W., 2017, MNRAS, 468, 1994 (Cited on page 47.)

Cameron A. D., et al., 2018, MNRAS, 475, L57 (Cited on page 62.)

Camilo F., 2018, Nature Astronomy, 2, 594 (Cited on page 51.)
Camilo F., Reynolds J., Johnston S., Halpern J. P., Ransom S. M., 2008, ApJ, 679, 681 (Cited on page 16.)
Camilo F., et al., 2016, ApJ, 820, 110 (Cited on page 21.)
Carli E., et al., 2024, MNRAS, 531, 2835 (Cited on page 25.)
Chandrasekhar S., 1931, MNRAS, 91, 456 (Cited on page 14.)
Chandrasekhar S., 1935, MNRAS, 95, 207 (Cited on page 14.)
Chen K., Ruderman M., 1993, ApJ, 402, 264 (Cited on page 21.)
Chen W., Barr E., Karuppusamy R., Kramer M., Stappers B., 2021, Journal of Astronomical Instrumentation, 10, 2150013 (Cited on pages 26 and 54.)
Chen W., et al., 2023, MNRAS, 520, 3847 (Cited on page 63.)
Clark J. S., Negueruela I., Crowther P. A., Goodwin S. P., 2005, A&A, 434, 949 (Cited on pages 65 and 73.)
Colgate S. A., White R. H., 1966, ApJ, 143, 626 (Cited on page 11.)
Comella J. M., Craft H. D., Lovelace R. V. E., Sutton J. M., 1969, Nature, 221, 453 (Cited on page 12.)
Cooley J. W., Tukey J. W., 1965, Math. Comput., 19, 297 (Cited on page 37.)
Cordes J. M., Lazio T. J. W., 2002a, ArXiv Astrophysics e-prints, (Cited on pages 19 and 27.)
Cordes J. M., Lazio T. J. W., 2002b, arXiv e-prints, pp astro–ph/0207156 (Cited on page 68.)
Cordes J. M., Lazio T. J. W., 2003, ArXiv Astrophysics e-prints, (Cited on page 19.)
D'Amico N., Lyne A. G., Manchester R. N., Possenti A., Camilo F., 2001, ApJ, 548, L171 (Cited on page 44.)
Dai S., Johnston S., Kerr M., Camilo F., Cameron A., Toomey L., Kumamoto H., 2020, ApJ, 888, L18 (Cited on pages 49 and 63.)
Deller A. T., et al., 2012, ApJ, 756, L25 (Cited on page 27.)
Dewdney P. E., Hall P. J., Schilizzi R. T., Lazio T. J. L. W., 2009, IEEE Proceedings, 97, 1482 (Cited on page 51.)
Dewey R., Stokes G., Segelstein D., Taylor J., Weisberg J., 1984, in Reynolds S. P., Stinebring D. R., eds, Birth and Evolution of Neutron Stars: Issues Raised by Millisecond Pulsars. p. 234 (Cited on page 34.)
Douglas A., et al., 2022, ApJ, 927, 126 (Cited on pages 44 and 51.)
Duncan R. C., Thompson C., 1992, ApJ, 392, L9 (Cited on page 21.)
Edwards R. T., Hobbs G. B., Manchester R. N., 2006, MNRAS, 372, 1549 (Cited on page 71.)
Esposito P., et al., 2020, ApJ, 896, L30 (Cited on page 21.)
Fabian A. C., Pringle J. E., Rees M. J., 1975, MNRAS, 172, 15p (Cited on page 24.)
Falxa M., et al., 2023, MNRAS, 521, 5077 (Cited on page 28.)
Fenech D. M., et al., 2018, A&A, 617, A137 (Cited on page 75.)
Fowler W. A., Hoyle F., 1964, ApJS, 9, 201 (Cited on page 11.)
Frail D. A., Weisberg J. M., 1990, AJ, 100, 743 (Cited on page 69.)
Freire P. C., Kramer M., Lyne A. G., 2001, MNRAS, 322, 885 (Cited on page 29.)
Freire P. C. C., et al., 2012, MNRAS, 423, 3328 (Cited on page 27.)

Freire P. C. C., et al., 2017, MNRAS, 471, 857 (Cited on page 29.)
Gennaro M., Goodwin S. P., Parker R. J., Allison R. J., Brandner W., 2017, MNRAS, 472, 1760 (Cited on page 74.)
Gold T., 1968, Nature, 218, 731 (Cited on page 12.)
Goldreich P., Julian W. H., 1969, ApJ, 157, 869 (Cited on page 14.)
Graber V., Ronchi M., Pardo-Araujo C., Rea N., 2023, arXiv e-prints, p. arXiv:2312.14848 (Cited on page 76.)
Han J. L., et al., 2021, Research in Astronomy and Astrophysics, 21, 107 (Cited on page 63.)
Harris W. E., 2010, arXiv e-prints, p. arXiv:1012.3224 (Cited on page 56.)
Hazard C., Mackey M. B., Shimmins A. J., 1963, Nature, 197, 1037 (Cited on page 49.)
Hessels J. W. T., Ransom S. M., Stairs I. H., Freire P. C. C., Kaspi V. M., Camilo F., 2006, Science, 311, 1901 (Cited on page 25.)
Hewish A., Bell S. J., Pilkington J. D. H., Scott P. F., Collins R. A., 1968, Nature, 217, 709 (Cited on page 12.)
Ho A., Ransom S. M., Demorest P., 2014, in American Astronomical Society Meeting Abstracts #223. p. 153.18 (Cited on page 29.)
Hobbs G., et al., 2020, PASA, 37, e012 (Cited on pages 35 and 63.)
Hotan A. W., van Straten W., Manchester R. N., 2004a, PASA, 21, 302 (Cited on page 34.)
Hotan A. W., van Straten W., Manchester R. N., 2004b, PASA, 21, 302 (Cited on page 68.)
Hoyle F., Narlikar J. V., Wheeler J. A., 1964, Nature, 203, 914 (Cited on page 11.)
Hulse R. A., Taylor J. H., 1975, ApJ, 195, L51 (Cited on page 28.)
Israel G. L., Campana S., Dall'Osso S., Muno M. P., Cummings J., Perna R., Stella L., 2007, ApJ, 664, 448 (Cited on page 68.)
Jackson J. D., 1962, Classical Electrodynamics (Cited on page 14.)
Johnston H. M., Kulkarni S. R., 1991, ApJ, 368, 504 (Cited on page 41.)
Jonas J., MeerKAT Team 2016, in MeerKAT Science: On the Pathway to the SKA. p. 1, doi:10.22323/1.277.0001 (Cited on page 51.)
Jouteux S., Ramachandran R., Stappers B. W., Jonker P. G., van der Klis M., 2002, A&A, 384, 532 (Cited on page 44.)
Kaspi V. M., Beloborodov A. M., 2017, ARA&A, 55, 261 (Cited on page 21.)
Keith M. J., et al., 2010, MNRAS, 409, 619 (Cited on page 12.)
Kijak J., Lewandowski W., Maron O., Gupta Y., Jessner A., 2011, A&A, 531, A16 (Cited on page 16.)
Knispel B., et al., 2013, ApJ, 774, 93 (Cited on page 46.)
Kocz J., Bailes M., Barnes D., Burke-Spolaor S., Levin L., 2012, MNRAS, 420, 271 (Cited on page 35.)
Komesaroff M. M., Ables J. G., Cooke D. J., Hamilton P. A., McCulloch P. M., 1973, Astrophys. Lett., 15, 169 (Cited on page 69.)
Kramer M., Xilouris K. M., Lorimer D. R., Doroshenko O., Jessner A., Wielebinski R., Wolszczan A., Camilo F., 1998, ApJ, 501, 270 (Cited on page 16.)
Kramer M., et al., 2021, Physical Review X, 11, 041050 (Cited on page 28.)

Krimm H., Barthelmy S., Campana S., Cummings J., Israel G., Palmer D., Parsons A., 2006, GRB Coordinates Network, 5581, 1 (Cited on page 65.)
Large M. I., Vaughan A. E., Mills B. Y., 1968, Nature, 220, 340 (Cited on page 12.)
Lattimer J. M., Prakash M., 2001, ApJ, 550, 426 (Cited on page 14.)
Lazarus P., et al., 2015, ApJ, 812, 81 (Cited on page 47.)
Lee K. J., et al., 2013, MNRAS, 433, 688 (Cited on page 39.)
Lorimer D. R., 2011, (Cited on pages 34 and 68.)
Lorimer D. R., Kramer M., 2004, Handbook of Pulsar Astronomy (Cited on pages 17, 19, 34, 36, 54, 71, 75 and 76.)
Lorimer D. R., Bailes M., McLaughlin M. A., Narkevic D. J., Crawford F., 2007, Science, 318, 777 (Cited on pages 48 and 49.)
Lyne A. G., et al., 2004, Science, 303, 1153 (Cited on page 28.)
Maan Y., van Leeuwen J., Vohl D., 2021, A&A, 650, A80 (Cited on page 35.)
Manchester R. N., 2013, Classical and Quantum Gravity, 30, 224010 (Cited on page 28.)
Manchester R. N., et al., 2001, MNRAS, 328, 17 (Cited on page 12.)
Manchester R. N., Hobbs G. B., Teoh A., Hobbs M., 2005, AJ, 129, 1993 (Cited on pages 12 and 19.)
Manchester R. N., Fan G., Lyne A. G., Kaspi V. M., Crawford F., 2006, ApJ, 649, 235 (Cited on page 25.)
Maron O., Kijak J., Kramer M., Wielebinski R., 2000, A&AS, 147, 195 (Cited on page 16.)
Martsen A. R., et al., 2022, ApJ, 941, 22 (Cited on page 29.)
McLaughlin M. A., et al., 2006, Nature, 439, 817 (Cited on page 48.)
Mereghetti S., et al., 2020, ApJ, 898, L29 (Cited on page 66.)
Middleditch J., Kristian J., 1984, ApJ, 279, 157 (Cited on page 42.)
Morello V., Barr E. D., Bailes M., Flynn C. M., Keane E. F., van Straten W., 2014, MNRAS, 443, 1651 (Cited on page 39.)
Morello V., et al., 2020a, MNRAS, 493, 1165 (Cited on page 46.)
Morello V., Barr E. D., Stappers B. W., Keane E. F., Lyne A. G., 2020b, MNRAS, 497, 4654 (Cited on pages 47 and 69.)
Morello V., Rajwade K. M., Stappers B. W., 2022, MNRAS, 510, 1393 (Cited on page 35.)
Muno M. P., et al., 2006, ApJ, 636, L41 (Cited on pages 65, 76 and 77.)
Muno M. P., Gaensler B. M., Clark J. S., de Grijs R., Pooley D., Stevens I. R., Portegies Zwart S. F., 2007, MNRAS, 378, L44 (Cited on page 65.)
Navarete F., Damineli A., Ramirez A. E., Rocha D. F., Almeida L. A., 2022, MNRAS, 516, 1289 (Cited on pages 65, 72, 73, 74 and 76.)
Nita G. M., Hellbourg G., 2020, in 2020 XXXIIIrd General Assembly and Scientific Symposium of the International Union of Radio Science. pp 1–4, doi:10.23919/URSIGASS49373.2020.9232200 (Cited on page 70.)
Noutsos A., Johnston S., Kramer M., Karastergiou A., 2008, MNRAS, 386, 1881 (Cited on page 29.)
Noutsos A., Schnitzeler D. H. F. M., Keane E. F., Kramer M., Johnston S., 2013, MNRAS, 430, 2281 (Cited on page 23.)

Olausen S. A., Kaspi V. M., 2014a,] 10.26093/cds/vizier.22120006, (Cited on page 77.)
Olausen S. A., Kaspi V. M., 2014b, ApJS, 212, 6 (Cited on page 21.)
Oppenheimer J. R., Volkoff G. M., 1939, Physical Review, 55, 374 (Cited on page 11.)
Pacini F., 1967, Nature, 216, 567 (Cited on page 11.)
Pan Z., Hobbs G., Li D., Ridolfi A., Wang P., Freire P., 2016, MNRAS, 459, L26 (Cited on page 47.)
Pan Z., et al., 2023, Nature, 620, 961 (Cited on page 63.)
Papitto A., et al., 2013, Nature, 501, 517 (Cited on pages 22 and 29.)
Parent E., et al., 2018, ApJ, 861, 44 (Cited on page 47.)
Petroff E., Hessels J. W. T., Lorimer D. R., 2022, A&A Rev., 30, 2 (Cited on page 70.)
Podsiadlowski P., Rappaport S., Pfahl E. D., 2002, ApJ, 565, 1107 (Cited on page 22.)
Portegies Zwart S. F., McMillan S. L. W., Gieles M., 2010, ARA&A, 48, 431 (Cited on page 65.)
Possenti A., D'Amico N., Manchester R. N., Camilo F., Lyne A. G., Sarkissian J., Corongiu A., 2003, ApJ, 599, 475 (Cited on page 49.)
Prager B., Ransom S., Freire P., Hessels J., Stairs I., Arras P., Cadelano M., 2016, preprint, (arXiv:1612.04395) (Cited on page 29.)
Press W. H., Teukolsky S. A., 1977, ApJ, 213, 183 (Cited on page 24.)
Press W. H., Teukolsky S. A., Vetterling W. T., Flannery B. P., 1992, Numerical recipes in FORTRAN. The art of scientific computing (Cited on page 37.)
Price D. C., Flynn C., Deller A., 2021, PASA, 38, e038 (Cited on pages 56 and 68.)
Radhakrishnan V., Srinivasan G., 1982, Current Science, 51, 1096 (Cited on page 22.)
Rajwade K., Lorimer D. R., Anderson L. D., 2016, MNRAS, 455, 493 (Cited on page 16.)
Ransom S., 2011, PRESTO: PulsaR Exploration and Search TOolkit, Astrophysics Source Code Library, record ascl:1107.017 (ascl:1107.017) (Cited on pages 58 and 68.)
Ransom S. M., Eikenberry S. S., Middleditch J., 2002, AJ, 124, 1788 (Cited on page 42.)
Ransom S. M., Cordes J. M., Eikenberry S. S., 2003, ApJ, 589, 911 (Cited on pages 44 and 45.)
Ridolfi A., et al., 2021, MNRAS, 504, 1407 (Cited on pages 25, 44 and 59.)
Rocha D. F., Almeida L. A., Damineli A., Navarete F., Abdul-Masih M., Mace G. N., 2022, MNRAS, 517, 3749 (Cited on page 76.)
Ronchi M., Rea N., Graber V., Hurley-Walker N., 2022, ApJ, 934, 184 (Cited on page 76.)
Ruderman M., 1972, ARA&A, 10, 427 (Cited on page 77.)
Russell H. N., 1931, MNRAS, 91, 951 (Cited on page 12.)
Scheuer P. A. G., 1968, Nature, 218, 920 (Cited on page 19.)
Schnitzeler D. H. F. M., 2012, MNRAS, 427, 664 (Cited on page 27.)
Sieber W., 1973, A&A, 28, 237 (Cited on page 16.)
Silich S., Turner J., Mackey J., Martínez-González S., 2023, ApJ, 944, L32 (Cited on page 75.)

Staelin D. H., 1969, IEEE Proceedings, 57, 724 (Cited on pages 47 and 69.)
Staelin D. H., Reifenstein III E. C., 1968, Science, 162, 1481 (Cited on page 12.)
Stappers B., Kramer M., 2016, in MeerKAT Science: On the Pathway to the SKA. p. 9, doi:10.22323/1.277.0009 (Cited on page 51.)
Staveley-Smith L., et al., 1996, PASA, 13, 243 (Cited on pages 53 and 66.)
Tan C. M., et al., 2018, ApJ, 866, 54 (Cited on page 46.)
Tauris T. M., van den Heuvel E. P. J., 2006, Formation and evolution of compact stellar X-ray sources. pp 623–665 (Cited on page 21.)
Tauris T. M., van den Heuvel E. P. J., Savonije G. J., 2000, ApJ, 530, L93 (Cited on page 28.)
Tauris T. M., et al., 2017, ApJ, 846, 170 (Cited on page 28.)
Torne P., et al., 2017, MNRAS, 465, 242 (Cited on pages 16 and 21.)
Toscano M., Bailes M., Manchester R. N., Sandhu J. S., 1998, ApJ, 506, 863 (Cited on page 16.)
Verbiest J. P. W., Weisberg J. M., Chael A. A., Lee K. J., Lorimer D. R., 2012, ApJ, 755, 39 (Cited on page 69.)
Vogt H., 1926, Astronomische Nachrichten, 226, 301 (Cited on page 12.)
Wang Y., et al., 2022, ApJ, 930, 38 (Cited on page 25.)
Westerlund B., 1961, PASP, 73, 51 (Cited on page 65.)
Wongphechauxsorn J., et al., 2024, MNRAS, 527, 3208 (Cited on page 69.)
Yao J. M., Manchester R. N., Wang N., 2016, preprint, (arXiv:1610.09448) (Cited on pages 19 and 27.)
Yao J. M., Manchester R. N., Wang N., 2017, ApJ, 835, 29 (Cited on page 68.)
Zhang L., et al., 2020, ApJ, 905, L8 (Cited on page 49.)
Zhou D., et al., 2024, Science China Physics, Mechanics, and Astronomy, 67, 269512 (Cited on pages 47 and 64.)
Zhu W. W., et al., 2014, ApJ, 781, 117 (Cited on page 39.)
van Haarlem M. P., et al., 2013, A&A, 556, A2 (Cited on page 27.)
van Straten W., Bailes M., 2011, PASA, 28, 1 (Cited on page 68.)
van Straten W., Demorest P., Oslowski S., 2012, Astronomical Research and Technology, 9, 237 (Cited on page 68.)